Line Lists Including Intensities for Diatomic Molecules of Astronomical Interest and Remote Sensing Measurements of Greenhouse Gases

James S. A. Brooke

Doctor of Philosophy

University of York
Chemistry

September 2014

Abstract

Line lists including positions and absolute intensities have been produced using a combination of theoretical and experimental methods, for several spectroscopic systems of diatomic molecules, including the C_2 and $^{12}C^{13}C$ Swan systems, the CN, ^{13}CN, and $C^{15}N$ $A^2\Pi$-$X^2\Sigma^+$ (red), $B^2\Sigma^+$-$X^2\Sigma^+$ (violet), and $X^2\Sigma^+$ state rovibrational systems, the CP $A^2\Pi$-$X^2\Sigma^+$ system, and the NH $X^3\Sigma^-$ state rovibrational and rotational transitions. Preliminary calculations for the OH $X^2\Pi$ state rovibrational transitions have also been performed. RKR potential energy curves, vibrational wavefunctions, and matrix elements (MEs) were calculated using the programs RKR1 and LEVEL. The MEs were transformed from Hund's case (b) to (a), for which an equation was derived. Einstein A values were calculated from the case (a) MEs and molecular constants using PGOPHER. These lists will be useful in the fields of astronomy, combustion science, materials science, and anywhere else that transitions of these diatomic molecules are investigated.

Line intensities have also been used to retrieve an atmospheric CO_2 volume mixing ratio. A new technique for the satellite remote sensing of atmospheric greenhouse gases via absorption of short-wave infrared laser signals transmitted between counter-rotating satellites in low Earth orbit has recently been proposed; this would enable the acquisition of a long-term, stable, global set of altitude-resolved concentration measurements. The first ground-based experimental demonstration of this new infrared-laser occultation method is presented, in which the atmospheric absorption of CO_2 near 2.1 µm and CH_4 near 2.3 µm were measured over a 144 km path length between two peaks in the Canary Islands, using relatively low power diode lasers. The retrieved CO_2 volume mixing ratio of 400 ppm (±15 ppm) is consistent within experimental uncertainty with simultaneously recorded validation measurements. The new method has a sound basis for monitoring atmospheric CO_2 and other greenhouse gases.

Contents

Abstract **3**

List of figures **10**

List of tables **20**

Acknowledgements **25**

Declaration **27**

1 Introduction **31**

1.1 Stellar Molecules and Elemental Composition 31

1.2 Stellar Elemental Abundance Calculations 32

1.3 Other Astronomical Environments 33

1.4 Spectral Lines, Concentrations, and Absolute Line Intensities 33

1.5 General Procedure for the Production of Line Lists 34

1.6 Thesis Structure 35

2 Theory **37**

2.1 Electronic, Vibrational, and Rotational Energy Levels 37

2.1.1 Schrödinger Equation 37

2.1.2 Nuclear Rotation 38

2.1.3 Nuclear Vibration 40

2.1.3.1 One-Dimensional Schrödinger equation 40

2.1.3.2 Quantum Harmonic Oscillator 41

2.1.3.3 Real Potential Energy Curves 42

2.1.4 Calculation of Potential Energy Curves using the RKR Method . . 44

2.1.5 LEVEL program and example 45

2.2 Electronic Angular Momentum 50

2.2.1 Electronic Angular Momentum in Atoms 50

2.2.2 Good Quantum Numbers 51

2.2.3 Electronic and Nuclear Rotational Angular Momentum in Diatomic Molecules 51

2.2.4 Hund's Cases 54

2.2.4.1 Hund's Case (a) 54

2.2.4.2 Hund's Case (b) 55

2.2.4.3 Other Hund's Cases 56

2.3 Parity 57

2.3.1 Total and Rotationless Parity 57

2.3.2 Gerade/Ungerade Parity 59

2.3.3 Symmetric/Antisymmetric Parity 59

2.4 The Effective Hamiltonian 60

2.4.1 Example with a $^3\Pi$ State 62

2.4.2 Other Molecular Constants 65

2.4.2.1 Spin-Rotation Constant γ 65

2.4.2.2 Spin-Spin Constant λ 66

2.4.2.3 Lambda-Doubling Constants o, p, and q 68

2.4.2.4 Centrifugal Constants 69

2.4.3 Parity Matrices 70

2.4.4 Perturbations 71

2.5 Line Intensities 72

2.5.1 Notation 73

2.5.2 The Line Intensity, $S_{J'F'JF}$ 74

2.5.3 The Vibronic Part 76

2.5.4 Case (b) to (a) Transformation 77

2.5.5 The Herman-Wallis (H-W) Effect 84

2.5.6 The "N Only" Method 84

2.5.7 Transformation of Hund's Case (a) Transition Matrix 87

2.5.8 Band intensities and lifetimes 90

2.6 Summary 90

3 The C_2 Swan System **93**

3.1 Preface 93

3.2 Introduction 93

3.2.1 C_2 $a^3\Pi_u$ and $d^3\Pi_g$ States 97

3.2.2 $d^3\Pi_g$ Perturbations 98

3.3 Recalculation of Molecular Constants 103

3.3.1 The (4,8) and (5,9) bands 104
3.3.2 Data Included in the Global Fit 105
3.4 Calculation of Line Intensities 106
3.4.1 Electronic Transition Dipole Moment 108
3.4.2 Vibrational Band Intensities 109
3.5 Analysis and Discussion 112
3.5.1 Spectral Validation 112
3.5.2 $d^3\mathbf{\Pi}_g$ Perturbations 117
3.5.3 Updated Molecular Constants 117
3.5.4 Vibrational Band Einstein A and f-values 117
3.6 $^{12}\mathbf{C}^{13}\mathbf{C}$ Swan System 118
3.7 Conclusion 119
3.8 Future Work 121

4 The CN $A^2\Pi$-$X^2\Sigma^+$ (red), $B^2\Sigma^+$-$X^2\Sigma^+$ (violet), and Ground State Rovibrational Systems 123

4.1 Preface 123
4.2 Introduction 123
4.2.1 CN $B^2\mathbf{\Sigma}^+$-$X^2\mathbf{\Sigma}^+$ and $X^2\mathbf{\Sigma}^+$-$X^2\mathbf{\Sigma}^+$ Systems 126
4.2.2 CN $A^2\mathbf{\Pi}$-$X^2\mathbf{\Sigma}^+$ System 128
4.3 Method of Calculation 130
4.3.1 Calculation of Transitions Dipole Moment Functions 132
4.3.2 The H-W Effect 134
4.3.3 Transformation from Hund's Case (a) to Case (b) MEs 136
4.3.4 The $A^2\mathbf{\Pi}$-$X^2\mathbf{\Sigma}^+$ System 137
4.3.5 The $B^2\mathbf{\Sigma}^+$-$X^2\mathbf{\Sigma}^+$ System 139
4.3.6 The $X^2\mathbf{\Sigma}^+$-$X^2\mathbf{\Sigma}^+$ System 139
4.3.7 Vibrational Einstein $\boldsymbol{A}_{v'v}$ and $\boldsymbol{f}_{v'v}$ Values 139
4.4 Results and Discussion 140
4.4.1 The $A^2\mathbf{\Pi}$ State 140
4.4.2 The $B^2\mathbf{\Sigma}^+$ State 141
4.4.3 The $X^2\mathbf{\Sigma}^+$ State 142
4.4.4 Validation of Computed Results 143
4.5 Isotopes of CN 146

4.6 The CP $A^2\Pi$-$X^2\Sigma^+$ System . . . 147
4.6.1 Introduction . . . 147
4.6.2 Calculations . . . 147
4.6.3 Results and Analysis . . . 149
4.7 Conclusion . . . 149

5 NH $X^3\Sigma^-$ Ground State Rovibrational and Rotational Transitions 155
5.1 Preface . . . 155
5.2 Introduction . . . 155
5.3 NH $X^3\Sigma^-$ Ground State . . . 158
5.4 Calculation of line intensities . . . 161
5.4.1 Calculation of the New Dipole Moment Function . . . 161
5.4.2 Hund's case (b) to (a) transformation . . . 163
5.4.3 H-W Effect . . . 165
5.5 Results and Discussion . . . 165
5.5.1 New NH FTS Spectrum . . . 165
5.5.2 Spectral Validation . . . 166
5.5.3 Lifetimes and Band Strengths . . . 168
5.5.4 Calculations With the 1975 Meyer and Rosmus Dipole Moment Function . . . 171
5.6 Conclusion . . . 171

6 The OH $X^2\Pi$ Rovibrational Transitions 173
6.1 Preface . . . 173
6.2 Introduction . . . 173
6.3 Initial Calculations . . . 175
6.4 Initial Data Analysis . . . 176
6.5 Intensity Investigation . . . 178
6.6 Hund's Case (b) and Adjusted Transformation Methods . . . 182
6.7 Conclusion . . . 183

7 IRDAS 187
7.1 Preface . . . 187
7.2 Introduction . . . 187
7.3 Plan . . . 189

7.3.1 Basic Setup, Site, and Equipment Design 189
7.3.2 Initial Measurement Mode 192
7.4 Preparation and Testing 195
7.4.1 First Gas Cell Tests 195
7.4.2 Fast Scan Mode 195
7.4.2.1 Preliminary Wavelength Calibration for Fast Scan 196
7.4.3 Rx Étalon Performance 197
7.4.4 Corridor Testing 198
7.4.5 Static Modes 198
7.4.6 Roof testing 199
7.5 Campaign 200
7.5.1 Final Tx Setup 200
7.5.2 Final Rx Setup 201
7.5.3 Changes to Modes of Operation 201
7.5.4 Good Data Acquisition 203
7.6 Data Analysis 203
7.6.1 Level 0 to Level 1 Data Processing 203
7.6.2 Final Results 204
7.6.3 Fitting 204
7.6.4 Error Calculations 206
7.6.5 Floated Fitting Parameters 206
7.6.6 CO_2 and H_2O VMR Values 207
7.6.7 Detector Gain and Offsets 207
7.6.8 Conditions for Calculated Spectra 210
7.7 Conclusion and Future Work 210

8 Summary, Conclusion, and Further Work 213
8.1 General Calculation Method 213
8.1.1 Changes to Calculation Method 214
8.2 Summary of Results 215
8.3 Application to Astronomy 217
8.4 Further Work 221

Abbreviations 223

Bibliography **224**

List of Figures

2.1 Potential energy curve within the harmonic oscillator approximation. Also shown are the first three energy levels and wavefunctions. 41

2.2 Realistic diatomic molecule potential energy curve (solid line), and a harmonic potential energy curve (dotted line) 43

2.3 Outward integration for the first iteration by LEVEL in the calculation of the NH $X^3\Sigma^-$, v=0, J=0 wavefunction. 47

2.4 Inward and outward integration for the first iteration by LEVEL in the calculation of the NH $X^3\Sigma^-$, v=0, J=0 wavefunction 48

2.5 Normalised wavefunction for the first iteration by LEVEL for the NH $X^3\Sigma^-$, v=0, J=0 level. The shaded area shows the point at which in inward and outward integrations meet. 48

2.6 Normalised wavefunctions for the first, second, and sixth of six iterations performed by LEVEL, with its first estimate of E, for the NH $X^3\Sigma^-$, v=0, J=0 level. The shaded area shows the point at which the inward and outward integrations meet. The expanded area shows that the second iteration still has a noticeable slope change, and the final wavefunction does not. The wavefunctions from the third to fifth iterations are omitted as they would appear almost identical to the final wavefunction. 49

2.7 Angular momentum in a diatomic molecule 52

2.8 Molecular orbital diagram of the C_2 $X^1\Sigma_g^+$ state 53

2.9 Molecular orbital diagram of the C_2 $a^3\Pi_u$ state 53

2.10 Angular momentum coupling in a Hund's case (a) diatomic molecule . . . 54

2.11 Energy levels of the C_2 $a^3\Pi_u$ state. The order is correct but they are not to scale. 55

2.12 Angular momentum coupling in a Hund's case (b) diatomic molecule . . 56

2.13 Energy levels of the CN $B^2\Sigma^+$ state. The order is correct but they are not to scale (the splitting between spin components is much exaggerated for clarity). 56

2.14 Energy levels of the NH $X^3\Sigma^-$ state including different constants. 67

2.15 The effect of a single perturbation on two nearby energy levels of different electronic states. 72

2.16 Calculation of a ME by LEVEL, using a C_2 Swan v′=4 and v″=3 transition as an exmaple. 78

2.17 Effect of rotation on the vibrational wavefunctions of the $d^3\Pi_g$, v=4 state of C_2 and the $X^3\Sigma^-$, v=4 state of NH (v=4 levels chosen arbitrarily as examples). Reprinted with permission from Brooke et al. JCP, 141, 054310, (2014). Copyright 2014, American Institute of Physics. 85

2.18 Transformation from a Hund's case (b) to (a) state for an inverted $^2\Pi$ state. The energy levels are ordered correctly but are not to scale. 86

2.19 Overall method for the production of line lists for diatomic molecules. The green boxes indicate the parts that could be mostly automated, whilst more specific considerations are required for those in red. 91

3.1 Low lying electronic states and electronic systems of C_2 (adapted from Tanabashi et al. (2007)). 95

3.2 Calculated energy level progressions (excluding local perturbations) of the three F components for the C_2 $a^3\Pi_u$ v=0 level. The energy is relative to the vibrational origin of the v=0 level. 98

3.3 Possible transitions in the C_2 Swan system from a single J and F level. . . 99

3.4 Calculated stick spectrum of the C_2 Swan system (1,1) band, at 1500 K. . . 100

3.5 Potential energy curves of the C_2 $d^3\Pi_g$ and $b^3\Sigma_g^-$ states, showing the locations of the vibrational levels for which local perturbations are analysed. The potential energy curve and vibrational levels for the $b^3\Sigma_g^-$ state were calculated using equilibrium constants based on molecular constants for v=0-4 from Davis et al. (1988) and v=16 and 19 from this work. 102

3.6 The potential energy curves of the C_2 Swan System. Reprinted from JQSRT, 124, Brooke et al., Line strengths and updated molecular constants for the C_2 Swan system, 11-20, Copyright (2013), with permission from Elsevier. 109

3.7 The electronic transition dipole moment of the C_2 Swan system. Reprinted from JQSRT, 124, Brooke et al., Line strengths and updated molecular constants for the C_2 Swan system, 11-20, Copyright (2013), with permission from Elsevier. 110

3.8 A section of the (0,0) band of the C_2 Swan system. P branch: J''=36-41, R branch: J''=7-13. Reprinted from JQSRT, 124, Brooke et al., Line strengths and updated molecular constants for the C_2 Swan system, 11-20, Copyright (2013), with permission from Elsevier. 114

3.9 A section of the Δv=+1 sequence of the C_2 Swan system, showing that the (1,0) R branch lines match well. The less intense lines do not match as closely. They are a mixture of the (1,0) P branch, the (9,8) R branch and the (8,7) P branch. (1,0) R branch: J''=39-45. Reprinted from JQSRT, 124, Brooke et al., Line strengths and updated molecular constants for the C_2 Swan system, 11-20, Copyright (2013), with permission from Elsevier. . . . 114

3.10 A section of the Δv=+2 sequence of the C_2 Swan system. Shown is a mixture of the (2,0) R branch, the (3,1) R and P branches, the (4,2) and the P branch,(5,3) P branch,(6,4) P branch.(2,0) R branch: J''=13-16, (3,1) R branch: J''=47-51, (3,1) P branch: J''=2-4, (4,2) P branch: J''=5-12 and 39-48, (5,3) P branch: J''=5-17 and 45-52, (6,4) P branch: J''=1-5. Reprinted from JQSRT, 124, Brooke et al., Line strengths and updated molecular constants for the C_2 Swan system, 11-20, Copyright (2013), with permission from Elsevier. 114

3.11 A section of the Δv=-1 sequence of the C_2 Swan system. The less intense lines belong to the (0,1) Q branch. (0,1) P branch: J''=1-6, (0,1) R branch: J''=25-31. 115

3.12 A section of the Δv=-2 sequence of the C_2 Swan system, located near the (0,2) band head. All of the features belong to the (2,0) P branch. J''=1-5 and 17-22 115

3.13 A section of the Δv=0 sequence of the C_2 Swan system. The less intense lines are caused by the (1,1) P branch and the (0,0) P branch. (1,1) R branch: J''=10-17, (0,0) R branch: J''=27-32. 115

3.14 A section of the Δv=0 sequence of the C_2 Swan system. The less intense lines are caused by the (3,3) P and R branches, the (2,2) P branch the (1,1) P branch and the (8,8) P branch. (2,2) R branch: J''=17-22, (1,1) R branch: J''=30-34, (0,0) R branch: J''=41-44. 116

3.15 A section of the Δv=-2 sequence of the C_2 Swan system. (2,4) R branch: J''=10-15, (2,4) P branch: J''=33-38, (1,3) R branch: J''=28-31. The circular labels refer to the calculated lines 116

4.1 Possible transitions with N'=3 in the CN $B^2\Sigma^+$-$X^2\Sigma^+$ system. Stronger lines are indicated with thicker arrows. 127

4.2 Possible transitions with N'=3 in the CN $A^2\Pi$-$X^2\Sigma^+$ system. Generally stronger lines are indicated with thicker arrows. (for the upper state, N is not a good quantum number, but can still be useful a a label) 129

4.3 Calculated stick spectrum of the CN $A^2\Pi$-$X^2\Sigma^+$, (2,1) band, using a temperature of 2500 K. 130

4.4 Relative intensities of the CN $B^2\Sigma^+$-$X^2\Sigma^+$ system, 9-7 and 10-2 bands. The black lines are calculated by using only one TDM matrix element for the whole band and including no H-W effect ("N only" method). The green dots include the H-W effect and the Hund's case (b) to (a) transformation of the matrix elements. The red lines are calculated by not performing the Hund's case transformation, and using the quantum number N instead of J to account for the H-W effect. For both parts of the figure, the intensities have been calculated using a rotational temperature of 500 K, showing J up to 30.5. The 9-7 band was used as one example as this has the largest H-W effect for any observed band of the $B^2\Sigma^+$-$X^2\Sigma^+$ system. The 10-2 band is a typical example of the extent of the effect for the very weak bands. Reproduced from (Brooke et al., 2014*b*) by permission of the AAS. 135

4.5 Theoretical DMFs for the CN $X^2\Sigma^+$ ground state. Reproduced from (Brooke et al., 2014*b*) by permission of the AAS. 142

4.6 A comparison of the observed (upper) and simulated (lower) spectra of the v=-1 sequence of the $A^2\Pi$-$X^2\Sigma^+$ system of CN. The unmarked emission lines near the 6-7 and 7-8 bands are rovibrational lines of the 2-0 overtone of HCl, present as an impurity. The absence of the 5-6 band in both spectra is consistent with the very small Franck-Condon factor calculated by LEVEL. Reproduced from (Brooke et al., 2014*b*) by permission of the AAS.144

4.7 A comparison of a part of the observed (upper) and simulated (lower) spectra of the $A^2\Pi$-$X^2\Sigma^+$, 0-1 band near the R_2 head showing a very good correspondence between the two spectra. Reproduced from (Brooke et al., 2014*b*) by permission of the AAS. 145

4.8 A comparison of the observed (upper) and simulated (lower) spectra of the $A^2\Pi$-$X^2\Sigma^+$, 1-0, ${}^sR_{21}$ branch. Reproduced from (Brooke et al., 2014*b*) by permission of the AAS. 145

4.9 A section of the observed (upper) and simulated (lower) spectra of the $B^2\Sigma^+$-$X^2\Sigma^+$, 13-13 band comparing the intensity distribution of the R and P branches. Reproduced from (Brooke et al., 2014*b*) by permission of the AAS. 146

4.10 A comparison of intensity distribution in the observed (upper) and simulated (lower) spectra of the CP $A^2\Pi$-$X^2\Sigma^+$, (0,0) band, showing good agreement. Reprinted from JQSRT, 138, Ram et al., Einstein A-values and oscillator strengths of the $A^2\Pi$-$X^2\Sigma^+$ system of CP, 107-115, Copyright (2014), with permission from Elsevier. 150

4.11 Relative intensities of the CP $A^2\Pi$-$X^2\Sigma^+$, (1,1) and (8,5) bands. The black lines are calculated by using only one TDM matrix element for the whole band and including no H-W effect. The green diamonds include the H-W effect and the Hund's case (b) to (a) transformation of the matrix elements. The red circles are calculated by not performing Hund's case transformation, and using the " N only" method, described in Section 2.5.6. For both parts of the figure, the intensities have been calculated using a rotational temperature of 500 K. J up to 55.5 is shown for the (1,1) band and to 30.5 for the (8.5) band. The (1,1) band was used as a typical example of the difference between the methods for the observed vibrational levels. The (8.5) band is shown as an example of when the H-W effect is strong. Reprinted from JQSRT, 138, Ram et al., Einstein A-values and oscillator strengths of the $A^2\Pi$-$X^2\Sigma^+$ system of CP, 107-115, Copyright (2014), with permission from Elsevier. 151

4.12 A comparison of a portion of the observed (upper) and simulated (lower) spectra of the $A^2\Pi$-$X^2\Sigma^+$, (1,0) band of CP, showing a good correspondence between the two spectra. Reprinted from JQSRT, 138, Ram et al., Einstein A-values and oscillator strengths of the $A^2\Pi$-$X^2\Sigma^+$ system of CP, 107-115, Copyright (2014), with permission from Elsevier. 152

4.13 Comparison of the observed (upper) and simulated (lower) spectra of the (0,0), $^sR_{21}$ branch, showing good agreement. Reprinted from JQSRT, 138, Ram et al., Einstein A-values and oscillator strengths of the $A^2\Pi$-$X^2\Sigma^+$ system of CP, 107-115, Copyright (2014), with permission from Elsevier. . 153

5.1 Energy levels of the NH $X^3\Sigma^-$ state. The distribution of F levels within each N level is approximately correct, but the difference between the F levels is greatly exaggerated. 159

5.2 Possible transitions in emission from an N=6 level in the NH $X^3\Sigma^-$ state. The distribution of F levels within each N level is approximately correct, but the difference between the F levels is greatly exaggerated. 160

5.3 Calculated potential energy curves and DMFs for the $X^3\Sigma^-$ ground state of NH. The black line is the potential used in LEVEL, and the green circles are the ab initio potential (calculated along with the DMF and reported by Campbell et al. (2008)). The red dashed line is the DMF used in this study (reported by Campbell et al. (2008)), and the blue diamonds are the DMF calculated by Meyer and Rosmus (1975). Reprinted with permission from Brooke et al. JCP, 141, 054310, (2014). Copyright 2014, American Institute of Physics. 162

5.4 H-W effect for the NH $X^3\Sigma^-$ state (1,0) band. $F(m)$ is equal to the ME divided by the ME for the Q(0) transition. 165

5.5 Observed (at Old Dominion University, Norfolk, VA, USA) and calculated spectra of NH. The lines that continue past the top of the y-axis are intense atomic lines. The features that can clearly be seen are the R branches of the 1-0, 2-1, 3-2, 4-3 and 5-4 bands. The calculated spectrum was convolved with a Gaussian function to best match the observed broadening. Effective rotational and vibrational temperatures of 1800 K and 5000 K were used, respectively. Reprinted with permission from Brooke et al. JCP, 141, 054310, (2014). Copyright 2014, American Institute of Physics. 167

5.6 Ratio of P and R branch relative intensities for the new experimental spectrum (recorded at Old Dominion University, Norfolk, VA, USA), the calculated spectrum, the spectrum observed by Boudjaadar et al. (1986) and analysed by Chackerian et al. (1989), and the calculated spectrum without the inclusion of the H-W effect. The error bars are large for the higher N' values due to the low signal to noise ratio observed in the P branch. A good match is seen between both sets of observed values and the calculated values including the H-W effect, except for N'=5 from the spectrum observed in this work. This could be due to a line overlapping the ${}^{\mathrm{P}}\mathrm{P}_3(6)$ line as this appears more intense than expected. Reprinted with permission from Brooke et al. JCP, 141, 054310, (2014). Copyright 2014, American Institute of Physics. 169

5.7 Observed and calculated IR spectra of NH. a - FTS spectrum obtained at Old Dominion University, Norfolk, VA. The red line and dots indicate the intensity of the 1-0 band P branch (left) and R branch (right). The lines that continue past the top of the y axis are intense atomic lines. The R branches of the 2-1, 3-2, and 4-3 bands are the other features that are clearly visible here. b and c - Calculated spectra of the NH 1-0 band only, with and without the inclusion of the H-W effect. Its inclusion gives a better relative intensity difference between the P and R branches. The calculated spectrum was convolved with a Gaussian function to best match the observed broadening. A rotational temperature of 1300 K was used. Reprinted with permission from Brooke et al. JCP, 141, 054310, (2014). Copyright 2014, American Institute of Physics. 170

6.1 Calculated and experimental dipole moment functions for the OH $X^2\Pi$ state. 175

6.2 Calculated and experimental μ_v values of OH ($X^2\Pi$). The error bars of the experimental values for v=0 and v=1 are not shown as they are slightly smaller than the size of the symbols. 177

6.3 Ratio of Einstein $A_{J'F'JF}$ values calculated in this work to those in HITRAN. Intensities for lines that have been observed are shown in blue, while non-observed lines are in red. 178

6.4 Ratio of Einstein $A_{J'F'JF}$ values calculated in this work to those in HITRAN. Intensities for lines that have been observed are shown in blue, while non-observed lines are in red. Only transitions with F'=F'' are present. 179

6.5 H-W effect in the OH $X^2\Pi$, (2,0) band. The values plotted are equal to the R branch intensity divided by the P branch intensity for specified F transitions that share an upper level. The observed (green) and HITRAN (blue) lines are the same on each graph, and are present for the purpose of comparison with our calculations using four different methods (red lines). The red lines on the top row are calculated using the transformation method, and those on the bottom use the N only method. The red lines on the left use the newly calculated DMF, and those on the right use the HITRAN DMF. 181

7.1 Illustration of the laser link between the Canary Islands La Palma and Tenerife. Image 2012 Google © 2012 TerraMetrics © and 2012 GRAFCAN ©. 189

7.2 Calculated spectrum of the CH_4 (2.1 μm) region. This shows the region covered by the two IR lasers for CH_4 and H_2O measurements (L1 and L2). CH_4 only - calculated for CH_4 only. All species - calculated including all relevant atmospheric species; almost all extra absorption is due to H_2O. The labels indicate the originally targeted absorption line positions and reference (minimum absorption) position (Table 7.2). Depending on actual frequency scan ranges (Table 7.1), other spectral sections are used. For conditions see Section 7.6.8. 191

7.3 Calculated spectrum of the CH_4 (2.3 μm) signal region. This region is covered by the IR laser for CH_4 measurements (L4). CH_4 only - calculated for CH_4 only. All species - calculated including all relevant atmospheric species; almost all extra absorption is due to H_2O. The label indicates the target absorption line position (Table 7.2). Depending on actual frequency scan ranges, other spectral sections can be used. For conditions see Section 7.6.8. 191

7.4 Calculated spectrum of the CH_4 (2.3 µm) reference region. This region is covered by the IR laser for CH_4 reference measurements (L3). CH_4 only - calculated for CH_4 only. All species - calculated including all relevant atmospheric species; almost all extra absorption is due to H_2O. The label indicates the target reference (minimum absorption) position (Table 7.2). Depending on actual frequency scan ranges, CH_4 might also be retrieved in this region. For conditions see Section 7.6.8. 192

7.5 Initial Tx breadboard schematic **1-4:** SWIR diode lasers **10:** 1-5 µm wavemeter **5, 6, 14, 19, 23, 25, 26:** Protected silver-coated mirrors with reflectivity of ca. 96% at 2.1 µm **7, 11:** Dichroic mirrors: Maximum reflectivity at ca. 2310 nm and maximum transmission at ca. 2096 nm **12, 13, 17, 18, 24, 27:** Beam splitters **21, 22:** InGaAs Photodiode detectors **28:** Polarising beam splitter (used as combiner) **29:** Chopper **15, 20:** parabolic mirror 193

7.6 Initial Rx breadboard schematic **3:** Beam from telescope **4:** Rx Étalon **5:** Protected silver-coated mirror with reflectivity of ca. 96% at 2.1 µm **6, 7:** Parabolic Mirrors **8, 9:** InGaAs Photodiode detectors 194

7.7 Pre-campaign fast scan mode 196

7.8 Schematic diagram of the optical Tx and Rx breadboards. **a -** Tx. **b -** Rx. **AT** - Neutral density filter to attenuate green laser (when necessary), **BD** - Beam dump in motorized flipping mount, **BS** - Dichroic beam splitter with transmission enhancing coating for ca. 2000 nm. **C** - ARTEMIS beam collimator (focal length = 1350 mm, beam diameter = 34 mm), **GT** - Glan-Thomson polarising prism, **L** - CaF2 lens (focal length = 10 mm), **LG** - Frequency-doubled, Nd:YAG laser (200 mW, 532 nm). **LR** - IR diode laser 2 (serial number 592/21-24/nanoplus) or 4 (592/21-19/nanoplus), **LS** - IR diode laser 1 (264/3-9/nanoplus) or 3 (264/17-19/nanoplus), **M** - Protected silver-coated mirrors with reflectivity of ca. 96% at 21 µm, **MF** - Silver-coated IR mirrors (M) in motorised flipping mount, **PD** - InGaAs photodiode detector, **PM** - Gold-plated parabolic mirror, **Wavemeter** - 1.0-5.0 µm wavemeter (Bristol Instruments 621-a). 202

7.9 Observed and calculated atmospheric transmittance spectra in the CO_2 region. All features arise from CO_2 absorption except for one, which is due to H_2O (labelled). 205

7.10 Observed and calculated atmospheric transmittance spectra in the CH_4 region. 205

8.1 H-W effect for the NH $X^3\Sigma^-$, (1,0) band, including the results with the adjusted transformation equation. 216

List of Tables

2.1 Operators and their eigenvalues when operating on a set of simultaneous eigenfunctions, in the absence of spin-orbit coupling (discussed later.) . . 52

2.2 Possible combinations of Λ and Σ to give Ω in a $^3\Pi$ state. 54

2.3 Total and rotationless parity 58

2.4 Relationships between +/-, g/u, and s/a parity 60

2.5 Possible combinations of Λ and Σ to give Ω in a $^3\Pi$ state. 63

2.6 Hamiltonian matrix for a $^3\Pi$ state in a Hund's case (a) basis 63

2.7 $\mathbf{\hat{H}_{rot}} + \mathbf{\hat{H}_{so}}$ for a $^3\Pi$ state in a Hund's case (a) basis 63

2.8 Evaluated $\mathbf{\hat{H}_{rot}} + \mathbf{\hat{H}_{so}}$ matrix for a $^3\Pi$ state in a Hund's case (a) basis . . . 64

2.9 $\mathbf{\hat{H}_{rot}}$ for the $\mathrm{C_2}$ $\mathrm{a^3\Pi_u}$ state, v=0, J=2 level in a Hund's case (a) basis. 64

2.10 Eigenvector coefficient matrix ($\mathbf{\hat{X}}$) from the diagonalisation of $\mathbf{\hat{H}_{rot}}$, for the $\mathrm{C_2}$ $\mathrm{a^3\Pi_u}$ state, v=0, J=2 level in a Hund's case (a) basis. 64

2.11 $\mathbf{\hat{H}_{rot}} + \mathbf{\hat{H}_{so}}$ for the $\mathrm{C_2}$ $\mathrm{a^3\Pi_u}$ state, v=0, J=2 level in a Hund's case (a) basis (in $\mathrm{cm^{-1}}$). 65

2.12 Eigenvector coefficient matrix ($\mathbf{\hat{X}^{-1}}$) from the diagonalisation of $\mathbf{\hat{H}_{rot}} + \mathbf{\hat{H}_{so}}$, for the $\mathrm{C_2}$ $\mathrm{a^3\Pi_u}$ state, v=0, J=2 level (in $\mathrm{cm^{-1}}$). 65

2.13 Possible combinations of Λ and Σ to give Ω in a $^3\Sigma^-$ state. 66

2.14 Evaluated $\mathbf{\hat{H}_{sr}}$ matrix for a $^3\Sigma^-$ state in a Hund's case (a) basis 66

2.15 Evaluated $\mathbf{\hat{H}_{ss}}$ matrix for a $^3\Sigma^-$ state in a Hund's case (a) basis 67

2.16 $\mathbf{\hat{H}_{ld}}$ ($\Delta\Lambda = +2$ section) for a $^3\Pi$ state in a Hund's case (a) basis. 69

2.17 $\mathbf{\hat{H}_{ld}}$ ($\Delta\Lambda = -2$ section) for a $^3\Pi$ state in a Hund's case (a) basis. 69

2.18 Evaluated $\mathbf{\hat{H}_{ld}}$ matrix for a $^3\Pi$ state in a Hund's case (a) basis 69

2.19 Evaluated $\mathbf{\hat{N}}^4$ matrix for a $^3\Pi$ state in a Hund's case (a) basis, where $x = J(J+1)$. 70

2.20 Parity transformation matrix for a $^3\Pi$ state 71

2.21 Pure Ω transition matrix set up by PGOPHER for the CN $\mathrm{A^2\Pi}$-$\mathrm{X^2\Sigma^+}$ (1,0) R(4.5) example transition, using the transformation method. 83

2.22 Pure Ω transition matrix set up by PGOPHER for the CN $\mathrm{A^2\Pi}$-$\mathrm{X^2\Sigma^+}$, (1,0), R(4.5) example transition, using the N only method. 87

2.23 Pure Ω transition matrix set up by PGOPHER for the (1,0), R(4) example transition. 88
2.24 Symmetrised parity transition matrices for the (1,0), R(4) example transition. 88
2.25 Left - Symmetrised *e* Hamiltonian matrix for the v=1, *J*=4 example level. Right - eigenvectors resulting from the diagonalisation of this matrix. . . . 88
2.26 Left - Symmetrised *f* Hamiltonian matrix for the v=1, *J*=4 example level. Right - eigenvectors. 89
2.27 Left - Symmetrised *e* Hamiltonian matrix for the v=0, *J*=3 example level. Right - eigenvectors. 89
2.28 Left - Symmetrised *f* Hamiltonian matrix for the v=0, *J*=3 example level. Right - eigenvectors. 89
2.29 Transformed parity transition matrices for the (1,0), R(4) example transition, in terms of the true *F* and parity levels 89

3.1 Perturbation constants for the $d^3\Pi_g$ v′=4 and v′=6 levels of the C_2 Swan system. Those of Bornhauser et al. (2010, 2011), and those resulting from the fit of all molecular constants are reported. 101
3.2 Molecular constants for the $b^3\Sigma_g^-$, v′=16 and v′=19 and $^5\Pi$ states, which perturb the $d^3\Pi_g$, v′=4 and v′=6 levels. Those of Bornhauser et al. (2010, 2011), and those resulting from the fit of all molecular constants are reported.101
3.3 Updated molecular constants for the $d^3\Pi_g$ state of the C_2 Swan system (in cm^{-1}). 107
3.4 Updated molecular constants for the $a^3\Pi_u$ state of the C_2 Swan system (in cm^{-1}). 107
3.5 Equilibrium molecular constants[a] for the C_2 Swan system. 108
3.6 Calculated TDMF for the C_2 Swan system. 110
3.7 Einstein $A_{v'v''}$ values of the C_2 Swan system. 111
3.8 $f_{v'v''}$ values of the C_2 Swan system (a), compared to those of Schmidt and Bacskay (2007) (b). 111
3.9 Section of the published line list for the C_2 Swan system. 113
3.10 Lifetimes of vibrational levels of the C_2 $d^3\Pi_g$ state. 118

4.1 Equilibrium molecular constants for the CN $X^2\Sigma^+$, $A^2\Pi$, and $B^2\Sigma^+$ states. 131
4.2 Spectroscopic constants for the CN $X^2\Sigma^+$ state. 131

4.3 Spectroscopic constants for the CN $B^2\Sigma^+$ state. 132
4.4 Spectroscopic constants for the CN $A^2\Pi$ state. 133
4.5 Comparison of lifetimes (in µs) with the selected experimental and theoretical lifetimes of the v=0-4 vibrational levels of the CN $A^2\Pi$ state. . . 138
4.6 Comparison of current and previous Einstein $A_{v'v}$ values for several vibrational bands within the $X^2\Sigma^+$ ground state of CN 138
4.7 Comparison of calculated lifetimes (in ns) with the available experimental and theoretical lifetimes of the v=0-5 vibrational levels of the CN $B^2\Sigma^+$ state.138
4.8 Spectroscopic constants for the CP $X^2\Sigma^+$ state. 148
4.9 Spectroscopic constants for the CP $A^2\Pi$ state. 148
4.10 Equilibrium molecular constants for the CP $X^2\Sigma^+$ and $A^2\Pi$ states. 148

5.1 Summary of equilibrium dipole moments, μ_e, and v=0 averaged dipole moments, μ_0, for the $X^3\Sigma^-$ ground state of NH, since 1974. All but Paldus and Li (1996) and the experimental study calculated full dipole moment functions. Our calculated values are also included. 158
5.2 Equilibrium molecular constants for the NH $X^3\Sigma^-$ state 161
5.3 Einstein $A_{v'v}$ and $f_{v'v}$ values for vibrational transitions within the $X^3\Sigma^-$ state of NH, where Δv=1 171

6.1 Calculated and experimental lifetimes of the OH $X^2\Pi$, v=1, J=1.5, F_1 level (all values in ms). 176
6.2 Left - Symmetrised e transition matrix for the (2,0), R(1.5) example transition level with original transformation equation. Right - including $\Delta\Sigma \neq 0$ MEs. 183
6.3 Stellar Model Parameters and Abundance Summary 185

7.1 SWIR lasers and regions. 190
7.2 Originally selected absorption lines. 190
7.3 SWIR lasers and regions 209

Acknowledgements

Peter, Rob, The Leverhulme Trust, Alan, Alex, Alfie, Ann, Anthony, Ava, Colin, Colonel Barry, Chris, Dan 2, Dave, Dene, Donna, Em, Gang, Georgie, Gonzalo, Grandma, Granny, Harriet, Harry, Jamie, Jenny, Jeremy, Jin, Jonathan, Josh, Julia, Julie, Keith, Laz, Lee, Mark, Mike, Naruo, Nick, Philip, Rich H, Rich L, Sarah, Steve, Stuart, Mum, Dad, and **Katy**.

Declaration

The research described in this thesis is original work, which I undertook at the University of York during 2010–2014. All of the work contained within this thesis represents the original contribution of the author, except where explicity stated below. Some parts of this thesis have been published in journals; where items were published jointly with collaborators, the author of this thesis is responsible for the material presented here, except where explicity stated below. For each published item the primary author is the first listed author, and publications are listed below.

Chapter 3 (main C_2 section)

All of the work is my own, except for the calculation of the TDMF, which was performed by Timothy W. Schmidt and George B. Bacskay (University of Sydney, Australia), and the calculations of stellar carbon abundance and isotopic ratio discussed in the conclusion, which were performed by Chris Sneden (University of Texas, Austin). The work described in this chapter has resulted in a first author publication (Brooke et al., 2013), and much of the text is based on this.

Chapter 3 (C_2 isotopologue section)

A coauthor paper was published (Ram et al., 2014). My contributions to this study were the calculations using LEVEL and PGOPHER, the creation of the final line list, and minor contributions to writing the paper and the line position fitting.

Chapter 4 (main CN section)

The work described in this chapter has resulted in a first author publication (Brooke et al., 2014*b*), and much of the text is based on this. The line position fit, the calculation of the equilibrium constants, and RKR calculations were performed by Ram S. Ram (University of York), as were the comparisons with previously reported lifetimes. The derivation of the transformation equation was performed by Colin M. Western (University of Bristol). The calculations of the DMF and TDMFs are the work of David W. Schwenke (NASA Ames Research Center, California). The calculation of the vibrational band intensities (Einstein $A_{\mathrm{v'v}}$ and $f_{\mathrm{v'v}}$ values) and lifetimes, and their comparisons to literature values were performed by Ram S. Ram and me. I took over the calculations with the LEVEL output files and PGOPHER files with the adjusted molecular constants. I wrote the computer programs to perform the case (b) to (a) transformation and produce the PGOPHER files with intensities. This also involved writing a program to fit polynomials to the transformed case (a) MEs to take the H-W effect into account. Finally, I created the final line lists from the PGOPHER output and lists of observed transitions.

Chapter 4 (CN isotopologues section)

A coauthor paper was published (Sneden et al., 2014). My contributions to this study were very minor contributions to writing the paper, and the same contributions to the calculations as for the main CN work described above.

Chapter 4 (CP section)

A coauthor paper was published (Ram et al., 2014). My contributions to this study were major contributions to writing the paper, and the same contributions to the calculations as above.

Chapter 5

The work described in this chapter has resulted in a first author publication (Brooke et al., 2014*a*), and much of the text is based on this. All of the work is my own, except for the calculation of the TDMF, which was performed by Gerrit Groenenboom (Radboud University, Nijmegen, The Netherlands) and Marc C. van Hemert (Universiteit Leiden, Leiden, The Netherlands).

Chapter 6

All of the work is my own, except for the calculation of the DMF, which was performed by Gang Li (Harvard-Smithsonian Center for Astrophysics, Cambridge), and the calculations of stellar oxygen abundances discussed in the conclusion, which were performed by Chris Sneden (University of Texas, Austin).

Chapter 7

This work has resulted in a first author publication (Brooke et al., 2012), and much of the text is based on this. I joined this project after absorption lines had been selected and initial breadboard designs had been made. The further design, testing, and campaign were carried out as a team, to which I had a major contribution. I performed all of the programming to control the equipment and record data, was exclusively responsible for the computing side of the campaign, and the main operator of the transmitter breadboard. I also performed the data processing to the "level 1" format required by the Wegener Center, Graz, Austria, and the initial concentration retrievals (using pre-coded equations provided by Philip Martin (University of Manchester)). A coauthor publication containing the full analysis of the data (performed at the Wegener Center) is currently under review.

Chapter 1

Introduction

In this thesis, the creation of spectroscopic line lists for diatomic molecules with a particular focus on intensities will be described. These molecules have been chosen mainly because they are of interest in astronomy, but also in other fields such as combustion, materials science (see Section 3.2), and high precision spectroscopy. To be able to understand and construct models of astronomical environments, it is vital to have information on molecular and atomic abundances, and this information can be provided in the form of extensive lists of transitions.

1.1 Stellar Molecules and Elemental Composition

Over the course of a star's life, as various nuclear fusion reactions occur, its elemental composition changes (Kaler, 1997). It is therefore vital to have knowledge of elemental abundances to be able to understand stellar evolution. Relatively young stars such as the Sun do not yet have hot enough cores to fuse helium and produce heavier elements (though some are produced by neutron capture (Kappeler et al., 1989)), but do contain heavier elements that were produced in older, and now dead stars. These heavier elements are important to a star's evolution, for example for a given stellar mass, the lifetime of a star is decreased by increasing metallicity (the ratio of the number of non-hydrogen or helium atoms to the number of hydrogen and helium atoms) (Adams and Laughlin, 1997).

Stars such as the Sun are cool enough for diatomic molecules to exist within their atmosphere (Russell, 1934; Fujita, 1939; Wallace et al., 1998*b*,*a*), for example CO, C_2, CN, CH, NH, OH, MgH, AlH, CaH, and TiO (Bernath, 2009). Polyatomic molecules, however, are only present in stars of lower temperature (Swings and McKellar, 1948; Tsuji, 1986). To properly classify a star and be able to develop accurate models, knowledge of the abundances of these diatomic molecules is vital (Tsuji, 1986; Bernath, 2009). The chemistry that occurs in a star is dependent on the elemental composition, for which a good example is the C/O ratio. In the photosphere (the area from which photons can escape from the star), most of the carbon and oxygen forms CO, and therefore various carbon-containing molecules will be more likely to exist with a high C/O ratio, and oxygen-containing molecules with a low C/O ratio. This dramatically affects the chemistry, resulting in different stellar classifications (Wood, 1985; Wallerstein and Knapp, 1998).

1.2 Stellar Elemental Abundance Calculations

Spectroscopic transitions of diatomic molecules have been used to calculate the elemental abundance in cool stars (Lambert et al., 1984; Lambert et al., 1986; Smith and Lambert, 1986; Aoki and Tsuji, 1997; Suntzeff, 1981) and the Sun (Grevesse et al., 1990; Asplund et al., 2009). Carbon, nitrogen, and oxygen atomic lines have been used for the same purpose (Gies and Lambert, 1992; Grevesse et al., 2007).

Molecular lines in stellar spectra are normally seen in absorption (emission also sometimes occurs). The spectral radiance of the Sun peaks in the visible region of the spectrum, and based on this alone, the best spectral lines to use for abundance calculations would be located in or near the visible region. However, as electronic transitions of atoms and molecules are mainly in this region, it is very congested in stellar spectra (Emerson, 1996), and so there are a limited number of atomic lines that can be used successfully. Also, as mentioned above, most of the carbon, nitrogen, and oxygen atoms exist in molecular form in stellar photospheres. Therefore, the infrared region that contains most vibrational transitions can be very useful. This is especially true for cool stars and brown dwarfs, in which the lower temperatures mean that diatomic molecules are more common and atomic transitions become faint, and the wavelength peak moves into the infrared. As a result, stellar elemental abundances are often determined using either atomic or molecular lines, or both, in combination with models that link the abundances of the molecules and atoms (Asplund et al., 2009).

1.3 Other Astronomical Environments

As a result of the ejection of heavy elements during the process of a star's late life and death, non-hydrogen or helium elements are found throughout astronomical environments. At the high temperatures in stellar atmospheres, only simple molecules can exist, and this results in the presence of some molecules that would be stable on Earth such as CO and N_2 (Kaler, 1997), but also others which would not, such as C_2 (Mayer and O'Dell, 1968). They also exist, along with larger molecules (Herbst, 2005), in cold environments such as interstellar clouds and planetary nebulae. This is mainly because at the low concentrations of matter in these regions, the systems are not in local thermodynamic equilibrium due to the scarcity of collisions (Dyson and Williams, 1980). Again, to be able to construct models of these systems, knowledge of molecular abundances is vital (Herbst, 2005). Other astronomical environments in which diatomic molecules have been detected include comets (Mumma and Charnley, 2011), exoplanets (Swain et al., 2009), and circumstellar envelopes (Ziurys, 2006).

1.4 Spectral Lines, Concentrations, and Absolute Line Intensities

In astronomy and in general for remote sensing, lists of line positions and absolute line intensities are essential for the determination of molecular abundances (Bernath, 2009). To obtain an abundance from an absorption spectrum, the spectrum needs be calculated. This is accomplished using the Beer-Lambert law (including stimulated emission),

$$\frac{I}{I_0} = e^{-\sigma\left(N_l - N_u\frac{2J''+1}{2J'+1}\right)l}, \tag{1.1}$$

where $\frac{I}{I_0}$ is the transmittance, N_l and N_u are the concentrations of molecules in the lower and upper level in molecule cm^{-3}, respectively, l is the path length in cm, J is the total angular momentum quantum number, and σ is the absorption cross section in cm^{2}s^{-1}molecule^{-1}:

$$\sigma = \frac{A_{J'J''}\, g(\tilde{\nu} - \tilde{\nu}_{u-l})}{8\pi\tilde{\nu}_{u-l}^2}\frac{2J'+1}{2J''+1}, \tag{1.2}$$

where $A_{J'J''}$ is the Einstein A coefficient, a "rate constant" for a transition that is independent of any level population factors (Section 2.5), $g(\tilde{\nu} - \tilde{\nu}_{u-l})$ is a lineshape function, $\tilde{\nu}$ is the wavenumber of the transition in cm^{-1}, and u and l are the upper and lower energy levels, respectively, so that $\tilde{\nu}_{u-l}$ represents the central wavenumber of the transition.

At thermodynamic equilibrium, the concentration of molecules in each state can be replaced as

$$N_{\mathrm{v}J} = \frac{N(2J+1)e^{-E_{\mathrm{v}J}/kT}}{Q}, \tag{1.3}$$

where v is the vibrational energy level, so that Equation 1.1 can be written as

$$-\ln\left(\frac{I}{I_0}\right) = \sigma(2J''+1)\frac{\left(e^{-E_{\mathrm{v}''J''}/kT} - e^{-E_{\mathrm{v}'J'}/kT}\right)}{Q}l \tag{1.4}$$

$$= \frac{A_{J'J''}(2J'+1)g(\tilde{\nu}-\tilde{\nu}_{u-l})}{8\pi\tilde{\nu}^2_{u-l}}\frac{\left(e^{-E_{\mathrm{v}''J''}/kT} - e^{-E_{\mathrm{v}'J'}/kT}\right)}{Q}Nl, \tag{1.5}$$

where N is in molecule cm^{-3}, and the lower state energy is relative to the zero point energy. The lineshape function can be removed by integrating over both sides, as $\int g(\tilde{\nu} - \tilde{\nu}_{u-l})\, d\tilde{\nu} = 1$:

$$-\int \ln\left(\frac{I}{I_0}\right) d\tilde{\nu} = \frac{A_{J'J''}(2J'+1)}{8\pi\tilde{\nu}^2_{u-l}}\frac{\left(e^{-E_l/kT} - e^{-E_u/kT}\right)}{Q}Nl. \tag{1.6}$$

This equation shows that the concentration of a molecular species can be obtained from the area under a line in a spectrum, the partition function, lower state energy, and Einstein A value (or other absolute line intensity value).

A convenient factor is made up of the terms preceding N and l and defined as the effective integrated cross section, S', where

$$S' = \frac{A_{J'J''}(2J'+1)}{8\pi\tilde{\nu}^2_{u-l}}\frac{\left(e^{-E_l/kT} - e^{-E_u/kT}\right)}{Q}, \tag{1.7}$$

and in these equations is in units of cm^{2}cm^{-1}molecule^{-1} ("HITRAN units"). S' is not usually written in terms of the Einstein A in this manner, but is in this case as absolute line intensities in this thesis are calculated as Einstein A values.

1.5 General Procedure for the Production of Line Lists

A combination of laboratory measurements of molecules and theoretical methods can be used effectively in the creation of line lists with positions and intensities (Bernath, 2009;

Ridgway and Brault, 1984). If a line list was made with purely experimental methods, it would likely contain the best possible positions, but only for the lines that were observed. In practice, information on more lines is often required, and this requires the assignment of quantum numbers and fitting of molecular constants using an appropriate Hamiltonian (Section 2.4), allowing the positions of many more lines to be estimated. Entirely theoretical methods rarely produce line positions as accurate as observations (Bernath, 2009).

Determining absolute intensities from the laboratory spectra of molecules that are not stable under normal laboratory conditions is extremely difficult or impossible. This is because of several reasons; the molecules are produced by methods that cause the concentration to be unknown, they are unlikely to be in local thermodynamic equilibrium, the y-axis calibration is often not performed, and the signal-to-noise for most lines is poor. Theoretical calculations of the (transition) dipole moment functions, in combination with line positions observed and calculated as described above, provide the best method of creating the required line lists.

1.6 Thesis Structure

After this introduction, all of the theory required for the line position and intensity calculations that follow is described in detail. This is mostly well-established theory, but also contains a derived "transformation" equation (Section 2.5.4).

The following four chapters describe the production of line lists using this theory, for the molecules C_2, CN (and the isovalent CP), NH, and OH. They are present in the order in which these projects were undertaken. The exact theory used changed as the PhD progressed. Specifically, the effect of rotation on vibrational wavefunctions was introduced after the C_2 calculations, as was the transformation equation mentioned above, which then underwent revisions during the final OH work. Despite not all being used initially, all of the theory is described in the next chapter.

Following the four line list chapters, work on a ground based demonstration of a potential satellite mission is presented. This involved measuring the carbon dioxide concentration over a 144 km path length between two of the Canary Islands, using laser absorption spectroscopy. This is in a slightly different area of spectroscopy to the preceding chapters, but they all have a common theme of spectroscopic line intensities.

Introductory information that is specific to each study is given at the start of Chapters 3 to 7, and short conclusions are also presented at the end of each of these chapters. The final chapter is a general conclusion chapter that refers to all of the work chapters, 3 to 7.

Chapter 2

Theory

2.1 Electronic, Vibrational, and Rotational Energy Levels

2.1.1 Schrödinger Equation

The energy of a molecule can be calculated from the Schrödinger equation,

$$\hat{H}\psi = E\psi \tag{2.1}$$

where $\hat{H}$ is is the total Hamiltonian operator (in atomic units; Bernath, 2005):

$$\begin{aligned} \hat{H} &= -\sum_{i=1}^{n_e} \frac{1}{2}\nabla_i^2 - \sum_{I=1}^{n_N} \frac{1}{2M_I}\nabla_I^2 - \sum_{i=1}^{n_e}\sum_{I=1}^{n_N} \frac{z_I}{r_{iI}} + \sum_{i=1}^{n_e}\sum_{j>i}^{n_e} \frac{1}{r_{ij}} + \sum_{I=1}^{n_N}\sum_{J>I}^{n_N} \frac{z_I z_J}{R_{IJ}} && (2.2) \\ &= \hat{T}_e + \hat{T}_N + \hat{V}_{eN} + \hat{V}_{ee} + \hat{V}_{NN}, && (2.3) \end{aligned}$$

in which n_e is the number of electrons, n_N is the number of nuclei, i and j represent the indices of the electrons, I and J represent the indices of the nuclei, z_I and M_I are the charge and mass of nucleus I, respectively, r_{ij} is the distance between particles i and j, and ∇^2 is the operator

$$\nabla^2 = \frac{\partial^2}{\partial x^2} + \frac{\partial^2}{\partial y^2} + \frac{\partial^2}{\partial z^2}. \tag{2.4}$$

The five operator terms in Equation 2.3 are:

- $\hat{T}_e$, the electronic kinetic energy
- $\hat{T}_N$, the nuclear kinetic energy
- $\hat{V}_{eN}$, the electron-nuclear attraction energy

- $\hat{V}_{ee}$, the electron-electron repulsion energy
- $\hat{V}_{NN}$, the nuclear-nuclear repulsion energy

In this form, the Schrödinger equation is too difficult to solve, and instead the Born-Oppenheimer approximation is invoked. Electrons move much faster than nuclei, as they experience forces of a similar magnitude but are much lighter. Within the Born-Oppenheimer approximation, electronic motion is separated from nuclear motion, and the adjustment of the electronic part of the wavefunction is assumed to occur instantaneously with a change in nuclear coordinates. The total wavefunction can then be approximated as a product of the electronic wavefunction, ψ_{el} and the nuclear wavefunction. The electronic structure part of the calculation can be performed separately with the nuclei fixed in space:

$$\hat{H}_{el}\psi_{el} = E_{el}\psi_{el}, \tag{2.5}$$

where

$$\hat{H}_{el} = \hat{T}_e + \hat{V}_{eN} + \hat{V}_{ee}. \tag{2.6}$$

As the nuclei are fixed, the nuclear repulsion energy is simply a constant, so the potential energy, V, can be calculated using the equation:

$$(\hat{H}_{el} + \hat{V}_{NN})\psi_{el} = V\psi_{el}. \tag{2.7}$$

This can be solved by ab initio methods, providing eigenvalues and eigenfunctions, and if the calculation is performed at multiple internuclear distances, a potential energy curve, $V(r)$, is obtained. The Rydberg-Klein-Rees procedure can also provide a potential energy curve, based on experimental observations (Section 2.1.4).

The electronic state of a molecule generally has the largest contribution to its total energy. This is determined by the electronic configuration, and the term symbols given to different electronic states are described in Section 2.2.3. The remaining term for the nuclear kinetic energy is the main subject of the next two sections.

2.1.2 Nuclear Rotation

The rotation of a diatomic molecule generally has a smaller contribution than the electronic and vibrational contributions. The classical equation for the kinetic energy,

E_K, of an object with linear momentum p, mass m, and velocity v, is

$$E_K = \tfrac{1}{2}mv^2 = \frac{p^2}{2m}. \tag{2.8}$$

In terms of angular momentum (L), the expression is

$$E_K = \tfrac{1}{2}m\omega^2 = \frac{L^2}{2I}, \tag{2.9}$$

where ω is the angular velocity, L is equal to $I\omega$, I is the moment of inertia, equal to mr^2, and r is the radius of the circular motion.

The term shown above for the nuclear kinetic energy, $\hat{T}_N$, is the quantum mechanical operator relating to Equations 2.8 and 2.9. The gradient operator, ∇, gives the change in coordinates, which is the equivalent here of momentum, and M_I is the nuclear mass.

As all directions of angular momentum must be considered, the classical rotational kinetic energy is

$$T_r = \frac{L_x^2}{2I_x} + \frac{L_y^2}{2I_y} + \frac{L_z^2}{2I_z}. \tag{2.10}$$

In a rigid diatomic molecule, the total angular momentum is $\boldsymbol{J}$, I_z=0, and I_x=I_y, so

$$\begin{aligned} T_r &= \frac{J_x^2}{2I} + \frac{J_y^2}{2I} \qquad (2.11)\\ &= \frac{\boldsymbol{J}^2}{2I}, \qquad (2.12)\end{aligned}$$

where $\boldsymbol{J}^2 = J_x^2 + J_y^2 + J_z^2$. The corresponding quantum mechanical Hamiltonian is simply $-\frac{\hbar^2\nabla^2}{2I} = \frac{\hat{\boldsymbol{J}}^2}{2I}$ (McQuarrie, 2008), and

$$\begin{aligned} \frac{\hat{\boldsymbol{J}}^2\psi_J}{2I} &= \frac{J(J+1)\hbar^2\psi_J}{2I} \qquad (2.13)\\ &= BJ(J+1)\psi_J, \qquad (2.14)\end{aligned}$$

where J is now the total angular momentum quantum number, B is the molecular rotational constant in joules, equal to $\frac{\hbar}{2I}$, and the wavefunctions ψ_J are the spherical harmonics, Y_{JM}. Therefore, the rotational energy levels of a rigid diatomic molecule, not considering electronic angular momentum, are equal to $BJ(J+1)$. Clearly, this spacing increases with J, and it is much smaller than the splitting due to the vibrational levels. In reality, molecules are not rigid, and are affected by centrifugal distortion. This is discussed further in Section 2.4.2.4. The effect of nuclear rotation on the line intensities is of great importance in this thesis, and is discussed throughout Section 2.5.

2.1.3 Nuclear Vibration

2.1.3.1 One-Dimensional Schrödinger equation

The vibrational kinetic energy generally has a smaller effect on the energy than the electronic part, and a greater effect than the rotational kinetic energy. The expression for the vibrational kinetic energy in terms of momentum for a diatomic molecule is (Bernath, 2005)

$$T_{\mathrm{v}} = \frac{p(r)^2}{2\mu}, \tag{2.15}$$

where μ is the reduced mass. The classical expression for the total energy is equal to $T_{\mathrm{v}} + V(r)$, and the quantum mechanical Hamiltonian version of this is:

$$\frac{-\hbar^2}{2\mu}\nabla^2\psi + V(r)\psi = E\psi. \tag{2.16}$$

If the vibrational and rotational parts of the total wavefunction are separated, so that $\psi = \psi_{\mathrm{v}J}\psi_J$, where ψ_J is a spherical harmonic function, and a transformation from cartesian to spherical polar coordinates is performed, then the one-dimensional Schrödinger equation can be obtained:

$$\frac{-\hbar^2}{2\mu}\frac{d^2\Psi_{\mathrm{v}J}}{dr^2} + V_{\mathrm{v}J}(r)\Psi_{\mathrm{v}J} = E\Psi_{\mathrm{v}J}, \tag{2.17}$$

where $\Psi_{\mathrm{v}J} = r\psi_{\mathrm{v}J}$, and

$$V_{\mathrm{v}J}(r) = \frac{\hbar^2 J(J+1)}{2\mu r^2} + V_{\mathrm{v}}(r) \tag{2.18}$$

Note that the potential $V_{\mathrm{v}J}(r)$, and wavefunctions $\Psi_{\mathrm{v}J}$, depend on rotation. This is due to the $J(J+1)$ term above. The program LEVEL is used to solve Equation 2.17, and the steps involved are described in the next few sections.

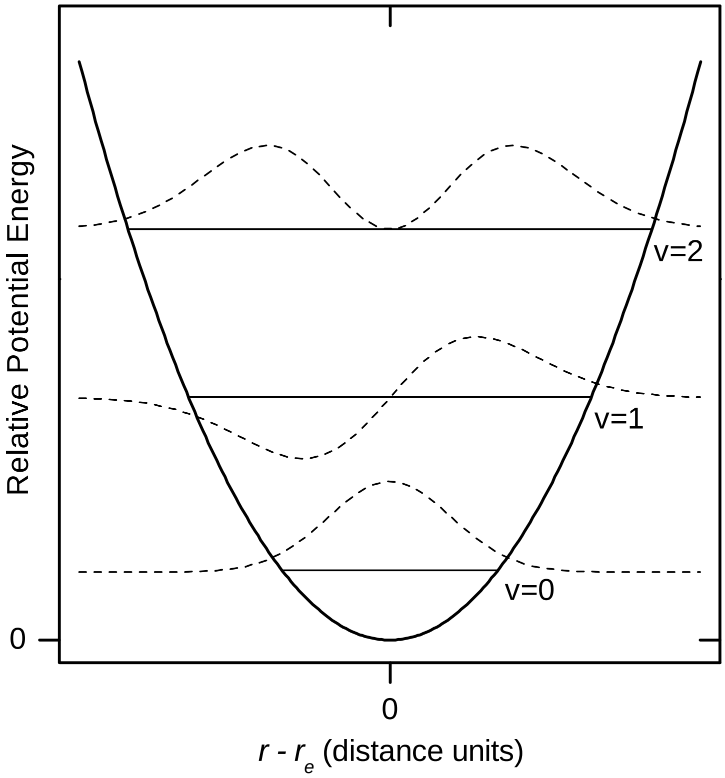

Figure 2.1 – Potential energy curve within the harmonic oscillator approximation. Also shown are the first three energy levels and wavefunctions.

2.1.3.2 Quantum Harmonic Oscillator

To solve Equation 2.17 exactly, an analytic form for the potential energy is required. One such simple analytic form comes from the harmonic oscillator approximation, in which the force acting on two objects connected by a spring, with $x = r_e - r$, where r is the separation distance and r_e is equilibrium separation, is (Herzberg and Spinks, 1950)

$$f = -kx, \tag{2.19}$$

where f is the force and k is the force constant. This potential is shown in Figure 2.1. Potential energy can be related to force through the equation (Hollas, 2004)

$$-\frac{dV}{dx} = f(x). \tag{2.20}$$

Therefore,

$$V(x) = \int -kx\;dx + c \tag{2.21}$$

$$= \frac{1}{2}kx^2, \tag{2.22}$$

where c is chosen so that $V(x) = 0$ at $x = 0$

If this is applied to a diatomic molecule, Equation 2.17 becomes

$$\frac{-\hbar^2}{2\mu}\frac{d^2\Psi_{\mathrm{v}J}}{dx^2} + \frac{1}{2}kx^2\Psi_{\mathrm{v}J} = E\Psi_{\mathrm{v}J} \tag{2.23}$$

$$\frac{d^2\Psi_{\mathrm{v}J}}{dx^2} + \frac{2\mu}{\hbar^2}\Big(E - \frac{1}{2}kx^2\Big)\Psi_{\mathrm{v}J} = 0. \tag{2.24}$$

The wavefunctions that solve this differential equation and satisfy the requirements that $\int_{-\infty}^{\infty} \Psi_{\mathrm{v}}\;dr = 1$ and that the wavefunctions are equal to zero at $r = \infty$ and $r = -\infty$, are (McQuarrie, 2008)

$$N_{\mathrm{v}}\alpha^{\frac{1}{2}}xH_{\mathrm{v}}e^{\frac{-\alpha x^2}{2}}, \tag{2.25}$$

where N_{v} is the normalisation factor, H_{v} are the Hermite polynomials, and specifically

$$N_{\mathrm{v}} = \left(\frac{1}{2^{\mathrm{v}}\mathrm{v}!}\left(\frac{\alpha}{\pi}\right)^{\frac{1}{2}}\right)^{\frac{1}{2}}, \quad H_{\mathrm{v}} = (-1)^{\mathrm{v}}e^{x^2}\frac{d^{\mathrm{v}}}{dx^{\mathrm{v}}}e^{-x^2}, \quad \text{and} \quad \alpha = \frac{\mu}{\hbar}\sqrt{\frac{k}{\mu}}. \tag{2.26}$$

The eigenvalues can then be shown to be equal to $\hbar\sqrt{\frac{k}{\mu}}(\mathrm{v} + \frac{1}{2})$ (McQuarrie, 2008). This shows that the energy levels are evenly spaced, with the lowest equal to $\frac{1}{2}\hbar\sqrt{\frac{k}{\mu}}$, and not zero. The eigenvalues and wavefunctions for the first three vibrational levels are shown in Figure 2.1. Each level has two classical "turning points", where $E = V$.

2.1.3.3 Real Potential Energy Curves

The harmonic oscillator is only a good approximation for the vibrational motion of a diatomic molecule at low energies (around the bottom of the well). At higher energies, as the internuclear distance increases, the bond becomes weaker, and with enough energy will dissociate, and a real potential energy curve is normally of the form shown in Figure 2.2.

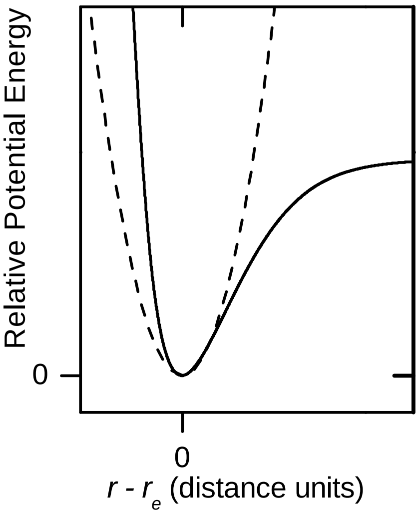

Figure 2.2 – Realistic diatomic molecule potential energy curve (solid line), and a harmonic potential energy curve (dotted line)

A common analytical form for a real potential is the Dunham potential (Dunham, 1932)

$$V(\xi) = a_0\xi^2(1 + a_1\xi + a_2\xi^2 \dots), \tag{2.27}$$

where

$$\xi = (\frac{r - r_e}{r_e}). \tag{2.28}$$

If this is expanded and only the first term is retained, it is equal to the harmonic oscillator approximation (Bernath, 2005), so the other terms are those that account for the anharmonic behaviour shown in Figure 2.2. The Schrödinger equation cannot be solved exactly for the Dunham potential, but approximate forms for the wavefunctions can be found.

When attempting to solve the equation in the same manner in which the harmonic oscillator version is solved, $V(x)$ cannot be replaced by a single term like $\frac{1}{2}kx^2$, but the potential and wavefunctions can be calculated approximately by ab initio methods, where the potential is the sum of the electronic energy and $\hat{V}_{NN}$. In this thesis however, semi-empirical methods are used. The semiclassical WKB approximation (Child, 1991; Schatz and Ratner, 2002) shows that the wavefunction can be approximated by different equations before the first turning point, between the turning points, and after the second turning point. The approximation does not work at the turning points, and the equations must be joined together. For example, between the turning points

$$\Psi_{\mathrm{v}}(r) \propto \big(E - V(r)\big)^{-1/4} \exp\left(- \sqrt{2\mu/\hbar^2} \int^{r} \sqrt{(E - V(r')}\ \mathrm{d}r' \right). \tag{2.29}$$

This also leads to an expression for the energy eigenvalues:

$$v + \frac{1}{2} = \frac{1}{\pi}\sqrt{\frac{2\mu}{\hbar^2}} \int_{r_1}^{r_2} \Big(E - V(r)\Big)^{\frac{1}{2}}\, dr \tag{2.30}$$

where r_1 and r_2 are the classical turning points. This equation requires a potential, the calculation of which is described in the next section.

2.1.4 Calculation of Potential Energy Curves using the RKR Method

The potential energy curves calculated in this thesis are based on experimental measurements and the Rydberg-Klein-Rees procedure (RKR; Rydberg, 1932, 1933; Klein, 1932; Rees, 1947). The RKR procedure calculates turning points for specified vibrational levels, and is performed by the program RKR1 (Le Roy, 2004). The important RKR equation provides equations for the turning points in terms of known values:

$$r_1(\mathrm{v}) = \sqrt{f^2 + f/g} - f r_2(\mathrm{v}) = \sqrt{f^2 + f/g} + f, \tag{2.31}$$

where

$$f = \sqrt{\frac{\hbar^2}{2\mu}} \int_{\mathrm{v}_{min}}^{\mathrm{v}} \frac{1}{\big(G_{\mathrm{v}} - G_{\mathrm{v}'}\big)^{1/2}}\, d\mathrm{v}', \text{ and} \tag{2.32}$$

$$g = \sqrt{\frac{2\mu}{\hbar^2}} \int_{\mathrm{v}_{min}}^{\mathrm{v}} \frac{B_{\mathrm{v}'}}{\big(G_{\mathrm{v}} - G_{\mathrm{v}'}\big)^{1/2}}\, d\mathrm{v}'. \tag{2.33}$$

As this is a semiclassical method, v is a continuous variable, and so turning points can be calculated for as many points as required, as opposed to only for a small number of real vibrational levels. This means that as input it requires equilibrium constants for the electronic state, ω_e, $\omega_e x_e$, $\omega_e y_e$, $\omega_e z_e$, etc. and B_e, α_{e_1}, α_{e_2}, α_{e_2} etc. (defined below), so that it can calculate G_{v} and B_{v} for any value of v. These equilibrium constants can be calculated with least squares fits to the equations (Bernath, 2005)

$$G_{\mathrm{v}} = \omega_e(\mathrm{v} + \frac{1}{2}) - \omega_e x_e(\mathrm{v} + \frac{1}{2})^2 + \omega_e y_e(\mathrm{v} + \frac{1}{2})^3 + \omega_e z_e(\mathrm{v} + \frac{1}{2})^4 + \dots \tag{2.34}$$

and

$$B_{\mathrm{v}} = B_e - \alpha_{e_1}(\mathrm{v} + \frac{1}{2}) + \alpha_{e_2}(\mathrm{v} + \frac{1}{2})^2 + \alpha_{e_3}(\mathrm{v} + \frac{1}{2})^3 + \dots, \tag{2.35}$$

where higher order terms can be used if required. Values for G_{v} and B_{v} are obtained along with the other molecular constants described in Section 2.4 by fitting to the observed line positions, so that the RKR potentials generated are based on experimentally observed transitions.

2.1.5 LEVEL program and example

LEVEL calculates a solution to Equation 2.17 numerically using the Cooley procedure (Cooley, 1961), which is briefly described here. It requires the input of a potential energy function, $V(r)$, for the electronic state in question $\Big($these can be calculated using the program RKR1 (Section 2.1.4)$\Big)$. Vibrational wavefunctions and energies are calculated for any specified values of the quantum numbers v and J.

Equation 2.17 can be rearranged as

$$\frac{d^2\Psi_{\mathrm{v}J}(r)}{dr^2} = (V_{\mathrm{v}J}(r) - E)\Psi_{\mathrm{v}J}(r), \tag{2.36}$$

where $\frac{-\hbar^2}{2\mu}$ has been incorporated into $V_{\mathrm{v}J}(r)$ and E, adjusting their units accordingly. An equation can be derived (derivation not shown here) for the calculation of $\Psi_{\mathrm{v}J}(r)$ at a specific internuclear distance, using an equally spaced grid of spacing h, and the series expressions:

$$\Psi_{\mathrm{v}J}(r+h) + \Psi_{\mathrm{v}J}(r-h) = \sum_{k=0}^{\infty} \frac{2h^{2k}}{(2k)!}\Psi_{\mathrm{v}J}^{(2k)}(r), \tag{2.37}$$

and

$$\Psi_{\mathrm{v}J}^{(2)}(r+h) + \Psi_{\mathrm{v}J}^{(2)}(r-h) = \sum_{k=0}^{\infty} \frac{2h^{2k}}{(2k)!}\Psi_{\mathrm{v}J}^{(2k+2)}(r), \tag{2.38}$$

where

$$\Psi_{\mathrm{v}J}^{(n)}(r) = \frac{d^n\Psi_{\mathrm{v}J}(r)}{dr^{(n)}}, \tag{2.39}$$

so that

$$\Psi_{vJ}(r+h) = \frac{h^2(V_{vJ}(r)-E)\Psi_{vJ}(r) + 2\Big(1-\frac{h^2}{12}\big(V_{vJ}(r)-E\big)\Big)\Psi_{vJ}(r) - \Big(1-\frac{h^2}{12}\big(V_{vJ}(r-h)-E\big)\Big)\Psi_{vJ}(r-h)}{\Big(1-\frac{h^2}{12}\big(V_{vJ}(r+h)-E\big)\Big)}. \tag{2.40}$$

Due to the discarding of higher order terms from the series expressions, this equation is not complete, but is a good approximation (Cooley, 1961). The first discarded term is very small, and equal to $\frac{-h^6}{240}\Psi_{vJ}(r)^{(6)}$. This equation is used in an iterative process, in which an initial guess is made for E, and this is improved until the resulting wavefunction is acceptable according to some convergence criteria. As E is estimated, values for $\big(V_{vJ}(r-h)-E\big)$ can be easily calculated at any value of r, and all that is required are the values of the two preceding points of the wavefunction.

A grid with minimum and maximum values of r, r_{min} and r_{max}, is chosen so that effectively all of the wavefunction will be present in this range. The wavefunction at r_{min} is set to zero, and at $r_{min}+h$ it is set to a small arbitrary number, which is all that is required for Equation 2.29 to be used. The wavefunction is calculated up to a certain specified point between r_{min} and r_{max}, and this part is the "outward integration".

As an example, this calculation will be shown for the v=0, J=0 level of the NH $X^3\Sigma^-$ state. For the first iteration, LEVEL initially estimates E to be equal to 3951.3301 cm^{-1}. The correct value is 1619.3251 cm^{-1}, so this will also illustrate what happens with a very poor initial estimate. The outward integration is shown in Figure 2.3

A similar process is then performed for the inward integration. First, a suitable starting point is chosen where the value of the wavefunction is likely to be negligible, then two points are assigned values so that the inward integration can proceed in the same fashion. These two points are calculated using the WKB approximation for a wavefunction where r is greater than the outer turning point:

$$\Psi_{vJ}(r) \propto \big(V_{vJ}(r)-E\big)^{-1/4}\exp\left(-\sqrt{2\mu/\hbar^2}\int^{r}\sqrt{V_{vJ}(r')-E}\ \mathrm{d}r'\right), \tag{2.41}$$

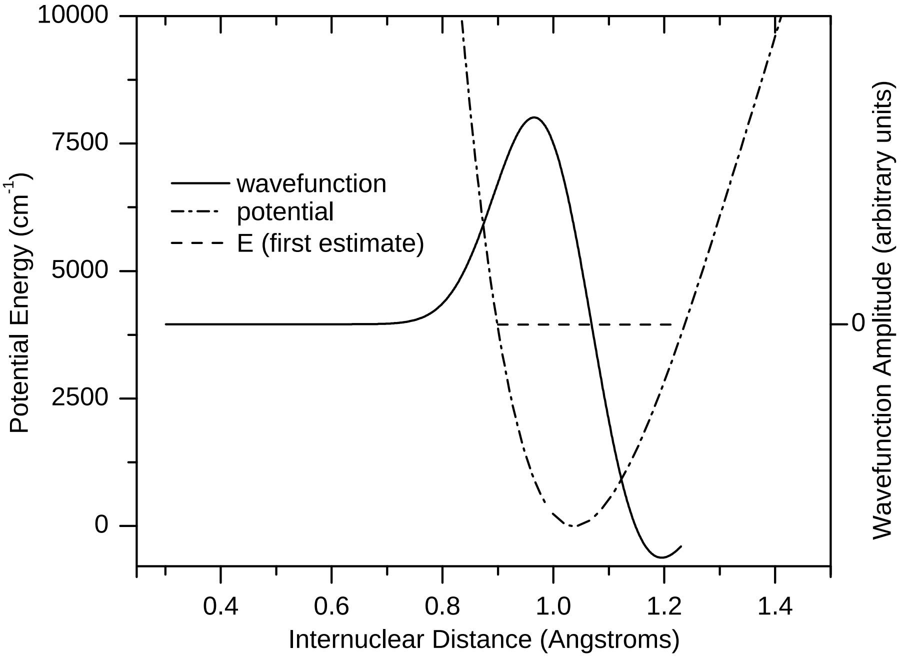

Figure 2.3 – Outward integration for the first iteration by LEVEL in the calculation of the NH $X^3\Sigma^-$, v=0, J=0 wavefunction.

so that

$$\Psi_{vJ}(r-h) = \Psi_{vJ}(r)\big(V_{vJ}(r)-E\big)^{-1/4}\exp\left(\frac{h\sqrt{V_{vJ}(r)-E}+h\sqrt{V_{vJ}(r-h)-E}}{2}\right), \tag{2.42}$$

where $\frac{-\hbar^2}{2\mu}$ has been incorporated into $V_{vJ}(r)$ and E as before.The inward integration is then performed up to the same internuclear distance as before. For the example, this results in the wavefunction in Figure 2.4.

Both sections are then separately normalised so that their values at the meeting point are equal to unity, giving the example wavefunction in Figure 2.5. At the point at which the two parts of the wavefunction meet, the slopes are compared, and if their difference is less than a specified threshold, the wavefunction is accepted. If they are not, as clearly must be the case in Figure 2.5, a new energy is estimated based on the result of the previous iteration and the next iteration begins. For this example, LEVEL performs six iterations, the wavefunctions for three of which are shown in Figure 2.6. Clearly, the wavefunction arrived at has a node in the centre, and therefore it is for the v=1 J=0 level. This is due to the poor quality of the initial estimate of E, however now that the energy for the v=1 level is known, LEVEL can improve its estimate, and the actual wavefunction is found using the same procedure.

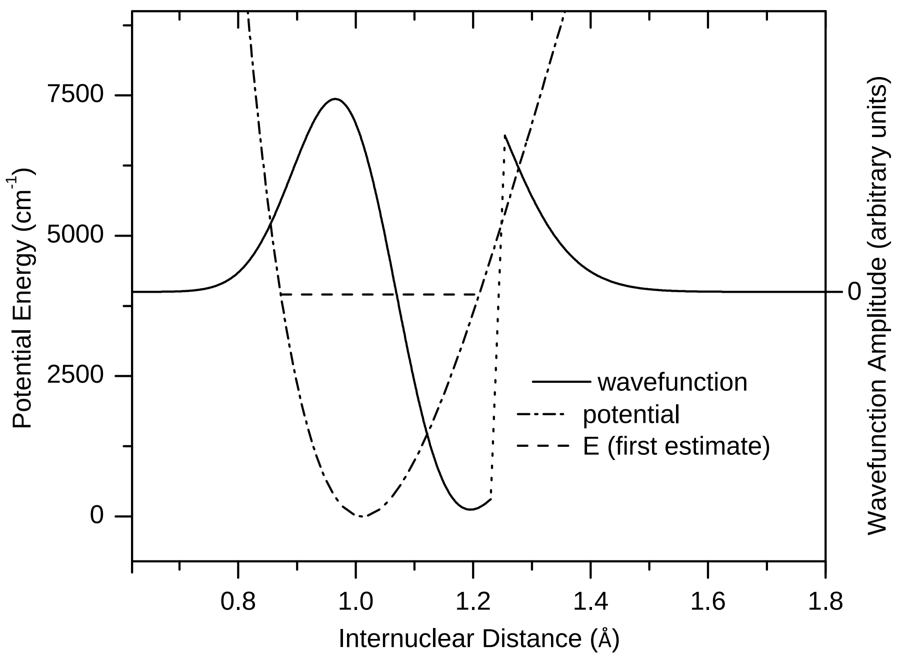

Figure 2.4 – Inward and outward integration for the first iteration by LEVEL in the calculation of the NH $X^3\Sigma^-$, v=0, J=0 wavefunction

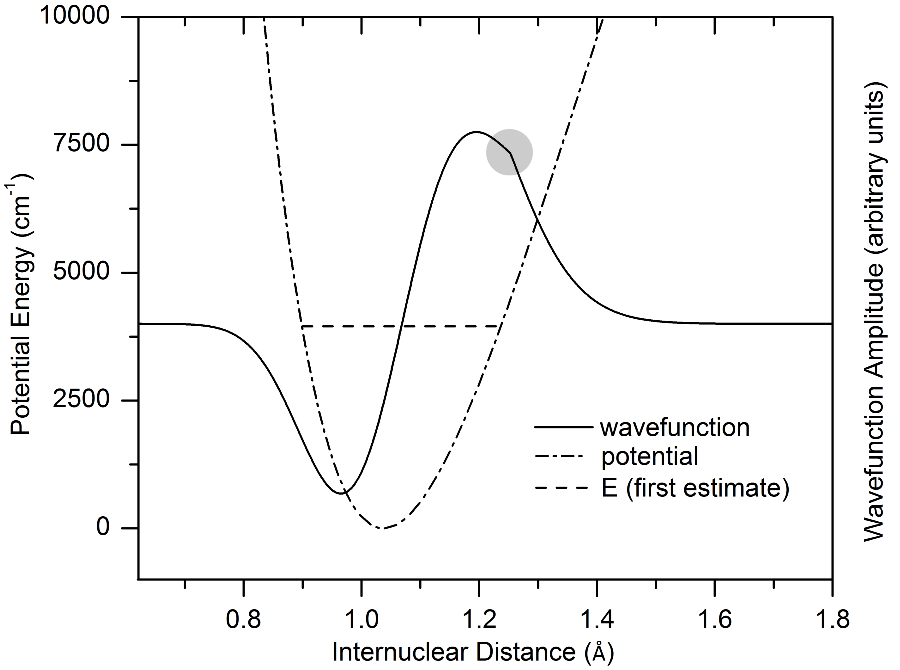

Figure 2.5 – Normalised wavefunction for the first iteration by LEVEL for the NH $X^3\Sigma^-$, v=0, J=0 level. The shaded area shows the point at which in inward and outward integrations meet.

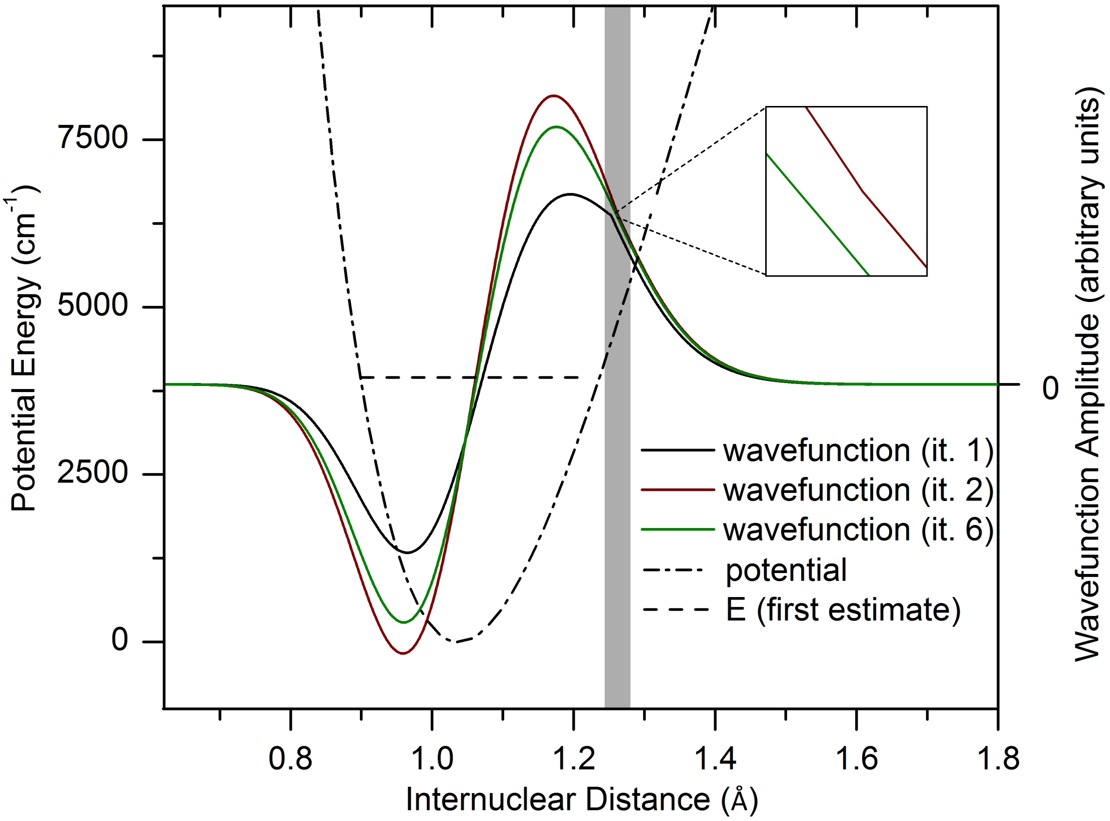

Figure 2.6 – Normalised wavefunctions for the first, second, and sixth of six iterations performed by LEVEL, with its first estimate of E, for the NH $X^3\Sigma^-$, v=0, J=0 level. The shaded area shows the point at which the inward and outward integrations meet. The expanded area shows that the second iteration still has a noticeable slope change, and the final wavefunction does not. The wavefunctions from the third to fifth iterations are omitted as they would appear almost identical to the final wavefunction.

2.2 Electronic Angular Momentum

2.2.1 Electronic Angular Momentum in Atoms

The different quantised energy levels of an atom within an electronic state exist due entirely to the angular momentum of the electrons and nuclei. The definition of angular momentum, $\hat{\boldsymbol{l}}$, is

$$\hat{\boldsymbol{l}} = \hat{\boldsymbol{r}} \times \hat{\boldsymbol{p}}, \tag{2.43}$$

where $\hat{\boldsymbol{r}}$ is the radius and $\hat{\boldsymbol{p}}$ is the linear momentum. The quantum mechanical operator for linear momentum on the x axis is (Zare, 1988) is

$$\hat{p}_x = -i\hbar\frac{\partial}{\partial x}. \tag{2.44}$$

Using Equation 2.43, Equation 2.44, and equivalent expressions for the y- and z-axes, expressions for the quantum mechanical operator versions of the component angular momenta 2.10, $\hat{l}_x$, $\hat{l}_y$, and $\hat{l}_z$, can be derived:

$$\hat{l}_x = y\hat{p}_z - z\hat{p}_y \tag{2.45}$$

$$\hat{l}_y = z\hat{p}_x - x\hat{p}_z \tag{2.46}$$

$$\hat{l}_z = x\hat{p}_y - y\hat{p}_x. \tag{2.47}$$

A further operator that commutes with these, $\hat{\boldsymbol{l}}^2$, is defined as

$$\hat{\boldsymbol{l}}^2 = \hat{l}_x^2 + \hat{l}_y^2 + \hat{l}_z^2. \tag{2.48}$$

The spherical harmonics, $Y_{lm}(\theta, \Phi)$, are simultaneous eigenfunctions of $\hat{\boldsymbol{l}}^2$ and $\hat{l}_z$, with the eigenvalues $l(l+1)\hbar^2$ and $m_l\hbar$, respectively. This indicates that the energy levels are quantised and described by l and m_l, where l is the angular momentum quantum number of a single electron, and m_l is the projection of the vector $\boldsymbol{l}$ on the laboratory z-axis. The quantum number l is based on which orbital an electron occupies, and l=0,1,2,3... correspond to *s*,*p*,*d*,*f*... orbitals, respectively.

Equivalent electron spin operators can also be defined ($\hat{s}_x$, $\hat{s}_y$, $\hat{s}_z$, and $\hat{\boldsymbol{s}}^2$), where s and m_s are analogous quantum numbers. The difference in energy levels caused by different nuclear angular momenta (hyperfine structure) is extremely small (for example, around 40 MHz (0.0013 cm^{-1}) for OH), and the spectral line splitting caused as a result is not resolved in any of the spectra discussed in this thesis. All the intensities reported are actually a sum over both upper and lower states of the unresolved hyperfine intensities, and hyperfine structure is not discussed further.

2.2.2 Good Quantum Numbers

When a quantum number is described as "good", a simultaneous set of eigenfunctions exist for both it and the total Hamiltonian operator, eg. for the operator $\hat{\boldsymbol{J}}^2$,

$$\hat{H}\psi = E\psi \text{ and } \hat{J}^2\psi = J(J+1)\hbar\psi. \tag{2.49}$$

Here, the operators commute:

$$[\hat{H}, \hat{J}^2] = \hat{H}\hat{J}^2 - \hat{J}^2\hat{H} = 0 \tag{2.50}$$

When an operator does not commute with the Hamiltonian, and simultaneous eigenfunctions cannot be found, the associated quantum number is no longer good. However, it is often still useful to use the quantum numbers as labels for states even when they are not good, especially if the operator almost commutes with the Hamiltonian, and if considering, say, $\hat{\boldsymbol{S}}^2$,

$$\hat{\boldsymbol{S}}^2\psi \approx S(S+1)\hbar\psi. \tag{2.51}$$

2.2.3 Electronic and Nuclear Rotational Angular Momentum in Diatomic Molecules

A diatomic molecule has reduced symmetry compared to an atom, and the electrons are forced to precess about the internuclear z-axis. The vector $\boldsymbol{l}$ is no longer known (and the quantum number l is no longer good; see above), but its projection on the internuclear axis, $\lambda\hbar$, is. This is the eigenvalue from $\hat{l}_z$ operating on the electronic wavefunction. The sign of λ can be thought of as the electrons precessing in opposite directions around the internuclear axis. σ, π, and δ orbitals have λ values of 0, ±1, and ±2, respectively.

At this point it should be noted that the quantum numbers Σ, λ, Λ, and Ω are defined as only having positive values (Herzberg and Spinks, 1950). However, there are various points, for example when the basis states in the effective Hamiltonian (Section 2.4) are considered, that the possible negative values need to be accounted for. Therefore,

Table 2.1 – Operators and their eigenvalues when operating on a set of simultaneous eigenfunctions, in the absence of spin-orbit coupling (discussed later.)

Operator	Eigenvalue	Equation
$\hat{\boldsymbol{J}}^2$	$J(J+1)\hbar^2$	$\hat{\boldsymbol{J}}^2\psi = J(J+1)\hbar^2\psi$
$\hat{J}_z$	$\Omega\hbar$	$\hat{J}_z\psi = \Omega\hbar\psi$
$\hat{L}_z$	$\Lambda\hbar$	$\hat{L}_z\psi = \Lambda\hbar\psi$
$\hat{\boldsymbol{S}}^2$	$S(S+1)\hbar^2$	$\hat{\boldsymbol{S}}^2\psi = S(S+1)\hbar^2\psi$
$\hat{S}_z$	$\Sigma\hbar$	$\hat{S}_z\psi = \Sigma\hbar\psi$

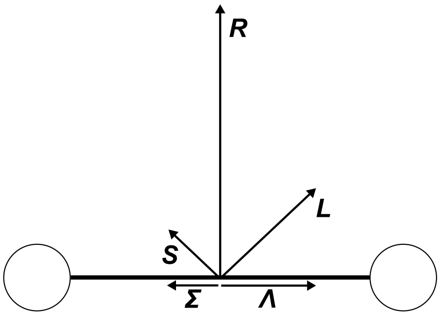

Figure 2.7 – Angular momentum in a diatomic molecule

throughout this thesis, these quantum numbers can take both positive and negative values.

Values of λ add together to give Λ, the quantum number associated with the projection of the total orbital angular momentum on the internuclear axis. Conveniently, they add as scalars as opposed to vectors, as the direction is always along the internuclear axis (see Figure 2.7).

The spin quantum numbers are still good, and add together to give the total spin quantum number, S. The projection of spin on the internuclear axis is given the symbol Σ, which can take values separated by 1 between -S and +S. Λ and Σ add together to give Ω, the total projection of angular momentum on the internuclear axis (see Figure 2.7). These angular momenta couple together to form the resulting total angular momentum, $\boldsymbol{J}$. This can occur in different ways, which are explained in Section 2.2.4. The operators and quantum numbers for the angular momentum in diatomic molecules are shown in Table 2.1 The notation for an electronic state of a diatomic molecule is $^{2S+1}\Lambda_{\Omega}$. Terms with Λ = 0,1,2 are given the symbols Σ, Π, and Δ. $2S+1$ is the multiplicity, where multiplicities of 1, 2, 3, *etc.* are described as singlets, doublets, triplets, *etc.*.

For example, in the C_2 $X^1\Sigma_g^+$ ground state, the atomic orbitals combine to give

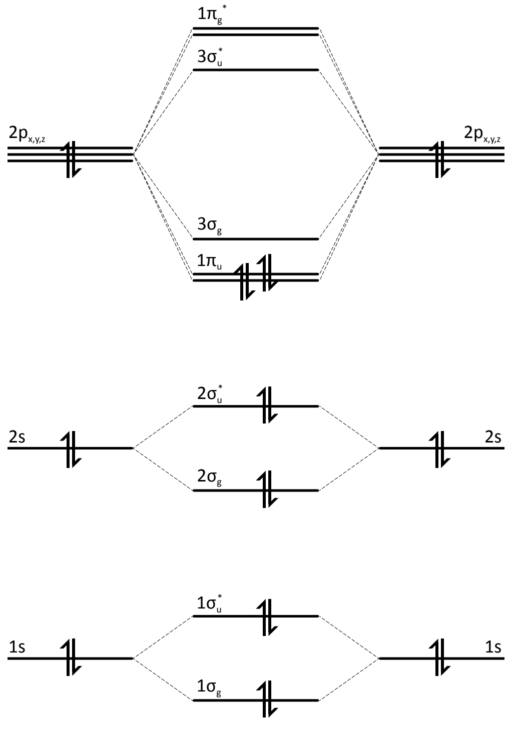

Figure 2.8 – Molecular orbital diagram of the C_2 $X^1\Sigma_g^+$ state

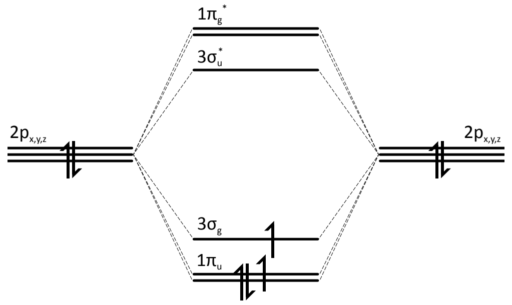

Figure 2.9 – Molecular orbital diagram of the C_2 $a^3\Pi_u$ state

molecular orbitals as shown in Figure 2.8. The first four molecular orbitals, $1\sigma_g$ to $2\sigma_u^*$ have l=0, so only the two degenerate $1\pi_u$ orbitals must be considered. One $1\pi_u$ orbital has $\lambda = +1$, and the other -1, so the λ values add together to give $\Lambda = 0$, so this is a Σ state. All of the electrons are paired, meaning that this is a singlet state. The next lowest electronic state of C_2 is the $a^3\Pi_u$ state, the configuration for which is shown in Figure 2.9. Here, there are two electrons in one degenerate $1\pi_u$ orbital, and one in the other. Electrons in these two orbitals have equal and opposite values of λ, giving rise to $\Lambda = \pm 1 + \pm 1 + \mp 1 = \pm 1$ (the electron in the $3\sigma_g$ orbital does not contribute to Λ as it has $\lambda = 0$). There are two unpaired electrons with the same spin, and therefore $S = 1$.

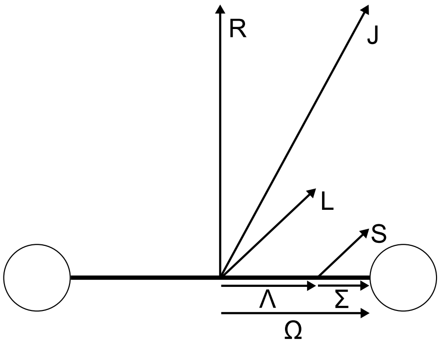

Figure 2.10 – Angular momentum coupling in a Hund's case (a) diatomic molecule

Table 2.2 – Possible combinations of Λ and Σ to give Ω in a $^3\Pi$ state.

Λ	Σ	Ω
+1	+1	+2
+1	0	+1
+1	-1	0
-1	+1	0
-1	0	-1
-1	-1	-2

2.2.4 Hund's Cases

The angular momenta can couple with each other and the internuclear and rotational axes to different extents, resulting in different energy level patterns. These are called Hund's cases, and the two main cases, (a) and (b), are described in detail below. Cases (c), (d), and (e) are briefly discussed.

2.2.4.1 Hund's Case (a)

If, as described above, $\boldsymbol{L}$ couples strongly to the internuclear axis, then Λ is a good quantum number. If spin-orbit coupling is very strong, ie. $\boldsymbol{S}$ and $\boldsymbol{L}$ couple very strongly, then Σ and Ω are also good quantum numbers (Herzberg and Spinks, 1950). The vector $\boldsymbol{\Omega}$ then couples with the nuclear rotation, $\boldsymbol{R}$, to give $\boldsymbol{J}$. This is shown in Figure 2.10. Hund's case (a) is an idealised case in which $\boldsymbol{S}$ and $\boldsymbol{L}$ are completely coupled. Different components within an electronic state arise from the combination of possible values of Λ and Σ. Λ can be positive or negative, and $\Sigma = S, S-1, ..., -S$. For example, for the $a^3\Pi_u$ state of C_2 shown in Figure 2.9, which is best described by Hund's case (a) at low J, $\Lambda = \pm 1$ and $\Sigma = +1, 0, \text{ or } -1$. Therefore, values of $|\Omega|$ can be 0, 1, or 2, as shown in Table 2.2.

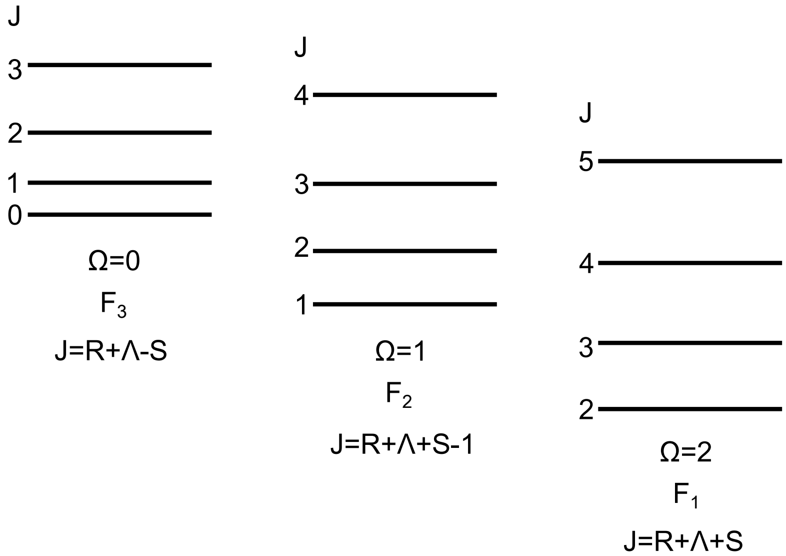

Figure 2.11 – Energy levels of the $\mathrm{C_2}$ $\mathrm{a^3\Pi_u}$ state. The order is correct but they are not to scale.

The resulting states from Table 2.2 are $^3\Pi_0$, $^3\Pi_1$, and $^3\Pi_2$. The positive and negative values of Ω result from Λ being able to take positive or negative values. F labels are given to the different components, with F_1 for $J = R + \Lambda + S$, F_2 for $J = R + \Lambda + S - 1$, up to F_{2S+1} for $J = R + \Lambda - S$ (Bernath, 2005). The quantum number R is used here because although it not a good quantum number for case (a), it is useful as a label.

The energy levels for the $\mathrm{C_2}$ $\mathrm{a^3\Pi_u}$ state are ordered as shown in Figure 2.11, and this is called an "inverted" $^3\Pi$ state, as the F_1 level is lowest in energy. The main point is that for a case (a) state, the energy levels are best described as first being split into Ω "spin components", and there then is a progression of J values within each component.

2.2.4.2 Hund's Case (b)

In a Hund's case (b) state, the electron spin $\boldsymbol{S}$ is not coupled to the internuclear axis, and Σ is not a good quantum number. In a case (a) system, $\boldsymbol{S}$ is coupled to the internuclear axis indirectly, via its coupling to the orbital angular momentum $\boldsymbol{L}$. If $\boldsymbol{L}$ is zero, then this indirect coupling doesn't occur, resulting in a case (b) state. It can also occur when $\boldsymbol{L} > 0$ if the spin-orbit coupling is small, which can occur in light molecules (Brown and Carrington, 2003).

$\boldsymbol{R}$ combines with $\boldsymbol{\Lambda}$ to form $\boldsymbol{N}$, and N is a good quantum number in case (b) ($\boldsymbol{R} = \boldsymbol{N}$ if $\boldsymbol{L} = 0$. $\boldsymbol{N}$ then combines with $\boldsymbol{S}$ in $2S + 1$ possible ways to give the $2S + 1$ spin components (see Figure 2.12).

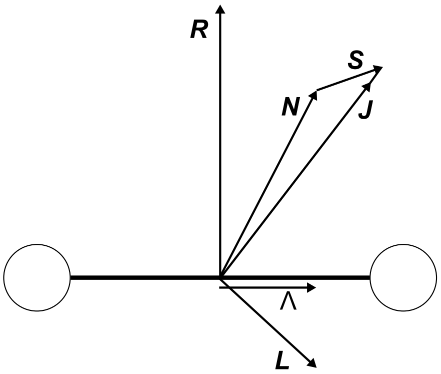

Figure 2.12 – Angular momentum coupling in a Hund's case (b) diatomic molecule

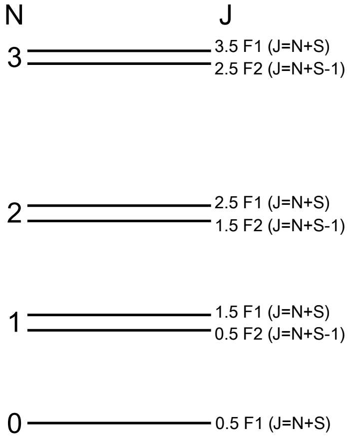

Figure 2.13 – Energy levels of the CN $B^2\Sigma^+$ state. The order is correct but they are not to scale (the splitting between spin components is much exaggerated for clarity).

At first it may appear that the different spin components would be degenerate for a specific value of N, but in fact the spin couples to an extent to the rotation, lifting this degeneracy (see Section 2.4.2.1). The energy levels are therefore mostly affected by their value of N, and are then split slightly into spin components, with the labels F_1 for $J = N + S$, F_2 for $J = N + S - 1$, up to F_{2S+1} for $J = N - S$. Figure 2.13 shows the energy levels of the CN $B^2\Sigma^+$ state as an example of an electronic state best described by case (b).

2.2.4.3 Other Hund's Cases

As mentioned, cases (a) and (b) are the extreme cases, and in reality, states with $\Lambda > 0$ lie somewhere between the two. This is based on the amount of spin-orbit coupling, which is quantified by the molecular constant A, discussed in Section 2.4. Most electronic states of diatomic molecules, including all of those investigated in this thesis, are either case (b) or somewhere between (a) and (b).

There are three other Hund's cases: (c), (d), and (e), although (e) was not identified by Hund (Brown and Carrington, 2003). Case (c) results from $\boldsymbol{L}$ and $\boldsymbol{S}$ being more strongly coupled to each other than the internuclear axis, and Ω is a good quantum number, but Λ and Σ are not. In case (d), $\boldsymbol{L}$ is coupled to the molecular rotation and not the internuclear axis, with no spin-orbit coupling. In case (e), $\boldsymbol{L}$ is not coupled to the internuclear axis, but spin-orbit coupling is strong.

2.3 Parity

2.3.1 Total and Rotationless Parity

An energy level of a diatomic molecule can also be described by parity, which is based on its symmetry. This is particularly important as there are selection rules based on parity that govern which types of transition are possible.

The parity is calculated, like the angular momentum quantum numbers, with an eigenvalue/eigenfunction equation, using a symmetry operator. For the total parity (+ or –), the inversion (in laboratory coordinates) operator, $\hat{E}^*$, is used, which inverts all of the coordinates of nuclei and electrons, but does not act on nuclear spin. The parity equation (which excludes nuclear spin) is:

$$\hat{E}^*\psi = \pm\psi. \tag{2.52}$$

If the operation produces +ψ, the original wavefunction has + parity, and if it produces -ψ, it has – parity. The result of its action on the vibrational wavefunction is simply the same vibrational wavefunction, and acting on the rotational wavefunction it gives $(-1)^{J-\Omega}|-\Omega JM\rangle$. The electronic wavefunction, however, is not known in the laboratory frame, and so the effect of $\hat{E}^*$ on ψ_{el} cannot be expressed as easily. It is found that $\hat{E}^*$ is equivalent to the $\hat{\sigma}_{\mathrm{v}}$ operator (Hougen, 1970), which reflects in the symmetry plane of the molecular frame. Acting on the electronic wavefunction, $\hat{\sigma}_{\mathrm{v}}$ gives $(-1)^{S-\Sigma}|S,-\Sigma\rangle$ and $\pm(-1)^{\Lambda}|-\Lambda\rangle$, for the spin and orbital parts, respectively.

The operation of $\hat{\sigma}$ on a total wavefunction (but excluding nuclear spin) is as follows

Table 2.3 – Total and rotationless parity

J ($J-0.5$ for half integer J)	Total parity	Rotationless parity
even	+	e
even	–	f
odd	+	f
odd	–	e

for a Hund's case (a) wavefunction (Bernath, 2005):

$$\hat{\sigma}_{\mathrm{v}}|\mathrm{v};\Lambda S\Sigma;\Omega JM\rangle = (-1)^{J-2\Sigma+S+\sigma}|\mathrm{v};-\Lambda S-\Sigma;-\Omega JM\rangle, \tag{2.53}$$

where σ=1 for Σ^- states and 0 for all other states. The results of Equation 2.53 do not conform with Equation 2.52 due to the change of sign of the projection quantum numbers. This is resolved if the basis functions are changed to the parity functions + and –. States with $\Lambda \neq 0$, for example a $^3\Pi$ state, for which the quantum numbers in a Hund's case (a) basis are shown in Table 2.2, have two levels for each $|\Omega|$. The parity function for a particular $|\Omega|$ is a linear combination of the $+|\Omega|$ and $-|\Omega|$ basis functions, and this is explained in Section 2.5.7. Then,

$$\hat{\sigma}_{\mathrm{v}}|^{2S+1}\Lambda_{|\Omega|}(+)\rangle = \pm\,|^{2S+1}\Lambda_{|\Omega|}(+)\rangle \;\text{ and} \tag{2.54}$$

$$\hat{\sigma}_{\mathrm{v}}|^{2S+1}\Lambda_{|\Omega|}(-)\rangle = \pm\,|^{2S+1}\Lambda_{|\Omega|}(-)\rangle. \tag{2.55}$$

which conforms with Equation 2.52.

In the $(-1)^{J-2\Sigma+S+\sigma}$ term, the presence of J means that the total parity will alternate signs with each change in J, for a sequence of levels in which the other quantum numbers are the same. This irritation is eliminated with the use of rotationless (e/f) parity, which adds another $(-1)^J$ term $\left((-1)^{J-0.5}\text{ for half integer }J\right)$, so that e and f parity are given to levels as shown in Table 2.3. The two levels produced due to Λ-doubling (see Section 2.4.2.3)have opposite parities (both total and rotationless parity) when the basis functions are transformed to parity functions. The operation of $\hat{\sigma}_{\mathrm{v}}$ on just the orbital part of the wavefunction, $|\Lambda\rangle$, gives $\pm|\Lambda\rangle$. This results in the two degenerate positive and negative values of Λ mentioned above for states with $\Lambda > 0$. For Σ states however, Λ can only equal zero. The levels can still be described by the parity values e/f and $+/-$, but only one of them exists for each J/Ω level. The operation of $\hat{\sigma}_{\mathrm{v}}$ on the orbital part of a Σ state is

$$\hat{\sigma}_{\mathrm{v}}|\Lambda = 0\rangle = \pm|\Lambda = 0\rangle. \tag{2.56}$$

If the result is $+|\Lambda\rangle$, a Σ state is given a + subscript and so is a Σ^{+} state, and if it is $-|\Lambda\rangle$, it is a Σ^{-} state.

If $\hat{E}^{*}$ operates on the transition moment, μ, it returns $-\mu$. This means that μ has negative parity, and so for a transition moment matrix element (ME) to be non-zero the parity must change between the upper and lower wavefunctions, giving rise to the total parity selection rule ($+ \to -$ or $- \to +$).

2.3.2 Gerade/Ungerade Parity

For homonuclear diatomic molecules, another inversion operation, $\hat{\imath}$, acts in the molecular frame, as opposed to $\hat{E}^{*}$ (described above) which acts in the laboratory frame. $\hat{\imath}$ acts on the electronic coordinate part of the wavefunction only, resulting in negative or positive versions of the original electronic coordinates:

$$\hat{\imath}|\Lambda\rangle = \pm|\Lambda\rangle, \tag{2.57}$$

A result of $+|\Lambda\rangle$ or $-|\Lambda\rangle$ means that the wavefunction has g or u parity, respectively. Since the dipole moment operator has u parity, the selection rule ($g \to u$ or $u \to g$) applies to homonuclear diatomic molecules.

2.3.3 Symmetric/Antisymmetric Parity

Consideration of nuclear spin (for the only time in this thesis) means that another type of symmetry (s/a for symmetric/antisymmetric) exists. The Pauli exclusion principle requires the total wavefunction (including nuclear spin) to be either symmetric $\big($or antisymmetric (see below)$\big)$ with respect to the interchange of two identical nuclei (Bernath, 2005). This means that for homonuclear diatomic molecules, (s/a) symmetry must be considered. The operator $\hat{P}_{12}$ exchanges two identical nuclei, which is equivalent to the symmetry operation $\hat{E}^{*}$ followed by $\hat{\imath}$, giving the relationships between +/-, g/u, and s/a parity shown in Table 2.4.

With respect to the interchange of the two identical nuclei, the total wavefunction must be symmetric if the nuclei have integer nuclear spin (bosons), and antisymmetric if

Table 2.4 – Relationships between +/-, g/u, and s/a parity

Total parity	Gerade/ ungerade	Symmetric/ antisymmetric
+	g	s
-	g	a
+	u	a
-	u	s

they have half-integer nuclear spin (fermions). This becomes particularly important for homonuclear diatomic molecules that have zero nuclear spin, as clearly only symmetric nuclear wavefunctions can exist, and to satisfy the condition above, the rest of the wavefunction and therefore the total wavefunction must have s symmetry. This means that only + total parity levels exist for g electronic states, and – total parity levels for u states.

2.4 The Effective Hamiltonian

This section describes the Hamiltonian matrix that is used to reproduce energy levels and transitions from observed spectra. It is important to note that it is an "effective" Hamiltonian, and not a full Hamiltonian. The effective Hamiltonian can be set up for a single electronic state, and correctly reproduce the energy levels (in the absence of local perturbations (see Section 2.4.4)). A full Hamiltonian would include basis functions for all electronic states, and linking Hamiltonian MEs between basis functions in different electronic states and different vibrational levels that are far apart in energy would exist. The effective Hamiltonian is, effectively, a pre-diagonalised version of the full Hamiltonian, in terms of the basis functions of one (or more if required) electronic state, so that those linking MEs are zero. This means that the parameters described in this section are "effective" parameters, and not the real ones that would be present in the full Hamiltonian, and as a result, their physical interpretation is not always clear.

A vibrational level of a diatomic molecule in a specific electronic state can be described by a series of molecular constants. The individual fine-structure energy levels can be calculated using these constants by setting up and diagonalising the Hamiltonian matrix. The Schrödinger equation, $\hat{H}\psi = E\psi$, can be expressed as the linear algebra equation:

$$\hat{\mathbf{H}}\mathbf{X} = \mathbf{X}\mathbf{E} \tag{2.58}$$

$$\mathbf{E} = \mathbf{X}^{-1}\hat{\mathbf{H}}\mathbf{X}, \tag{2.59}$$

where $\hat{\mathbf{H}}$ is the Hamiltonian matrix (discussed below), $\mathbf{E}$ is the diagonal eigenvalue matrix, and $\mathbf{X}$ is a transformation matrix in which the eigenvectors are defined.

First of all, a suitable basis set must be chosen, and the matrix $\hat{\mathbf{H}}$ must be set up. $\hat{H}$ can be split into electronic, vibrational, rotational, and spin-orbit parts so that

$$\hat{H} = \hat{H}_{el} + \hat{H}_{vib} + \hat{H}_{rot} + \hat{H}_{so}. \tag{2.60}$$

Other terms are also required for more precise calculations, which will be discussed later. The basis set that is normally used is a Hund's case (a) basis set, which can be analytically represent by the symmetric top basis functions with spin. This means that the standard angular momentum operators that commute and can be evaluated are those shown in Table 2.2 ($\hat{\boldsymbol{J}}^2$, $\hat{J}_z$, $\hat{\boldsymbol{S}}^2$, $\hat{S}_z$, and $\hat{L}_z$). The case (a) wavefunctions can be written as $|\eta\Lambda; S\Sigma; J\Omega\rangle$, where η represents the electronic state and vibrational quantum number. The electronic and vibrational kinetic energy parts of the Hamiltonian can be absorbed into a single value, the energy origin of the vibrational level, G_{v}. The most convenient angular momentum operator to use for $\hat{H}_{rot}$ is $\hat{N}^2$, as although it cannot be evaluated directly as it does not commute with the others, it can expanded as follows:

$$\hat{H}_{rot} = B\hat{\mathbf{N}}^2 = B\left((\hat{\mathbf{J}} - \hat{\mathbf{S}})^2\right) \tag{2.61}$$

$$= B\left(\hat{\mathbf{J}}^2 + \hat{\mathbf{S}}^2 - 2\hat{\mathbf{J}}\cdot\hat{\mathbf{S}}\right) \tag{2.62}$$

$$= B\left(\hat{\mathbf{J}}^2 + \hat{\mathbf{S}}^2 - 2(\hat{J}_z\hat{S}_z + \hat{J}_x\hat{S}_x + \hat{J}_y\hat{S}_y)\right) \tag{2.63}$$

$$= B\left(\hat{\mathbf{J}}^2 + \hat{\mathbf{S}}^2 - 2\hat{J}_z\hat{S}_z - \hat{J}_+\hat{S}_- - \hat{J}_-\hat{S}_+\right), \tag{2.64}$$

where B is the rotational constant discussed in Section 2.1.2,

$$\hat{J}_\pm = \hat{J}_x \pm i\hat{J}_y, \quad \text{and} \quad \hat{S}_\pm = \hat{S}_x \pm i\hat{S}_y. \tag{2.65}$$

The step between Equations 2.63 and 2.64 occurs because the terms cancel:

$$\begin{aligned}
\hat{J}_+\hat{S}_+\hat{J}_-\hat{S}_+ &= \Big((\hat{J}_x + i\hat{J}_y)(\hat{S}_x - i\hat{S}_y) + (\hat{J}_x - i\hat{J}_y)(\hat{S}_x + i\hat{S}_y)\Big) && (2.66)\\
&= \Big((\hat{J}_x\hat{S}_x - i\hat{J}_x\hat{S}_y + i\hat{S}_x\hat{J}_y - i^2\hat{J}_y\hat{S}_y) + (\hat{J}_x\hat{S}_x - i\hat{S}_x\hat{J}_y + i\hat{J}_x\hat{S}_y - i^2\hat{J}_y\hat{S}_y)\Big) && (2.67)\\
&= \Big((\hat{J}_x\hat{S}_x - i\hat{J}_x\hat{S}_y + i\hat{S}_x\hat{J}_y + \hat{J}_y\hat{S}_y) + (\hat{J}_x\hat{S}_x - i\hat{S}_x\hat{J}_y + i\hat{J}_x\hat{S}_y + \hat{J}_y\hat{S}_y)\Big) && (2.68)\\
&= \Big(2\hat{J}_x\hat{S}_x + \hat{J}_y\hat{S}_y)\Big)\,, && (2.69)
\end{aligned}$$

so that

$$\begin{aligned}
\hat{J}_x\hat{S}_x + \hat{J}_y\hat{S}_y &= \tfrac{1}{2}(\hat{J}_+\hat{S}_- + \hat{J}_-\hat{S}_+). && (2.70)\\
\hat{\mathbf{J}}\cdot\hat{\mathbf{S}} &= \tfrac{1}{2}(\hat{J}_+\hat{S}_- + \hat{J}_-\hat{S}_+) + \hat{J}_z\hat{S}_z. && (2.71)
\end{aligned}$$

The new operators, $\hat{J}_\pm$ and $\hat{S}_\pm$, are raising and lowering operators. This means that when they operate on the wavefunction, the wavefunction produced is one where one of the quantum numbers has been raised or lowered:

$$\begin{aligned}
\hat{J}_\pm|\eta\Lambda; S\Sigma; J\Omega\rangle &= \hbar\sqrt{J(J+1) - \Omega(\Omega\mp 1)}\,|\eta\Lambda; S\Sigma; J\Omega\mp 1\rangle && (2.72)\\
\hat{S}_\pm|\eta\Lambda; S\Sigma; J\Omega\rangle &= \hbar\sqrt{S(S+1) - \Sigma(\Sigma\pm 1)}\,|\eta\Lambda; S\Sigma\mp 1; J\Omega\rangle && (2.73)
\end{aligned}$$

The spin-orbit part of Equation 2.60 is calculated as follows:

$$\begin{aligned}
\hat{H}_{so} &= A\big(\hat{\mathbf{L}}\cdot\hat{\mathbf{S}}\big) && (2.74)\\
&= A\big(\hat{L}_x\hat{S}_x + \hat{L}_y\hat{S}_y + \hat{L}_z\hat{S}_z\big) && (2.75)\\
&= A\left(\hat{L}_z\hat{S}_z + \tfrac{1}{2}(\hat{L}_+\hat{S}_- + \hat{L}_-\hat{S}_+)\right), && (2.76)
\end{aligned}$$

where $\hat{L}_+$ and $\hat{L}_-$ are the orbital angular momentum equivalent of the total and spin angular momentum raising and lowering operators, and the step between Equations 2.75 and 2.76 is due to equivalent reasoning as shown in deriving Equation 2.71.

2.4.1 Example with a $^3\Pi$ State

Using a $^3\Pi$ state as an example, there are six possible combinations of Λ and Σ as shown in Table 2.2. For this example, the following notation will be used: With the operators defined above, the MEs for Λ=1 and Λ=-1 with the same Ω will be equal, so only the Λ=1

Table 2.5 – Possible combinations of Λ and Σ to give Ω in a ${}^3\Pi$ state.

Λ	Σ	Ω	full notation ($\lvert\eta\Lambda; S\Sigma; J\Omega\rangle$)	$\lvert{}^3\Pi_{\lvert\Omega\rvert}\rangle$
+1	+1	+2	$\lvert\eta\Lambda{=}{+}1; S{=}1,\Sigma{=}{+}1; J,\Omega{=}{+}2\rangle$	$\lvert{}^3\Pi_2\rangle$
+1	0	+1	$\lvert\eta\Lambda{=}{+}1; S{=}1,\Sigma{=}0; J,\Omega{=}{+}1\rangle$	$\lvert{}^3\Pi_1\rangle$
+1	-1	0	$\lvert\eta\Lambda{=}{+}1; S{=}1,\Sigma{=}{-}1; J,\Omega{=}0\rangle$	$\lvert{}^3\Pi_0\rangle$

Table 2.6 – Hamiltonian matrix for a ${}^3\Pi$ state in a Hund's case (a) basis

	$\langle{}^3\Pi_0\rvert$	$\langle{}^3\Pi_1\rvert$	$\langle{}^3\Pi_2\rvert$
$\lvert{}^3\Pi_0\rangle$	$\langle{}^3\Pi_0\lvert\hat{H}\rvert{}^3\Pi_0\rangle$	$\langle{}^3\Pi_1\lvert\hat{H}\rvert{}^3\Pi_0\rangle$	$\langle{}^3\Pi_2\lvert\hat{H}\rvert{}^3\Pi_0\rangle$
$\lvert{}^3\Pi_1\rangle$	$\langle{}^3\Pi_0\lvert\hat{H}\rvert{}^3\Pi_1\rangle$	$\langle{}^3\Pi_1\lvert\hat{H}\rvert{}^3\Pi_1\rangle$	$\langle{}^3\Pi_2\lvert\hat{H}\rvert{}^3\Pi_1\rangle$
$\lvert{}^3\Pi_2\rangle$	$\langle{}^3\Pi_0\lvert\hat{H}\rvert{}^3\Pi_2\rangle$	$\langle{}^3\Pi_1\lvert\hat{H}\rvert{}^3\Pi_2\rangle$	$\langle{}^3\Pi_2\lvert\hat{H}\rvert{}^3\Pi_2\rangle$

MEs will be considered here. This Hamiltonian matrix is shown in Table 2.6

Using the previous definitions of the operators, each ME is equal to

$$\begin{aligned} &B\Big(\langle{}^3\Pi_{\lvert\Omega'\rvert}\rvert\hat{\boldsymbol{J}}^2+\hat{\boldsymbol{S}}^2+2\hat{J}_z\hat{S}_z-\hat{J}_+\hat{S}_- -\hat{J}_-\hat{S}_+\lvert{}^3\Pi_{\lvert\Omega\rvert}\rangle\Big) \\ &\quad +A\bigg(\langle{}^3\Pi_{\lvert\Omega'\rvert}\rvert\hat{L}_z\hat{S}_z+\tfrac{1}{2}\Big(\hat{L}_+\hat{S}_-+\hat{L}_-\hat{S}_+\Big)\lvert{}^3\Pi_{\lvert\Omega\rvert}\rangle\bigg), \end{aligned} \tag{2.77}$$

however, $\hat{\boldsymbol{J}}^2$, $\hat{J}_z$, $\hat{\boldsymbol{S}}^2$, $\hat{S}_z$, and $\hat{L}_z$ will only have non-zero values if ${}^3\Pi_{\Omega'}{=}{}^3\Pi_\Omega$. Therefore, for the five operators listed above, only diagonal MEs are non-zero. For the raising and lowering operators $\hat{J}_\pm$ and $\hat{S}_\pm$, only MEs with $\Delta\Omega = \pm1$ are non zero, for the same reason. Finally, the $\hat{L}_\pm$ raising and lowering operators require a change in Λ of ±1, which only occurs between different electronic states, and so these terms can be completely discarded here.

The $\hat{\mathbf{H}}_{\mathbf{rot}}+\hat{\mathbf{H}}_{\mathbf{so}}$ is therefore:

Using Equations 2.72 and 2.73, and those in Table 2.1, the MEs become (in cm^{-1}): For a single value of J, this matrix is diagonalised (i.e. a matrix $\mathbf{X}$ is found so that Equation 2.58 yields a diagonal matrix $\mathbf{E}$), and the eigenvalues are those along the diagonal of the

Table 2.7 – $\hat{\mathbf{H}}_{\mathbf{rot}}+\hat{\mathbf{H}}_{\mathbf{so}}$ for a ${}^3\Pi$ state in a Hund's case (a) basis

	$\langle{}^3\Pi_0\rvert$	$\langle{}^3\Pi_1\rvert$	$\langle{}^3\Pi_2\rvert$
$\lvert{}^3\Pi_0\rangle$	$\langle{}^3\Pi_0\rvert B(\hat{\boldsymbol{J}}^2+\hat{\boldsymbol{S}}^2+2\hat{J}_z\hat{S}_z)$ $+A(\hat{L}_z\hat{S}_z)\lvert{}^3\Pi_0\rangle$	$\langle{}^3\Pi_1\rvert -B\hat{J}_-\hat{S}_+\lvert{}^3\Pi_0\rangle$	0
$\lvert{}^3\Pi_1\rangle$	$\langle{}^3\Pi_0\rvert -B\hat{J}_+\hat{S}_-\lvert{}^3\Pi_1\rangle$	$\langle{}^3\Pi_1\rvert B(\hat{\boldsymbol{J}}^2+\hat{\boldsymbol{S}}^2+2\hat{J}_z\hat{S}_z)$ $+A(\hat{L}_z\hat{S}_z)\lvert{}^3\Pi_1\rangle$	$\langle{}^3\Pi_2\rvert -B\hat{J}_-\hat{S}_+\lvert{}^3\Pi_1\rangle$
$\lvert{}^3\Pi_2\rangle$	0	$\langle{}^3\Pi_1\rvert -B\hat{J}_+\hat{S}_-\lvert{}^3\Pi_2\rangle$	$\langle{}^3\Pi_2\rvert B(\hat{\boldsymbol{J}}^2+\hat{\boldsymbol{S}}^2+2\hat{J}_z\hat{S}_z)$ $+A(\hat{L}_z\hat{S}_z)\lvert{}^3\Pi_2\rangle$

Table 2.8 – Evaluated $\hat{\mathbf{H}}_{\mathbf{rot}} + \hat{\mathbf{H}}_{\mathbf{so}}$ matrix for a $^3\Pi$ state in a Hund's case (a) basis

	$\langle ^3\Pi_0 \vert$	$\langle ^3\Pi_1 \vert$	$\langle ^3\Pi_2 \vert$
$\vert ^3\Pi_0 \rangle$	$B\Big(J(J+1)+2\Big)-A$	$-B\sqrt{2J(J+1)}$	0
$\vert ^3\Pi_1 \rangle$	$-B\sqrt{2J(J+1)}$	$B\Big(J(J+1)+2\Big)$	$-B\sqrt{2J(J+1)-4}$
$\vert ^3\Pi_2 \rangle$	0	$-B\sqrt{2J(J+1)-4}$	$B\Big(J(J+1)-2\Big)+A$

Table 2.9 – $\hat{\mathbf{H}}_{\mathbf{rot}}$ for the C_2 $a^3\Pi_u$ state, v=0, J=2 level in a Hund's case (a) basis.

	$\langle ^3\Pi_2 \vert$	$\langle ^3\Pi_1 \vert$	$\langle ^3\Pi_0 \vert$
$\vert ^3\Pi_2 \rangle$	6.496	-4.593	0
$\vert ^3\Pi_1 \rangle$	-4.593	12.992	-5.626
$\vert ^3\Pi_0 \rangle$	0	-5.626	12.992

resulting matrix $\mathbf{E}$. For example, if we first of all exclude the spin-orbit term ($A\hbar^2$), for the C_2 $a^3\Pi_u$ state, v=0, J=2 level, this matrix is (in cm^{-1}): The order of the Ω states in Table 2.8 has been reversed so that they are in order of increasing energy. Diagonalising this matrix gives the eigenvalues 3.2481, 9.7443, and 19.4885 cm^{-1} for the F_1, F_2, and F_3 states, respectively. As only the terms involving the constant B have been included, these numbers will be degenerate with other levels (for example, the J=2, F_2 energy is equal to the J=3, F_1 energy. The transformation matrix, $\mathbf{X}$, contains the eigenvector coefficients: The first row of this matrix states that the real F_1 wavefunction is equal to $0.7746|^3\Pi_2\rangle + 0.5477|^3\Pi_1\rangle + 0.3162|^3\Pi_0\rangle$, and so on. If the spin-orbit term (A_0=-15.26986) is now included, Tables 2.9 and 2.10 become: The eigenvalues are now -9.737, 12.053 and 30.165 cm^{-1}. In Section 2.2.4.1 it was stated that a Hund's case (a) state has strong spin-orbit coupling, and can be described by the quantum number Ω. The C_2 $a^3\Pi_u$ state is best described by Hund's case (a), but it can be seen here that it is actually slightly towards case (b). The eigenvector coefficients in Table 2.10 show that all of the F_i states are mixtures of all three Ω states. When the spin-orbit coupling terms are included in

Table 2.10 – Eigenvector coefficient matrix ($\hat{\mathbf{X}}$) from the diagonalisation of $\hat{\mathbf{H}}_{\mathbf{rot}}$, for the C_2 $a^3\Pi_u$ state, v=0, J=2 level in a Hund's case (a) basis.

	$\vert ^3\Pi_2 \rangle$	$\vert ^3\Pi_1 \rangle$	$\vert ^3\Pi_0 \rangle$
F_1	0.7746	0.5477	0.3162
F_2	-0.5774	0.4082	0.7071
F_3	-0.2582	0.7303	-0.6325

Table 2.11 – $\mathbf{\hat{H}_{rot}} + \mathbf{\hat{H}_{so}}$ for the C_2 $a^3\Pi_u$ state, v=0, J=2 level in a Hund's case (a) basis (in cm^{-1}).

	$\langle {}^3\Pi_2 \vert$	$\langle {}^3\Pi_1 \vert$	$\langle {}^3\Pi_0 \vert$
$\vert {}^3\Pi_2 \rangle$	-8.774	-4.593	0
$\vert {}^3\Pi_1 \rangle$	-4.593	12.992	-5.626
$\vert {}^3\Pi_0 \rangle$	0	-5.626	28.262

Table 2.12 – Eigenvector coefficient matrix ($\mathbf{\hat{X}^{-1}}$) from the diagonalisation of $\mathbf{\hat{H}_{rot}} + \mathbf{\hat{H}_{so}}$, for the C_2 $a^3\Pi_u$ state, v=0, J=2 level (in cm^{-1}).

	$\vert {}^3\Pi_2 \rangle$	$\vert {}^3\Pi_1 \rangle$	$\vert {}^3\Pi_0 \rangle$
F_1	0.9782	0.2052	0.0304
F_2	-0.2040	0.9249	0.3210
F_3	0.0378	-.3202	0.9466

the Hamiltonian, it can be seen in Table 2.12 that the F_1 state is mostly Ω=2, F_2 is mostly Ω=1, and F_3 is mostly Ω=0. There are some contributions from the other Ω states, which indicates that this state is not completely case (a), but that it can be reasonably well described by the quantum number Ω.

2.4.2 Other Molecular Constants

2.4.2.1 Spin-Rotation Constant γ

As explained in Section 2.2.4.2, spin can also be coupled to the rotational axis. To include this effect, an $\hat{H}_{sr}$ term must be added to the Hamiltonian in 2.60, where (Brown and Carrington, 2003)

$$\begin{aligned}\hat{H}_{sr} &= \gamma \mathbf{\hat{N}} \cdot \mathbf{\hat{S}} && (2.78)\\ &= \gamma(\mathbf{\hat{J}} - \mathbf{\hat{S}}) \cdot \mathbf{\hat{S}} && (2.79)\\ &= \gamma(\mathbf{\hat{J}} \cdot \mathbf{\hat{S}} - \mathbf{\hat{S}} \cdot \mathbf{\hat{S}}) && (2.80)\\ &= \gamma\left(\tfrac{1}{2}(\hat{J}_+\hat{S}_- + \hat{J}_-\hat{S}_+) + \hat{J}_z\hat{S}_z - \mathbf{\hat{S}}^2\right) \quad \text{(from Equation 2.71).} && (2.81)\end{aligned}$$

A state with no orbital angular momentum is the best example to demonstrate this; a ${}^3\Sigma^-$ state will be used. The possible Ω components for this state are shown in Table 2.13. Diagonal MEs will be equal to $\gamma(\hat{J}_z\hat{S}_z - \mathbf{\hat{S}}^2) = \gamma(\Omega\Sigma - 2)$. Using Equations 2.72 and 2.73 along with 2.81, it is found that MEs with $\Delta\Omega = \pm 1$ are all equal, as shown below: If Hamiltonians as defined in Equation 2.60 are set up for the NH $X^3\Sigma^-$ state, v=0, J=2-4 levels, including only the term involving B as in the previous example ($\hat{H}_{so} = 0$

Table 2.13 – Possible combinations of Λ and Σ to give Ω in a $^3\Sigma^-$ state.

Λ	Σ	Ω	full notation ($\lvert\eta\Lambda; S\Sigma; J\Omega\rangle$)	$\lvert^3\Pi_\Omega\rangle$
0	+1	+1	$\lvert\eta\Lambda$=0; S=1,Σ=+1; J, Ω=+1$\rangle$	$\lvert^3\Sigma^-_{+1}\rangle$
0	0	0	$\lvert\eta\Lambda$=0; S=1,Σ=0; J, Ω=0$\rangle$	$\lvert^3\Sigma^-_0\rangle$
0	-1	-1	$\lvert\eta\Lambda$=0; S=1,Σ=-1; J, Ω=-1$\rangle$	$\lvert^3\Sigma^-_{-1}\rangle$

Table 2.14 – Evaluated $\hat{\mathbf{H}}_{\mathbf{sr}}$ matrix for a $^3\Sigma^-$ state in a Hund's case (a) basis

	$\langle^3\Sigma^-_1\rvert$	$\langle^3\Sigma^-_0\rvert$	$\langle^3\Sigma^-_{-1}\rvert$
$\lvert^3\Sigma^-_1\rangle$	$-\gamma\hbar^2$	$\gamma\hbar^2\Big(\frac{1}{2}\sqrt{2J(J+1)}\Big)$	0
$\lvert^3\Sigma^-_0\rangle$	$\gamma\hbar^2\Big(\frac{1}{2}\sqrt{2J(J+1)}\Big)$	$-2\gamma\hbar^2$	$\gamma\hbar^2\Big(\frac{1}{2}\sqrt{2J(J+1)}\Big)$
$\lvert^3\Sigma^-_{-1}\rangle$	0	$\gamma\hbar^2\Big(\frac{1}{2}\sqrt{2J(J+1)}\Big)$	$-\gamma\hbar^2$

as there is no orbital angular momentum), the three resulting eigenvalues for N=3 are degenerate (196.1193 cm^{-1}). When the $\hat{H}_{sr}$ Hamiltonian (Table 2.14) is added to the total Hamiltonian, using γ=-0.05485506 cm^{-1} (from (Ram and Bernath, 2010)), the N=3 eigenvalues are split into 195.9547, 196.1742, and 196.3387 cm^{-1}, for F_1, F_2, and F_3, respectively. This is shown in Figure 2.14. This occurs partly because with increased rotation, the circulation of the electrons about the internuclear axis affected, including in Σ states, and a magnetic moment occurs in the direction of $\boldsymbol{N}$. Therefore, electrons with their spin aligned with this field will have slightly lower energy than those aligned in the opposite direction.

2.4.2.2 Spin-Spin Constant $\boldsymbol{\lambda}$

When there are two unpaired electrons, the spin-spin constant, λ is required. The part of the Hamiltonian for this is (Hirota et al., 1994):

$$\hat{H}_{ss} = \lambda\left(\frac{2}{3}\right)\left(3\hat{S}_z^2 - \hat{\mathbf{S}}^2\right). \tag{2.82}$$

This is also most easily illustrated using a state with $\Lambda = 0$. Using the same example as for the spin-rotation constant, diagonal MEs will be equal to $\lambda\left(\frac{2}{3}\right)\left(3\Sigma^2 - S(S+1)\right) = \lambda\left(\frac{2}{3}\right)\left(3\Sigma^2 - 2\right)$, and as there are no raising or lowering operators present, all-off-diagonal MEs will be equal to zero: Starting again with the Hamiltonian that includes only the B term, and therefore degenerate N levels, adding the $\hat{H}_{ss}$ operator gives eigenvalues split into 195.9120, 196.7326, and 195.6337 cm^{-1}, for F_1, F_2, and F_3, respectively. This is shown in Figure 2.14.

Table 2.15 – Evaluated $\hat{\mathbf{H}}_{\mathbf{ss}}$ matrix for a $^3\Sigma^-$ state in a Hund's case (a) basis

	$\langle ^3\Sigma_1^- \|$	$\langle ^3\Sigma_0^- \|$	$\langle ^3\Sigma_{-1}^- \|$
$\| ^3\Sigma_1^- \rangle$	$\frac{2}{3}\lambda\hbar^2$	0	0
$\| ^3\Sigma_0^- \rangle$	0	$-\frac{4}{3}\lambda\hbar^2$	0
$\| ^3\Sigma_{-1}^- \rangle$	0	0	$\frac{2}{3}\lambda\hbar^2$

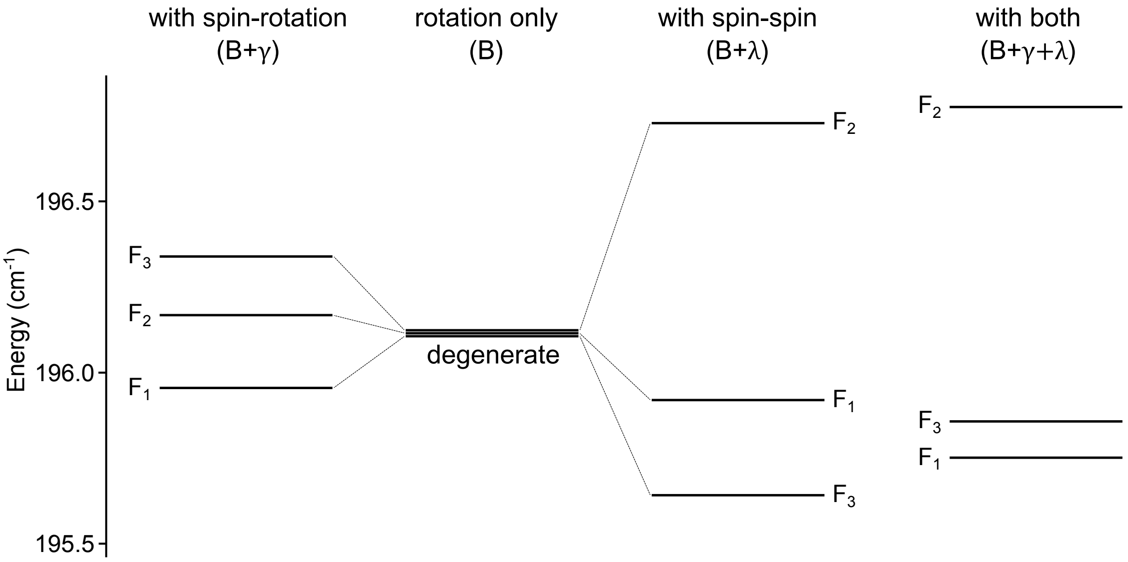

Figure 2.14 – Energy levels of the NH $X^3\Sigma^-$ state including different constants.

2.4.2.3 Lambda-Doubling Constants *o*, *p*, and *q*

As explained in Section 2.3 and shown in Table 2.2, the fact the Λ can have positive or negative values means that two energy levels exist for each set of other quantum numbers. The direction of the angular momentum along the internuclear axis itself does not cause a difference in energy, and the real levels are actually linear combinations of the positive and negative Λ wavefunctions.

There are three Hamiltonian terms that contribute to Λ-doubling. They connect states in the Hamiltonian matrix with opposite values of Λ, resulting in the two levels being slightly separated after diagonalisation. The Hamiltonian term is (Brown and Carrington, 2003; Western, 2014):

$$\hat{H}_{ld} = \tfrac{1}{2}o\left(\hat{S}_+^2 + \hat{S}_-^2\right) - \tfrac{1}{2}p\left(\hat{N}_+\hat{S}_+ + \hat{N}_-\hat{S}_-\right) + \tfrac{1}{2}q\left(\hat{N}_+^2 + \hat{N}_-^2\right) \tag{2.83}$$

There is another term, $e^{\pm 2i\theta}$, that is included so as to connect only $\Delta\Lambda = \pm 2$ states, but it has been omitted here for simplicity. Equation 2.4.2.3 can be evaluated by replacing $\hat{N}_\pm$ with $\hat{J}_\pm - \hat{S}_\pm$, ultimately resulting in (Brown and Merer, 1979):

$$\hat{H}_{ld} = \tfrac{1}{2}(o + p + q)\left(\hat{S}_+^2 + \hat{S}_-^2\right) - \tfrac{1}{2}(p + 2q)\left(\hat{J}_+\hat{S}_+ + \hat{J}_-\hat{S}_-\right) + \tfrac{1}{2}q\left(\hat{J}_+^2 + \hat{J}_-^2\right), \tag{2.84}$$

which is easier to evaluate.

In the previous examples of a $^3\Pi$ state using the C_2 $\mathrm{a}^3\Pi_\mathrm{u}$ state, the –Λ basis states were omitted. The full matrices would include all six basis states, and be made of two identical and diagonal 3×3 blocks, with the other elements all being equal to zero. The $\mathbf{\hat{H}_{ld}}$ matrix has non zero terms in two identical off-diagonal 3×3 blocks, and zeroes in the two diagonal 3×3 blocks.

The separation of the two levels resulting from the diagonalisation is generally on a similar order of magnitude to the spin-spin and spin-rotation splitting, depending on the molecule and amount of rotation. The q term will contribute to any Π state, connect all basis states with $\Delta\Lambda = \pm 2$, and will split the levels equally across values of Σ. p is required for states with $S \geq 0$, and connects basis states in the Hamiltonian with $\Delta\Lambda = \pm 2$ and $\Delta\Omega = \pm 1$ or 0. o only connects basis states with $\Delta\Lambda = \pm 2$ and $\Delta\Omega = 0$, and is required when $S \geq 1$. The 3×3 block where Λ' is positive is: The other 3×3 block where Λ' is negative is: In these two matrices, $\langle {}^3\Pi_{-0}|$ represents the basis state $|\eta, \Lambda\text{=-}1; S\text{=}1, \Sigma\text{=+}1; J, \Omega\text{=}0\rangle$. The evaluated form of these matrices is the same:

Table 2.16 – $\hat{\mathbf{H}}_{\mathbf{ld}}$ ($\Delta\Lambda = +2$ section) for a $^3\Pi$ state in a Hund's case (a) basis.

	$\langle ^3\Pi_2 \vert$	$\langle ^3\Pi_1 \vert$	$\langle ^3\Pi_0 \vert$
$\vert ^3\Pi_{-2}\rangle$	0	0	$\frac{1}{2}q\hat{J}_-^2$
$\vert ^3\Pi_{-1}\rangle$	0	$\frac{1}{2}q\hat{J}_-^2$	$\frac{1}{2}(p+2q)\hat{J}_-\hat{S}_-$
$\vert ^3\Pi_{-0}\rangle$	$\frac{1}{2}q\hat{J}_-^2$	$\frac{1}{2}(p+2q)\hat{J}_-\hat{S}_-$	$\frac{1}{2}(o+p+q)\hat{S}_-^2$

Table 2.17 – $\hat{\mathbf{H}}_{\mathbf{ld}}$ ($\Delta\Lambda = -2$ section) for a $^3\Pi$ state in a Hund's case (a) basis.

	$\langle ^3\Pi_{-2} \vert$	$\langle ^3\Pi_{-1} \vert$	$\langle ^3\Pi_{-0} \vert$
$\vert ^3\Pi_2\rangle$	0	0	$\frac{1}{2}q\hat{J}_+^2$
$\vert ^3\Pi_1\rangle$	0	$\frac{1}{2}q\hat{J}_+^2$	$\frac{1}{2}(p+2q)\hat{J}_+\hat{S}_+$
$\vert ^3\Pi_0\rangle$	$\frac{1}{2}q\hat{J}_+^2$	$\frac{1}{2}(p+2q)\hat{J}_+\hat{S}_+$	$\frac{1}{2}(o+p+q)\hat{S}_+^2$

2.4.2.4 Centrifugal Constants

In Section 2.4, it was stated that $\hat{H}_{rot}$ is equal to B$\hat{\mathbf{N}}^2$. This indicates that the energy level spacing increases by the same amount with increased rotation. However, centrifugal distortion causes the spacing to change with increasing rotation, and in fact,

$$\hat{H}_{rot} = B\hat{\mathbf{N}}^2 - D\hat{\mathbf{N}}^4 + H\hat{\mathbf{N}}^6 + L\hat{\mathbf{N}}^8.... \tag{2.85}$$

The MEs of these higher order operators are obtained by taking the appropriate power of the evaluated $\hat{\mathbf{N}}^2$ matrix. For example, using the same $^3\Pi$ system as previously, the $\hat{\mathbf{N}}^4$ matrix would be equal to Higher powers of $\hat{\mathbf{N}}$ are obtained in a similar fashion.

Similarly, centrifugal distortion constants exist for the other molecular constants, to which the subscripts D, H, L etc. are appended. The centrifugal distortion is included in

Table 2.18 – Evaluated $\hat{\mathbf{H}}_{\mathbf{ld}}$ matrix for a $^3\Pi$ state in a Hund's case (a) basis

	$\langle ^3\Pi_2 \vert$	$\langle ^3\Pi_1 \vert$	$\langle ^3\Pi_0 \vert$
$\vert ^3\Pi_{-2}\rangle$	0	0	$\frac{1}{2}q\Big(\sqrt{J(J+1)}\times\sqrt{J(J+1)-2}\Big)$
$\vert ^3\Pi_{-1}\rangle$	0	$\frac{1}{2}q\Big(J(J+1)\Big)$	$\frac{-\frac{1}{2}(p+2q)}{\times\sqrt{2J(J+1)}}$
$\vert ^3\Pi_{-0}\rangle$	$\frac{1}{2}q\Big(\sqrt{J(J+1)}\times\sqrt{J(J+1)-2}\Big)$	$\frac{-\frac{1}{2}(p+2q)}{\times\sqrt{2J(J+1)}}$	$o+p+q$

Table 2.19 – Evaluated $\hat{\mathbf{N}}^4$ matrix for a $^3\Pi$ state in a Hund's case (a) basis, where $x = J(J+1)$.

	$\langle ^3\Pi_0 \vert$	$\langle ^3\Pi_1 \vert$	$\langle ^3\Pi_2 \vert$
$\vert ^3\Pi_0\rangle$	$-D\Big(x^2 + 6x + 4\Big)$	$D\Big(2\sqrt{2x}(x+2)\Big)$	$-D\Big(\sqrt{2x}\sqrt{2x-4}\Big)$
$\vert ^3\Pi_1\rangle$	$D\Big(2\sqrt{2x}(x+2)\Big)$	$-D\Big(x^2 + 8x\Big)$	$D\Big(2x\sqrt{2x-4}\Big)$
$\vert ^3\Pi_2\rangle$	$-D\Big(\sqrt{2x}\sqrt{2x-4}\Big)$	$D\Big(2x\sqrt{2x-4}\Big)$	$-D\Big(4x\Big)$

the same manner; by including more $\hat{\mathbf{N}}^2$ terms. For example, the term including A_D is

$$A_D\frac{[\hat{\mathbf{N}}^2, \hat{\mathbf{L}}\cdot\hat{\mathbf{S}}]_+}{2} \tag{2.86}$$

$$=A_D\frac{[\hat{\mathbf{N}}^2, \hat{L}_z\hat{S}_z]_+}{2} \tag{2.87}$$

$$=A_D\frac{\hat{\mathbf{N}}^2\hat{L}_z\hat{S}_z + \hat{L}_z\hat{S}_z\hat{\mathbf{N}}^2}{2} \tag{2.88}$$

The same procedure of including extra $\hat{\mathbf{N}}^2$ terms also applies to the other constants that have been described.

Other constants are required when $\Lambda > 1$ or $S > 1$, but no such molecule is analysed in this thesis.

2.4.3 Parity Matrices

As described in Section 2.4.2.3, the full Hamiltonian is in terms of basis states that take into account Λ-doubling, which for example means six basis states for a $^3\Pi$ state. There are then non zero values in the $\Lambda = \pm 2$ MEs. This can be simplified by transforming the pure Ω matrix into a "parity" matrix, where the parity basis states are linear combinations of their corresponding Ω states:

$$|^{2S+1}\Lambda_{(|\Omega|)}(\pm)\rangle = \frac{|^{2S+1}\Lambda_{+\Omega}\rangle \pm (-1)^{J-2\Sigma+S+\sigma}|^{2S+1}\Lambda_{-\Omega}\rangle}{\sqrt{2}} \tag{2.89}$$

$$|^{2S+1}\Lambda_{\Omega=0}(\pm)\rangle = |^{2S+1}\Lambda_{\Omega=0}\rangle \quad \text{(for } \Sigma \text{ states only)}, \tag{2.90}$$

where σ=1 for Σ^- states and is zero for all other states, and the parentheses in the Ω subscripts indicate that Ω is no longer a good quantum number. For the example $^3\Pi$

Table 2.20 – Parity transformation matrix for a $^3\Pi$ state

	$\langle ^3\Pi_{+0}\vert$	$\langle ^3\Pi_{+1}\vert$	$\langle ^3\Pi_{+2}\vert$	$\langle ^3\Pi_{-0}\vert$	$\langle ^3\Pi_{-1}\vert$	$\langle ^3\Pi_{-2}\vert$
$\vert ^3\Pi_{(0)}(f)\rangle$	$1/\sqrt{2}$	0	0	$1/\sqrt{2}$	0	0
$\vert ^3\Pi_{(1)}(f)\rangle$	0	$1/\sqrt{2}$	0	0	$1/\sqrt{2}$	0
$\vert ^3\Pi_{(2)}(f)\rangle$	0	0	$1/\sqrt{2}$	0	0	$1/\sqrt{2}$
$\vert ^3\Pi_{(0)}(e)\rangle$	$1/\sqrt{2}$	0	0	$-1/\sqrt{2}$	0	0
$\vert ^3\Pi_{(1)}(e)\rangle$	0	$1/\sqrt{2}$	0	0	$-1/\sqrt{2}$	0
$\vert ^3\Pi_{(2)}(e)\rangle$	0	0	$1/\sqrt{2}$	0	0	$-1/\sqrt{2}$

state, the parity basis functions are, for odd J,

$$|^3\Pi_{(0)}(+)\rangle = \frac{|^3\Pi_{+0}\rangle + |^3\Pi_{-0}\rangle}{\sqrt{2}} \qquad |^3\Pi_{(0)}(-)\rangle = \frac{|^3\Pi_{+0}\rangle - |^3\Pi_{-0}\rangle}{\sqrt{2}} \tag{2.91}$$

$$|^3\Pi_{(1)}(+)\rangle = \frac{|^3\Pi_{+1}\rangle + |^3\Pi_{-1}\rangle}{\sqrt{2}} \qquad |^3\Pi_{(1)}(-)\rangle = \frac{|^3\Pi_{+1}\rangle - |^3\Pi_{-1}\rangle}{\sqrt{2}} \tag{2.92}$$

$$|^3\Pi_{(2)}(+)\rangle = \frac{|^3\Pi_{+2}\rangle + |^3\Pi_{-2}\rangle}{\sqrt{2}} \qquad |^3\Pi_{(2)}(-)\rangle = \frac{|^3\Pi_{+2}\rangle - |^3\Pi_{-2}\rangle}{\sqrt{2}} \tag{2.93}$$

For even J, the subtraction and addition of the negative Ω states are reversed. This alternation with J is removed, as usual, by the use of rotationless parity (e/f parity; Section 2.3). The Ω Hamiltonian matrix can be transformed into the parity Hamiltonian matrix using a transformation matrix made up of eigenvectors based on the above definitions. For the $^3\Pi$ state, this transformation matrix is shown in Table 2.20.

2.4.4 Perturbations

As shown in the preceding sections, the Hamiltonian matrices link states with the same J value within an electronic state. The result is that the energy levels are split from where they would be if the linking MEs were zero. Hamiltonian MEs can also link states of the same J value in different electronic states, and a larger Hamiltonian can be set up including multiple electronic states. The result of diagonalising this Hamiltonian matrix is that eigenvalues from the different electronic states that have a linking ME are "pushed apart" by the same amount, compared to what their values would have been if there were no linking ME. This change in energy is called a perturbation, and a simple illustration is shown in Figure 2.15.

The amount that they are perturbed is related to both the value of the ME and the

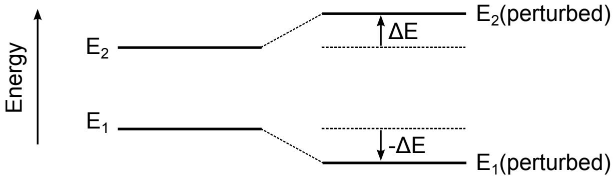

Figure 2.15 – The effect of a single perturbation on two nearby energy levels of different electronic states.

difference between the unperturbed energy levels, so that the closer the unperturbed levels, the greater the perturbation. This means that such perturbations occur when the J progression within a vibrational level of one electronic state is similar in energy to that of one in a different electronic state (for which interactions are possible).

2.5 Line Intensities

Transitions can occur between the energy levels described in Section 2.1, if certain selection rules are obeyed. The interaction of electromagnetic radiation with a molecule can cause it to absorb a photon and cause a transition from a lower to an upper level, if the photon energy is equal to the energy level spacing. This occurs because of the interaction of the oscillating electric field of the radiation with the electric dipole of the molecule. The probability of a photon being absorbed is defined by the Einstein B coefficient, which can be thought of as a "rate constant" for absorption. Radiation can also cause stimulated emission of a photon, and a transition from an upper to a lower level. The rate constant for this process is actually also the Einstein B coefficient. Spontaneous emission of a photon can also occur from a molecule in an excited state, causing a transition to a lower level, for which the rate constant is the Einstein A coefficient.

The Einstein A and B coefficient are related by:

$$A = \frac{8\pi h\nu^3}{c^3}B, \tag{2.94}$$

where ν is the frequency of the transition in Hz and c is the speed of light in ms^{-1}. Therefore, only one is required. The link between Einstein A coefficients and a real spectrum was explained in Section 1.4. The main purpose of the "Line Intensities for Diatomic Molecules of Astronomical Interest" section of this work is to provide absolute line intensities so that other workers can use them to calculate spectra, and Einstein A

coefficients are provided for this purpose. They are calculated using the equation

$$\begin{aligned} A_{J'F'JF} &= \frac{16\pi^3\nu^3 S_{J'F'JF}}{3\epsilon_0 hc^3(2J'+1)} && (2.95)\\ &= 3.136\,18932\times 10^{-7}\frac{\tilde{\nu}^3 S_{J'F'JF}}{(2J'+1)}, && (2.96)\end{aligned}$$

where $A_{J'F'JF}$ is in s^{-1}, $S_{J'F'JF}$ is the line intensity in debye, $\tilde{\nu}$ is in cm^{-1}, ϵ_0 is the vacuum permittivity constant in $\mathrm{A}^2\mathrm{s}^4\mathrm{kg}^{-1}\mathrm{m}^{-3}$,, and e is the elementary charge in C.

Astronomers often prefer the oscillator strength, $f_{J'F'JF}$, which can easily be converted from $A_{J'F'JF}$ using

$$\begin{aligned} f_{J'F'JF} &= \frac{m_e\epsilon_0 c^3}{2\pi e^2\nu^2}\frac{(2J'+1)}{(2J+1)}A_{J'F'JF} && (2.97)\\ &= 1.499\,193\,78\,27\frac{1}{\tilde{\nu}^2}\frac{(2J'+1)}{(2J+1)}A_{J'F'JF}, && (2.98)\end{aligned}$$

where m_e is the mass of the electron in kg.

2.5.1 Notation

There are different Einstein A values for every possible individual transition, between the real spin components, denoted by F (as described in Section 2.4.1), that can be described by linear combinations of the Hund's case (a) basis states, $|\eta\Lambda; S\Sigma; \Omega J\rangle$. It may seem reasonable to use either the symbols $A_{\eta'\Lambda'S'\Sigma'\Omega'J'\eta\Lambda S\Sigma\Omega J}$ or $A_{J'J}$. However, clearly the former is too cumbersome, and $A_{J'J}$ implies that it is for only a J transition, whereas in reality there are multiple transitions for each J transition (when $S \geq 0$, which is the case for all of the electronic states considered in this thesis). As an alternative, $A_{J'F'JF}$ and $S_{J'F'JF}$ are used. This still has the issue that the symbol F is also used as a quantum number for nuclear spin, but as this is not considered in this thesis, F always refers to the real fine structure component, and never the hyperfine structure quantum number.

In addition, MEs and wavefunctions in terms of the real F components will use the symbol ψ_{JF}, as opposed to $|\eta\Lambda; S\Sigma; \Omega J\rangle$. This is to make a clear distinction between wavefunctions that describe the real F components and those that represent a basis state.

Finally, primes will always be used to indicate upper states, and so within an equation or symbol where one state is clearly labelled as the upper state, the double primes indicating a lower state will normally be omitted to improve readability. Sometimes, however, they will be included for clarity.

2.5.2 The Line Intensity, $S_{J'F'JF}$

The line intensity, $S_{J'F'JF}$, in Equation 2.95 is defined as (Whiting and Nicholls, 1974; Whiting et al., 1980):

$$S_{J'F'JF} = \langle \psi_{J'F'} | \hat{\boldsymbol{\mu}} | \psi_{JF} \rangle^2 \tag{2.99}$$

where $\hat{\boldsymbol{\mu}}$ is the dipole moment operator. The MEs in Equation 2.99 are obtained from the combination of the eigenvectors from the diagonalisation of the upper and lower state Hamiltonians, and a transition matrix in the same basis as the Hamiltonians (case (a) in this thesis). This process is explained in Section 2.5.7. The required quantities are the elements of this case (a) basis transition matrix, which are:

$$\langle \eta'\Lambda'; S'\Sigma'; J'\Omega' | \hat{\boldsymbol{\mu}} | \eta\Lambda; S\Sigma; J\Omega \rangle^2 = \Sigma_{p,M',M} \langle \eta'\Lambda'; S'\Sigma'; J'\Omega'M' | \hat{\boldsymbol{\mu}} | \eta\Lambda; S\Sigma; J\Omega M \rangle^2, \tag{2.100}$$

where M is the projection of the total angular momentum J on the laboratory Z-axis, and can take values from $-J$ to J in steps of unity.

The dipole moment operator is a vector operator:

$$\hat{\boldsymbol{\mu}} = \sum_i z_i \boldsymbol{r}_i. \tag{2.101}$$

Here, the sum is over all of the charges z_i in the molecule and $\boldsymbol{r}_i$ is a vector representing their coordinates. The wavefunctions in Equation 2.100 can be defined as product wavefunctions:

$$|\eta\Lambda; S\Sigma; J\Omega M\rangle = |\eta\Lambda; S\Sigma\rangle |J\Omega M\rangle, \tag{2.102}$$

so that the MEs can be expressed (Bernath, 2005) as

$$\langle \eta'\Lambda'; S'\Sigma'; J'\Omega'M' | \hat{\boldsymbol{\mu}} | \eta\Lambda; S\Sigma; J\Omega M \rangle = \langle \eta'\Lambda'; S'\Sigma' | \hat{\boldsymbol{\mu}} | \eta\Lambda; S\Sigma \rangle \langle \Omega' J' M' | \hat{\boldsymbol{\mu}} | \Omega J M \rangle. \tag{2.103}$$

$\boldsymbol{\mu}$ can be split in into its cartesian components, μ_x, μ_y and μ_z, where μ_z is the dipole moment along the internuclear axis. Three other dipole moment operators can then be defined (Bernath, 2005):

$$\hat{\mu}_0 = \hat{\mu}_z \tag{2.104}$$

$$\hat{\mu}_+ = \frac{1}{\sqrt{2}}(\hat{\mu}_x + i\hat{\mu}_y) \tag{2.105}$$

$$\hat{\mu}_- = \frac{1}{\sqrt{2}}(\hat{\mu}_x - i\hat{\mu}_y). \tag{2.106}$$

The positive, negative, and zero subscripts indicate that $\hat{\mu}$ raises, lowers, or doesn't effect Λ, respectively.

For a $\Delta\Lambda = 0$ transition, $S_{J'F'JF}$ would be equal to $\langle \eta'\Lambda'; S'\Sigma'; J'\Omega'|\hat{\mu}^0|\eta\Lambda; S\Sigma; J\Omega\rangle^2$ if the problem only needed to be considered in the molecular frame. However, real intensities need to be calculated in the laboratory frame.

For the evaluation of $\langle \Omega' J' M'|\hat{\boldsymbol{\mu}}|\Omega J M\rangle$ it is convenient to express the dipole moment operator in the spherical tensor form, $T_p^k(\hat{\boldsymbol{\mu}})$ and $T_q^k(\hat{\boldsymbol{\mu}})$. Here, k is the rank of the tensor, equal to 1 for single photon transitions, and p and q are the components, in the laboratory and molecular frames, respectively, and can take integer values from $-k$ to k. These spherical tensors represent a rotation of the three-dimensional coordinate system that defines a vector operator, and the important relationships here are: $T^1_{q=0} = \hat{\mu}_0$, $T^1_{q=1} = \hat{\mu}_+$, and $T^1_{q=-1} = \hat{\mu}_-$.

The reason for changing into spherical tensor notation is because the dipole moment operator can easily be transformed from the molecular to the laboratory coordinate system, and the MEs can be easily evaluated. For this, the relationship (Brown and Carrington, 2003)

$$T_p^k(\hat{\boldsymbol{\mu}}) = \sum_q D^k_{p,q}(\omega)^* T_q^k(\hat{\boldsymbol{\mu}}) \tag{2.107}$$

is used, where $D^k_{p,q}(\omega)^*$ is a rotation matrix with MEs of the form $\langle j, m'|R(\omega)|j, m\rangle$, R is the rotation operator, and ω represents the three angles through which the coordinate system axes are rotated. The wavefunctions in the rotation matrix are the spherical harmonics. The MEs in Equation 2.103 can then be expressed as:

$$\begin{aligned} &\langle \eta'\Lambda'; S'\Sigma'; J'\Omega' M'|\sum_q D^1_{p,q}(\omega)^* T_q^1(\hat{\boldsymbol{\mu}})|\eta\Lambda; S\Sigma; J\Omega M\rangle \\ =&\sum_q \langle \Omega' J' M'|D^1_{p,q}(\omega)^*|\Omega J M\rangle\langle \eta'\Lambda'; S'\Sigma'|T_q^1(\hat{\boldsymbol{\mu}})|\eta\Lambda; S\Sigma\rangle. \end{aligned} \tag{2.108}$$

The dipole moment operator has no effect on S and Σ, and the case (a) basis set is orthonormal, so Equation 2.103 can be rewritten as

$$\sum_q \langle \Omega' J' M' | D^1_{p,q}(\omega)^* | \Omega J M \rangle \langle \eta' \Lambda' | T^1_q(\hat{\boldsymbol{\mu}}) | \eta \Lambda \rangle \delta_{S',S} \delta_{\Sigma',\Sigma}, \tag{2.109}$$

where δ is the Kronecker delta. The MEs $\langle \Omega' J' M' | D^1_{p,q}(\omega)^* | \Omega J M \rangle$ can be evaluated analytically (Brown and Carrington, 2003), so that the full ME has a rotational part and a vibronic part:

$$\sum_q (-1)^{M'-\Omega'} \sqrt{(2J'+1)(2J+1)} \begin{pmatrix} J' & 1 & J \\ -\Omega' & q & \Omega \end{pmatrix} \begin{pmatrix} J' & 1 & J \\ -M' & q & M \end{pmatrix} \langle \eta' \Lambda' | T^1_q(\hat{\boldsymbol{\mu}}) | \eta \Lambda \rangle. \tag{2.110}$$

The selection rules for S and Σ in the form of the Kronecker deltas will be enforced later. Summing over M gives

$$\sum_q (-1)^{J'-\Omega'} \sqrt{(2J'+1)(2J+1)} \begin{pmatrix} J' & 1 & J \\ -\Omega' & q & \Omega \end{pmatrix} \langle \eta' \Lambda' | T^1_q(\hat{\boldsymbol{\mu}}) | \eta \Lambda \rangle. \tag{2.111}$$

These values are those that make up the Hund's case (a) transition matrix, which is transformed into a transition matrix in terms of the real F components as described in Section 2.5.7.

Another very important point to note about Equation 2.110 is that it gives the selection rules $\Delta M = 0, \pm 1$ and $\Delta J = 0, \pm 1$.

2.5.3 The Vibronic Part

The ME $\langle \eta' \Lambda' | T^1_q(\hat{\boldsymbol{\mu}}) | \eta \Lambda \rangle$ is the vibronic only ME. Only diatomic molecules are being considered and the rotation part is not present, so the wavefunctions here are the solution of the one-dimensional Schrödinger equation, discussed previously and shown in Equation 2.17.

For a rovibrational transition within the same electronic state (so $\Delta\Lambda = 0$) this ME is equal to $\langle \eta\Lambda | \hat{\mu}_0(r) | \eta\Lambda \rangle$, where $\hat{\mu}_0(r)$ is the dipole moment function (DMF) and r is the internuclear distance. Using the Born-Oppenheimer approximation, the electronic wavefunction can be assumed to adjust immediately to any change in the nuclear positions, so that the value of the dipole moment can be calculated at a number of values of r by fixing the positions of the nuclei, providing a DMF. The calculation of the DMF is performed using ab initio methods. The calculation of the MEs requires the DMF, and the solutions of the one-dimensional Schrödinger equation for the upper and lower levels, which can be obtained using the program LEVEL (discussed in Section 2.1.5).

When there is also an electronic transition, the Born-Oppenheimer approximation is used to separate the electronic and vibrational wavefunctions, so that

$$\langle \eta'\Lambda'|\hat{\boldsymbol{\mu}}|\eta\Lambda\rangle = \langle \mathrm{v}'|\langle n'\Lambda'|\hat{\boldsymbol{\mu}}(r)|n\Lambda\rangle|\mathrm{v}\rangle = \langle \mathrm{v}'|\hat{\mathbf{R}}_{\mathbf{e}}(r)|\mathrm{v}\rangle. \tag{2.112}$$

$\hat{\mathbf{R}}_{\mathbf{e}}(r)$ is a transition dipole moment function (TDMF; note the separation of η into n, the electronic quantum number, and v, the vibrational quantum number). This is also calculated by ab initio methods, in which the electronic wavefunctions of the upper and lower state are calculated at various fixed internuclear distances and the value $\hat{\mathbf{R}}_{\mathbf{e}}(r)$ is evaluated, giving another function of r. The MEs of $\hat{\mathbf{R}}_{\mathbf{e}}(r)$ can then be calculated similarly by LEVEL.

LEVEL requires the input of a potential energy curve and a DMF if MEs are to be calculated between levels of the same electronic state, or two potentials and a TDMF if between two electronic states. The calculation of the MEs by LEVEL is very simple; the (T)DMF operates on the lower state wavefunction, and the resulting function which is then multiplied by the upper state wavefunction. An example for the C_2 Swan system is given in Figure 2.16, in which the purple line is the function resulting from the above process. This is then integrated with respect to r to give a single value for the ME.

2.5.4 Case (b) to (a) Transformation

There is a vital part of the line intensity calculations that is not performed by any of the computer programs used (RKR1, LEVEL, or PGOPHER). The MEs that are calculated by LEVEL (Section 2.1.5) do not include electron spin. This means that the basis functions of the LEVEL MEs are in terms of N as opposed to J, and can be referred to as case (b) MEs, which are of the form

$$\langle \eta'\Lambda'N'|T^1_q(\hat{\boldsymbol{\mu}})|\eta\Lambda N\rangle. \tag{2.113}$$

Note that these are vibronic MEs, and exclude the angular dependence of the wavefunction, which is included later as shown in Equation 2.111 (but they do include the rotational dependence of the vibronic wavefunctions). The values that are required

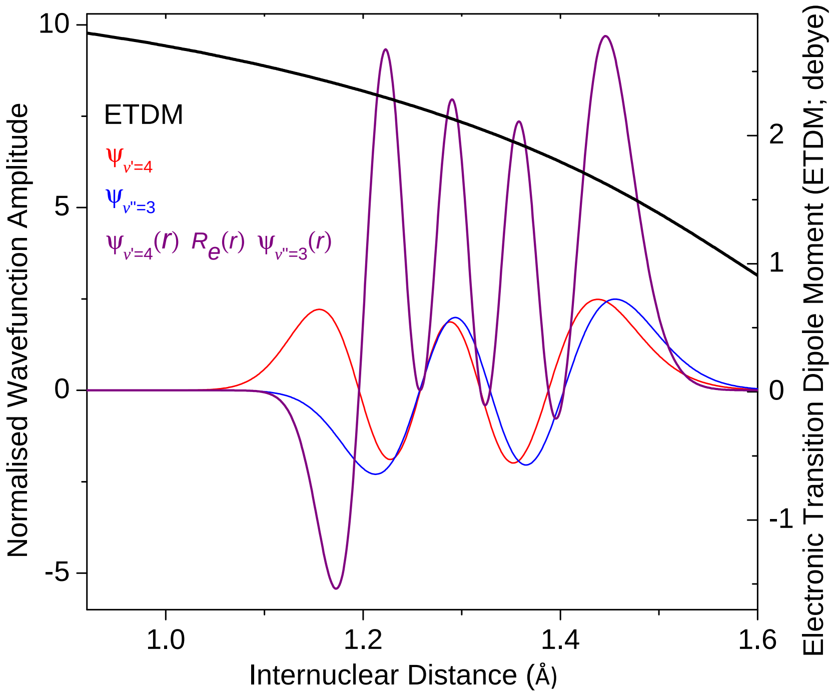

Figure 2.16 – Calculation of a ME by LEVEL, using a C_2 Swan v′=4 and v″=3 transition as an exmaple.

are those on the right hand side of Equation 2.111, $\langle \eta' \Lambda' | T^1_q(\hat{\boldsymbol{\mu}}) | \eta \Lambda \rangle$, that are used to make up the transition matrix described in the previous section. As PGOPHER uses a case (a) basis set, these are case (a) MEs with spin that depend on J and Ω, and those from LEVEL are case (b) without spin, that depend on N. Therefore a transformation from case (b) to case (a) with spin is required, and an equation to perform this transformation, the "transformation equation", was derived by Colin M. Western (University of Bristol), as follows:

Starting from the general relationship given by Brown and Howard (1976),

$$|\eta\Lambda; NKSJM\rangle = \sum_{\Sigma,\Omega} (-1)^{N-S+\Omega} \sqrt{2N+1} \begin{pmatrix} J & S & N \\ \Omega & -\Sigma & -K \end{pmatrix} |\eta\Lambda; S\Sigma; JM\Omega\rangle, \qquad (2.114)$$

and applying the constraint $K = \Lambda$ appropriate for linear molecules we have

$$|\eta\Lambda; N\Lambda SJM\rangle = \sum_{\Sigma} (-1)^{N-S+\Lambda+\Sigma} \sqrt{2N+1} \begin{pmatrix} J & S & N \\ \Lambda+\Sigma & -\Sigma & -\Lambda \end{pmatrix} |\eta\Lambda; S\Sigma; JM\Omega\rangle. \qquad (2.115)$$

Both sides are multiplied by a trial function:

$$(-1)^{N-S+\Lambda+\Sigma}\sqrt{2N+1}\begin{pmatrix} J & S & N \\ \Lambda+\Sigma & -\Sigma & -\Lambda \end{pmatrix}|\eta\Lambda; N\Lambda SJM\rangle$$
$$= \sum_{\Sigma'}(-1)^{\Sigma'-\Sigma}(2N+1)\begin{pmatrix} J & S & N \\ \Lambda+\Sigma' & -\Sigma & -\Lambda \end{pmatrix}\begin{pmatrix} J & S & N \\ \Lambda+\Sigma & -\Sigma & -\Lambda \end{pmatrix}|\eta\Lambda; S\Sigma'; JM\Omega'\rangle. \tag{2.116}$$

Summing both sides over N gives:

$$\sum_N(-1)^{N-S+\Lambda+\Sigma}\sqrt{2N+1}\begin{pmatrix} J & S & N \\ \Lambda+\Sigma & -\Sigma & -\Lambda \end{pmatrix}|\eta\Lambda; N\Lambda SJM\rangle$$
$$= \sum_N\sum_{\Sigma'}(-1)^{\Sigma'-\Sigma}(2N+1)\begin{pmatrix} J & S & N \\ \Lambda+\Sigma' & -\Sigma & -\Lambda \end{pmatrix}\begin{pmatrix} J & S & N \\ \Lambda+\Sigma & -\Sigma & -\Lambda \end{pmatrix}|\eta\Lambda; S\Sigma'; JM\Omega'\rangle$$
$$= \sum_{\Sigma'}(-1)^{\Sigma'-\Sigma}\sum_N(2N+1)\begin{pmatrix} J & S & N \\ \Lambda+\Sigma' & -\Sigma & -\Lambda \end{pmatrix}\begin{pmatrix} J & S & N \\ \Lambda+\Sigma & -\Sigma & -\Lambda \end{pmatrix}|\eta\Lambda; S\Sigma'; JM\Omega'\rangle$$
$$= |\eta\Lambda; S\Sigma; JM\Omega\rangle. \tag{2.117}$$

The last step follows from the orthogonality relationship:

$$\sum_{N,\gamma}(2N+1)\begin{pmatrix} J & S & N \\ \alpha & \beta & \gamma \end{pmatrix}\begin{pmatrix} J & S & N \\ \alpha' & \beta' & \gamma \end{pmatrix} = \delta_{\alpha\alpha'}\delta_{\beta\beta'}, \tag{2.118}$$

given that the additional sum over γ collapses to the term with $\alpha+\beta+\gamma = 0 = \alpha'+\beta'+\gamma$. Overall the conversion from a case (b) to case (a) wavefunction is

$$|\eta\Lambda; S\Sigma; JM\Omega\rangle = \sum_N(-1)^{N-S+\Omega}\sqrt{2N+1}\begin{pmatrix} J & S & N \\ \Omega & -\Sigma & -\Lambda \end{pmatrix}|\eta\Lambda; N\Lambda SJM\rangle. \tag{2.119}$$

For transition strengths, we require the MEs of the space fixed electric dipole operator:

$$T^k_p(\mu) = \sum_q D^k_{p,q}(\omega)^* T^k_q(\mu). \tag{2.120}$$

The MEs of this are well known; in a Hund's case (a) basis they are

$$\begin{aligned}&\langle\eta'\Lambda;S\Sigma';J'M'\Omega'|T^k_p(\mu)|\eta\Lambda;S\Sigma;JM\Omega\rangle=\\&\sum_q(-1)^{M'-\Omega'}\sqrt{(2J'+1)(2J+1)}\begin{pmatrix}J'&k&J\\-\Omega'&q&\Omega\end{pmatrix}\begin{pmatrix}J'&k&J\\-M'&q&M\end{pmatrix}\langle\eta'\Lambda'|T^k_q(J'\Omega'J\Omega)|\eta\Lambda\rangle\end{aligned}\tag{2.121}$$

This is essentially Equation (6.320) of Brown and Carrington (2003) generalised to any value of p and q. In addition, to a first approximation the electronic ME $\langle\eta'\Lambda'|T^k_q(J'\Omega'J\Omega)|\eta\Lambda\rangle$ should not depend on J or Ω, but these have been added as parameters here to allow for centrifugal distortion. A similar equation can be derived for Hund's case (b) wavefunctions:

$$\begin{aligned}&\langle\eta'\Lambda;N'SJ'M'|T^k_p(\mu)|\eta\Lambda;NSJM\rangle=\\&(-1)^{J'-M'}\begin{pmatrix}J'&k&J\\-M'&q&M\end{pmatrix}(-1)^{N'+S+J+k}\sqrt{(2J'+1)(2J+1)}\begin{Bmatrix}N'&J'&S\\J&N&k\end{Bmatrix}\\&\times\sum_q(-1)^{N'-\Lambda'}\sqrt{(2N'+1)(2N+1)}\begin{pmatrix}N'&k&N\\-\Lambda'&q&\Lambda\end{pmatrix}\langle\eta'\Lambda'|T^k_q(N'N)|\eta\Lambda\rangle\end{aligned}\tag{2.122}$$

This is a generalisation of Equation (6.321) of Brown and Carrington (2003). Again the purely electronic ME $\langle\eta'\Lambda'|T^k_q(N'N)|\eta\Lambda\rangle$ should not depend on N, but we allow it to do so to account for centrifugal distortion. We now need to relate these two using the transformation between bases derived above:

$$\begin{aligned}&\langle\eta'\Lambda;S\Sigma';J'M'\Omega'|T^k_p(\mu)|\eta\Lambda;S\Sigma;JM\Omega\rangle=\\&\sum_{N,N'}(-1)^{N'-N+\Lambda'-\Lambda}\sqrt{(2N'+1)(2N+1)}\begin{pmatrix}J'&S&N'\\\Omega'&-\Sigma&-\Lambda'\end{pmatrix}\begin{pmatrix}J&S&N\\\Omega&-\Sigma&-\Lambda\end{pmatrix}\\&\times\langle\eta'\Lambda;N'SJ'M'|T^k_p(\mu)|\eta\Lambda;NSJM\rangle.\end{aligned}\tag{2.123}$$

Substituting on both sides:

$$\begin{aligned}
&\sum_q (-1)^{M'-\Omega'} \sqrt{(2J'+1)(2J+1)} \begin{pmatrix} J' & k & J \\ -\Omega' & q & \Omega \end{pmatrix} \begin{pmatrix} J' & k & J \\ -M' & q & M \end{pmatrix} \langle \eta' \Lambda' | T^k_q (J'\Omega' J\Omega) | \eta \Lambda \rangle \\
&\quad = \sum_{N,N'} (-1)^{N'-N+\Lambda'-\Lambda} \sqrt{(2N'+1)(2N+1)} \begin{pmatrix} J' & S & N' \\ \Omega' & -\Sigma & -\Lambda' \end{pmatrix} \begin{pmatrix} J & S & N \\ \Omega & -\Sigma & -\Lambda \end{pmatrix} \\
&\quad \times (-1)^{J'-M'} \begin{pmatrix} J' & k & J \\ -M' & q & M \end{pmatrix} (-1)^{N'+S+J+k} \sqrt{(2J'+1)(2J+1)} \begin{Bmatrix} N' & J' & S \\ J & N & k \end{Bmatrix} \\
&\quad \times \sum_q (-1)^{N'-\Lambda'} \sqrt{(2N'+1)(2N+1)} \begin{pmatrix} N' & k & N \\ -\Lambda' & q & \Lambda \end{pmatrix} \langle \eta' \Lambda' | T^k_q (N'N) | \eta \Lambda \rangle .
\end{aligned} \tag{2.124}$$

The terms in M cancel out:

$$\begin{aligned}
&\sum_q (-1)^{J'-\Omega'} \sqrt{(2J'+1)(2J+1)} \begin{pmatrix} J' & k & J \\ -\Omega' & q & \Omega \end{pmatrix} \langle \eta' \Lambda' | T^k_q (J'\Omega' J\Omega) | \eta \Lambda \rangle \\
&\quad = \sum_{N,N'} (-1)^{N'-N+\Lambda'-\Lambda} \sqrt{(2N'+1)(2N+1)} \begin{pmatrix} J' & S & N' \\ \Omega' & -\Sigma & -\Lambda' \end{pmatrix} \begin{pmatrix} J & S & N \\ \Omega & -\Sigma & -\Lambda \end{pmatrix} \\
&\quad \times (-1)^{N'+S+J+k} \sqrt{(2J'+1)(2J+1)} \begin{Bmatrix} N' & J' & S \\ J & N & k \end{Bmatrix} \\
&\quad \times \sum_q (-1)^{N'-\Lambda'} \sqrt{(2N'+1)(2N+1)} \begin{pmatrix} N' & k & N \\ -\Lambda' & q & \Lambda \end{pmatrix} \langle \eta' \Lambda' | T^k_q (N'N) | \eta \Lambda \rangle ,
\end{aligned} \tag{2.125}$$

and with a little more simplification:

$$\begin{aligned}
&\sum_q (-1)^{J'-\Omega'} \begin{pmatrix} J' & k & J \\ -\Omega' & q & \Omega \end{pmatrix} \langle \eta' \Lambda' | T^k_q (J'\Omega' J\Omega) | \eta \Lambda \rangle \\
&\quad = \sum_{N,N'} (-1)^{N'-N+\Lambda'-\Lambda} (2N'+1)(2N+1) \begin{pmatrix} J' & S & N' \\ \Omega' & -\Sigma & -\Lambda' \end{pmatrix} \begin{pmatrix} J & S & N \\ \Omega & -\Sigma & -\Lambda \end{pmatrix} \\
&\quad \times (-1)^{N'+S+J+k} \begin{Bmatrix} N' & J' & S \\ J & N & k \end{Bmatrix} \sum_q (-1)^{N'-\Lambda'} \begin{pmatrix} N' & k & N \\ -\Lambda' & q & \Lambda \end{pmatrix} \langle \eta' \Lambda' | T^k_q (N'N) | \eta \Lambda \rangle .
\end{aligned} \tag{2.126}$$

To enforce the $\Delta\Sigma = 0$ rule, Λ and Λ' must be the same on both sides, so the equation can be used for a single value of q:

$$\begin{aligned}
&(-1)^{J'-\Omega'} \begin{pmatrix} J' & k & J \\ -\Omega' & q & \Omega \end{pmatrix} \langle \eta'\Lambda' | T_q^k(J'\Omega' J\Omega) | \eta\Lambda \rangle \\
&\quad = \sum_{N,N'} (-1)^{N-N'+S+J+k+\Lambda} (2N'+1)(2N+1) \begin{pmatrix} J' & S & N' \\ \Omega' & -\Sigma & -\Lambda' \end{pmatrix} \begin{pmatrix} J & S & N \\ \Omega & -\Sigma & -\Lambda \end{pmatrix} \\
&\quad \times \begin{Bmatrix} N' & J' & S \\ J & N & k \end{Bmatrix} \begin{pmatrix} N' & k & N \\ -\Lambda' & q & \Lambda \end{pmatrix} \langle \eta'\Lambda' | T_q^k(N'N) | \eta\Lambda \rangle.
\end{aligned} \tag{2.127}$$

Finally,

$$\begin{aligned}
&\langle \eta'\Lambda' | T_q^k(J'\Omega' J\Omega) | \eta\Lambda \rangle = (-1)^{J'-\Omega'} \begin{pmatrix} J' & k & J \\ -\Omega' & q & \Omega \end{pmatrix}^{-1} \\
&\quad \times \sum_{N,N'} (-1)^{N-N'+S+J+k+\Lambda} (2N'+1)(2N+1) \begin{pmatrix} J' & S & N' \\ \Omega' & -\Sigma & -\Lambda' \end{pmatrix} \begin{pmatrix} J & S & N \\ \Omega & -\Sigma & -\Lambda \end{pmatrix} \\
&\quad \times \begin{Bmatrix} N' & J' & S \\ J & N & k \end{Bmatrix} \begin{pmatrix} N' & k & N \\ -\Lambda' & q & \Lambda \end{pmatrix} \langle \eta'\Lambda' | T_q^k(N'N) | \eta\Lambda \rangle.
\end{aligned} \tag{2.128}$$

On the right hand side of the equation, $\langle \eta'\Lambda' | T_q^k(N'N) | \eta\Lambda \rangle$, is the Hund's case (b) ME that is calculated by LEVEL, which applies to a specific transition involving given values of N' and N''. The case (a) ME on the left hand side specifies the transition in terms of J and Ω, and these are calculated by summing over all of the case (b) MEs (specified in terms of N' and N'') that can contribute to the to the chosen $J'\Omega'$-$J''\Omega''$ transition. The final result is that a case (a) ME is calculated from a weighted average of the contributing case (b) MEs.

Using the CN A$^2\Pi$-X$^2\Sigma^+$ system as an example, for a particular combination of J values, say $J' = 5.5$ and $J'' = 4.5$, the sum part of Equation 2.5.4 will require 3 MEs from LEVEL with N'-N'' equal to 5-4, 5-5 and 6-5. The sum formally includes $N' - N'' = 6 - 4$ but this violates the selection rule on N, and so its contribution calculated in Equation 2.5.4 is equal to zero.

This equation must be used for each possible combination of J', Ω', J'', and Ω'', and

Table 2.21 – Pure Ω transition matrix set up by PGOPHER for the CN $A^2\Pi$-$X^2\Sigma^+$ (1,0) R(4.5) example transition, using the transformation method.

	$\vert{}^2\Pi^-_{\pm1.5}\rangle$	$\vert{}^2\Pi^-_{\pm0.5}\rangle$
$\vert{}^2\Sigma^+_{\pm0.5}\rangle$	-0.166203	0
$\vert{}^2\Sigma^+_{\pm0.5}\rangle$	0	-0.140229

for a particular J', J'' there are four possible combinations of Ω that have non zero MEs, corresponding to $\langle\Omega',\Lambda',\Sigma'|\Omega'',\Lambda'',\Sigma''\rangle$ = $\langle+1.5,+1,+0.5|+0.5,0,+0.5\rangle$, $\langle-1.5,-1,-0.5|-0.5,0,-0.5\rangle$, $\langle+0.5,-1,-0.5|+0.5,0,+0.5\rangle$, and $\langle-0.5,+1,+0.5|-0.5,0,-0.5\rangle$. The first and second are symmetry related as the ME is invariant to reversal of the signs of all the projections, as are the third and fourth. This means that the resulting MEs will be the same for the ones involving the $\Omega = \pm1.5$ spin component, and for the $\Omega = \pm0.5$ spin component.

The values of the LEVEL MEs for the example transition in the (7,5) band are -0.0850773, -0.0857546, and 0.0848928, for N'-N'' equal to 5-4, 5-5 and 6-5, respectively. The results of using Equation 2.5.4 with these three N transitions are -0.0850568 and -0.0849132, for the MEs with Ω' equal to ±1.5 and ±0.5, respectively. When these are multiplied by the factor in Equation 2.111, the transition matrix in Table 2.21 results.

Before continuing, it should be noted that in the course of the final project of my PhD, Chapter 6, "The OH X$^2\Pi$ Rovibrational Transitions", a revision was made to the transformation equation discussed above.

In the derivation, the assumption was made that $\Delta\Sigma = 0$, and in fact this selection rule was artificially enforced. This removed the sum over q that was present in Equation 2.5.4, and also made the Σ term in the second 3-j symbol equal to Σ'' as opposed to Σ'. If this assumption is not made, S and Σ can be retained in the case (a) ME, and the transformation equation can be rewritten as

$$\langle\eta'\Lambda';S'\Sigma'|T^k_q(J'J)|\eta\Lambda;S\Sigma\rangle = (-1)^{J'-\Omega'}\begin{pmatrix} J' & k & J \\ -\Omega' & \Omega'-\Omega & \Omega \end{pmatrix}^{-1}$$
$$\times\sum_{N,N'}(-1)^{N'-N+\Omega'-\Omega+S+J+\Lambda'+k}(2N'+1)(2N+1)\begin{pmatrix} J' & S & N' \\ \Omega' & -\Sigma' & -\Lambda' \end{pmatrix}\begin{pmatrix} J & S & N \\ \Omega & -\Sigma & -\Lambda \end{pmatrix}$$
$$\times\begin{Bmatrix} N' & J' & S \\ J & N & k \end{Bmatrix}\begin{pmatrix} N' & k & N \\ -\Lambda' & \Lambda'-\Lambda & \Lambda \end{pmatrix}\langle\eta'\Lambda'|T^k_q(N'N)|\eta\Lambda\rangle. \tag{2.129}$$

If this modified transformation equation is used, very small off-diagonal MEs are present in the transition matrix.

The CN (Chapter 4) and NH (Chapter 5) calculations were performed with the original version of the transformation equation, and the final OH (Chapter 6) calculations used the revised version. The revised version will be used in the future to adjust the CN and NH line lists. The full effect of this change is discussed in the OH chapter, Chapter 6.

2.5.5 The Herman-Wallis (H-W) Effect

The rotation of a diatomic molecule results in a centrifugal force, which displaces the atoms and increases the bond length (Herman and Wallis, 1955). This causes the vibrational wavefunctions to change with different amounts of rotation, which therefore means that the MEs depend on rotation. This is called the H-W effect. Also, as has been shown before by Chackerian et al. (1989) (see their Equation 3), the sign and magnitude of the H-W effect mainly depends on the dipole moment and its first derivative with respect to the internuclear distance.

Calculations of the type reported in this thesis often use one rotationless ME for a vibrational band, and the effect of rotation on the vibrational wavefunction is ignored. This can be a very good approximation for molecules with heavier atoms, but NH contains a light hydrogen atom which is strongly affected by the centrifugal force. An illustration of the magnitude of the H-W effect in NH is shown in Figure 2.17, which shows how the vibrational part of the wavefunction changes with N and J for NH and C_2. Although the effect is quite small for heavier atoms, if transitions in vibrational bands with a small Franck-Condon factor in an electronic transition are being calculated, it can still be noticeable (Le Roy and Vrscay, 1975; Brooke et al., 2014*b*; Ram et al., 2014). The H-W effect has been included in these calculations by calculating MEs for the full range of J values that are intended to be reported, and then entering the individual MEs into PGOPHER (one for each $J'\Omega'$-$J''\Omega''$ transition).

2.5.6 The "N Only" Method

Before the use of the transformation equation, a single rotationless ME for each vibrational band was taken directly from LEVEL and entered into PGOPHER (this was done for the C_2 Swan system calculations). This ignores two parts of the calculations; the inclusion of the H-W effect and the transformation between LEVEL's case (b) MEs and

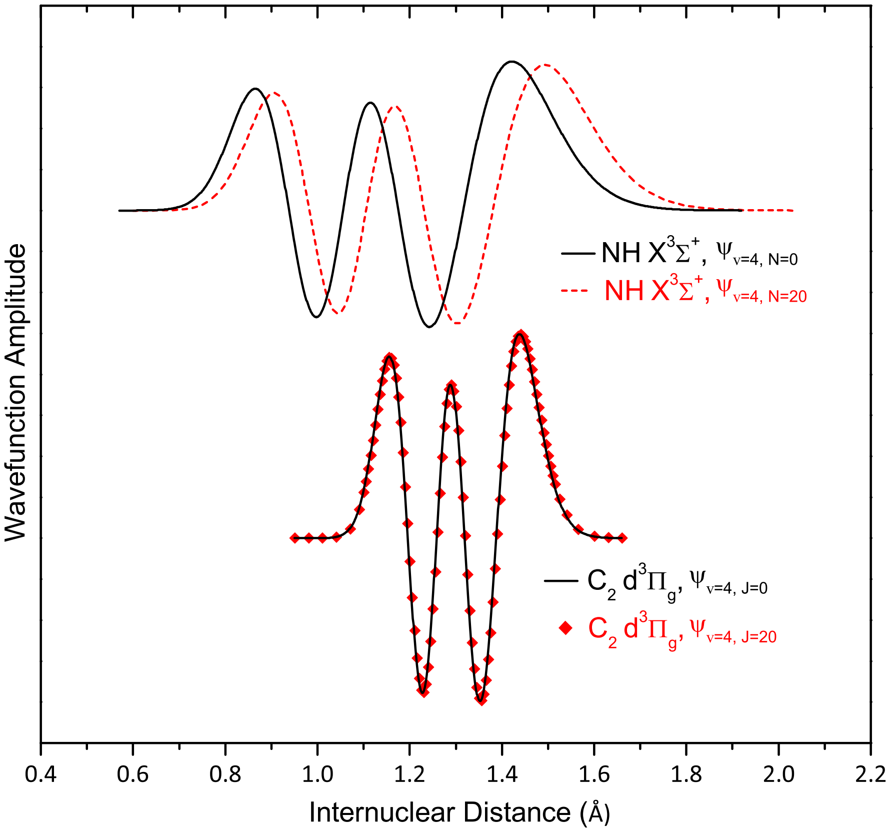

Figure 2.17 – Effect of rotation on the vibrational wavefunctions of the $d^3\Pi_g$, v=4 state of C_2 and the $X^3\Sigma^-$, v=4 state of NH (v=4 levels chosen arbitrarily as examples). Reprinted with permission from Brooke et al. JCP, 141, 054310, (2014). Copyright 2014, American Institute of Physics.

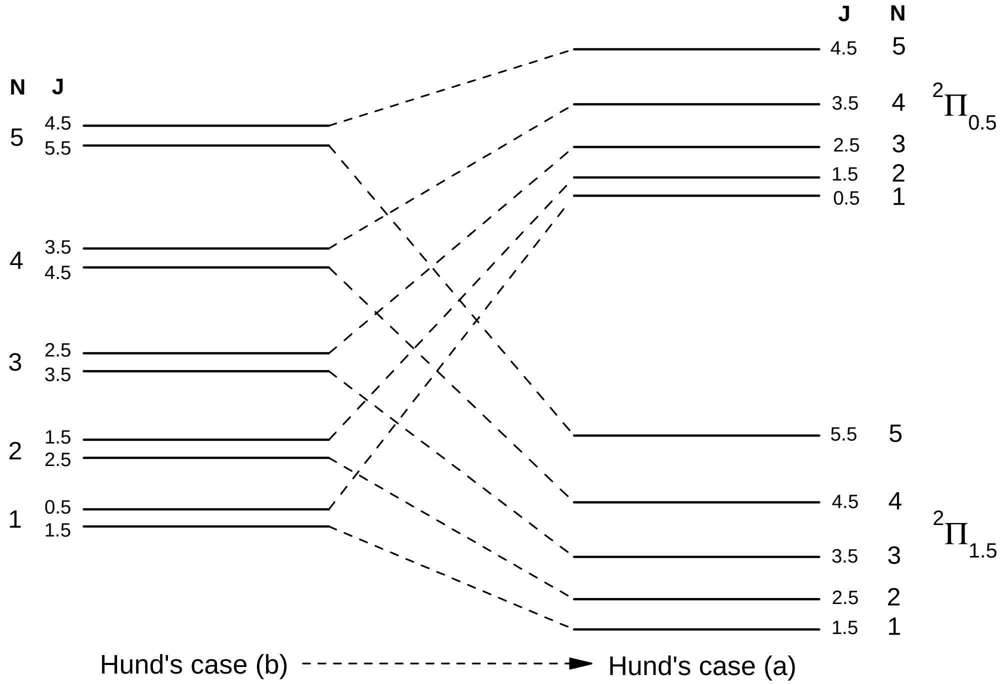

Figure 2.18 – Transformation from a Hund's case (b) to (a) state for an inverted $^2\Pi$ state. The energy levels are ordered correctly but are not to scale.

PGOPHER's case (a) MEs.

The reason that the case (a) and (b) MEs are different is that a case (a) ME, where Ω is a good quantum number and N is not, is made up of wavefunctions that are linear combinations of a number of case (b) wavefunctions, in which N is a good quantum number and Ω is not. Making a direct link between them is therefore not correct. However, if there is no H-W effect, the case (b) MEs will be identical, and the transformation to case (a) will leave them unchanged. Hence the two points that are ignored are strongly linked, and whether the approximation is reasonable or not depends on the extent of the H-W effect. This is an approximation that is valid for heavier molecules, like C_2, but not for lighter ones such as NH.

It is possible to take the H-W effect into account and not the transformation, by making the direct link described above between LEVEL and PGOPHER MEs, which is the approximation of assigning N labels (not good quantum numbers) to the levels of the case (a) state. This link is made using a diagram that shows the transformation between the cases, which is shown in Figure 2.18 for the CN $A^2\Pi$ state.

MEs can then be transferred from LEVEL to PGOPHER based only on their N values,

Table 2.22 – Pure Ω transition matrix set up by PGOPHER for the CN $A^2\Pi$-$X^2\Sigma^+$, (1,0), R(4.5) example transition, using the N only method.

	$\lvert^2\Pi^-_{\pm1.5}\rangle$	$\lvert^2\Pi^-_{\pm0.5}\rangle$
$\lvert^2\Sigma^+_{\pm0.5}\rangle$	-0.166242	0
$\lvert^2\Sigma^+_{\pm0.5}\rangle$	0	-0.139077

which is referred to as the "N only" method. Using the same example as in Section 2.5.4 (CN $A^2\Pi$-$X^2\Sigma^+$ (7,5) R(4.5)), the values taken from LEVEL would be R(4)=-0.0850773 and S(4)=-0.0848928 for the MEs with Ω' equal to ±1.5 and ±0.5, respectively. After inclusion of the factor in Equation 2.111, the transition matrix in Table 2.22 is formed, which is very similar but not identical to Table 2.21.

Another way of describing why the N only method is an approximation only, using this example transition, is that it ignores the contributions from the Q(5) and R(5) LEVEL MEs, and includes the contribution from the S(4) ME, which should be zero.

The "N only" method has been described here as it was the original method used for the CN, CP, and NH calculations discussed later, and was also used as a test in the OH calculations. Whatever the real Hund's case of an electronic state, the transformation between case (b) and (a) is always required (if the H-W effect is not negligible), as it is between the basis sets used by the programs LEVEL and PGOPHER, and doesn't involve the final states, the transformation to which is described in the next section.

2.5.7 Transformation of Hund's Case (a) Transition Matrix

As stated in Section 2.5.2, the MEs in terms of the real F components are obtained from the combination of the eigenvectors from the diagonalisation of the upper and lower state Hamiltonians, and a transition matrix in a case (a) basis. This process is performed by PGOPHER and it is described here using the NH $X^3\Sigma^-$ state as an example.

For each J transition, a 3×3 pure omega transition matrix is set up by PGOPHER using the case (a) MEs, $\langle\eta'\Lambda'; S'\Sigma'; J'\Omega'|T^1_0|\eta\Lambda; S\Sigma; J\Omega\rangle$. This is transformed to a symmetrised matrix, that has the basis functions described in Section 2.4.3. For the P and R branches, this results in one 2×2 and one 1×1 matrix, for the $|^3\Sigma^-_{(1)}(e)\rangle/|^3\Sigma^-_{(0)}(e)\rangle$ and $|^3\Sigma^-_{(1)}(f)\rangle$ basis functions, respectively. For example, for the (1,0), R(4) transition, the original and symmetrised matrices are shown in Tables 2.23 and 2.24.

The Hamiltonians are set up initially in the pure Ω case (a) form, and then transformed into the parity Hamiltonian matrices as described in Section 2.4.3. The "original"

Table 2.23 – Pure Ω transition matrix set up by PGOPHER for the (1,0), R(4) example transition.

	$\vert^3\Sigma^-_{+1}\rangle$	$\vert^3\Sigma^-_{0}\rangle$	$\vert^3\Sigma^-_{-1}\rangle$
$\vert^3\Sigma^-_{+1}\rangle$	-0.148373	0	0
$\vert^3\Sigma^-_{0}\rangle$	0	-0.151539	0
$\vert^3\Sigma^-_{-1}\rangle$	0	0	-0.148373

Table 2.24 – Symmetrised parity transition matrices for the (1,0), R(4) example transition.

	$\vert^3\Sigma^-_{(1)}(e)\rangle$	$\vert^3\Sigma^-_{(0)}(e)\rangle$
$\vert^3\Sigma^-_{(1)}(e)\rangle$	-0.148373	0
$\vert^3\Sigma^-_{(0)}(e)\rangle$	0	-0.151539

	$\vert^3\Sigma^-_{(1)}(f)\rangle$
$\vert^3\Sigma^-_{(1)}(f)\rangle$	-0.148373

parity transition matrices, **O**, are then combined with the eigenvector matrices from the diagonalisation of the parity Hamiltonian matrices, giving the "transformed" transition matrices, **T**, in terms of the real *F* levels, using

$$\mathbf{T} = \mathbf{X_l^T O X_u}, \tag{2.130}$$

where $\mathbf{X_u}$ and $\mathbf{X_l}$ are the upper and lower eigenvector matrices, respectively.

For the example transition, the parity Hamiltonians diagonalise to give the eigenvectors shown in Tables 2.25 to 2.28:

Application of Equation 2.130 to the eigenvalues in the above matrices and the "original" transition matrices shown in Table 2.24 gives the *e* parity **T** matrix for shown in Table 2.29.

These are the $\langle\psi_{J'F'}|\hat{\boldsymbol{\mu}}|\psi_{JF}\rangle$ MEs, and so $S_{J'F'JF}$ and then the Einstein A values can be calculated directly. For the example transition, $S_{J'F'JF}$ is equal to the values in Table 2.29 squared, and the Einstein A values are 21.8182, 22.9405, .0067193 and 0.00001923 s^{-1} for the F_{11}, F_{33}, F_{13} and F_{31} transitions, respectively.

Table 2.25 – Left - Symmetrised *e* Hamiltonian matrix for the v=1, J=4 example level. Right - eigenvectors resulting from the diagonalisation of this matrix.

	$\vert^3\Sigma^-_{(1)}(e)\rangle$	$\vert^3\Sigma^-_{(0)}(e)\rangle$
$\vert^3\Sigma^-_{(1)}(e)\rangle$	3439.3603	-139.9945
$\vert^3\Sigma^-_{(0)}(e)\rangle$	-139.9945	3468.8251

	$\vert^3\Sigma^-_{(1)}(e)\rangle$	$\vert^3\Sigma^-_{(0)}(e)\rangle$
$\psi_{J=4,N=3,F_1}$	-0.7432	-0.6691
$\psi_{J=4,N=5,F_3}$	-0.6691	0.7432

Table 2.26 – Left - Symmetrised *f* Hamiltonian matrix for the v=1, J=4 example level. Right - eigenvectors.

	$\|^3\Sigma^-_{(1)}(f)\rangle$
$\|^3\Sigma^-_{(1)}(f)\rangle$	3439.4947

	$\|^3\Sigma^-_{(1)}(f)\rangle$
$\psi_{J=4,N=4,F_2}$	1

Table 2.27 – Left - Symmetrised *e* Hamiltonian matrix for the v=0, J=3 example level. Right - eigenvectors.

	$\|^3\Sigma^-_{(1)}(e)\rangle$	$\|^3\Sigma^-_{(0)}(e)\rangle$
$\|^3\Sigma^-_{(1)}(e)\rangle$	196.4604	-113.1125
$\|^3\Sigma^-_{(0)}(e)\rangle$	-113.1125	227.2733

	$\|^3\Sigma^-_{(1)}(e)\rangle$	$\|^3\Sigma^-_{(0)}(e)\rangle$
$\psi_{J=3,N=2,F_1}$	-0.7533	-0.6577
$\psi_{J=3,N=4,F_3}$	-0.6577	-0.7533

Table 2.28 – Left - Symmetrised *f* Hamiltonian matrix for the v=0, J=3 example level. Right - eigenvectors.

	$\|^3\Sigma^-_{(1)}(f)\rangle$
$\|^3\Sigma^-_{(1)}(f)\rangle$	196.5422

	$\|^3\Sigma^-_{(1)}(f)\rangle$
$\psi_{J=3,N=3,F_2}$	1

Table 2.29 – Transformed parity transition matrices for the (1,0), R(4) example transition, in terms of the true F and parity levels

	$\psi_{J=4,F_{1e}}$	$\psi_{J=4,F_{3e}}$
$\psi_{J=3,F_{1e}}$	-0.149798	0.000121
$\psi_{J=3,F_{3e}}$	0.003030	-0.150099

	$\psi_{J=4,F_{2f}}$
$\psi_{J=3,F_{2f}}$	-0.148373

2.5.8 Band intensities and lifetimes

One of the most useful methods of validation of our calculated line intensities is to compare them to experimentally observed radiative lifetimes. The radiative lifetime (hereafter referred to only as lifetimes), τ (in s), of a quantum state is defined as the time taken for the population of molecules in that quantum state to reach $1 - 1/e$ times the original population, by spontaneous radiative decay to lower levels . Its value is equal to the reciprocal of the sum of the Einstein A coefficients for all of the possible transitions to lower levels (Larsson, 1983) from a single upper level. This can be observed experimentally by monitoring the change in population with time of a specific quantum state.

Vibrational band intensities are often reported in theoretical line intensity studies, so they are also useful for validation. They are calculated in this thesis as the sum of Einstein A coefficients for all possible transitions within a specific band, from the F level of lowest energy in the upper state. These can also be converted into band oscillator strengths using the equation (Larsson, 1983)

$$f_{\mathrm{v}'\mathrm{v}} = \frac{m_e c}{8\pi^2 e^2} \frac{1}{\tilde{\nu}^2} \frac{(2 - \delta_{0,\Lambda'})}{(2 - \delta_{0,\Lambda''})} A_{\mathrm{v}'\mathrm{v}} \tag{2.131}$$

$$= 1.49919368 \, \frac{1}{\tilde{\nu}^2} \frac{(2 - \delta_{0,\Lambda'})}{(2 - \delta_{0,\Lambda''})} A_{\mathrm{v}'\mathrm{v}}. \tag{2.132}$$

2.6 Summary

The full procedure for the production of line intensities, though not all is used in every chapter, can be summarised as follows.

Spectroscopic molecular constants are obtained in PGOPHER (Western, 2014), which sets up standard N^2 Hamiltonians, by least-squares fitting to a set of observed transitions. Perturbation constants are included here if required. Equilibrium constants are calculated by fitting to the power series expansions in v + 1/2, using the constants T_{v} and B_{v}. These are employed in the program RKR1 (Le Roy, 2004) to generate potential energy curves, which are then entered into LEVEL (Le Roy, 2007) along with an ab initio DMF or TDMF. LEVEL generates vibrational wavefunctions and transition matrix elements (MEs), but does not include electron spin. These MEs are therefore in terms of N and not J, and we refer to them as Hund's case (b) MEs. They are converted to case (a) MEs which include

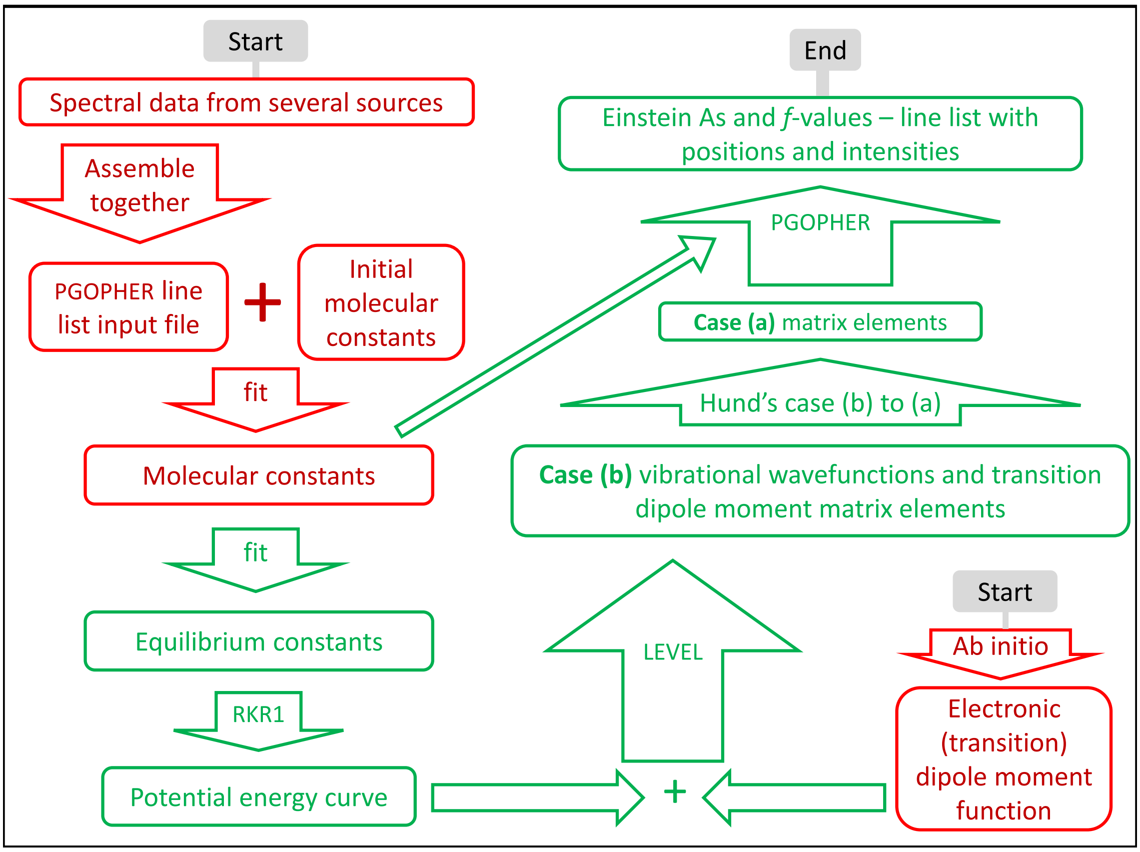

Figure 2.19 – Overall method for the production of line lists for diatomic molecules. The green boxes indicate the parts that could be mostly automated, whilst more specific considerations are required for those in red.

electron spin using the "transformation equation". PGOPHER sets up case (a) transition matrices, and converts the MEs from the molecular frame to the laboratory frame. The case (a) Hamiltonians are then diagonalised, and the resulting eigenvectors are combined with the transition matrices to give "transformed" transition matrices in terms of the real states. These MEs are the line strengths, S, which can be used with the line positions to calculate Einstein A values. This method is also summarised in Figure 2.19, in which the parts that could be mostly automated are highlighted.

The following chapter is the first work chapter, and involves the first use of the theory described to produce a line list. This chapter includes all of the methods described above, except for the H-W effect and transformation equation.

Chapter 3

The C_2 Swan System

3.1 Preface

This chapter describes the first use of the theory that has just been introduced, to produce a line list for the C_2 Swan system, which is a prominent electronic system of the C_2 molecule.

3.2 Introduction

The most prominent electronic system in the visible region is the Swan system, which involves the electronic transition $d^3\Pi_g$-$a^3\Pi_u$, with the (0,0) band near 19400 cm^{-1}. The $a^3\Pi_u$ state was originally believed to be the ground state (Herzberg et al., 1969) as it was observed to be easily excited, which is because it lies only about 700 cm^{-1} above the actual $X^1\Sigma_g^+$ ground state (this difference being that between the T_v values of v=0 for each state). Figure 3.1 shows a number of low lying electronic states and electronic systems of C_2, with the Swan system in bold.

C_2 is an important molecule in the fields of astronomy, combustion science, and materials science. It has often been observed in comets (Mayer and O'Dell, 1968; Jackson, 1976; Lambert and Danks, 1983; Johnson et al., 1983; Sorkhabi et al., 1997; Kaiser et al., 2003) and in other astronomical environments such as interstellar clouds (Souza and Lutz, 1977; Chaffee and Lutz, 1978; Green, 1981; Hobbs and Campbell, 1982; Federman and Huntress, 1989; Kaźmierczak et al., 2010; Casu and Cecchi-Pestellini, 2012), late-type stars (Vardya, 1970; Querci et al., 1971; Klochkova et al., 2000; Hema et al., 2012) and the Sun (Grevesse and Sauval, 1973; Brault et al., 1982). Its reactions are believed to be involved in the formation of hydrocarbons and other organic compounds in interstellar clouds (Kaiser, 2002).

C_2 has also been found in flames (Gaydon, 1957; Bleekrode and Nieuwpoort, 1965; Baronavski and McDonald, 1977). It is present as a transient species, in the highest temperature environment near the reaction centre (Nyholm et al., 1994, 1995; Bengtsson et al., 1990), and its electronic transitions have been used to determine its concentration and the temperature at each measurement point. These two properties are both important in combustion modelling (Allen et al., 1986), and to improve the accuracy results, line lists with intensities for the relevant transitions are vital.

The C_2 Swan system has been exploited in soot detection and characterisation (Goulay et al., 2010), as C_2 in the $d^3\Pi_g$ state is produced in the laser irradiation of soot (Goulay et al., 2009). Soot detection is important in several areas, such in the as analysis of combustion in diesel engines (Goulay et al., 2009)

C_2 is also relevant to materials science, as it is involved in the production of carbon nanostructures (such as fullerenes and carbon nanotubes). Carbon is vaporised, and the resulting mixture, which includes C_2, forms the nanostructures (Nemes and Irle, 2011; Jakowski et al., 2012). The exact mechanisms are still poorly understood (Saveliev et al., 2003; Jakowski et al., 2012), and to understand the role played by C_2 and improve the processes, knowledge of the C_2 concentration is required.

The Swan system has been investigated extensively. Early vibrational band intensity analyses include those of King (1948), Phillips (1957) and Hagan (1963). Mentall and Nicholls (1965) reanalysed the data of three previous works to provide an updated list of absolute band strengths, oscillator strengths, and Einstein A values for most vibrational bands up to v'=4. A full review of previous work was given in 1967 by Tyte et al. (1967). Phillips and Davis (1968) combined earlier published data with their most recent rotational analysis. They calculated spectroscopic constants for the Swan system, and published a full rotational line list including relative intensities. Danylewych and Nicholls published a list of absolute band strengths, oscillator strengths and Einstein A values covering most vibrational bands up to v'=9, with $\Delta v \leq 4$ (Danylewych and Nicholls, 1974). The properties of C_2 were extensively reviewed by Huber and Herzberg (1979).

As new experimental techniques have become available, new studies of the lower vibrational bands have been conducted at high resolution. These include the work of

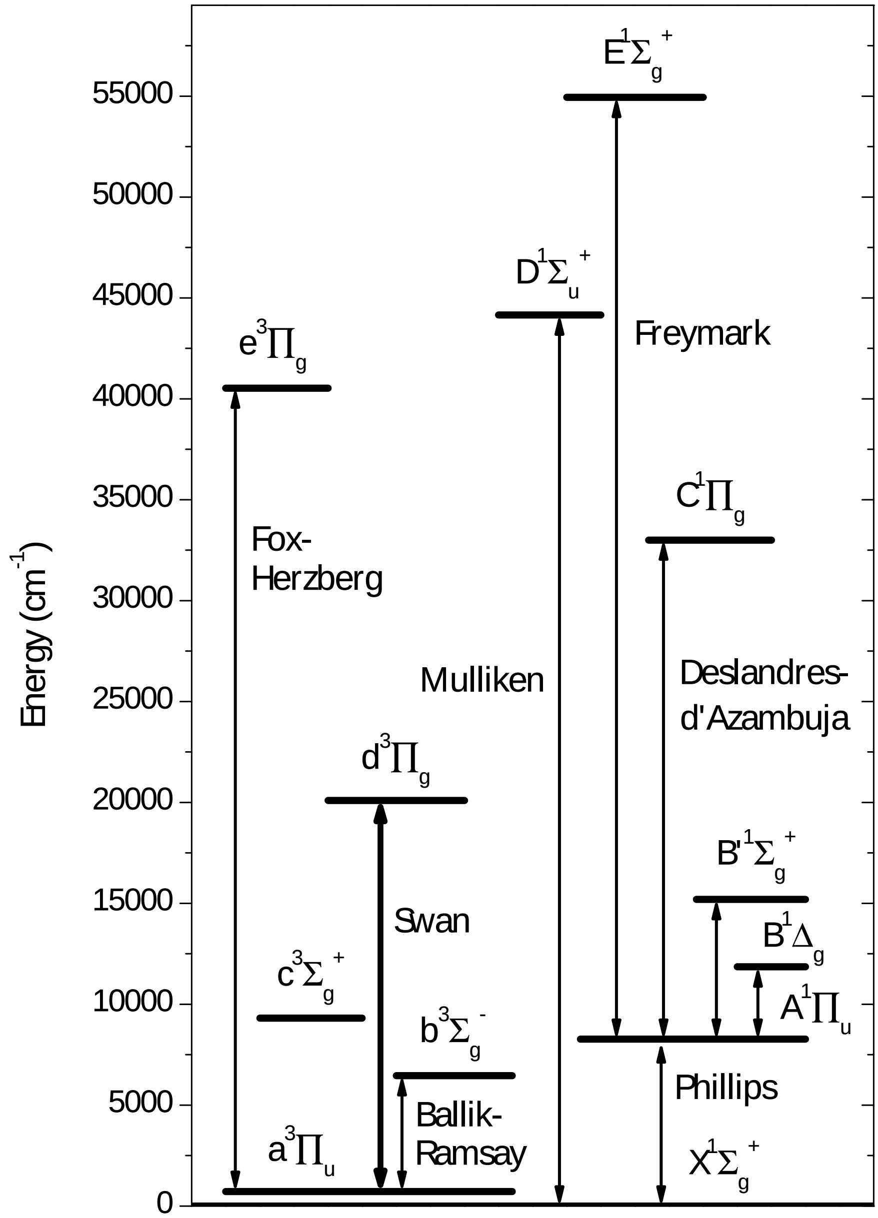

Figure 3.1 – Low lying electronic states and electronic systems of C_2 $\big($adapted from Tanabashi et al. (2007)$\big)$.

Amiot (1983), Curtis and Sarre (1985) and Suzuki et al. (1985), who investigated the (0-0), (0-1) and (1-0) bands, respectively, using laser excitation techniques. Dhumwad et al. (1981) observed the Swan system using a quartz discharge tube with tungsten electrodes for the excitation of CO. Prasad and Bernath (1994) analysed nine low vibrational bands $v' \leq 3$ and $v'' \leq 4$) of the Swan system of jet-cooled C_2 (for low-J), and of C_2 produced in a composite wall hollow cathode (for J up to 25-46) with a Fourier Transform Spectrometer (FTS). The previous observations of Amiot (1983) and Prasad and Bernath (1994) on the (0,0) band were improved upon by Lloyd and Ewart (1999), using degenerate four-wave mixing spectroscopy. These and other investigations have improved the accuracy of the line assignments originally published by Phillips and Davis (1968).

The higher vibrational bands had not been analysed with modern high resolution instrumentation until 2002, when Tanabashi and Amano observed the Swan system by a direct absorption technique using a tunable dye laser. They measured three bands, assigned as (5,7), (6,8) and (7,9). They found that their line positions did not agree with those reported by Phillips and Davis (1968), which was the most recent rotational analysis of the high vibrational bands. These discrepancies led to the reanalysis of the entire Swan system with a high resolution FTS (Tanabashi et al., 2007). The assigned line positions from this new comprehensive analysis agreed with their previous one for the (5,7), (6,8) and (7,9) bands. Moreover, their line positions for bands involving the higher vibrational levels differed significantly from those of Phillips and Davis (1968).

The old rotational line list reported by Phillips and Davis (1968) has recently been used in deriving the carbon abundance and $^{12}C/^{13}C$ ratio in R Coronae Borealis and hydrogen-deficient carbon stars (Hema et al., 2012), and in comets (Rousselot et al., 2012). It would be beneficial to have a new rotational line list, based on recent measurements and calculations. The purpose of this work is to use the data mainly of Tanabashi et al. (2007) to calculate theoretical line intensities, and publish an extensive line list.

Tanabashi et al. assigned around 5700 observed rotational lines, for 34 vibrational bands belonging to the Δv = -3 to +2 sequences. Transitions up to a maximum of between J=30 and 80, depending on the band, were assigned. Perturbations were found in the $d^3\Pi_g$ state for v = 0, 1, 2, 4, 6, 8, 9 and 10, and for v = 4, 6 and 9 they affected almost all of the observed lines. They calculated molecular constants (Tables 3 and 4 in Tanabashi et al. (2007)) for both electronic states.

Deperturbation studies of the $d^3\Pi_g$ v'=4 (Bornhauser et al., 2010) and v'=6

(Bornhauser et al., 2011) levels have been performed, using double-resonant four-wave mixing spectroscopy. This enabled them to assign lines unambiguously, and calculate perturbation constants (Table 3.1) and molecular constants (Table 3.2) of the interacting $\mathrm{b}^3\Sigma_\mathrm{g}^-$ (v=16 and v=19) and $^5\Pi$ states. They also gave a list of the few transitions that were assigned incorrectly by Tanabashi et al.. Recently, the (4,8) and (5,9) bands were observed by Yeung et al. (2013) using high resolution laser absorption spectroscopy.

In this work, the molecular constants from Tanabashi et al. (2007) are improved slightly using the data from the deperturbation studies, but the main focus is the calculation of line intensities using these constants and theoretical methods. This enables the production of a comprehensive line list that can be used by those in the fields of astronomy, combustion science, and materials science to calculate abundances from C_2 Swan spectra.

3.2.1 $\mathrm{C_2}$ $\mathrm{a^3\Pi_u}$ and $\mathrm{d^3\Pi_g}$ States

For the reasons described in Section 2.3.3, only e parity levels exist for odd J and f for even J in the lower $\mathrm{a}^3\Pi_\mathrm{u}$ state, and the reverse in the upper $\mathrm{d}^3\Pi_\mathrm{g}$ state. Both states have similar molecular constants, and at low J, are closer to Hund's case (a). At higher J they get closer to case (b), and so N becomes a reasonably good quantum number. This is illustrated in Figure 3.2, in which it can be seen that the energy levels are mostly defined by N at higher J, whereas for lower J, the F components of the same N have noticeably different energies.

Taking the selection rules for parity into account, transitions between any levels with ΔJ=$-1, 0$, or +1 are possible in this electronic system. Therefore, any upper level will have nine possible transitions to lower levels (in the same vibrational band, and for $J' \geq$ 3), as shown in Figure 3.3.

At high J $\big($case (b)$\big)$, the main features of the spectrum are triplets made up of the F'=F'' transitions with the same ΔJ, for three consecutive J values, for example R(10)F_{11}, R(11)F_{11}, and R(12)F_{11}. However, at low J, as the states are closer to case (a), the pattern is not as consistent. Lines with $F'$$\neq$$F''$ are mostly too weak to be observed.

For the important bands of the Swan system, $B_\mathrm{v}' > B_\mathrm{v}''$. This means that as J increases, the R branch spacing always increases. The P branch spacing, however, decreases until it is zero, and then the branch turns round to follow the direction of the R branch, resulting in a pile up at lines at the ‘‘band head''. The J value at which this occurs varies from band

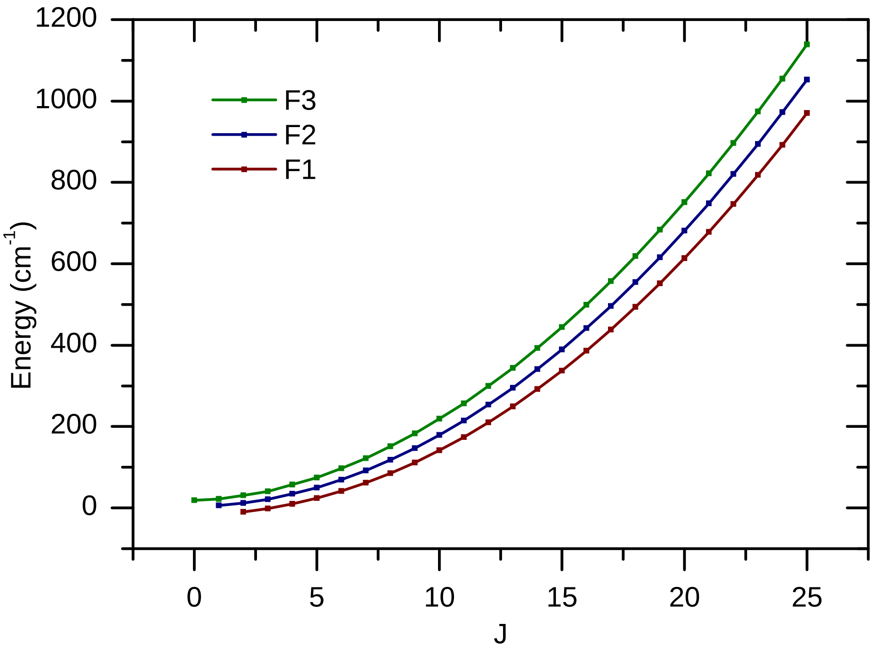

Figure 3.2 – Calculated energy level progressions (excluding local perturbations) of the three F components for the C_2 $a^3\Pi_u$ v=0 level. The energy is relative to the vibrational origin of the v=0 level.

to band, based on the difference between the B_v values. Figure 3.4 shows an example for the (1,1) band.

3.2.2 $d^3\Pi_g$ Perturbations

Rotational perturbations were identified in the $d^3\Pi_g$ v=0-2 levels by Callomon and Gilby (1963), through their observations of the C_2 Swan system. They identified the main perturbing state as $b^3\Sigma_g^-$ (upper state of the Ballik-Ramsay system), and also suggested that a level within the v′=0 level could be perturbed by an as yet undiscovered $^1\Delta_g$ state (now $b^1\Delta_g$ (Douay et al., 1988)). Phillips identified further perturbations in these levels and in v′=4-6, and similarly identified the perturbing state as $b^3\Sigma_g^-$, though he also suggested that the $X^1\Sigma_g^+$ ground state could be perturbing v′=0. In 1983, Amiot investigated the (0,0) band and gave further information about perturbations due to the $b^3\Sigma_g^-$ state, explained that the $X^1\Sigma_g^+$ state could not be perturbing v′=0, and also suggested the unidentified $^1\Delta_g$ state ($b^1\Delta_g$) as a possible perturbing state. Tanabashi et al. (2007) observed numerous perturbations in v′=0-2,4,6 and 8-10, and they agreed with the above identifications by Callomon and Gilby (1963) and Amiot (1983). They confirmed that the $b^1\Delta_g$ state was perturbing a v′=0 level as suggested by Callomon

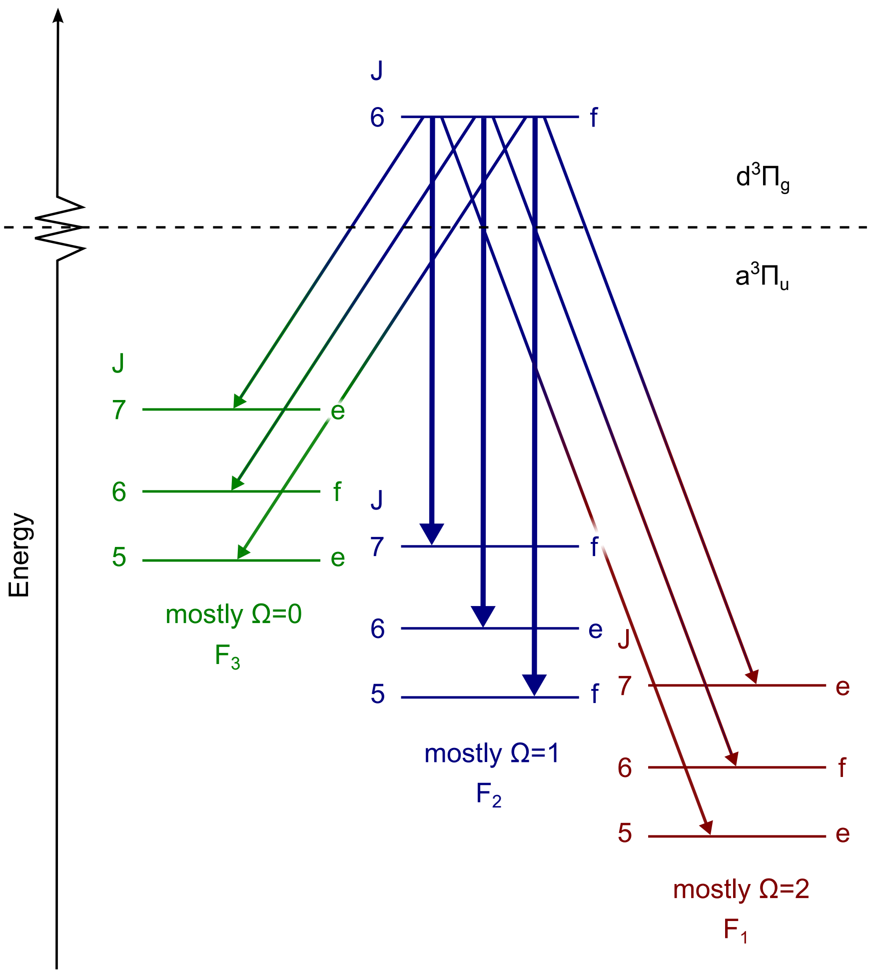

Figure 3.3 – Possible transitions in the C_2 Swan system from a single J and F level.

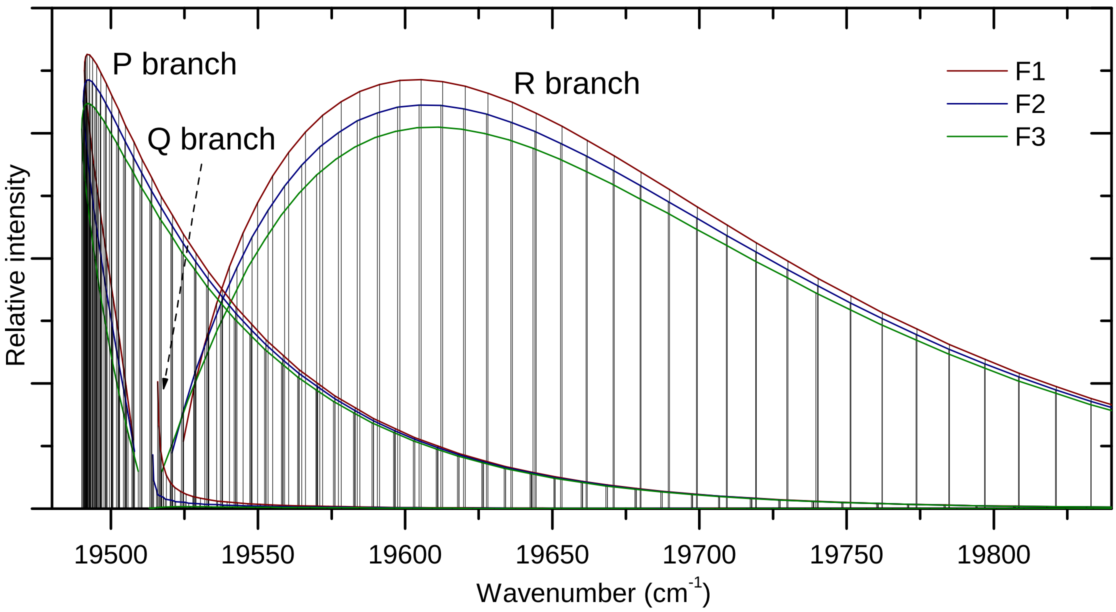

Figure 3.4 – Calculated stick spectrum of the C_2 Swan system (1,1) band, at 1500 K.

and Gilby (1963) and Amiot (1983), and also suggested that it may be perturbing some v′=2 levels. Most other perturbations were believed to be caused by the $b^3\Sigma_g^-$ state. The previously mentioned deperturbation studies (Bornhauser et al., 2010, 2011) then quantified the perturbations between the $d^3\Pi_g$ v=4 and $b^3\Sigma_g^-$ v=16 levels, and the $d^3\Pi_g$ v=6 and $b^3\Sigma_g^-$ v=19 levels. They also observed and quantified perturbations between $d^3\Pi_g$ v=6 and a new electronic state, $^5\Pi$. Their final values for the perturbation MEs are shown in Table 3.1, and their $b^3\Sigma_g^-$ molecular constants are in Table 3.2. The ordering of the levels relevant to the perturbations involving the $b^3\Sigma_g^-$ state is shown in Figure 3.5.

For local perturbations to occur, levels with the same J in different electronic states that have non-zero Hamiltonian matrix elements linking them must have similar unperturbed energies. For this to be likely to occur between two electronic states with somewhat similar B_v values, at low J, the vibrational origins of two v levels in each state must be of similar energy, with the level that has a lower B_v value below in energy. It can be seen in Figure 3.5 that this occurs between the levels mentioned above. The B_v values are different enough however for a vibrational level of the $b^3\Sigma_g^-$ state to cross more than one vibrational level of the $d^3\Pi_g$ state (on a graph of energy against J) within the J range covered by this work. For example, the $b^3\Sigma_g^-$, v=16 level crosses the $d^3\Pi_g$, v=4 level between around J=0 and J=20 (accounted for here), and then crosses the v=3 level between around J=50 and J=70 (not accounted for here). Many other perturbations

Table 3.1 – Perturbation constants[a] for the $d^3\Pi_g$ v′=4 and v′=6 levels of the C_2 Swan system. Those of Bornhauser et al. (2010, 2011), and those resulting from the fit of all molecular constants are reported.

Parameter	Bornhauser et al. value	Value from fit[b]
$\langle d^3\Pi_g, v'{=}4 \vert \hat{H}_{SO} \vert b^3\Sigma_g^-, v'{=}16\rangle$	-0.6401(86)	-0.6147(59)
$\langle d^3\Pi_g, v'{=}4 \vert B\hat{L}_+ \vert b^3\Sigma_g^-, v'{=}16\rangle$	0.24737(61)	0.24869(21)
$\langle d^3\Pi_g, v'{=}6 \vert \hat{H}_{SO} \vert b^3\Sigma_g^-, v'{=}19\rangle$	0.7855(110)	0.7417(82)
$\langle d^3\Pi_g, v'{=}6 \vert B\hat{L}_+ \vert b^3\Sigma_g^-, v'{=}19\rangle$	0.31192(37)	0.31123(12)
$\langle d^3\Pi_g, v'{=}6 \vert \hat{H}_{SO} \vert {}^5\Pi\rangle$	4.6220(88)	4.6150(94)

[a] Numbers in parentheses indicate one standard deviation to the last significant digits of the constants.

[b] Please note that these values were floated to improve the fit, but the studies of Bornhauser et al. (2010, 2011) were directly aimed at calculating these constants.

Table 3.2 – Molecular constants[a] for the $b^3\Sigma_g^-$, v′=16 and v′=19 and $^5\Pi$ states, which perturb the $d^3\Pi_g$, v′=4 and v′=6 levels. Those of Bornhauser et al. (2010, 2011), and those resulting from the fit of all molecular constants are reported.

State	Parameter	Bornhauser et al. value	Value from fit
$b^3\Sigma_g^-$, v=16	T	26191.865(14)	26191.1742(29)
	B	1.22858(15)	1.233492(68)
	$D\times10^6$	6.4351(fixed)[b]	6.4351(fixed)[b]
	λ	0.172(18)	0.335(17)
$b^3\Sigma_g^-$, v=19	T	29442.1348(843)	29442.589(14)
	B	1.179368(214)	1.178182(49)
	$D\times10^6$	6.5066(fixed)[b]	6.5066(fixed)[b]
	λ	0.142(22)	0.135(26)
$^5\Pi$	T	29258.5922(48)	29258.5824(65)
	B	1.14413(11)	1.14442(11)
	A	8.9450(47)	8.9428(54)
	λ_v	-0.0428(23)	-0.0427(27)
	o	-0.0744(39)	-0.0812(44)

[a] Numbers in parentheses indicate one standard deviation to the last significant digits of the constants.

[b] As with Bornhauser et al., these D constants were fixed at values extrapolated from the molecular constants of Amiot et al. (1979).

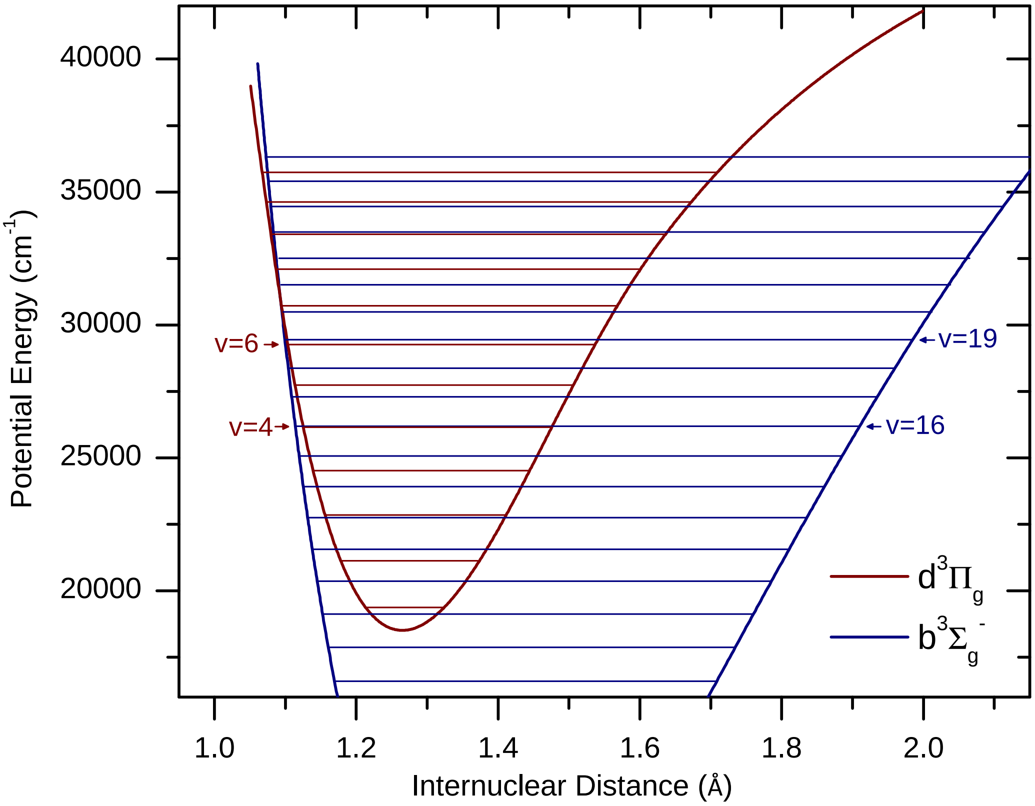

Figure 3.5 – Potential energy curves of the C_2 $d^3\Pi_g$ and $b^3\Sigma_g^-$ states, showing the locations of the vibrational levels for which local perturbations are analysed. The potential energy curve and vibrational levels for the $b^3\Sigma_g^-$ state were calculated using equilibrium constants based on molecular constants for v=0-4 from Davis et al. (1988) and v=16 and 19 from this work.

that have not been accounted for here will therefore be caused by the various vibrational levels of the b$^3\Sigma_g^-$ state. The $^5\Pi$ state also causes perturbations and crosses more than one vibrational level, but its vibrational level is unknown. The perturbations are included by adding the basis states of the perturbing state to the Hamiltonian and including linking MEs. The diagonalisation then results in eigenvalues for both electronic states. The Hamiltonian terms that are included to link the b$^3\Sigma_g^-$ and d$^3\Pi_g$ states are $\hat{L}_+\hat{S}_- + \hat{L}_-\hat{S}_+$ and $\hat{J}_+\hat{L}_- + \hat{J}_-\hat{L}_+$. These terms arose (Section 2.4) in the definition of the spin-orbit and rotational Hamiltonians, respectively, but were not required previously as they raised or lowered Λ. The term linking the $^5\Pi$ and d$^3\Pi_g$ states is $\hat{L}_z\hat{S}_z$. The $\hat{H}_{SO}$ MEs shown in Table 3.1 are the values $\langle\eta'\Lambda'; S'\Sigma'; \Omega'|\hat{H}_{SO}|\eta\Lambda; S\Sigma; \Omega\rangle$, as these were reported by Bornhauser et al.. This is however ambiguous, as there is more than one ME connecting the two states. PGOPHER accepts the value $\langle\eta'\Lambda'; S'|\hat{H}_{SO}|\eta\Lambda S\rangle$, and the connection between these two MEs is (Western, 2014)

$$\langle\eta' S'\Sigma'\Lambda'\Omega'|\hat{H}_{SO}|\eta S\Sigma\Lambda\Omega\rangle = (-1)^{S'-\Sigma'}\begin{pmatrix} S' & 1 & S \\ -\Sigma' & \Sigma'-\Sigma & \Sigma \end{pmatrix}\langle\eta' S'\Lambda'|\hat{H}_{SO}|\eta S\Lambda\rangle. \quad (3.1)$$

The $B\hat{L}_+$ MEs reported by Bornhauser et al. are identical to the input to PGOPHER. These are not ambiguous, as the MEs of B$\hat{L}_+$ can be used to calculate the full MEs of $B\big(\hat{J}_+\hat{L}_- + \hat{J}_-\hat{L}_+\big)$.

3.3 Recalculation of Molecular Constants

With the recent publication of perturbation constants for the d$^3\Pi_g$ v=4 and v=6 levels by Bornhauser et al. (2010, 2011) (Table 3.1), there was an opportunity to improve the molecular constants reported by Tanabashi et al. (Tables 3 and 4 in Tanabashi et al. (2007)). The computer program PGOPHER (Western, 2014) was used to recalculate the molecular constants, with the inclusion of the v′=4 and v′=6 perturbations, using the standard N^2 Hamiltonian for a $^3\Pi$ state (Brown and Merer, 1979; Hirota et al., 1994). A global least squares fit was performed including all lines from Tanabashi and Amano (2002), Curtis and Sarre (1985), Suzuki et al. (1985), Lloyd and Ewart (1999) (for the (0,0) band), the two deperturbation studies by Bornhauser et al. (both the Swan system lines and the transitions between the perturbing states and the a$^3\Pi_u$ state), and most lines from Yeung et al. (2013) (see below).

3.3.1 The (4,8) and (5,9) bands

Yeung et al. (2013) observed 153 and 121 transitions in the (4,8) and (5,9) bands, respectively. They reported that the (5,9) band was unperturbed and that line assignment was simple, and so all of these lines were included in our fit. The (4,8) band however was heavily perturbed. To help in assigning the lines, they attempted to use the perturbation constants from Bornhauser et al. (2010, 2011) to estimate line positions, but could not find agreement with a number of lines. Ultimately, they assigned all of the lines without the use of the perturbation constants. They gave two examples of transitions, $R_1(9)$ and $R_2(8)$ (reported to be at 13907.568 and 13905.145 cm^{-1}), for which no lines could be found in the region of the calculated positions. Using molecular constants directly from Tanabashi and Amano, these line positions are calculated as 13907.821 and 13905.788 cm^{-1}, respectively, and with the inclusion of the Bornhauser et al. perturbation constants, this changes to 13904.778 and 13907.437 cm^{-1}, respectively. Therefore, there is a line in their data in the region of the estimated (perturbation included) position for the $R_2(8)$ transition (at 13907.568 cm^{-1}). For the $R_1(9)$ transition, the closest reported line is 0.37 cm^{-1} away at 13905.145 cm^{-1}. Also, the reported positions are still 0.25 and 0.64 cm^{-1} away from the expected positions using Tanabashi et al. molecular constants only. In fact, the average difference between the expected positions using Tanabashi et al. molecular constants only and those reported by Yeung et al., for all (4,8) lines that were retained in our fit, was as high as 0.44 cm^{-1}.

The inclusion of the perturbation constants improves the residuals of all of the lines of the Swan system that Bornhauser et al. observed. Therefore, many of the (4,8) lines seem to have been incorrectly assigned by Yeung et al.. However, the line positions have an accuracy of 0.003 cm^{-1}, and so it was considered worthwhile to investigate the assignments and include as many of the lines as possible in our fit.

To check their assignments, a preliminary fit was performed using all other data described (including the perturbation constants) to estimate positions for the (4,8) band. This showed 19 (of 153) transitions whose assigned positions were more than 0.5 cm^{-1} away from the estimated value. The observed positions were compared with all nearby calculated values with the aim of changing assignments, if there was only one obvious option. Seven positions were reassigned, and most of the other positions either had several nearby options and so could not confidently be reassigned, or had already been assigned to a more likely transition as well (and noted as an overlapped line). Only three lines had no nearby (within 0.1 cm^{-1}) options. Due to the lack of confidence in the assignments, any lines that differed significantly from their calculated values and could not be reassigned were removed from the fit. The fit was continued, and any lines whose residuals were greater than 0.03 cm^{-1} were then removed. This process was repeated iteratively until no lines differed by more than 0.03 cm^{-1}. The entire process was repeated several times, using the updated constants as the starting point. 100 of the initial 153 lines remained after this treatment. This probably removed a number of correctly assigned lines, but more importantly, it significantly decreased the chance of including any incorrect lines in the fit.

3.3.2 Data Included in the Global Fit

In their calculation of molecular constants in 2007, Tanabashi et al. included lines from several other studies. For nine bands up to (3,4), gaps in observations were filled in by using lines from Prasad and Bernath (1994). High resolution measurements of the (0,1) band by Curtis and Sarre (1985) were included, as were cross transitions ($\Delta F \neq 0$) from Suzuki et al. (1985) for the (1,0) band. Some cross transitions were also observed by Curtis and Sarre, and these are particularly useful for the accurate calculation of the spin-orbit coupling and Λ-doubling constants. All lines from Tanabashi and Amano (2002) for the (5,7), (6,8) and (7,9) bands were also included.

Prasad and Bernath (1994) also calculated molecular constants, and included in their fit all lines from Curtis and Sarre (1985), Suzuki et al. (1985) and Amiot (1983) (for the (0,0) band). The recalculation is based mainly on that of Tanabashi et al., and also this fit by Prasad and Bernath. An explanation of the specific differences is presented below.

The weights for the lines from Tanabashi et al. (including those from Tanabashi and Amano (2002)) were unchanged here, except for those involving the v'=4 and v'=6 levels. These had mostly been deweighted, and were weighted more strongly in this study as the perturbations had been included in the fit. In their calculation of the perturbation constants, Bornhauser et al. (2010, 2011) observed lines involving J'=1-6, 10-12 and 17-23 for the v'=6 level, and J'=4-14 for the v'=6 level. Lines involving these J levels were weighted strongly, and other line weights were decreased with greater difference between their J' level and these ranges. The actual lines observed by Bornhauser et al. were weighted similarly to those of Tanabashi et al. for the same bands. The lines for both bands observed by Yeung et al. (2013) were weighted based on the reported accuracy

(0.003 cm^{-1}). Lines marked as overlapped by Yeung et al. were slightly deweighted.

The five remaining sets of lines were treated as follows. The sets from Prasad and Bernath (1994) (two sets), Curtis and Sarre (1985) and Suzuki et al. (1985) were given the same weights as in the fit performed by Prasad and Bernath. Lloyd and Ewart (1999) lines were assigned weights to be similar to those of Tanabashi et al. (2007) for the (0,0) band. To ensure that all lines were on the same wavenumber scale, transitions from these five sets were then compared to matching Tanabashi et al. transitions, and a weighted average wavenumber difference (one for each set) using matching lines was calculated, based on the assigned weights. This was added to all of the lines from each set as a wavenumber offset, to compensate for any systematic differences between studies. In their fit, Tanabashi et al. deweighted many lines due to the extensive perturbations, and those lines were also deweighted here if they were present in these five sets. This process excluded approximately 11% of these lines. To further decrease the possibility of using any misassigned lines in the fit, any line whose wavenumber differed from a matching Tanabashi et al. line by more than 0.03 cm^{-1} was deweighted, excluding a further $\sim$6%. A preliminary fit was then performed to obtain calculated values of each transition. Lines that had not been matched to Tanabashi et al. transitions were then deweighted if their observed minus calculated values, as a result of this fit, were greater than 0.03 cm^{-1}.

A final global weighted least squares fit was performed, in which all reported molecular constants for the $a^3\Pi_u$ and $d^3\Pi_g$ states were floated, except for A_D for v′=8, 9 and 10, A_D for v″=5, 7 and 8, and λ for v′=8. These were fixed at values based on those calculated for the other levels to obtain a good fit. The updated molecular constants are shown in Tables 3.3 and 3.4, where the constants are those described in Section 2.4. The magnitudes of the perturbation constants reported by Bornhauser et al. (2010, 2011) and the constants for the perturbing states were also floated to improve the fit, and both the previous and changed values are shown in Tables 3.1 and 3.2. Bornhauser et al. fixed the D constants for the $b^3\Sigma_g^-$ state at values extrapolated from the molecular constants of Amiot et al. (1979), and the same was done here.

3.4 Calculation of Line Intensities

Equilibrium constants (as described in Section 2.1.4) were calculated (Table 3.5) in a weighted least squares fit using the energy level expressions for a vibrating rotator, and

Table 3.3 – Updated molecular constants[a] for the $d^3\Pi_g$ state of the C_2 Swan system (in cm^{-1}).

v	T	A	A_D	B	$D\times10^6$	λ	o	p	q
0	19378.46749(51)	-14.00139(63)	0.0005068(83)	1.7455663(43)	6.8205(16)	0.03301(47)	0.61076(52)	0.003973(43)	-0.0007752(43)
1[b]	21132.14977(25)	-13.87513(49)	0.0005740(83)	1.7254062(53)	7.0194(77)	0.02972(38)	0.61713(36)	0.004133(44)	-0.0008171(43)
2	22848.3877(21)	-13.8205(23)	0.000600(43)	1.704516(21)	7.308(22)	0.0253(41)	0.6208(32)	0.00624(38)	-0.000835(14)
3	24524.2201(19)	-13.5361(28)	0.000775(17)	1.681437(16)	7.438(24)	0.0470(26)	0.5827(26)	0.00579(17)	-0.0008568(85)
4	26155.0448(29)	-13.3892(50)	0.001451(14)	1.656859(26)	7.684(43)	0.0219(38)	0.6313(32)	0.00954(29)	-0.000923(21)
5	27735.6720(43)	-13.0324(66)	0.000723(37)	1.630205(23)	8.573(32)	0.0601(28)	0.6161(23)	0.00685(32)	-0.000912(15)
6	29259.3548(36)	-12.820(10)	0.001203(56)	1.599876(31)	8.998(44)	0.0529(71)	0.5773(71)	0.00874(47)	-0.000986(22)
7	30717.9011(46)	-12.3458(71)	0.000814(41)	1.566047(32)	10.044(66)	0.0960(34)	0.5532(31)	0.00936(35)	-0.001175(17)
8	32102.655(22)	-12.107(22)	0.00076(fixed)	1.52675(31)	9.60(97)	0.095(fixed)	0.546(22)	0.0055(21)	-0.00088(21)
9	33406.230(22)	-11.698(39)	0.00076(fixed)	1.485755(96)	11.85(10)	0.172(26)	0.498(28)	0.0097(14)	-0.002062(44)
10	34626.7860(94)	-11.297(15)	0.00076(fixed)	1.441138(72)	12.837(73)	0.115(16)	0.399(12)	0.00745(90)	-0.000977(30)

[a] Numbers in parentheses indicate one standard deviation to the last significant digits of the constants.

[b] In addition, H = 2.14(30)$\times10^{-11}$ for v=1 was used to obtain a good fit.

Table 3.4 – Updated molecular constants[a] for the $a^3\Pi_u$ state of the C_2 Swan system (in cm^{-1}).

v	T	A	A_D	B	$D\times10^6$	λ	o	p	q
0[b]	0	-15.26986(43)	0.0002634(71)	1.6240452(44)	6.4506(19)	-0.15450(36)	0.67525(35)	0.002537(42)	-0.0005281(44)
1	1618.02244(53)	-15.25197(61)	0.0002266(73)	1.6074266(44)	6.4439(21)	-0.15373(51)	0.67017(51)	0.002705(44)	-0.0005772(42)
2	3212.72793(96)	-15.2328(15)	0.0001996(94)	1.5907513(61)	6.4527(44)	-0.1526(12)	0.6649(14)	0.003132(77)	-0.0006457(48)
3	4784.0688(31)	-15.1972(39)	0.000186(42)	1.574088(24)	6.455(24)	-0.1333(61)	0.6815(51)	0.00488(42)	-0.000618(17)
4	6332.1364(51)	-15.2043(65)	0.000318(36)	1.557117(31)	6.338(39)	-0.1551(72)	0.6674(67)	0.00632(36)	-0.000894(16)
5	7856.8175(32)	-15.2096(35)	0.00025(fixed)	1.540139(24)	6.312(35)	-0.1492(36)	0.6546(37)	0.00734(25)	-0.001246(12)
6	9358.1565(40)	-15.1646(60)	0.000355(33)	1.523439(26)	6.034(38)	-0.1551(46)	0.6886(38)	0.00504(32)	-0.000676(16)
7	10836.1430(92)	-15.085(11)	0.00025(fixed)	1.50869(25)	3.51(92)	-0.1641(90)	0.704(14)	-0.0244(23)	0.00632(49)
8	12290.7997(29)	-15.1702(46)	0.00025(fixed)	1.488684(28)	5.329(52)	-0.1665(36)	0.6742(30)	0.01449(29)	-0.002053(23)
9	13722.0897(43)	-15.0980(61)	0.000419(31)	1.472818(24)	6.066(35)	-0.1584(27)	0.6926(23)	0.00303(33)	-0.000081(16)

[a] Numbers in parentheses indicate one standard deviation to the last significant digits of the constants.

[b] In addition, H = 6.73(16)$\times10^{-12}$, o_D = -6.86(114)$\times10^{-6}$ and q_D = -9.60(41)$\times10^{-9}$ were used for v=0 to obtain a good fit.

Table 3.5 – Equilibrium molecular constants[a] for the C_2 Swan system.

Constant	$d^3\Pi_g$	$a^3\Pi_u$
ω_e	1788.45(33)	1641.3463(55)
$\omega_e x_e$	16.87(19)	11.6595(19)
$\omega_e y_e$	-0.259(36)	-0.00079(16)
$\omega_e z_e$	-0.0396(20)	-
B_e	1.755408(92)	1.632355(78)
α_e	0.01960(13)	0.016582(63)
γ_e	-0.000144(39)	-0.0000273(75)
δ_e	-0.0000806(31)	-

[a] Numbers in parentheses indicate one standard deviation to the last significant digits of the constants.

the updated B_v and G_v values in Tables 3.3 and 3.4. The weightings of the vibrational levels were based on the standard deviation of B_v and G_v values from the PGOPHER line position fit. The equilibrium constants were used to calculate potential energy curves using RKR1, and these are shown in Figure 3.6.

LEVEL was used as explained in Section 2.1.5. The C_2 work was performed before the derivation of the transformation equation (Equation 2.5.4), and the method of transferring MEs from LEVEL to PGOPHER used involved taking only one rotationless ME for each vibrational band. This was a reasonable approximation as the H-W effect is very small for C_2 (the average maximum H-W effect (Section 4.3.4) for observed bands is only 4.3%).

3.4.1 Electronic Transition Dipole Moment

The calculations in this section were performed by Timothy W. Schmidt and George B. Bacskay (University of Sydney, Australia).

This calculation of the electronic TDMF of the Swan system has been reported previously (Kokkin et al., 2007; Schmidt and Bacskay, 2007; Nakajima et al., 2009), with the results shown in Table 3.6 and Figure 3.7. A brief description is given here. Wavefunctions were computed using the multi-reference configuration interaction (MRCI) method (Werner and Knowles, 1988; Knowles and Werner, 1988), whereby all single and double excitations from a complete active space self-consistent field (CASSCF; Werner and Knowles, 1985; Knowles and Werner, 1985) reference state are included in the MRCI wave functions. The active space included all molecular orbitals arising from the C atoms' $2s$ and $2p$ valence orbitals. The basis set is the augmented correlation-consistent

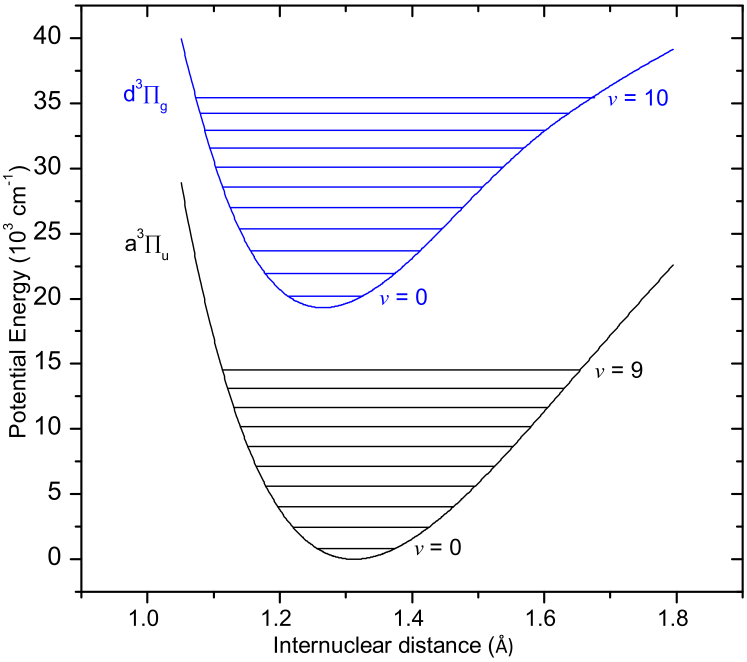

Figure 3.6 – The potential energy curves of the C_2 Swan System. Reprinted from JQSRT, 124, Brooke et al., Line strengths and updated molecular constants for the C_2 Swan system, 11-20, Copyright (2013), with permission from Elsevier.

polarised aug-cc-pV6Z set of Dunning and co-workers (Dunning, 1989; Kendall et al., 1992; Woon and Dunning, 1995; Wilson et al., 1996) and de Jong et al. (2001). Core and core-valence correlation corrections were obtained using the aug-cc-pCVQZ basis set (Dunning, 1989; Kendall et al., 1992; Woon and Dunning, 1995). Scalar relativistic energy corrections were evaluated via the Douglas-Kroll-Hess approach (Douglas and Kroll, 1974; Hess, 1985, 1986), in conjunction with the appropriate cc-pVQZ basis sets. The transition moments were computed by utilizing the technique of bi-orthogonal transformation (Mitrushchenkov and Werner, 2007) of the mutually non-orthogonal orbitals of the two states. These quantum chemical calculations were carried out using the MOLPRO 2006.1 program (Werner et al., 2006).

3.4.2 Vibrational Band Intensities

Einstein $A_{\mathrm{v'v}}$ values for each vibrational band were also calculated, and are shown in Table 3.7. They were calculated as the sum of all single rotational Einstein A values for possible transitions within the relevant band from the J'=1, F_3 level. These were converted into $f_{\mathrm{v'v}}$ values using Equation 2.131, which are shown in Table 3.8.

Table 3.6 – Calculated TDMF for the C_2 Swan system.

r (au)	R_e (au)	r (au)	R_e (au)	r (au)	R_e (au)	r (au)	R_e (au)
1.50	1.15048	2.25	0.94723	2.70	0.67689	3.30	0.08683
1.60	1.13942	2.30	0.92430	2.75	0.63482	3.40	0.00847
1.70	1.12242	2.35	0.89994	2.80	0.58959	3.50	-0.06088
1.80	1.10056	2.40	0.87406	2.85	0.54125	3.60	-0.12274
1.90	1.07442	2.45	0.84653	2.90	0.49020	3.70	-0.17787
2.00	1.04372	2.50	0.81717	2.95	0.43709	3.80	-0.22590
2.10	1.00858	2.55	0.78578	3.00	0.38287	3.90	-0.26485
2.15	0.98935	2.60	0.75212	3.10	0.27558	4.00	-0.29146
2.20	0.96887	2.65	0.71591	3.20	0.17578		

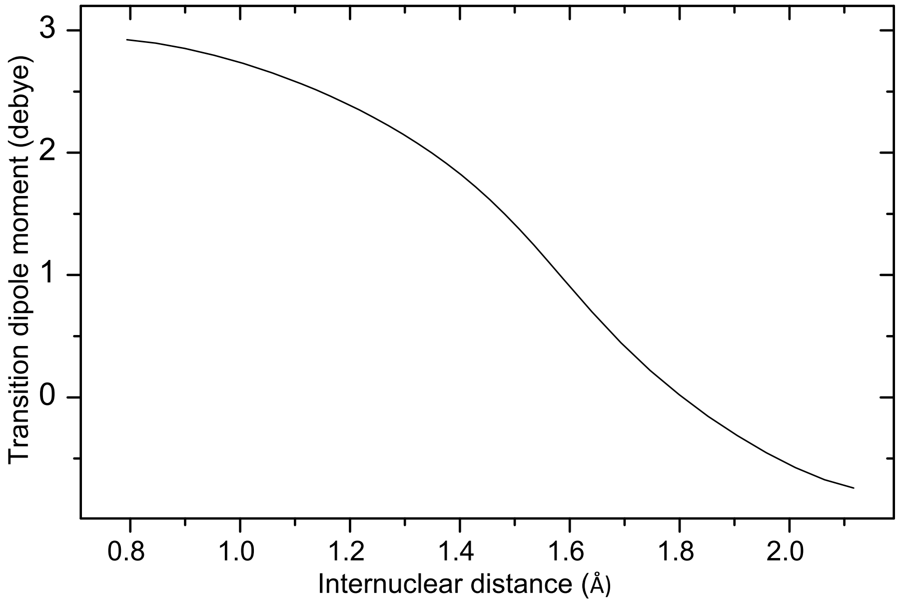

Figure 3.7 – The electronic transition dipole moment of the C_2 Swan system. Reprinted from JQSRT, 124, Brooke et al., Line strengths and updated molecular constants for the C_2 Swan system, 11-20, Copyright (2013), with permission from Elsevier.

Table 3.7 – Einstein $A_{\mathrm{v}'\mathrm{v}''}$ values[a] of the C_2 Swan system.

	v′										
v″	0	1	2	3	4	5	6	7	8	9	10
0	7.626 (+6)	2.814 (+6)	2.809 (+5)	4.333 (+3)	2.033 (+2)	3.642 (+1)	2.470 (-2)	2.140 (-1)	9.989 (-4)	3.827 (-3)	3.140 (-9)
1	2.135 (+6)	3.427 (+6)	4.072 (+6)	6.429 (+5)	8.720 (+3)	1.608 (+3)	1.591 (+2)	4.744 (+0)	1.822 (+0)	4.947 (-2)	3.540 (-2)
2	3.832 (+5)	2.746 (+6)	1.270 (+6)	4.422 (+6)	9.615 (+5)	7.432 (+3)	6.154 (+3)	3.223 (+2)	6.379 (+1)	4.108 (+0)	1.567 (+0)
3	5.590 (+4)	8.273 (+5)	2.568 (+6)	3.236 (+5)	4.301 (+6)	1.168 (+6)	1.085 (+3)	1.805 (+4)	1.707 (+2)	3.472 (+2)	1.346 (-2)
4	7.224 (+3)	1.710 (+5)	1.169 (+6)	2.066 (+6)	2.505 (+4)	4.005 (+6)	1.149 (+6)	4.993 (+3)	3.581 (+4)	1.535 (+2)	9.452 (+2)
5	8.592 (+2)	2.886 (+4)	3.215 (+5)	1.352 (+6)	1.510 (+6)	1.513 (+4)	3.459 (+6)	1.120 (+6)	5.272 (+4)	4.975 (+4)	4.445 (+3)
6	9.574 (+1)	4.280 (+3)	6.793 (+4)	4.745 (+5)	1.381 (+6)	1.038 (+6)	8.028 (+4)	3.438 (+6)	8.558 (+5)	1.863 (+5)	4.075 (+4)
7	1.006 (+1)	5.775 (+2)	1.218 (+4)	1.218 (+5)	6.009 (+5)	1.302 (+6)	6.443 (+5)	1.343 (+5)	3.253 (+6)	4.834 (+5)	4.111 (+5)
8	9.931 (-1)	7.206 (+1)	1.945 (+3)	2.582 (+4)	1.830 (+5)	6.840 (+5)	1.087 (+6)	4.546 (+5)	1.285 (+5)	3.081 (+6)	1.342 (+5)
9	9.005 (-2)	8.335 (+0)	2.828 (+2)	4.785 (+3)	4.495 (+4)	2.421 (+5)	6.721 (+5)	9.993 (+5)	3.120 (+5)	8.080 (+4)	2.824 (+6)

[a] The numbers in parentheses indicate the exponent.

Table 3.8 – $f_{\mathrm{v}'\mathrm{v}''}$ values[a] of the C_2 Swan system (a), compared to those of Schmidt and Bacskay (2007) (b).

	v′											
	0		1		2		3		4		5	
v″	a	b	a	b	a	b	a	b	a	b	a	b
0	3.045 (-2)	3.069 (-2)	9.450 (-3)	9.414 (-3)	8.067 (-4)	7.885 (-4)	1.080 (-5)	9.656 (-6)	4.455 (-7)	5.104 (-7)	7.100 (-8)	6.854 (-8)
1	1.015 (-2)	1.015 (-2)	1.350 (-2)	1.374 (-2)	1.355 (-2)	1.353 (-2)	1.837 (-3)	1.786 (-3)	2.172 (-5)	1.838 (-5)	3.536 (-6)	3.794 (-6)
2	2.199 (-3)	2.185 (-3)	1.283 (-2)	1.287 (-2)	4.939 (-3)	5.146 (-3)	1.460 (-2)	1.462 (-2)	2.739 (-3)	2.650 (-3)	1.853 (-5)	1.407 (-5)
3	3.936 (-4)	3.878 (-4)	4.642 (-3)	4.618 (-3)	1.180 (-2)	1.190 (-2)	1.245 (-3)	1.379 (-3)	1.412 (-2)	1.421 (-2)	3.326 (-3)	3.201 (-3)
4	6.365 (-5)	6.204 (-5)	1.171 (-3)	1.154 (-3)	6.428 (-3)	6.403 (-3)	9.361 (-3)	9.529 (-3)	9.560 (-5)	1.417 (-4)	1.311 (-2)	1.325 (-2)
5	9.707 (-6)	9.338 (-6)	2.456 (-4)	2.392 (-4)	2.145 (-3)	2.113 (-3)	7.296 (-3)	7.288 (-3)	6.764 (-3)	6.987 (-3)	5.741 (-5)	2.853 (-5)

[a] It should be noted that in the calculation of these values, a wavenumber for the band had to be used. The value chosen was the wavenumber at which the forbidden Q(0) transition would appear. If the use of different wavenumbers here or $f_{\mathrm{v}'\mathrm{v}}$ values for other bands are desired, the Einstein $A_{\mathrm{v}'\mathrm{v}}$ values in Table 3.7 can be used in conjunction with Equation 2.131 to calculate new $f_{\mathrm{v}'\mathrm{v}}$ values. The numbers in parentheses indicate the exponent.

3.5 Analysis and Discussion

The final line list including positions, f-values and Einstein A values, contains lines for all possible vibrational bands between v'=10 and v'=9, up to a maximum J of between 34 and 96, depending on the band. These maximum J values are based on the highest observed J values for each vibrational level. A small section of the published line list is shown in Table 3.9, as an example of the line lists produced in this thesis.

3.5.1 Spectral Validation

PGOPHER (Western, 2014) was also used for the purpose of validation, as it is able to calculate and plot spectra based on a line list. Spectra were calculated and compared to those recorded by Tanabashi et al. (2007). In all of the calculated spectra shown, a constant Gaussian instrument function was added to best match the observed broadening. The experimental procedure that Tanabashi et al. used involved observing C_2 emission from a microwave discharge in a flow of acetylene (C_2H_2) diluted in argon through a discharge tube. In such a system the molecular vibration, and to a lesser extent the rotation, will not be at thermal equilibrium. For this reason, the rotational and vibrational temperatures of the simulation were also adjusted for best agreement. Two spectra were recorded, one for the Δv=-1 to +2 sequences and another for the Δv=-2 and -3 sequences. Rotational and vibrational temperatures of 1140 K and 6800 K, and 940 K and 5000 K were used for the Δv=-1 to +2 and Δv=-2 to -3 spectra, respectively. The final parameter that had to be added manually was a linear scaling factor, as the y-axis units of the recorded spectrum are arbitrary. This value could not be kept constant during the production of each figure given below (Figures 3.8 to 3.10). This is due to the presence of an instrument response function, which cannot be corrected for at this point.

The spectra match very well for the lower vibrational and rotational levels; most of the inaccuracies mentioned are present in the higher vibrational and rotational levels. Typical example sections of the Δv=-2 to +2 sequences are shown in Figures 3.8 to 3.15 that are typical of the rest of the range. These were chosen to show that there are many regions where the observed and calculated positions show an excellent match, and also some where they do not. This is mainly due to perturbations that are yet to be quantified and included, as explained in Section 3.5.2.

Table 3.9 – Section of the published line list for the C_2 Swan system.

v'	v''	J'	J''	F'	F''	p'	p''	Observed	Calculated	Residual	Perturbation	E''	A	f	Description	Paper	Quality	Weight
0	0	86	85	2	1	e	e	NaN	20782.9060	NaN	0.00000	11270.9180	5.245346E+2	1.841914E-6	sR21e(85)	None		NaN
0	0	87	86	2	1	f	f	NaN	20818.9055	NaN	0.00000	11527.1154	5.502454E+2	1.925264E-6	sR21f(86)	None		NaN
0	0	88	87	2	1	e	e	NaN	20833.4922	NaN	0.00000	11794.5860	5.263347E+2	1.838784E-6	sR21e(87)	None		NaN
0	0	89	88	2	1	f	f	NaN	20870.3430	NaN	0.00000	12055.9205	5.500218E+2	1.914513E-6	sR21f(88)	None		NaN
0	0	90	89	2	1	e	e	NaN	20884.7516	NaN	0.00000	12328.9780	5.290010E+2	1.838574E-6	sR21e(89)	None		NaN
0	0	91	90	2	1	f	f	NaN	20922.4610	NaN	0.00000	12595.3900	5.506139E+2	1.906566E-6	sR21f(90)	None		NaN
0	0	92	91	2	1	e	e	NaN	20936.6708	NaN	0.00000	12873.9900	5.325030E+2	1.841133E-6	sR21e(91)	None		NaN
0	0	93	92	2	1	f	f	NaN	20975.2463	NaN	0.00000	13145.4187	5.519844E+2	1.901255E-6	sR21f(92)	None		NaN
0	0	94	93	2	1	e	e	NaN	20989.2362	NaN	0.00000	13429.5158	5.368160E+2	1.846333E-6	sR21e(93)	None		NaN
0	0	95	94	2	1	f	f	NaN	21028.6851	NaN	0.00000	13705.8994	5.541017E+2	1.898430E-6	sR21f(94)	None		NaN
0	0	96	95	2	1	e	e	NaN	21042.4335	NaN	0.00000	13995.4473	5.419198E+2	1.854064E-6	sR21e(95)	None		NaN
0	0	1	2	2	2	f	f	19372.33000	19372.3355	-0.00550	0.00000	12.2806	3.696676E+6	8.860468E-3	pP2f(2)	T7	a	0.00500
0	0	2	3	2	2	e	e	19369.65500	19369.6599	-0.00490	0.00000	21.4847	3.981100E+6	1.136290E-2	pP2e(3)	T7	a	0.00500
0	0	3	4	2	2	f	f	19367.02600	19367.0356	-0.00960	0.00000	34.4016	4.010756E+6	1.246848E-2	pP2f(4)	T7	a	0.00500
0	0	4	5	2	2	e	e	19364.84600	19364.7915	0.05450	0.00000	49.9905	4.008555E+6	1.311195E-2	pP2e(5)	T7	y	99999.00000
0	0	5	6	2	2	f	f	19362.67000	19362.6715	-0.00150	0.00000	69.6260	3.989757E+6	1.349967E-2	pP2f(6)	T7	a	0.00500
0	0	6	7	2	2	e	e	19360.94400	19360.9221	0.02190	0.00000	91.6854	3.975586E+6	1.378028E-2	pP2e(7)	T7	c	0.05000
0	0	7	8	2	2	f	f	19359.31700	19359.3173	-0.00030	0.00000	117.9882	3.959235E+6	1.397434E-2	pP2f(8)	T7	a	0.00500
0	0	8	9	2	2	e	e	19358.02900	19358.0647	-0.03570	0.00000	146.5269	3.947455E+6	1.413019E-2	pP2e(9)	T7	c	0.05000
0	0	9	10	2	2	f	f	19356.94900	19356.9631	-0.01410	0.00000	179.4380	3.935418E+6	1.424653E-2	pP2f(10)	T7	a	0.00500
0	0	10	11	2	2	e	e	19356.15900	19356.1998	-0.04080	0.00000	214.4449	3.926587E+6	1.434584E-2	pP2e(11)	T7	c	0.05000
0	0	11	12	2	2	f	f	19355.61300	19355.5958	0.01720	0.00000	253.9230	3.917701E+6	1.442325E-2	pP2f(12)	T7	c	0.05000
0	0	12	13	2	2	e	e	19355.35600	19355.3163	0.03970	0.00000	295.3835	3.911126E+6	1.449217E-2	pP2e(13)	T7	y	99999.00000
0	0	13	14	2	2	f	f	19355.19600	19355.2093	-0.01330	0.00000	341.4016	3.904451E+6	1.454750E-2	pP2f(14)	T7	a	0.00500
0	0	14	15	2	2	e	e	19355.35600	19355.4099	-0.05390	0.00000	389.3010	3.899543E+6	1.459841E-2	pP2e(15)	T7	y	99999.00000
0	0	15	16	2	2	f	f	19355.79700	19355.8014	-0.00440	0.00000	441.8402	3.894488E+6	1.463975E-2	pP2f(16)	T7	a	0.00500
0	0	16	17	2	2	e	e	19356.51400	19356.4793	0.03470	0.00000	496.1634	3.890846E+6	1.467890E-2	pP2e(17)	T7	c	0.05000
0	0	17	18	2	2	f	f	19357.36400	19357.3714	-0.00740	0.00000	555.2093	3.887039E+6	1.471128E-2	pP2f(18)	T7	a	0.00500
0	0	18	19	2	2	e	e	19358.51300	19358.5242	-0.01120	0.00000	615.9406	3.884398E+6	1.474262E-2	pP2e(19)	T7	a	0.00500
0	0	19	20	2	2	f	f	19359.92000	19359.9191	0.00090	0.00000	681.4807	3.881598E+6	1.476869E-2	pP2f(20)	T7	a	0.00500
0	0	20	21	2	2	e	e	19361.54400	19361.5446	-0.00060	0.00000	748.6037	3.879778E+6	1.479449E-2	pP2e(21)	T7	a	0.00500
0	0	21	22	2	2	f	f	19363.44500	19363.4443	0.00070	0.00000	820.6261	3.877821E+6	1.481618E-2	pP2f(22)	T7	a	0.00500
0	0	22	23	2	2	e	e	19365.54200	19365.5405	0.00150	0.00000	894.1232	3.876699E+6	1.483799E-2	pP2e(23)	T7	a	0.00500
0	0	23	24	2	2	f	f	19367.94800	19367.9470	0.00100	0.00000	972.6164	3.875471E+6	1.485651E-2	pP2f(24)	T7	a	0.00500
0	0	24	25	2	2	e	e	19370.52500	19370.5117	0.01330	0.00000	1052.4689	3.874956E+6	1.487537E-2	pP2e(25)	T7	a	0.00500
0	0	25	26	2	2	f	f	19373.42800	19373.4269	0.00110	0.00000	1137.4206	3.874373E+6	1.489157E-2	pP2f(26)	T7	a	0.00500
0	0	26	27	2	2	e	e	19376.50400	19376.4580	0.04600	0.00000	1223.6086	3.874400E+6	1.490818E-2	pP2e(27)	T7	c	0.05000

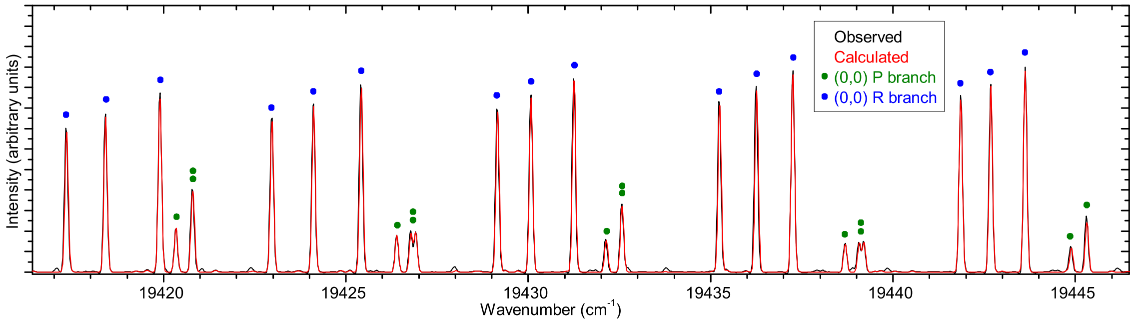

Figure 3.8 – A section of the (0,0) band of the C_2 Swan system. P branch: J''=36-41, R branch: J''=7-13. Reprinted from JQSRT, 124, Brooke et al., Line strengths and updated molecular constants for the C_2 Swan system, 11-20, Copyright (2013), with permission from Elsevier.

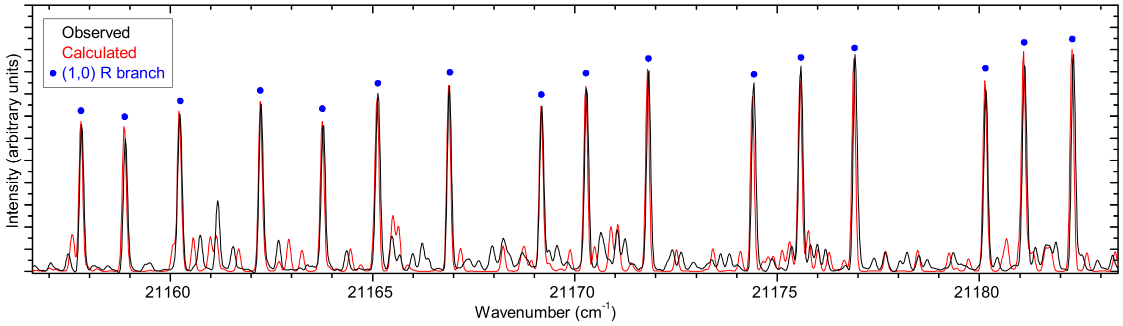

Figure 3.9 – A section of the Δv=+1 sequence of the C_2 Swan system, showing that the (1,0) R branch lines match well. The less intense lines do not match as closely. They are a mixture of the (1,0) P branch, the (9,8) R branch and the (8,7) P branch. (1,0) R branch: J''=39-45. Reprinted from JQSRT, 124, Brooke et al., Line strengths and updated molecular constants for the C_2 Swan system, 11-20, Copyright (2013), with permission from Elsevier.

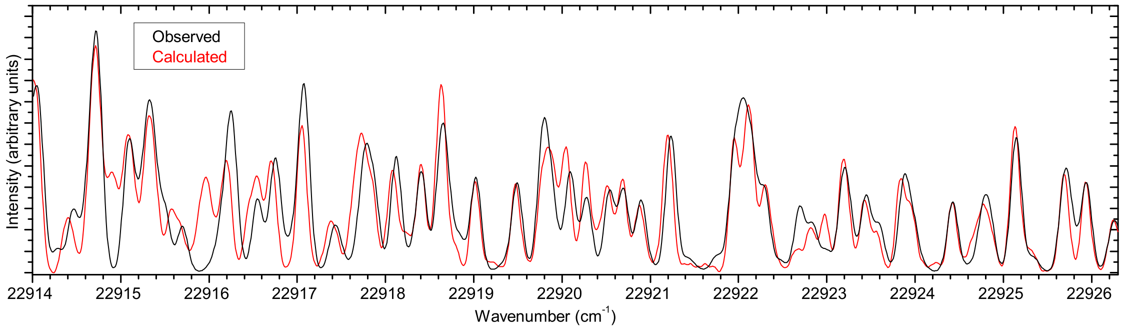

Figure 3.10 – A section of the Δv=+2 sequence of the C_2 Swan system. Shown is a mixture of the (2,0) R branch, the (3,1) R and P branches, the (4,2) and the P branch,(5,3) P branch,(6,4) P branch.(2,0) R branch: J''=13-16, (3,1) R branch: J''=47-51, (3,1) P branch: J''=2-4, (4,2) P branch: J''=5-12 and 39-48, (5,3) P branch: J''=5-17 and 45-52, (6,4) P branch: J''=1-5. Reprinted from JQSRT, 124, Brooke et al., Line strengths and updated molecular constants for the C_2 Swan system, 11-20, Copyright (2013), with permission from Elsevier.

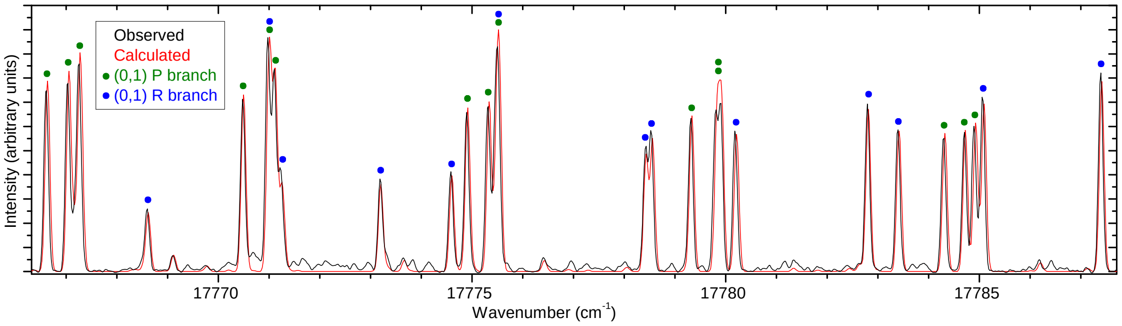

Figure 3.11 – A section of the Δv=-1 sequence of the C_2 Swan system. The less intense lines belong to the (0,1) Q branch. (0,1) P branch: J''=1-6, (0,1) R branch: J''=25-31.

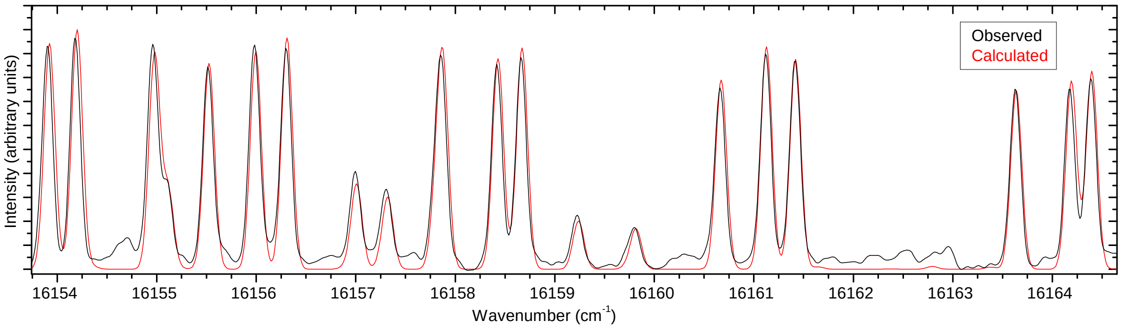

Figure 3.12 – A section of the Δv=-2 sequence of the C_2 Swan system, located near the (0,2) band head. All of the features belong to the (2,0) P branch. J''=1-5 and 17-22

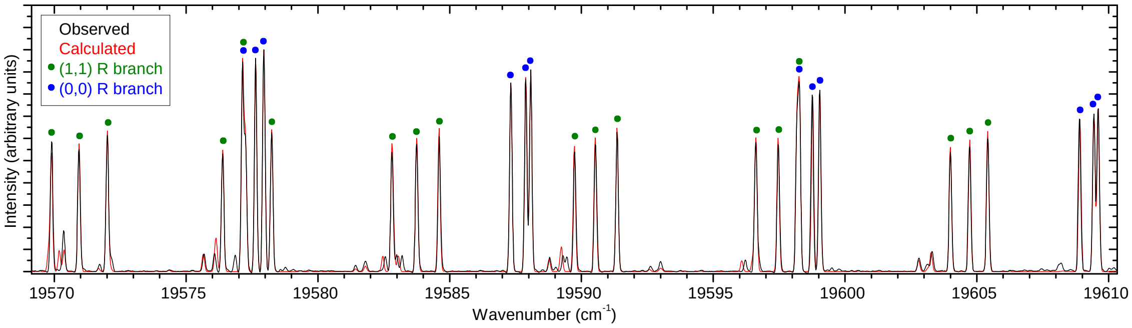

Figure 3.13 – A section of the Δv=0 sequence of the C_2 Swan system. The less intense lines are caused by the (1,1) P branch and the (0,0) P branch. (1,1) R branch: J''=10-17, (0,0) R branch: J''=27-32.

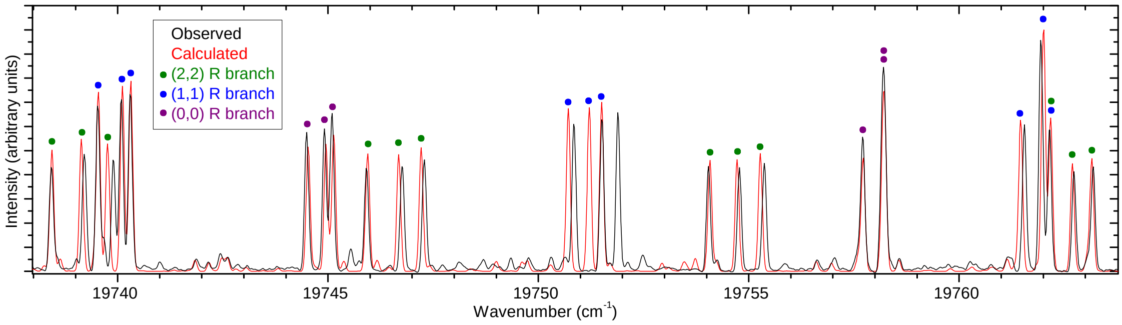

Figure 3.14 – A section of the Δv=0 sequence of the C$_2$ Swan system. The less intense lines are caused by the (3,3) P and R branches, the (2,2) P branch the (1,1) P branch and the (8,8) P branch. (2,2) R branch: J''=17-22, (1,1) R branch: J''=30-34, (0,0) R branch: J''=41-44.

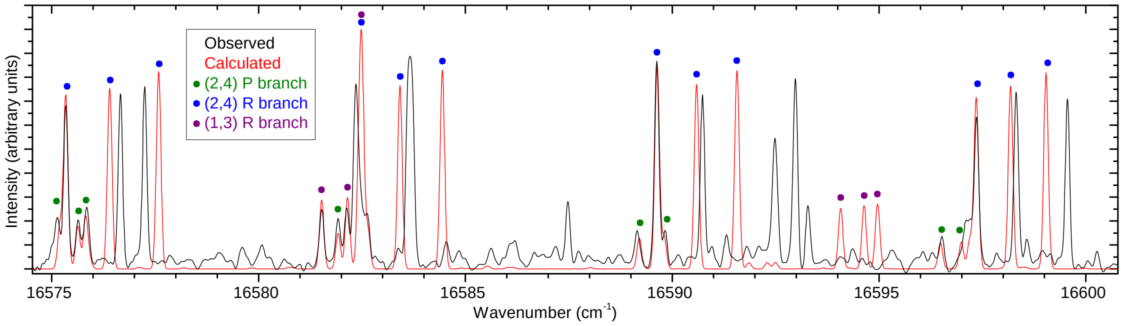

Figure 3.15 – A section of the Δv=-2 sequence of the C$_2$ Swan system. (2,4) R branch: J''=10-15, (2,4) P branch: J''=33-38, (1,3) R branch: J''=28-31. The circular labels refer to the calculated lines

3.5.2 $d^3\Pi_g$ Perturbations

The numerous perturbations have caused many of the line positions calculated by PGOPHER to be slightly inaccurate, and in turn have also had a small effect on the reported intensities. With the inclusion of the perturbation constants for the v′=4 and v′=6 levels, the average error for lines involving those upper levels is improved from 0.210 to 0.069 cm^{-1} and 0.571 to 0.038 cm^{-1}, respectively. The average error for all included lines was improved from 0.071 to 0.025 cm^{-1}. The first values were calculated using the molecular constants of Tanabashi et al., and the second using those in Tables 3.3 and 3.4, excluding any lines that had been heavily deweighted in the final fit. The average error for all of the (4,8) lines that were included was reduced to 0.010 cm^{-1}. These improvements are due to the perturbation studies of Bornhauser et al. (2010, 2011).

3.5.3 Updated Molecular Constants

As was seen by Tanabashi et al. (2007), the major molecular constants T_v, B_v and A_v show a reasonably smooth vibrational dependence; the smoothness for A_v for the $d^3\Pi_g$ state has improved from Tanabashi et al., specifically with a change in v′=6 level. This improvement is presumably due to the inclusion of the perturbations. The other constants still show several irregularities, particularly for v″=7-9 and v′=9-10. This is unsurprising as many fewer unperturbed/deperturbed observations are available for these levels. Some A_D constants showed a large uncertainty when floated, and so were fixed at estimated values based on the other more certain A_{D_v} values. This applied to v′=5, 7 and 8 and v′=8, 9 and 10. The same was also done for the spin-spin coupling constant λ for v′=8.

3.5.4 Vibrational Band Einstein *A* and *f*-values

For further validation, lifetimes of vibrational levels have been calculated and are compared to previous theoretical and experimental results in Table 3.10. For each upper vibrational level, lifetimes were calculated as the reciprocal of the sum of the Einstein *A* values for all possible transitions from the J'=1, F_3 level. Good agreement is shown with both sets of data. The theoretical values of Schmidt and Bacskay (2007) include transitions to the $c^3\Sigma_g^+$ state, and they state that this system contributes 3-4% to their radiative lifetimes. If this is taken into account, excellent agreement with our values is

Table 3.10 – Lifetimes of vibrational levels of the C_2 $d^3\Pi_g$ state.

v′	Our value (ns)	Theoretical[a] [1] (ns)	Expt. [2] (ns)	Expt. [3] (ns)
0	98.0	95.1	101.8±4.2	106±15
1	99.8	96.7	96.7±5.2	105±15
2	102.4	99.1	104.0±17	
3	106.0	102		
4	110.9	107		
5	118.2	113		

[a] The theoretical values (of (Schmidt and Bacskay, 2007)) include transitions to the $c^3\Sigma_u^+$ state. They state that this system contributes 3-4% to their radiative lifetimes. If this is taken into account, excellent agreement with our values is shown.

References: [1] Schmidt and Bacskay (2007), [2] Naulin et al. (1988), [3] Bauer et al. (1986)

shown. Our Einstein $A_{v'v}$ values were converted into $f_{v'v}$ values for comparison with those of Schmidt and Bacskay (for up to v′=5 and v″=5) (Schmidt and Bacskay, 2007), using Equation 2.131 and the wavenumber at which the forbidden Q(0) transition would appear as the band wavenumber. It should be noted that slightly different $f_{v'v}$ values would be obtained with a different choice of band wavenumber. Excellent agreement is shown for most bands, however some of the higher vibrational bands disagree by up to ∼50% of the calculated values, as shown in Table 3.8.

3.6 $^{12}C^{13}C$ Swan System

Different isotopes are produced in stars by various processes, and so relative isotopic abundances can provide an insight into the processes that are occurring (Burbidge et al., 1957). The $^{12}C/^{13}C$ ratio is related to the extent to which the CNO cycle, a hydrogen burning mechanism catalysed by carbon, nitrogen, and oxygen, is operating (Climenhaga et al., 1977), and can help in characterising other types of stars, for example R Coronae Borealis stars (Hema et al., 2012). The $^{12}C/^{13}C$ ratio is much higher in many types of stars than it is on Earth, for example it is normally between 2 and 20 in carbon stars (Climenhaga et al., 1977). Therefore $^{12}C^{13}C$ lines are common, and accurate line intensities are useful to calculate the $^{12}C/^{13}C$ ratio in stars, and other astronomical environments such as comets (Rousselot et al., 2012; Lambert and Danks, 1983).

Unlike $^{12}C_2$, $^{12}C^{13}C$ is not symmetrical, and so the levels that do not exist in $^{12}C_2$ due to g/u and a/s parity, do exist in $^{12}C^{13}C$, doubling the number of lines in the spectrum.

The available laboratory data for the $^{12}C^{13}C$ Swan system is much less extensive than for $^{12}C_2$; only lines in the (0,0) band have been recorded Amiot (1983). A line position fit was performed including these lines, and also lines from the Ballik-Ramsay system with v''=0-2 (Amiot and Verges, 1982; Islami and Amiot, 1986), which shares its lower electronic level with the Swan system. This provided accurate energy levels for the $a^3\Pi_u$, v=0-2 levels and the $d^3\Pi_g$, v=0 level. The $d^3\Pi_g$, v = 1 and 2 levels were estimated using $^{12}C_2$ spectroscopic constants and isotopic relationships, and the accurate v=0 constants. Previous $v \geq 1$ line positions have been approximated using only the $^{12}C_2$ spectroscopic constants and isotopic relationships, and so the new line positions are an improvement.

Intensity calculations equivalent to those for $^{12}C_2$ were performed, and the result was a line list of all possible rovibronic transitions between v=0-2 in both electronic states, up to J=60.

3.7 Conclusion

Many perturbations are present in the $d^3\Pi_g$ state, and only those shown in Table 3.1 (involving the $d^3\Pi_g$, v=4 and v=6 levels) have been accounted for in these calculations. While many of the line positions in the new line list do not match experiment precisely, the intensities are an improvement on previously available data, where results have been based on the partly incorrect assignments made by Phillips and Davis (1968). The positions reported are also a slight improvement, mainly due to inclusion of the perturbation data of Bornhauser et al. (2010, 2011). The calculated vibrational level lifetimes show good agreement with experimental and theoretical studies. The $^{12}C^{13}C$ line list includes line position improvements as described in Section 3.6, and also intensities, and so is a more accurate and comprehensive list than was previously available. The line lists will be of use to astronomers, materials scientists, and combustion scientists in their analyses of the C_2 Swan system.

The concentration of C_2 in a star is strongly related to the C/O ratio. Almost all of the carbon and oxygen in stellar atmospheres will form CO until one of the elements is exhausted, and therefore the more abundant of the two elements is free to also form other molecules (Wood, 1985), and the less abundant of the two exists almost entirely within CO. If carbon is more abundant, and the star is cool enough for C_2 to exist in relatively high concentrations, then C_2 spectral features will be observed. In fact, their presence defines a carbon star (Cohen et al., 2006). In stars that exhibit strong C_2 spectral features, they have been used to calculate the carbon abundance (Lambert et al., 1986; Hema et al., 2012).

However, for calculations of carbon abundances in stellar atmospheres, the CH and CN molecules are also available and are often used instead (Cohen et al., 2006; Asplund et al., 2009). Transitions of C_2 are more commonly used to calculate the $^{12}C/^{13}C$ ratio. CH is much less useful for this purpose, because the separation of lines for different isotopes depends on the ratios of the reduced mass. For CH, this is only 1.006, whereas it is 1.04 for C_2. Therefore, $^{12}C^{13}C$ transitions are more separated from their $^{12}C_2$ counterparts than ^{13}CH from ^{12}CH, and so are more easily detected and analysed.

The studies of Cohen et al. (2006; extremely metal-poor carbon stars), Hema et al. (2012; R Coronae Borealis and hydrogen-deficient carbon stars), and Rousselot et al. (2012; comets) are recent examples of studies that use C_2 Swan transitions to calculate the $^{12}C^{13}C$ ratio (and carbon abundance in the case of the second study). The intensities used by Cohen et al. (2006) are from a line list developed in 1971 (Querci et al.). As is often the case with C_2 observations, Hema et al. (2012) and Rousselot et al. (2012) calculated their own line intensities. The line positions in all cases were mostly those of Phillips and Davis (1968), which contain a number of errors. Based on this, it would clearly be useful for astronomers to have access to the new C_2 Swan line list (of both main isotopologues), which is self consistent, has more accurate line positions and intensities, and covers all possible transitions that could be required. This would mean that they can more easily calculate C_2 and carbon abundances, and $^{12}C/^{13}C$ ratios by reading the line list with their code, and would not have to resort to older, less reliable data, or perform similar calculations themselves.

The new line list has been used to calculate the carbon abundance and $^{12}C/^{13}C$ ratio in one of the extremely metal-poor carbon stars analysed by Cohen et al. (2006), to test its effectiveness (Ram et al., 2014). For star HE 0212-0557, Cohen et al. (2006) obtained a carbon abundance of log ϵ(C)=8.06, where log ϵ(x) is the abundance of element x in dex, equal to $\log_{10}(N_x/N_{\mathrm{hydrogen}}) + 12$, and a $^{12}C/^{13}C$ ratio of $4.0\pm30\%$ using C_2 transitions, and 3-4 using CH transitions. The values obtained using the new line list are log ϵ(C)=8.09 ± 0.05 and $^{12}C/^{13}C=4.5\pm0.5$, which are in excellent agreement with those of Cohen et al. (2006).

The line list has also successfully been used to calculate the carbon abundance in the Sun (Sneden et al., 2014), despite the weakness of the C_2 Swan transitions. The values obtained from two spectra were log ϵ(C)=8.48 and 8.53, which show excellent agreement with equivalent calculations using CH lines in the same work, that suggested an abundance of log ϵ(C)=8.48. The currently recommended value, from Asplund et al. (2009), is log ϵ(C)=8.39± 0.04. The results using our line list are considered to be very successful, as they use only the weak transitions of C_2 and a 1D model as opposed to the 3D model used by Asplund et al. (2009).

These studies give good validation of the new line list, and indicates that it could be used with confidence in the future in larger studies to obtain reliable results.

3.8 Future Work

There are still many local perturbations in the C_2 Swan system that have not been accounted for. More studies such as those performed by Bornhauser et al. (2010, 2011) would be extremely useful, and hopefully a complete deperturbation study of all of the bands reported here will eventually be performed. There are a number of other electronic systems of C_2, as shown in Figure 3.1, which could be analysed in a similar manner. Specifically, all of the singlet systems shown in the figure could be analysed simultaneously in a global fit, which would be slightly simpler as they are singlets. The inclusion of the H-W effect as has been done for the other molecules in this thesis would also be useful, but it is not vital for the strong vibrational bands.

The methods used in this chapter were then improved, for application to other molecules. They were next applied to the CN molecule, for which the H-W effect and transformation equation are now included.

Chapter 4

The CN $A^2\Pi$-$X^2\Sigma^+$ (red), $B^2\Sigma^+$-$X^2\Sigma^+$ (violet), and Ground State Rovibrational Systems

4.1 Preface

The CN molecule was studied to continue the theme of producing line lists for astronomically important molecules. At this point, the calculation methods were developed to include the H-W effect, and the case (b) to (a) transformation equation was derived and applied. For C_2, one electronic system was studied. In this chapter, there are two electronic systems, both with states of different multiplicities to each other and to the C_2 Swan system, and also ground state vibration-rotation transitions were introduced. All of this made the calculations much more complicated than they would have been if simply another $^3\Pi$-$^3\Pi$ electronic system had been investigated. The computer programs written previously had to undergo major changes.

4.2 Introduction

CN is an important molecule in astronomy and has been known of for more than a century. Electronic spectra of CN consist of many transitions which span the near infrared to the vacuum ultraviolet regions. Of the known electronic transitions, the $A^2\Pi$-$X^2\Sigma^+$ (red) and $B^2\Sigma^+$-$X^2\Sigma^+$ (violet) systems have been studied extensively because of their detection in a wide variety of sources. This free radical has been identified in comets

(Greenstein, 1958; Ferrin, 1977; Johnson et al., 1983; Fray et al., 2005), stars (Fowler, 1912; Lambert et al., 1984), the Sun (Uitenbroek and Tritschler, 2007), circumstellar shells (Wootten et al., 1982; Wiedemann et al., 1991; Bakker and Lambert, 1998), interstellar clouds (Turner and Gammon, 1975; Meyer and Jura, 1985) and the integrated light of galaxies (Riffel et al., 2007). The CN lines of the violet system were also identified in the spectra of the Red Rectangle nebula, HD 44179 (Hobbs et al., 2004). The presence of CN in astronomical environments makes it a useful probe of C and N abundances, as well as isotopic ratios, which provide information on nucleosynthesis and chemical evolution (Wang et al., 2004; Riffel et al., 2007; Savage et al., 2002; Adamczak and Lambert, 2013; Smith et al., 2013). Interstellar lines of the CN $B^2\Sigma^+$-$X^2\Sigma^+$ system have been used to measure the temperature of the cosmic background radiation, for example by Leach (2004, 2012), who has found the cosmic temperature to be 29 ± 2 mK higher than the cosmological temperature of 2.725 ± 0.001 K, measured by the COBE satellite. This difference was attributed, in part, to the interaction between the $A^2\Pi$ and $B^2\Sigma^+$ states.

Extensive studies of the $A^2\Pi$-$X^2\Sigma^+$ (Ram et al., 2010*a*) and $B^2\Sigma^+$-$X^2\Sigma^+$ (Ram et al., 2006) systems of $^{12}C^{14}N$ have been reported recently. The red and violet systems of the $^{13}C^{14}N$ (Ram et al., 2010*b*; Ram and Bernath, 2011, 2012) and $^{12}C^{15}N$ (Colin and Bernath, 2012) isotopologues have also been analysed.

There have been several studies of the infrared rovibrational bands (Davis et al., 1991; Horká et al., 2004) as well as microwave and millimeter-wave studies of the $X^2\Sigma^+$ ground state (Hempel et al., 2003; Hübner et al., 2005; Dixon and Woods, 1977; Skatrud et al., 1983; Johnson et al., 1984; Ito et al., 1991; Klisch et al., 1995) that provided measurements of the pure rotational transitions for the v=0 to 10 vibrational levels. An experimental dipole moment of 1.45 ± 0.08 D for the $X^2\Sigma^+$ state was measured by Thomson and Dalby (1968), on which current available rotational line intensities in spectroscopic databases are based (Pickett et al., 1998; Müller et al., 2001). Other theoretical values include 1.48 D (Das et al., 1974), 1.36 D (Urban et al., 1994) and 1.416 ± 0.008 D (Neogrády et al., 2002). Langhoff and Bauschlicher (1989) calculated a full DMF using the MRCI method, which resulted in an equilibrium dipole moment of 1.35 D. Their value for the square of the 1-0 band transition dipole moment (7.5×10^{-4} au) was also in good agreement with an experimental value ($7.5 \pm 3.1 \times 10^{-4}$ au) reported by Treffers (1975), although there is clearly a large uncertainty in the experimental value. Intensities based on the Thomson and Dalby (1968) dipole moment are still in general use, for example recently by Riechers et al. (2007) and Bayet et al. (2011). A new calculation using a high level of theory, a large basis set and a greater range of bond distances would be of use in creating a larger and more accurate list of intensities, and to help to resolve the discrepancies highlighted above.

Jørgensen and Larsson (1990) have calculated line intensities for the $A^2\Pi$-$X^2\Sigma^+$ system of CN at temperatures ranging from 1000 K to 6000 K. In this study the rotational lines of different isotopologues of CN were calculated for transitions between vibrational levels with v=0-30 of the ground and excited states using a limited set of older spectroscopic constants.

There have been many experimental studies of the lifetimes of the $A^2\Pi$ state (Jeunehomme, 1965; Katayama et al., 1979; Sneden and Lambert, 1982; Nishi et al., 1982; Duric et al., 1978; Taherian and Slanger, 1984; Lu et al., 1992; Huang et al., 1993; Halpern et al., 1996) and the $B^2\Sigma^+$ state (Nishi et al., 1982; Duric et al., 1978; Jackson, 1974; Luk and Bersohn, 1973) over the past four decades. It has been noted that the experimental lifetimes of the $A^2\Pi$ state reported by different groups show poor agreement with each other. For example, the values reported by Katayama et al. (1979) are lower than the values of most of the other experimental studies. Their values range from 2.5 µs for v=2 to 4 µs for v=9 of the $A^2\Pi$ state. On the other hand, Sneden and Lambert (1982) have reported much higher values ranging from 14.2 µs for v=0 to 5.2 µs for v=10, based on an analysis of the solar spectrum. However, the most recent experimental values of Taherian and Slanger (1984) (6.67 ± 0.60 µs for v=2 to 4.3 ± 0.85 µs for v=5) and Lu et al. (1992) (6.96 ± 0.3 µs for v=2 to 3.38 ± 0.2 µs for v=5) show better agreement, at least for the lower vibrational levels. In contrast, the experimental lifetimes of the $B^2\Sigma^+$ state obtained in different studies agree reasonably well with each other (Nishi et al., 1982; Duric et al., 1978; Jackson, 1974; Luk and Bersohn, 1973).

There are also several theoretical studies of spectroscopic properties and radiative lifetimes of the $A^2\Pi$ and $B^2\Sigma^+$ states (Cartwright and Hay, 1982; Larsson et al., 1983; Lavendy et al., 1984; Knowles et al., 1988; Bauschlicher et al., 1988; Shi et al., 2010). It is found that the majority of the $A^2\Pi$ state theoretical results agree well with each other, but these lifetimes are considerably larger than the experimental values discussed above. In the case of the $B^2\Sigma^+$ state, the theoretical values agree well with each other as well as with the experimental results. It is still unclear why the experimental and the theoretical lifetimes of the $A^2\Pi$ state do not agree, other than the fact that measuring relatively long lifetimes in the near infrared is experimentally challenging, and long lifetimes in general are more sensitive to experimental issues such as collisional effects and molecules moving out of the field of view.

The spectra used for measuring the rotational line positions of the red (Ram et al., 2010*a*) and violet (Ram et al., 2006) systems of ^{12}C^{14}N were observed using different experimental sources including a microwave discharge, nitrogen afterglow and high temperature furnace. The spectra recorded using the nitrogen afterglow source provided extensive bands for both systems involving high vibrational levels. For the A$^2\Pi$-X$^2\Sigma^+$ system, a rotational analysis of 63 bands was obtained, with v=0-22 in the A$^2\Pi$ state and v=0-12 in the ground state (Ram et al., 2010*a*). For the B$^2\Sigma^+$-X$^2\Sigma^+$ system, 57 bands involving v=0-15 in both the ground and excited states (Ram et al., 2006) were analysed. The final data set of the two systems included the existing infrared rovibrational measurements by Davis et al. (1991), Horká et al. (2004), and Hübner et al. (2005) in addition to the available microwave and millimeter wave measurements of the ground state (Hempel et al., 2003; Hübner et al., 2005; Dixon and Woods, 1977; Skatrud et al., 1983; Johnson et al., 1984; Ito et al., 1991; Klisch et al., 1995).

4.2.1 CN $\mathbf{B^2\Sigma^+}$-$\mathbf{X^2\Sigma^+}$ and $\mathbf{X^2\Sigma^+}$-$\mathbf{X^2\Sigma^+}$ Systems

The energy level structure of the X$^2\Sigma^+$ and B$^2\Sigma^+$ states is very simple. The only parameter lifting the degeneracy of levels of the same N is $\gamma_{\rm v}$. The splitting is very small, and results in an F_{1e} and F_{2f} state for each N level. The energy levels of the X$^2\Sigma^+$ state are shown in Figure 4.1, and the arrangement of the B$^2\Sigma^+$ levels is the same.

Figure 4.1 shows the possible transitions from one upper N level. There are strong R and P branches (in terms of N) that are slightly split into doublets due to the different parity transitions, and very weak transitions that cross spin components. These are Q branches in terms of J, which are weak as $\Delta\Lambda = 0$. The $B_{\rm v}$ values are reasonably similar for the two states, so at what point and whether within the P or R branch that the lines turn round depends on v′ and v″. An example spectrum is shown later in Figure 4.9. The rovibrational transitions within the X$^2\Sigma^+$ state show the same pattern as the B$^2\Sigma^+$-X$^2\Sigma^+$ system, except that the branches do not turn round.

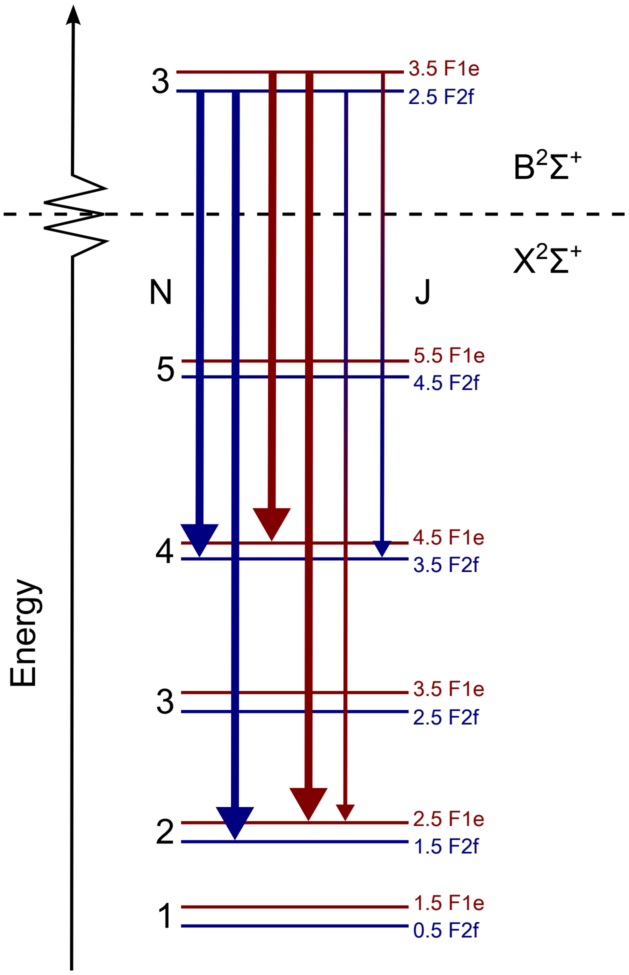

Figure 4.1 – Possible transitions with N'=3 in the CN $B^2\Sigma^+$-$X^2\Sigma^+$ system. Stronger lines are indicated with thicker arrows.

4.2.2 CN $\mathbf{A^2\Pi}$-$\mathbf{X^2\Sigma^+}$ System

The $\mathrm{A}^2\Pi$ levels have quite large A_v values compared to their B_v values. This means that at low J, the spin-orbit coupling has more of an effect than rotation on the energy, and it is therefore close to Hund's case (a). It is closer to case (a) than C_2, which can be deduced by examining the eigenvectors from the diagonalisation of the Hamiltonian. For example, for the v=0, J=2.5, F_{1e} level of the CN $\mathrm{A}^2\Sigma^+$ state, the eigenvectors are -0.996 and -0.085 relating to Ω=1.5(e) and 0.5(e), respectively. For the v=0, J=3, F_{1e} level of the C_2 $\mathrm{a}^3\Pi_\mathrm{u}$ state, they are 0.951, 0.303, and 0.0623 relating to Ω=2(e), 1(e), and 0(e), respectively. A pure case (a) state would have eigenvectors of 1 for one Ω state, and 0 for the others. Each J level within each spin component is split further into e and f parity levels. The general energy level structure is shown in Figure 4.2.

Figure 4.2 also shows the possible transitions from upper levels that have N=3 (for the upper state, N is not a good quantum number, but can still be useful a a label). The spectrum is much more complicated than the other examples seen so far. For the C_2 Swan system, the transition matrices only had non zero values where $\Delta\Omega$=0, as $\Delta\Lambda$=0. This results in the transitions that cross spin components being very weak, especially at high J where the states are closer to case (b). The CN $\mathrm{A}^2\Pi$-$\mathrm{X}^2\Sigma^+$ system has $\Delta\Lambda$=+1 however, and the parity transition matrices are made up of two MEs of similar values for each possible parity transition and ΔJ branch. These are $\langle{}^2\Pi_{(1.5)}(e/f)|\hat{\boldsymbol{\mu}}|{}^2\Sigma^+_{(0.5)}(e/f)\rangle$ and $\langle{}^2\Pi_{(0.5)}(e/f)|\hat{\boldsymbol{\mu}}|{}^2\Sigma^+_{(0.5)}(e/f)\rangle$. The transition matrices in terms of the real F components will therefore still have reasonably similar MEs, and the $F_1 - F_2$ and $F_2 - F_1$ transitions will have an intensity on the same order of magnitude as the $F_1 - F_1$ and $F_2 - F_2$ transitions. The difference is much greater as the $\mathrm{A}^2\Pi$ state tends towards case (b) at higher J. The result on the spectrum is that there are reasonably intense progressions for each possible type of transition: $^\mathrm{p}\mathrm{P}_{11}$, $^\mathrm{q}\mathrm{Q}_{11}$, $^\mathrm{r}\mathrm{R}_{11}$, $^\mathrm{p}\mathrm{P}_{22}$, $^\mathrm{q}\mathrm{Q}_{22}$, $^\mathrm{r}\mathrm{R}_{22}$, $^\mathrm{o}\mathrm{P}_{21}$, $^\mathrm{p}\mathrm{Q}_{21}$, $^\mathrm{q}\mathrm{R}_{21}$, $^\mathrm{q}\mathrm{P}_{12}$, $^\mathrm{r}\mathrm{Q}_{12}$, and $^\mathrm{s}\mathrm{R}_{12}$, using the notation $^{\Delta N}\Delta J_{F''F'}$. As the parity only splits levels by a small amount, some of these will appear as doublets, but with very different intensities. Specifically, as can be seen by the similar energy separations in Figure 4.2, the progressions that appear together are $^\mathrm{p}\mathrm{P}_{11}$ and $^\mathrm{p}\mathrm{Q}_{21}$, $^\mathrm{q}\mathrm{Q}_{11}$ and $^\mathrm{q}\mathrm{R}_{21}$, $^\mathrm{r}\mathrm{R}_{22}$ and $^\mathrm{r}\mathrm{Q}_{12}$, and $^\mathrm{q}\mathrm{Q}_{22}$ and $^\mathrm{q}\mathrm{P}_{12}$. As the upper state tends towards case (b) at higher J, the doublet structure of same-N transitions becomes clearer. The spectrum is further complicated as B_v in the upper state is greater than in the lower state, so that the S and R branches (in terms of N) turn round and cause all the branches to be on top of each other. The calculated spectrum

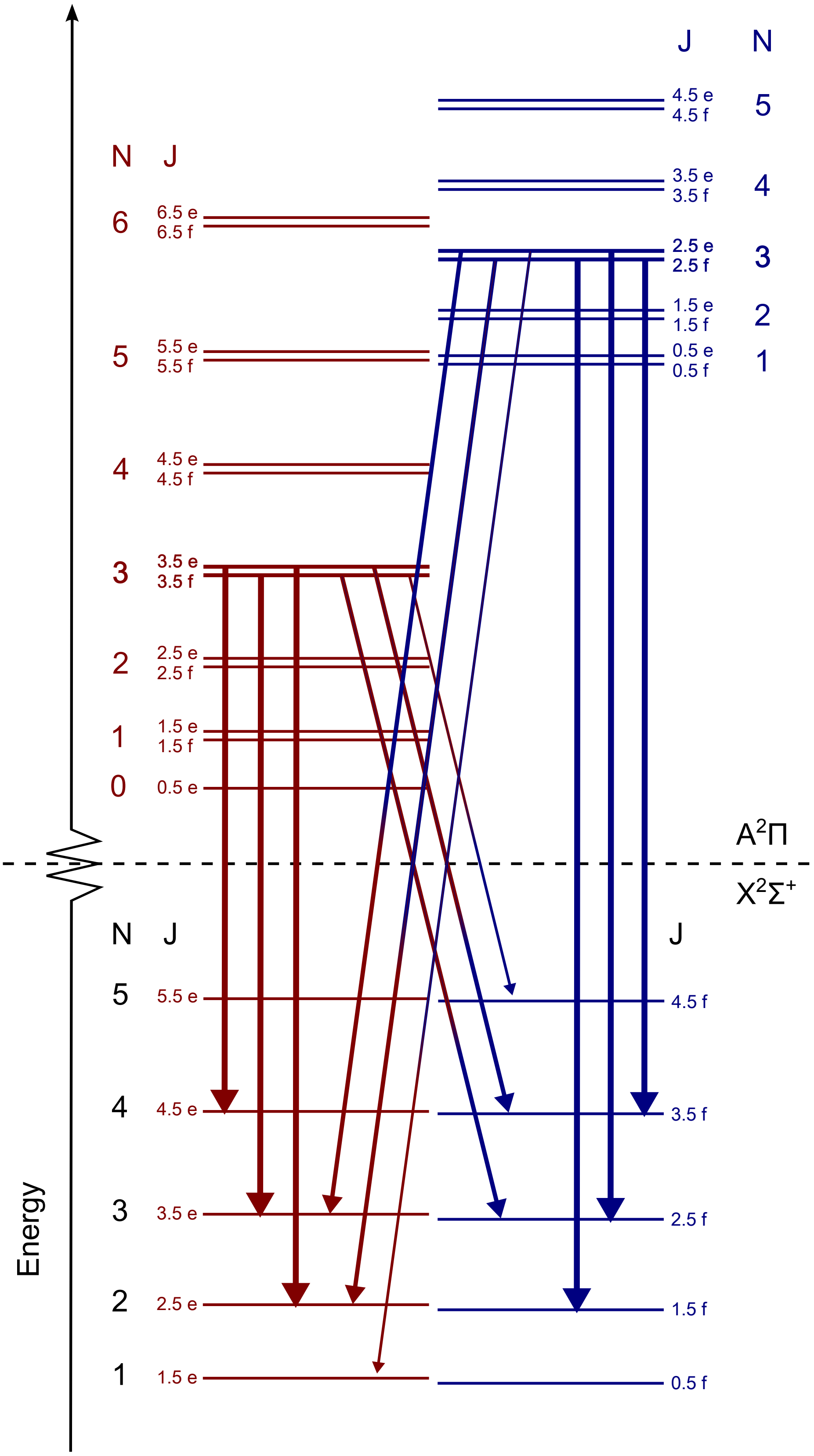

Figure 4.2 – Possible transitions with N'=3 in the CN A$^2\Pi$-X$^2\Sigma^+$ system. Generally stronger lines are indicated with thicker arrows. (for the upper state, N is not a good quantum number, but can still be useful a a label)

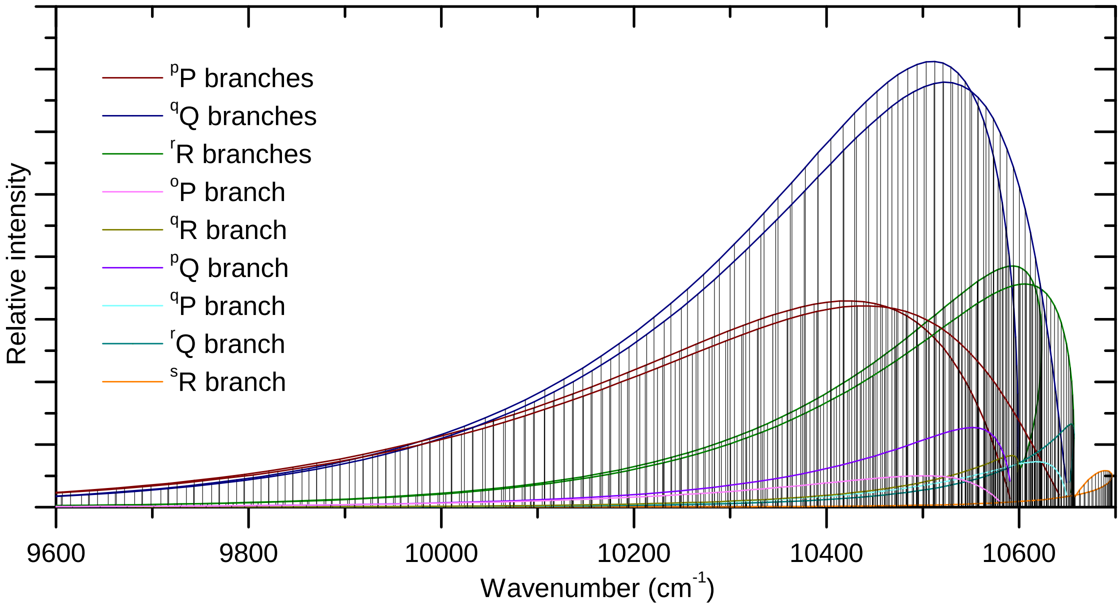

Figure 4.3 – Calculated stick spectrum of the CN $A^2\Pi$-$X^2\Sigma^+$, (2,1) band, using a temperature of 2500 K.

for the (2,0) band is shown in Figure 4.3, using an example temperature of 2500 K.

4.3 Method of Calculation

In the previous work (Ram et al., 2010*a*), a least-squares fitting program was used to fit the rotational lines. Several perturbations in the observed bands are caused by $X^2\Sigma^+ \sim A^2\Pi$, $A^2\Pi \sim B^2\Sigma^+$ and $B^2\Sigma^+ \sim a^4\Pi$ interactions (Kotlar et al., 1980; Ito et al., 1988, 1992; Ozaki et al., 1983*b*,*a*), and rotational lines affected by perturbations were given lower weights. A more detailed description of the observed perturbations is available in the previous paper (Ram et al., 2010*a*).

In the present work, the same lines were fitted using PGOPHER (Western, 2014). As mentioned by Ozaki et al. (1983*b*), the $B^2\Sigma^+$, v=10 level is perturbed by v=24 in the $A^2\Pi$ state, and the only change made to the data set was that the weights of some perturbed rotational lines of bands with v=10 in the $B^2\Sigma^+$ state were readjusted, and only the constants T, B, D and γ were floated. Without any adjustment of the weights, the calculated term values of the $B^2\Sigma^+$, v=10 level for higher J changed erratically with increasing J (so much so that at very high J (> 100), the term values were negative), because of incorrect values of the higher order constants used in the previous fit (Ram et al., 2006). The new PGOPHER fit was obtained using the previous constants as initial

Table 4.1 – Equilibrium molecular constants for the CN $X^2\Sigma^+$, $A^2\Pi$, and $B^2\Sigma^+$ states.

Constant	$X^2\Sigma^+$	$B^2\Sigma^+$	$A^2\Pi$
T_e	0	25752.590(12)	9243.29599(53)
ω_e	2068.68325(99)	2162.223(30)	1813.28845(74)
$\omega_e x_e$	13.12156(45)	19.006(22)	12.77789(27)
$\omega_e y_e$	0.1341(61)	−0.1346(65)	−0.001775(24)
$\omega_e z_e$	−0.005426(74)	−0.03673(85)	...
$\omega_e \eta_e$	−9.82(40)E-5	0.001430(37)	...
B_e	1.8997872(28)	1.96797(41)	1.7157690(24)
α_{e_1}	−0.0173802(27)	−0.01881(18)	−1.72528(35)E-2
α_{e_2}	−2.235(69)E-5	−0.000643(16)	−1.402(88)E-5
α_{e_3}	−6.64(48)E-7	...	−9.75(50)E-7
$r_e(\AA)$	1.17180630(86)	1.15133(12)	1.23304492(86)

Numbers in parentheses indicate one standard deviation to the last significant digits.

Table 4.2 – Spectroscopic constants for the CN $X^2\Sigma^+$ state.

v	T_v	B_v	$D_v \times 10^5$	H_v	γ_v	γ_{D_v}
0	0.0	1.891090248(84)	0.640771(18)	6.277(17)E-12	7.25393(56)E-3	−9.1(11)E-9
1	2042.42135(11)	1.873665679(78)	0.641647(18)	5.984(17)E-12	7.17190(82)E-3	−1.12(12)E-8
2	4058.54930(11)	1.856187457(76)	0.642639(18)	5.678(18)E-12	7.0801(12)E-3	−1.75(15)E-8
3	6048.34449(17)	1.83865289(13)	0.643809(23)	5.510(34)E-12	6.9798(14)E-3	−2.43(36)E-8
4	8011.76770(17)	1.82105955(22)	0.645051(29)	5.204(52)E-12	6.8636(16)E-3	−3.67(52)E-8
5	9948.77678(17)	1.80340446(25)	0.646440(35)	5.014(91)E-12	6.7213(16)E-3	−5.87(76)E-8
6	11859.32865(19)	1.78568518(26)	0.647525(51)	...	6.5456(17)E-3	...
7	13743.37581(21)	1.76789886(23)	0.649207(93)	...	6.3134(16)E-3	...
8	15600.87043(26)	1.75004067(30)	0.65094(18)	...	6.0118(18)E-3	...
9	17431.75566(40)	1.73210142(28)	0.65297(56)	...	5.6130(25)E-3	...
10	19235.96013(45)	1.71404986(30)	0.66358(75)	...	5.2324(30)E-3	...
11	21013.29410(84)	1.695088(22)	0.192(14)	−9.19(23)E-9	1.434(16)E-2	−8.111(76)E-5
12	22765.7282(10)	1.677608(27)	1.231(21)	1.099(47)E-8	1.3297(18)E-1	−2.274(11)E-4
13	24488.7305(13)	1.659501(23)	0.6610(68)	...	1.777(20)E-2	...
14	26185.6928(18)	1.641413(46)	0.742(27)	...	1.179(25)E-2	...
15	27856.2000[a]	1.62261(12)	0.617(46)	...	3.5(17)E-3	...

Numbers in parentheses indicate one standard deviation to the last significant digits.

[a] Value kept fixed

values and, as expected, the new spectroscopic constants were slightly modified after fitting the $A^2\Pi$-$X^2\Sigma^+$, $B^2\Sigma^+$-$X^2\Sigma^+$ and $X^2\Sigma^+$ rovibrational lines simultaneously in a combined fit. Most of the spectroscopic constants agree within the previous error bars except for some higher order constants. The updated spectroscopic constants for the $X^2\Sigma^+$, $A^2\Pi$ and $B^2\Sigma^+$ states have been provided in Tables 4.2, 4.4, and 4.3, respectively, where the constants are those described in Section 2.4. Several vibrational levels of the $A^2\Pi$ and $B^2\Sigma^+$ states are affected by perturbations, and therefore the values for the affected levels were given lower weights or were completely deweighted to determine the equilibrium constants. The equilibrium constants (as described in Section 2.1.4) for all three states are provided in Table 4.1.

Table 4.3 – Spectroscopic constants for the CN B$^2\Sigma^+$ state.

v	T_v	B_v	$D_\mathrm{v} \times 10^5$	γ_v	γ_{D_v}
0	25797.87041(49)	1.9587206(15)	0.659524(62)	1.7153(60)E-2	−6.81(31)E-7
1	27921.46673(58)	1.9380395(52)	0.67308(33)	1.8162(95)E-2	−8.96(93)E-7
2	30004.90702(83)	1.916503(12)	0.7031(32)	1.839(15)E-2	−2.40(69)E-6
3	32045.94782(75)	1.894182(17)	0.7115(69)	2.453(18)E-2	−7.3(13)E-6
4	34041.97171(62)	1.8704798(76)	0.7451(17)	2.117(11)E-2	−5.18(41)E-6
5	35990.0982(24)	1.847108(28)	0.9139(61)	4.27(96)E-3	1.693(45)E-4
6	37887.42564(54)	1.8193419(61)	0.8099(12)	2.524(10)E-2	−8.53(31)E-6
7	39730.53557(59)	1.790760(14)	1.1049(67)	6.098(67)E-3	...
8	41516.64447(62)	1.7621439(66)	0.9058(14)	3.488(11)E-2	−1.985(36)E-5
9	43242.98520(78)	1.730286(14)	0.9254(67)	1.576(12)E-2	−1.937(41)E-5
10	44908.7939(11)	1.696076(40)	0.313(40)	2.4897(38)E-1	−1.7970(62)E-3
11	46511.39737(85)	1.664979(12)	1.0253(31)	2.161(16)E-2	−1.866(62)E-5
12	48053.7308(11)	1.629785(33)	1.846(22)	−9.17(26)E-3	−7.56(25)E-5
13	49537.3409(13)	1.598044(22)	1.0871(61)	3.344(25)E-2	−2.565(72)E-5
14	50964.5889(26)	1.564126(94)	1.207(41)	3.49(49)E-3	...
15	52340.0287(20)	1.53238(13)	1.220(60)	8.61(17)E-2	−2.334(28)E-4

Numbers in parentheses indicate one standard deviation to the last significant digits.

4.3.1 Calculation of Transitions Dipole Moment Functions

The new calculations of the CN red and violet TDMFs were carried out by David W. Schwenke (NASA Ames Research Center, California), with a modified version of the quantum chemistry program MOLPRO 2012.6 (Werner et al., 2012).

The one electron basis set used started with the cc-pVQZ basis set of Dunning (Dunning, 1989). However to treat core-valence correlation, further functions were added (Schwenke, 2010). The molecular orbitals were determined by state-averaged multi-configuration Hartree-Fock (MCHF) calculations, using dynamic weighting of the state energies (Deskevich et al., 2004). The $1s$-like orbitals on C and N were kept doubly occupied in all configurations and the active space consisted of 4 a_1, 2 b_1 and 2 b_2 orbitals. In the state averaging, 21 A_1 states, 20 B_1 and 20 B_2 states, and 19 A_2 states, all of doublet spin, were included. These molecular orbitals were then used to compute wave functions using the internal-contracted MRCI (icMRCI) method (Knowles and Werner, 1988; Werner and Knowles, 1988; Knowles and Wener, 1992). In these calculations, all electrons were correlated. All calculations included scalar relativity via the Douglas-Kroll-Hess method (Douglas and Kroll, 1974; Hess, 1985, 1986). Calculations were carried out for 44 internuclear distances ranging from 100 bohr to 1 bohr (52.92 Åto 0.5292 Å), with step sizes 0.05 bohr (0.02646 Å) near the minima of the X$^2\Sigma^+$ A$^2\Pi$ and B$^2\Sigma^+$ states. The transition moments were computed from these wavefunctions as expectation values. Calculations were also carried out with the same procedure, but using the one electron basis derived the same way from the cc-pVTZ basis set. The results

Table 4.4 – Spectroscopic constants for the CN A$^2\Pi$ state.

Constants	v=0	v=1	v=2	v=3	v=4		
T_v	9115.685517(89)	10903.41299(22)	12665.56753(23)	14402.13990(19)	16113.12043(18)		
A_v	52.65443(18)	52.58078(50)	52.50526(49)	52.43236(32)	52.35628(25)		
$A_{D_\mathrm{v}} \times 10^4$	2.1998(31)	2.1979(93)	2.211(14)	1.9577(89)	1.8620(86)		
$A_{H_\mathrm{v}} \times 10^9$	4.959(43)	5.826(86)	7.96(24)	4.650(73)	4.307(82)		
B_v	1.70713832(13)	1.68986156(35)	1.67254021(59)	1.65516963(35)	1.63775143(36)		
$D_\mathrm{v} \times 10^6$	6.14473(18)	6.15575(20)	6.16910(37)	6.18175(21)	6.19839(22)		
$H_\mathrm{v} \times 10^{12}$	3.921(17)	3.552(19)	3.418(49)	2.734(19)	2.424(20)		
$q_\mathrm{v} \times 10^4$	3.87336(79)	3.9632(27)	4.0548(51)	4.1331(25)	4.2558(41)		
$q_{D_\mathrm{v}} \times 10^8$	0.9695(12)	1.0617(44)	1.143(13)	1.1065(33)	1.2038(47)		
$p_\mathrm{v} \times 10^3$	8.3764(65)	8.475(22)	8.364(30)	8.138(16)	8.067(16)		
$p_{D_\mathrm{v}} \times 10^7$	2.835(12)	3.486(44)	3.43(11)	2.548(39)	2.107(48)		
Constants	v=5	v=6	v=7	v=8	v=9	v=10	v=11
T_v	17798.49608(24)	19458.25763(28)	21092.46228(67)	22700.05200(57)	24283.17980(48)	25840.12165(54)	27371.2054(10)
A_v	52.28969(38)	52.24814(51)	52.3431(12)	50.6597(11)	51.4574(10)	51.4287(12)	51.3129(21)
$A_{D_\mathrm{v}} \times 10^4$	1.416(15)	0.770(26)	5.46(16)	1.43(13)	3.725(56)	3.515(72)	2.54(37)
$A_{H\mathrm{v}} \times 10^9$	0.0588(29)	0.0102(26)	4.69(15)	9.92(15)	0.202(20)	0.352(34)	1.43(57)
B_v	1.62028792(67)	1.60279825(96)	1.5851663(73)	1.5676896(73)	1.5497799(20)	1.5319138(24)	1.513983(16)
$D_\mathrm{v} \times 10^6$	6.22247(34)	6.25696(53)	5.629(17)	5.167(25)	6.3091(17)	6.3134(20)	6.208(47)
$H_\mathrm{v} \times 10^9$	0.002878(34)	0.003575(66)	...	1.228(26)	0.00364(31)	...	...
$q_\mathrm{v} \times 10^4$	4.3526(81)	4.629(17)	5.16(14)	6.97(12)	5.052(21)	5.067(15)	5.42(11)
$q_{D\mathrm{v}} \times 10^6$	0.01087(16)	0.01702(26)	0.909(37)	1.915(32)	0.0278(14)	...	...
$p_\mathrm{v} \times 10^1$	0.08079(27)	0.08062(43)	0.0964(15)	1.3920(21)	0.20683(86)	0.1558(10)	0.1487(18)
$p_{D\mathrm{v}} \times 10^4$	0.00562(17)	0.00084(10)	0.4116(66)	2.827(14)	0.04373(85)	0.0145(13)	...
$p_{H\mathrm{v}} \times 10^7$	...	...	...	2.247(23)	...	...	...
Constants	v=12	v=13	v=14	v=15	v=16	v=17	v=18
T_v	28876.3676(12)	30355.5525(12)	31808.62750(86)	33235.49687(69)	34635.99988(82)	36009.8741(34)	37357.20769(79)
A_v	51.1664(23)	51.0043(19)	50.8025(15)	50.6074(12)	50.3830(14)	50.5251(55)	49.8632(13)
$A_{Dv} \times 10^4$	0.390(23)	0.273(13)	0.446(14)	0.3251(83)	0.2443(92)	1.226(70)	0.3412(98)
B_v	1.496057(18)	1.477919(16)	1.459615(15)	1.4412985(90)	1.4229173(95)	1.404828(77)	1.3853108(96)
$D_\mathrm{v} \times 10^6$	6.372(53)	6.311(43)	6.329(45)	6.390(23)	6.556(22)	5.65(31)	6.572(25)
$q_\mathrm{v} \times 10^4$	0.587(23)	0.508(12)	0.698(12)	0.6739(87)	0.5708(82)	2.91(36)	0.678(12)
$p_\mathrm{v} \times 10^1$	1.476(30)	1.321(20)	1.747(20)	1.481(13)	1.236(14)	1.83(15)	1.507(17)
Constants	v=12	v=13	v=14	v=15	v=16	v=17	v=18
T_v	38677.42665(88)	39970.4623(14)	41235.86275(98)	42473.3725(12)	...	...	...
A_v	49.4910(12)	49.1747(28)	48.7582(16)	48.3969(12)	...	...	...
$A_{Dv} \times 10^4$	2.591(92)	6.14(57)	5.76(20)	...	...	...	...
$A_{H\mathrm{v}} \times 10^9$	...	2.80(11)	...	...	...	...	...
B_v	1.366389(11)	1.347266(25)	1.327242(16)	1.307745(21)	...	...	...
$D_\mathrm{v} \times 10^6$	6.663(30)	4.855(88)	6.211(49)	7.221(65)	...	...	...
$q_\mathrm{v} \times 10^4$	0.5859(79)	0.127(20)	1.177(17)	0.698(11)	...	...	...
$p_\mathrm{v} \times 10^1$	1.688(14)	0.360(42)	2.860(24)	1.575(21)	...	...	...
$p_{D\mathrm{v}} \times 10^4$	...	1.97(24)	...	...	...	...	...

Numbers in parentheses indicate one standard deviation to the last significant digits.

were very similar to that obtained with the cc-pVQZ basis set.

4.3.2 The H-W Effect

The magnitude of the H-W effect is mostly quite small for CN, especially for the observed bands, though there are some bands for which the effect is dramatic. Figure 4.4 shows a band on which the H-W effect has a typical effect (the observed B$^2\Sigma^+$-X$^2\Sigma^+$ (9, 7) band) and an extreme case (the weak, unobserved (10, 2) band). In Section 2 it states that the calculated Hund's case (a) MEs can be entered directly into PGOPHER. This newer method was not used until calculations were performed for NH. For CN, the H-W effect itself was entered into PGOPHER. To achieve this, the vibronic TDM, $\langle\eta'\Lambda|T^k_q(J'\Omega' J\Omega)|\eta\Lambda\rangle$, is written as having a dependence on J and Ω. This expression is used by PGOPHER to calculate line strengths, and the H-W effect can be included by expressing the normally constant vibronic transition moment as an arbitrary function of J', Ω', J, and Ω. A dimensionless H-W factor $F_{TDM}(m_{J'\Omega' J\Omega})$ is defined as a ratio to a reference value:

$$F_{TDM}(m_{J'\Omega' J\Omega}) = \frac{\langle\eta'\Lambda|T^k_q(J'\Omega' J\Omega)|\eta\Lambda\rangle}{\langle\eta'\Lambda|T^k_q(J' = \Omega'\Omega' J = \Omega\Omega)|\eta\Lambda\rangle} \tag{4.1}$$

which gives the correction scaling factor to the vibronic dipole moment, where $m_{J'\Omega' J\Omega}$ is equal to J'' plus a value based on ΔJ and $\Delta\Omega$. In Equation 4.1, Ω is used in the wavefunctions in the reference value in the denominator as it represents the lowest possible values of J in both of the A$^2\Pi$ spin components and in the B$^2\Sigma^+$ upper state. The H-W factors, $F_{TDM}(m_{J'\Omega' J\Omega})$, are calculated using the transformed Hund's case (a) MEs. These $F_{TDM}(m_{J'\Omega' J\Omega})$ values can be expressed as a polynomial according to the following equation:

$$F_{TDM}(m_{J'\Omega' J\Omega}) = 1 + Cm_{J'\Omega' J\Omega} + Dm^2_{J'\Omega' J\Omega} + Em^3_{J'\Omega' J\Omega} + \dots\ . \tag{4.2}$$

There are six possible versions of this equation for the A$^2\Pi$-X$^2\Sigma^+$ system, two for each change in J, corresponding to the two possible spin components, $\Omega = \pm 0.5$ and $\Omega = \pm 1.5$, in the A$^2\Pi$ state. The six different polynomials for each band were fitted to Equation 4.2 with effective polynomial orders (which were adjusted to give a good fit), using TDM matrix elements up to the highest reported J values. The resulting coefficients (C, D, E etc.; six sets for each band) were input into PGOPHER along with the reference TDM

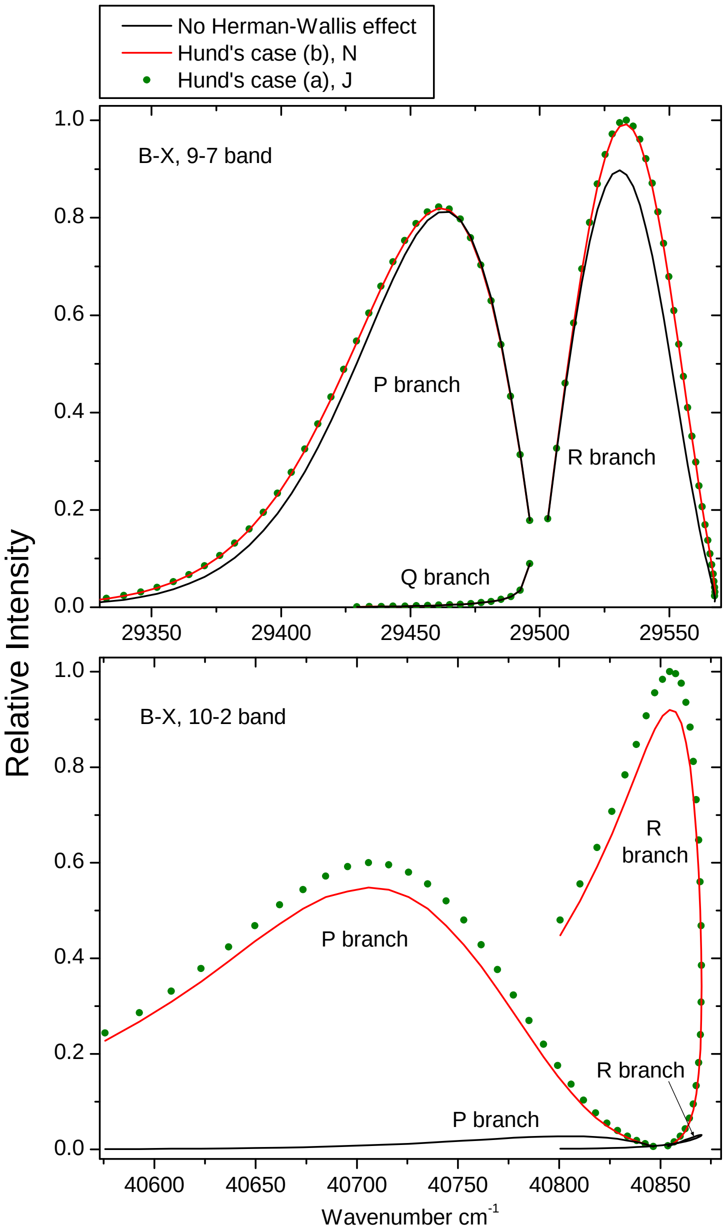

Figure 4.4 – Relative intensities of the CN $B^2\Sigma^+$-$X^2\Sigma^+$ system, 9-7 and 10-2 bands. The black lines are calculated by using only one TDM matrix element for the whole band and including no H-W effect ("N only" method). The green dots include the H-W effect and the Hund's case (b) to (a) transformation of the matrix elements. The red lines are calculated by not performing the Hund's case transformation, and using the quantum number N instead of J to account for the H-W effect. For both parts of the figure, the intensities have been calculated using a rotational temperature of 500 K, showing J up to 30.5. The 9-7 band was used as one example as this has the largest H-W effect for any observed band of the $B^2\Sigma^+$-$X^2\Sigma^+$ system. The 10-2 band is a typical example of the extent of the effect for the very weak bands. Reproduced from (Brooke et al., 2014*b*) by permission of the AAS.

matrix elements (the denominator in Equation 4.1). PGOPHER multiplies $\langle \eta'\Lambda|T_q^k(J' = \Omega'\Omega' J = \Omega\Omega)|\eta\Lambda\rangle$ by the appropriate polynomial value according to the value of $m_{J'\Omega' J\Omega}$, ΔJ, and the spin component for each transition. For the $\mathrm{B}^2\Sigma^+$-$\mathrm{X}^2\Sigma^+$ system, only three polynomials were required to be fitted to Equation 4.2 for each band, as there is only one spin component in both states. Please note that this is not the standard definition of the H-W factor; the subscripts "TDM" and "$J'\Omega' J\Omega$" are present to indicate this. Specifically, the correction must be made to the ME to allow for the Hund's case (a)/case (b) transformation rather than the square of the ME as is normally done for simpler systems. The standard definition would also make no correction to the Q branch.

4.3.3 Transformation from Hund's Case (a) to Case (b) MEs

The transformation equation in this case is

$$\begin{aligned}
\langle \eta'|\Lambda|' = 1|T_q^1(J'\Omega' J\Omega)|\eta\Lambda = 0\rangle &= (-1)^{J'-\Omega'} \begin{pmatrix} J' & 1 & J \\ -\Omega' & q & \Omega \end{pmatrix}^{-1} \\
&\times \sum_{N,N'} (-1)^{N-N'+J+1.5}(2N'+1)(2N+1) \begin{pmatrix} J' & 0.5 & N' \\ \Omega' & -\Sigma & -\Lambda' \end{pmatrix} \begin{pmatrix} J & 0.5 & N \\ \Omega & -\Sigma & 0 \end{pmatrix} \\
&\times \begin{Bmatrix} N' & J' & 0.5 \\ J & N & 1 \end{Bmatrix} \begin{pmatrix} N' & 1 & N \\ -\Lambda' & q & 0 \end{pmatrix} \langle \eta'|\Lambda'| = 1|T_q^1(N'N)|\eta\Lambda = 0\rangle,
\end{aligned} \tag{4.3}$$

where $q = \Omega' - \Omega''$. The transformation of the CN $\mathrm{A}^2\Pi$-$\mathrm{X}^2\Sigma^+$ MEs from case (b) to (a) was partly described previously in Section 2.5.4, where an R(J'') transition was used as an example. It required the case (b) MEs R($J'' - 0.5$), Q($J'' + 0.5$), and R($J'' + 0.5$). The P branch similarly requires P($J'' - 0.5$), Q($J'' - 0.5$), and R($J'' + 0.5$), and the Q branch requires P($J'' + 0.5$), Q($J'' - 0.5$), Q($J'' + 0.5$), and R($J'' - 0.5$) (when $J > 0.5$). For the $\mathrm{B}^2\Sigma^+$-$\mathrm{X}^2\Sigma^+$ and $\mathrm{X}^2\Sigma^+$-$\mathrm{X}^2\Sigma^+$ systems, the R branch requires R($J'' - 0.5$) and R($J'' + 0.5$), the P branch P($J'' - 0.5$) and P($J'' + 0.5$), and the Q branch R($J'' - 0.5$) and P($J'' + 0.5$). As the MEs only vary slowly with N, the functions of N and J are very similar, and this transformation only introduces a small correction in this case, as shown in Figure 4.4, along with the difference observed using the N only method (Section 2.5.6).

4.3.4 The $A^2\Pi$-$X^2\Sigma^+$ System

For most vibrational bands of the CN $A^2\Pi$-$X^2\Sigma^+$ system, the H-W effect is calculated to be relatively small (∼5%), but for some weaker bands the effect is large. The largest difference between the matrix elements for reported rotational transitions within a vibrational band and the reference matrix element for that band (the denominator in Equation 4.1; the maximum H-W effect) is 8% for the 0-0 band, 5% for the 6-8 band, and 67% for the 4-5 band (the greatest difference for an observed band). It is above 50% for several unobserved bands and one observed band. It was therefore decided that the effect should be included in these calculations.

In calculating the centrifugal part of the potential, $(N(N+1)-\Lambda^2)\hbar/2\mu r^2$, $\Lambda = 1$ is used by LEVEL for the $^2\Pi$ state. The effect of using $\Lambda = 1$ as opposed to $\Lambda = 0$ is mostly small ($< 0.5\%$), but for some bands it has a large effect. The bands in which this effect is large are mostly ones where the vibrational overlap is very small, and therefore any small alteration in the wavefunctions is more likely to cause a disproportionately large change in the overlap. The extent to which this change occurs has been investigated before (Le Roy and Vrscay, 1975), where a formula for its prediction, using rotational constants and vibrational spacings, was presented. It can also be seen from the centrifugal term that Λ will have more of an effect at lower J values.

The final output of this calculation consists of line positions, Einstein A-values and f-values for 295 possible vibrational bands (63 observed), and rotational lines with J up to between 25.5 and 120.5, depending on the band (see Table 3.9 for an example of the line list format). To decide on the highest J transitions to report for a specific band, the highest observed J values of each level (from any observed band) are taken, and to the lowest of these two values, 5 is added, and then this is rounded up to the nearest 0.5 or 5.5. For example, for the reported $A^2\Pi$-$X^2\Sigma^+$,(6,4) band, the highest observed J levels in the $A^2\Pi$, v=6 and $X^2\Sigma^+$, v=4 levels for any band are 88.5 and 72.5, respectively. 72.5 is the lower, and adding 5 and rounding up to nearest 5 gives 80.5. Therefore, all possible transitions up to $J'' = 80.5$ in the $A^2\Pi$-$X^2\Sigma^+$, (6,4) band are reported.

Using the Einstein A-values obtained from this calculation, the radiative lifetimes for some lower vibrational levels (v=0-4) of the $A^2\Pi$ state were calculated (as described in the following sections) and compared with the available experimental and theoretical lifetimes (see Table 4.5).

Table 4.5 – Comparison of lifetimes (in μs) with the selected experimental and theoretical lifetimes of the v=0-4 vibrational levels of the CN $A^2\Pi$ state.

This work			Experimental				Theoretical				
v	$A^2\Pi_{1/2}$	$A^2\Pi_{3/2}$	TS Ref. 1	LHH Ref. 2	DEL Ref. 3	J Ref. 4	KWHC Ref. 5	BLT Ref. 6	LGR Ref. 7	CH Ref. 8	LSA Ref. 9
0	11.08	11.29	8.50±0.5	...	3.83±0.5	...	11.16	11.2	11.3	11.1	8.1
1	9.60	9.76	8.02±0.6	...	4.05±0.4	7.29±0.2	9.71	9.7	9.6	9.6	7.0
2	8.53	8.66	6.67±0.6	6.96±0.3	3.98±0.4	7.05±0.3	8.66	8.6	8.4	8.6	6.3
3	7.73	7.84	6.67±0.6	5.09±0.2	4.20±0.4	6.95±0.3	7.87	7.8	7.6	7.2	5.7
4	7.12	7.21	4.70±0.2	3.83±0.3	4.35±0.4	6.58±0.4	7.25	7.2	6.9	6.7	4.9

References. (1) Taherian and Slanger (1984); (2) Lu et al. (1992); (3) Duric et al. (1978); (4) Jeunehomme (1965); (5) Knowles et al. (1988); (6) Bauschlicher et al. (1988); (7) Lavendy et al. (1984); (8) Cartwright and Hay (1982); (9) Larsson et al. (1983).

Table 4.6 – Comparison of current and previous Einstein $A_{v'v}$ values for several vibrational bands within the $X^2\Sigma^+$ ground state of CN

	Einstein $A_{v'v}$	
Band	Langhoff and Bauschlicher (1989)	This work
1-0	13.02	8.85
2-1	24.20	16.5
3-2	33.77	22.9
4-3	41.92	28.2
5-4	48.81	32.3
2-0	1.75	0.661
3-1	4.88	2.33
4-2	9.12	5.02
5-3	14.22	8.43
3-0	0.10	0.00563
4-1	0.38	0.0404
5-2	0.95	0.180

Table 4.7 – Comparison of calculated lifetimes (in ns) with the available experimental and theoretical lifetimes of the v=0-5 vibrational levels of the CN $B^2\Sigma^+$ state.

		Experimental				Theoretical			
v	This work	DEL Ref. 1	J Ref. 2	LB Ref. 3	NSH Ref. 4	BLT Ref. 5	KWHC Ref. 6	LSA Ref. 7	CH Ref. 8
0	62.74	66.2±0.8	65.6±1.0	60.8±2.0	65.0±2.0	62.69	60.73	66.80	62.29
1	62.97	66.3±0.8	...	...	...	63.25	61.21	66.63	62.88
2	63.46	64.3±2.0	...	...	...	64.19	61.97	67.10	63.67
3	64.25	65.6±3.0	...	...	...	65.52	63.13	68.22	64.84
4	65.39	68.2±4.0	...	...	...	67.23	65.00	69.72	66.42
5	66.95	67.3±5.0	...	...	...	69.32	66.44	71.43	68.42

References. (1) Duric et al. (1978); (2) Jackson (1974); (3) Luk and Bersohn (1973); (4) Nishi et al. (1982); (5) Bauschlicher et al. (1988); (6) Knowles et al. (1988) (7) Larsson et al. (1983) (8) Cartwright and Hay (1982); (9).

4.3.5 The $B^2\Sigma^+$-$X^2\Sigma^+$ System

The calculations for the $B^2\Sigma^+$-$X^2\Sigma^+$ system were performed in a similar manner as described for the $A^2\Pi$-$X^2\Sigma^+$ system. In this case a $^1\Sigma$-$^1\Sigma$ transition was calculated by LEVEL. The H-W effect was again included as it is of a similar magnitude as the $A^2\Pi$-$X^2\Sigma^+$ system. For example, the maximum H-W effect (defined in Section 4.3.4) is 0.4% for the 0-0 band, 10% for the 6-3 band, and 42% for the 9-7 band (the greatest difference for an observed band). For several of the unobserved bands, this difference is above 1000%.

The final line list consists of line positions and intensities for 253 bands of this system with $\mathrm{v}' = 0-15$, $\mathrm{v}'' = 0-15$, and J up to a maximum of between 25.5 and 70.5, depending on the band. The lifetimes of the $B^2\Sigma^+$ state levels calculated using the Einstein A-values agree well with the values obtained in previous experimental and theoretical studies.

4.3.6 The $X^2\Sigma^+$-$X^2\Sigma^+$ System

The main focus of these CN calculations was to calculate intensities for the two electronic systems mentioned. As this involved the calculation of a DMF and a potential energy curve for the $X^2\Sigma^+$ ground state, intensities were also calculated and reported for the rovibrational and rotational transitions within the ground state. The calculations for these transitions were the same as those for the $B^2\Sigma^+$-$X^2\Sigma^+$ system, but with the upper state wavefunctions replaced by $X^2\Sigma^+$ and using the $X^2\Sigma^+$ state DMF as opposed to the TDMF. Again, the H-W effect was included, as the maximum effect (defined in Section 4.3.4) was more than 5% for most bands. For example, it is 81% for the 2-0 band (the greatest difference for an observed band) and above 100% for several of the unobserved bands. The final reported line list contains line positions and intensities for 253 bands of rovibrational transitions with v=0-15, and J up to between 25.5 and 120.5, depending on the band. Einstein $A_{\mathrm{v}'\mathrm{v}}$ values have been calculated and compared to previous values in Table 4.6.

4.3.7 Vibrational Einstein $A_{\mathrm{v}'\mathrm{v}}$ and $f_{\mathrm{v}'\mathrm{v}}$ Values

Separate Einstein $A_{\mathrm{v}'\mathrm{v}}$ values were calculated for the different spin components, using J'=0.5 for $A^2\Pi_{1/2}$ and J'=1.5 for $A^2\Pi_{3/2}$. The Einstein $A_{\mathrm{v}'\mathrm{v}}$ values for the different spin components are slightly different, which is mainly due to the wavenumber difference of the two spin component transitions.

The Einstein $A_{v'v}$ values have been used to calculate the oscillator strengths ($f_{v'v}$) using Equation 2.131. The wavenumber of the ${}^{q}Q_2(0.5)$ line for the $A^2\Pi_{1/2}$-$X^2\Sigma^+$ sub-band and the ${}^{r}R_1(0.5)$ line for the $A^2\Pi_{3/2}$-$X^2\Sigma^+$ sub-band, located close to the band origins, were used in Equation 2.131. Einstein coefficients Einstein $A_{v'v}$ and oscillator strengths $f_{v'v}$ have been computed for 290 bands of the red system with v′=0-22 and v″=0-15, 250 bands of the $B^2\Sigma^+$-$X^2\Sigma^+$ transition with v=0-15 for both states, and 136 bands of the rovibrational transitions within the $X^2\Sigma^+$ state with v=0-15.

4.4 Results and Discussion

4.4.1 The $A^2\Pi$ State

There is generally good agreement between other theoretical values and our calculated $A^2\Pi_{1/2}$- $X^2\Sigma^+$ oscillator strengths. For example, Knowles and Werner (1988) have predicted $f_{3'0''}$=3.34 $\times10^{-4}$, compared to 3.35 $\times10^{-4}$ from Bauschlicher et al. (1988). The corresponding values from our calculation are $f_{3'0''}$=3.40$\times10^{-4}$ for $A^2\Pi_{1/2}$ and $f_{3'0''}$=3.39 $\times10^{-4}$ for $A^2\Pi_{3/2}$. A value of $f_{3'0''}$=4.58$\times10^{-4}$ was calculated by Larsson et al. (1983) but it was pointed out by Gredel et al. (1991) that the f-values of Larsson et al. (1983) were probably too large. Based on the calculations by Knowles and Werner (1988) and Bauschlicher et al. (1988), Bakker and Lambert (1998) have adopted the following $f_{v'v}$ values with a small correction: $f_{0'0''}$=23.7$\times10^{-4}$, $f_{1'0''}$=19.1$\times10^{-4}$, $f_{2'0''}$=9.0$\times10^{-4}$, $f_{3'0''}$=3.3$\times10^{-4}$, and $f_{4'0''}$=1.1$\times10^{-4}$. These values are in very good agreement with our values of $f_{0'0''}$=23.60$\times10^{-4}$, $f_{1'0''}$=19.15$\times10^{-4}$, $f_{2'0''}$=9.15$\times10^{-4}$, $f_{3'0''}$=3.39$\times10^{-4}$, $f_{4'0''}$=1.10$\times10^{-4}$ (values shown are for the $A^2\Pi_{1/2}$ component). Adamczak and Lambert (2013) have used the red system lines in their N abundance analysis of weak G band stars. In this study they have used a line list of the red system provided by Plez (2011) (unpublished data), which used the $f_{v'v}$ values recommended by Bakker and Lambert (1998). The wavelengths of the useful lines were re-computed from energy levels given by Ram et al. (2010*a*,*b*).

Although the calculated values agree well with the values obtained from several theoretical calculations for the $A^2\Pi$ state, they were significantly larger than the most recent experimental lifetimes Taherian and Slanger (1984); Lu et al. (1992). Also, the experimental lifetimes of the $A^2\Pi$ state measured by different groups do not agree with each other, as can be seen in Table 4.5. Among the experimental values, the lifetimes reported most recently by Taherian and Slanger (1984) and Lu et al. (1992) have better agreement. Lifetimes of 8.5±0.05, 8.02±0.6, 6.67±0.5, 5.5±0.5 and 4.70±0.2 µs have been reported for v=0, 1, 2, 3 and 4, respectively, by Taherian and Slanger (1984). Lu et al. (1992) did not determine the lifetimes for v=0 and 1 for the $A^2\Pi$ state, but have provided the values 6.96±0.3, 5.09±0.2 and 3.38±0.2 µs for v=2, 3 and 4, respectively. Their values for v=2 and 3 agree within their quoted error with the values of Taherian and Slanger (1984). Our $A^2\Pi_{1/2}$ ($A^2\Pi_{3/2}$) lifetimes are 11.08(11.29), 9.60(9.76), 8.53(8.66), 7.73(7.84) and 7.11(7.21) µs for v=0, 1, 2, 3 and 4, respectively. If the DMF is increased by 15%, these values become 8.38(8.54), 7.27(7.38), 6.45(6.55), 5.85(5.93) and 5.38(5.45) µs. These modified values agree better with the lifetimes reported by Taherian and Slanger (1984) and Lu et al. (1992), as well as the theoretical values of Larsson et al. (1983). However, there is no basis for such an adjustment.

The high level ab initio calculations $\big($except Larsson et al. (1983)$\big)$ of lifetimes agree with each other, and given the excellent quality of the calculations, it is unlikely that the ab initio values would change with an even higher level method. There are potentially problems with the experimental work, of which the most serious is collisional population transfer as discussed by Lu et al. (1992), which would reduce the experimental lifetimes. More experiments are needed, for example, on cold molecules in a collisionless environment with selective excitation of the upper state levels.

4.4.2 The $B^2\Sigma^+$ State

The calculated lifetimes of the $B^2\Sigma^+$ state agree well with the known experimental and theoretical values reported from previous studies. In particular, the present values of 62.74, 62.97, 63.46, 64.25, 65.39, 66.95 ns agree within $\sim$5% with the experimental values of Duric et al. (1978). The theoretical calculations of the oscillator strength of the $B^2\Sigma^+$-$X^2\Sigma^+$ bands by Knowles and Werner (1988) and Bauschlicher et al. (1988) predict $f_{0'0''}$=0.0345 and 0.0335, respectively, compared to $f_{0'0''}$=0.0337 in the present study. An earlier calculation by Larsson et al. (1983) has provided a value of $f_{0'0''}$=0.0324. Since the experimental lifetimes of the $B^2\Sigma^+$ state (Nishi et al., 1982; Duric et al., 1978; Jackson, 1974; Luk and Bersohn, 1973) agree well with theoretical results (Cartwright and Hay, 1982; Larsson et al., 1983; Lavendy et al., 1984; Knowles and Werner, 1988; Bauschlicher et al., 1988), an average value of $f_{0'0''}$=0.033 was adopted by Bakker and Lambert (1998)

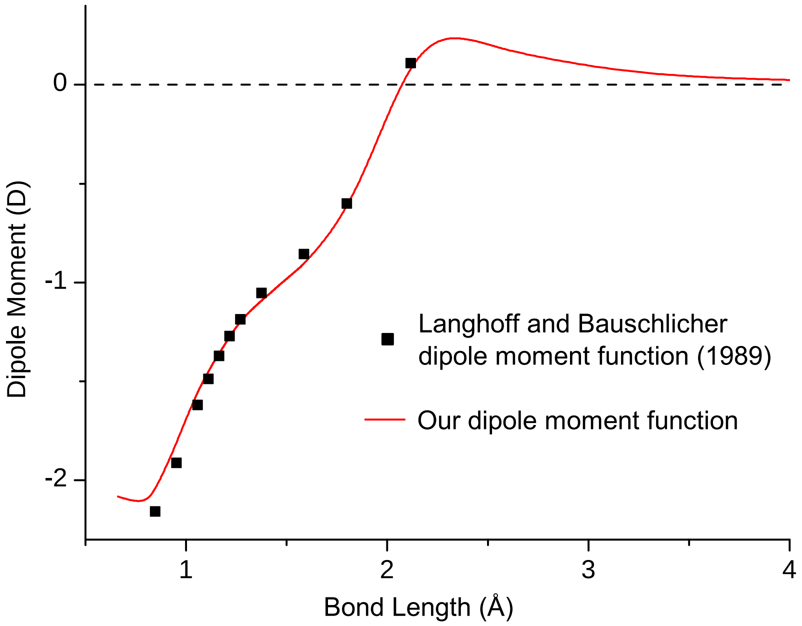

Figure 4.5 – Theoretical DMFs for the CN $X^2\Sigma^+$ ground state. Reproduced from (Brooke et al., 2014*b*) by permission of the AAS.

in their study of the ^{12}CN and ^{13}CN lines of the red and violet systems in the spectrum of the post-AGB star HD 56126. Our value of $f_{0'0''}$=0.0337 also supports the value adopted by Bakker and Lambert (1998). The much shorter lifetime of the $B^2\Sigma^+$ state means that the experimental measurements will be much less sensitive to neglected loss mechanisms in the excited state, so the existence of discrepancies in only the $A^2\Pi$ state lifetimes is not surprising.

4.4.3 The $X^2\Sigma^+$ State

The calculated Einstein $A_{v'v}$ values have been compared to those of Langhoff and Bauschlicher (1989) in Table 4.6. Our values are noticeably smaller; they are around 2/3 of the 1989 values for the Δv=1 sequence, and as low as about 1/10 in one case (the 4-1 band). The reason for this can be seen in Figure 4.5, which shows the difference between the 1989 DMF and ours. The differences here cause the discrepancies in the final Einstein $A_{v'v}$ values. To confirm this, the full calculations described were performed using the 1989 DMF, and the Einstein $A_{v'v}$ values were calculated to be almost identical to those reported by Langhoff and Bauschlicher.

4.4.4 Validation of Computed Results

The spectrum of the $A^2\Pi$-$X^2\Sigma^+$ system is spread over a wide range of wavenumbers (from 4000-21500 cm^{-1}), so it was recorded in two parts with different experimental conditions. As mentioned earlier, spectra were observed in emission from an active nitrogen afterglow source in which energy transfer takes place from the metastable triplet $A^3\Sigma_u^+$ and vibrationally-excited ground state of N_2 to higher vibrational levels of the excited and ground states of CN. In such a case, the vibrational and rotational temperatures are very different, and because of incomplete relaxation the concept of a vibrational temperature has little meaning. In this case, firstly the Lorentzian and Gaussian contributions to linewidths were adjusted in PGOPHER to find the best match between the observed and calculated line shapes. Next, the rotational temperature was estimated by monitoring the intensity distribution of a large number of rotational lines in a branch while varying the rotational temperature in small steps. A value of 500 K was estimated for the $A^2\Pi$-$X^2\Sigma^+$ bands in the 4000-12000 cm^{-1} region. In order to simulate the spectrum of a sequence of bands, the rotational temperature was held fixed but the vibrational temperature was adjusted in steps. It was found that a vibrational temperature of 15000 K produced a reasonable correspondence between the observed and simulated spectra. A part of the spectrum of the $\Delta v=-1$ sequence of the $A^2\Pi$-$X^2\Sigma^+$ system is presented in Figure 4.6.

As can be seen, the intensity of the 0-1, 1-2, 2-3, 3-4, 4-5 and 5-6 bands decrease rapidly and the 5-6 band is almost absent in the observed and simulated spectra. The higher vibrational bands again appear gradually in both the observed and simulated spectra. An expanded portion of the spectrum of the 0-1 band near the R_2 head is presented in Figure 4.7, and the ${}^sR_{21}$ branch of the 1-0 band is provided in Figure 4.8, showing good agreement between the observed and simulated spectra.

For the $B^2\Sigma^+$-$X^2\Sigma^+$ system, a similar comparison is more difficult because of the formation of a head of band heads in the different sequences. Also, interactions between the excited state and nearby perturbing levels cause abnormal intensities in some of the vibrational bands so the relative intensity of the simulated bands differs somewhat from the observations. For this transition, rotational and vibrational temperatures of 300 K and 3400 K result in a reasonable match between the observed and simulated spectra. A section of the 13-13 band showing very good agreement between observed and simulated spectra is provided in Figure 4.9.

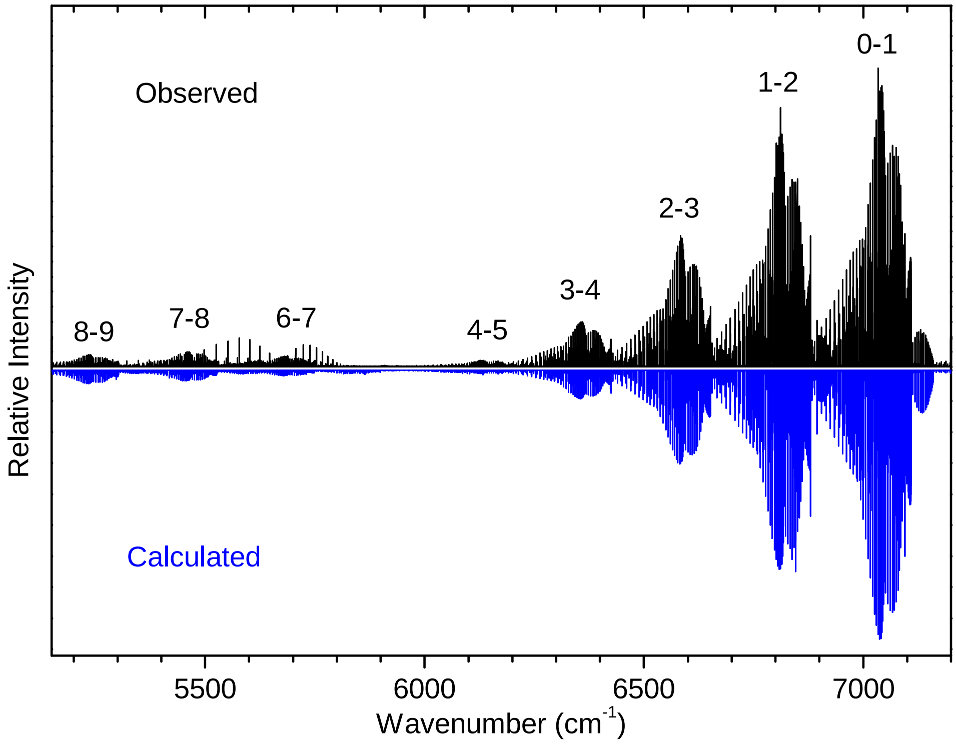

Figure 4.6 – A comparison of the observed (upper) and simulated (lower) spectra of the v=-1 sequence of the $A^2\Pi$-$X^2\Sigma^+$ system of CN. The unmarked emission lines near the 6-7 and 7-8 bands are rovibrational lines of the 2-0 overtone of HCl, present as an impurity. The absence of the 5-6 band in both spectra is consistent with the very small Franck-Condon factor calculated by LEVEL. Reproduced from (Brooke et al., 2014*b*) by permission of the AAS.

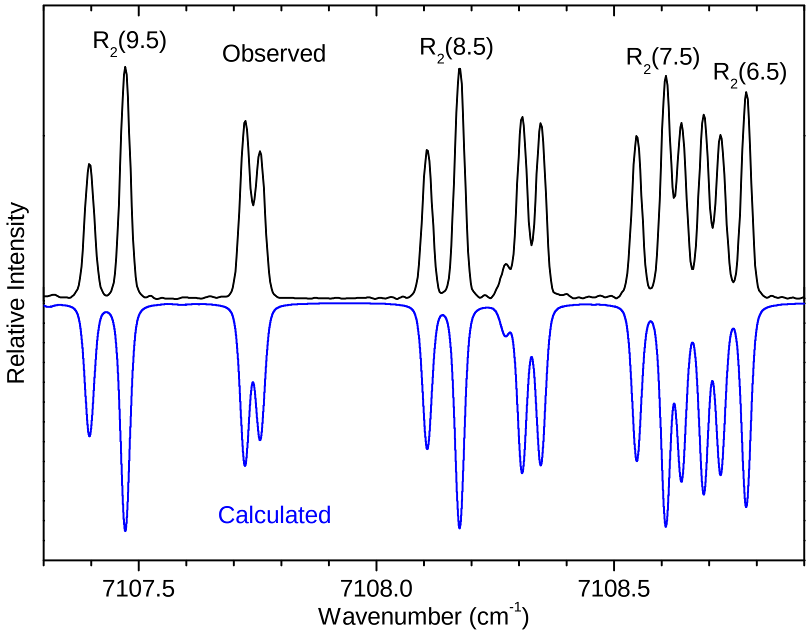

Figure 4.7 – A comparison of a part of the observed (upper) and simulated (lower) spectra of the $A^2\Pi$-$X^2\Sigma^+$, 0-1 band near the R_2 head showing a very good correspondence between the two spectra. Reproduced from (Brooke et al., 2014*b*) by permission of the AAS.

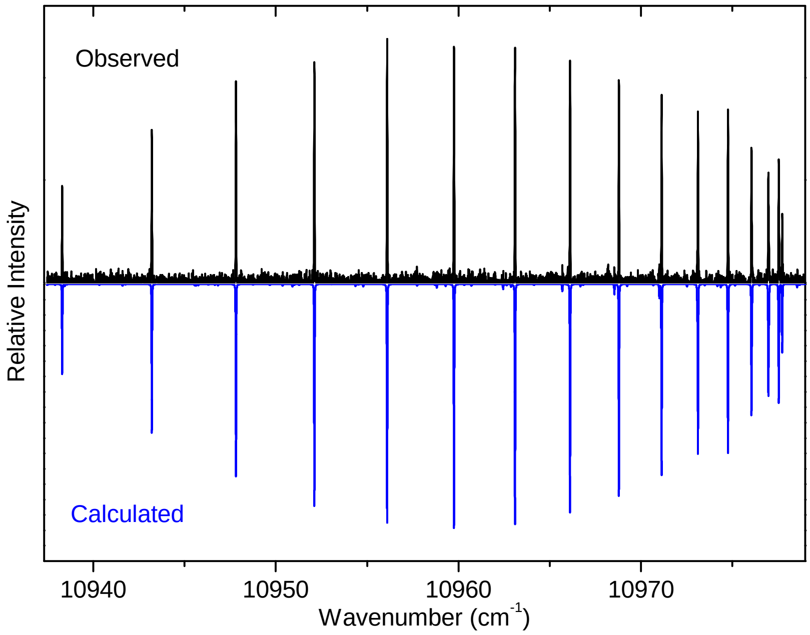

Figure 4.8 – A comparison of the observed (upper) and simulated (lower) spectra of the $A^2\Pi$-$X^2\Sigma^+$, 1-0, $^{s}R_{21}$ branch. Reproduced from (Brooke et al., 2014*b*) by permission of the AAS.

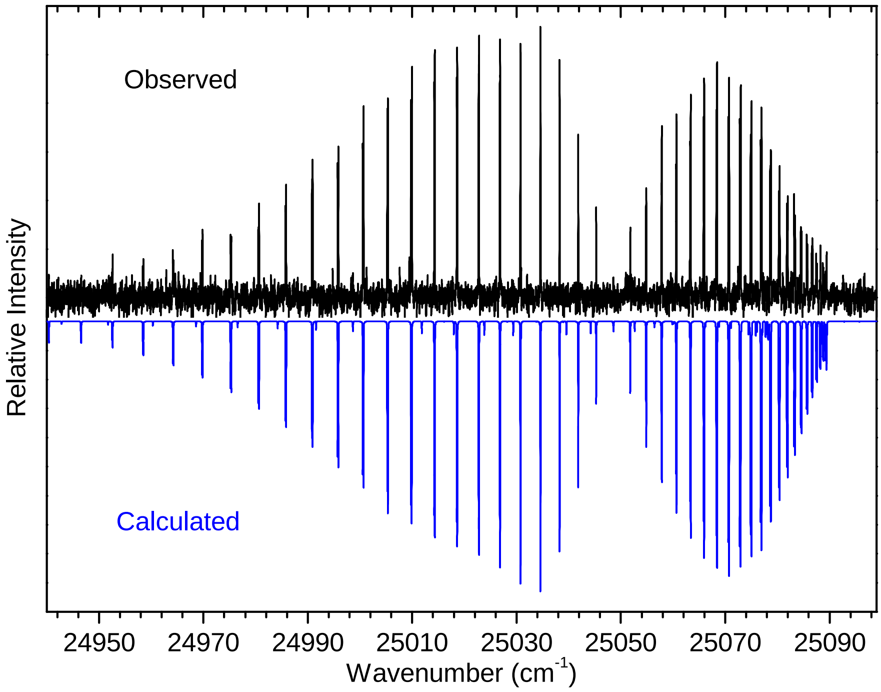

Figure 4.9 – A section of the observed (upper) and simulated (lower) spectra of the $B^2\Sigma^+$-$X^2\Sigma^+$, 13-13 band comparing the intensity distribution of the R and P branches. Reproduced from (Brooke et al., 2014*b*) by permission of the AAS.

4.5 Isotopes of CN

As the $^{12}C/^{13}C$ ratio is often much higher in some types of stars than on Earth, where CN spectral features are observed, ^{13}CN features are also likely to be present. Calculations using ^{13}CN observations can be used as well as $^{12}C^{13}C$ observations to calculate the $^{12}C/^{13}C$ ratio (Climenhaga et al., 1977; Lambert and Ries, 1977; Smith et al., 2013). The $^{14}N/^{15}N$ ratio is generally much higher than the $^{12}C/^{13}C$ ratio, and so $C^{15}N$ lines are encountered less often, but have still been used to calculate the $^{14}N/^{15}N$ ratio in some stars (Hedrosa et al., 2013).

Analogous calculations to those for CN were performed to generate line lists for ^{13}CN and $C^{15}N$. For ^{13}CN, the observed line positions and molecular constants were taken from Ram et al. (2010*b*), Ram and Bernath (2011), and Ram and Bernath (2012), and cover v=0-15 for the $B^2\Sigma^+$ state, v=0-22 for the $A^2\Pi$ state and v=0-15 for the $X^2\Sigma^+$ state. The experimental data for $C^{15}N$ are those of Colin and Bernath (2012) for v=0-3 for the $B^2\Sigma^+$ state, v=0-4 for the $A^2\Pi$ state, and v=0-5 for the $X^2\Sigma^+$ state. The final output of these calculations consists of line positions, Einstein A values, and f-values for all possible bands (101 observed) for ^{13}CN, and all possible bands (28 observed) for C^{15}N. These data files also contain predictions for pure rotational transitions and rovibrational transitions in the $X^2\Sigma^+$ state.

Previously available line lists have some substantial line position uncertainties (Jørgensen and Larsson, 1990; Hill et al., 2002; Kurucz, 2011), and this work provides increased line position and intensity accuracy in an internally consistent data set.

4.6 The CP $A^2\Pi$-$X^2\Sigma^+$ System

4.6.1 Introduction

CP is much less abundant than the other molecules examined in this thesis, but has nevertheless been observed in circumstellar shells (Guelin et al., 1990), and is one of the few gas phase phosphorous-containing molecules that have been astronomically observed. Knowledge of its abundance can contribute to the understanding of phosphorous chemistry in astronomical environments (Milam et al., 2008).

Despite being isovalent with CN, the CP $A^2\Pi$ state is quite different. CP's A_v values are around three times higher, and its B_v values are less than half those of CN $A^2\Pi$. This means that it is a very good Hund's case (a) state for all of the observed J levels. At J=1.5, the eigenvectors for the F_1 state are -0.99997 and -0.00779 for $^2\Pi_{(1.5)}(e/f)$ and $^2\Pi_{(0.5)}(e/f)$, respectively, and so Ω is a very good quantum number. The result is that the spectrum for a single vibrational band appears as two similar spectra separated by around 150 cm^{-1}, one for each spin component of the upper state. The possible transitions are of course the same as in the CN $A^2\Pi$-$X^2\Sigma^+$ system.

4.6.2 Calculations

A new line position fit was performed, using observational data from Ram and Bernath (1987), Saito et al. (1989), Ram et al. (1992), and Klein et al. (1999). These include lines involving the v=0-4 levels in both states, and the fitted molecular constants are shown in Tables 4.8 and 4.9, where the constants are those described in Section 2.4.

Equilibrium constants were calculated in the usual manner (as described in Section 2.1.4), and are shown in Table 4.10.

Predicted positions for the v=5-8 levels in each state were also included. To achieve this, T_v and B_v were estimated using the equilibrium constants, D_v and γ_v in the $X^2\Sigma^+$

Table 4.8 – Spectroscopic constants for the CP $X^2\Sigma^+$ state.

v	T_v	B_v	$D_v \times 10^6$	$\gamma_v \times 10^2$
0	0	0.7958810907(66)	1.328045(11)	1.8566387(96)
1	1226.12738(28)	0.78989476(80)	1.33152(43)	1.85056(75)
2	2438.57460(27)	0.78389278(88)	1.33625(54)	1.84458(80)
3	3637.33389(35)	0.7778735(13)	1.34164(96)	1.8390(10)
4	4822.3972(14)	0.771835(11)	1.345(20)	1.8376(73)

Numbers in parentheses indicate one standard deviation to the last significant digits.

Table 4.9 – Spectroscopic constants for the CP $A^2\Pi$ state.

v	T_v	B_v	$D_v \times 10^6$	A_v	$A_{D_v} \times 10^5$	$q_v \times 10^5$	$p_v \times 10^3$	$p_{D_v} \times 10^7$
0	6884.00566(21)	0.70927602(56)	1.28042(29)	−156.24385(22)	4.869(25)	−4.791(64)	9.410(18)	−1.26(15)
1	7934.41445(22)	0.70364906(66)	1.28296(37)	−156.12665(31)	4.305(43)	−4.85(13)	9.436(25)	−1.06(22)
2	8972.76570(26)	0.69801455(94)	1.28510(66)	−156.04334(37)	3.038(62)	−4.89(12)	9.632(39)	−0.88(48)
3	9999.06544(36)	0.6923799(13)	1.29156(89)	−156.01825(22)	2.00[b]	−4.96(16)	10.161(20)	−0.88[b]
4	11013.30165(66)	0.6867172(27)	1.2928(21)	−156.02[b]	2.00[b]	−4.96[b]	14.9(17)	−0.88[b]

Numbers in parentheses indicate one standard deviation to the last significant digits.

[b] Fixed close to the value for the last vibrational level varied.

Table 4.10 – Equilibrium molecular constants for the CP $X^2\Sigma^+$ and $A^2\Pi$ states.

Constant	$X^2\Sigma^+$	$A^2\Pi$
T_e	0	6972.46893(53)
ω_e	1239.79987(11)	1062.4724(14)
$\omega_e x_e$	6.834102(48)	6.03353(88)
$\omega_e y_e$	−0.0013211(62)	0.00105(15)
B_e	0.79886750(33)	0.7120860(26)
α_{e_1}	0.00596862(74)	0.0056184(34)
α_{e_2}	−8.56(17)E-6	−4.03(85)E-5
$r_e(\mathring{A})$	1.56197826(32)	1.6544214(30)

Numbers in parentheses indicate one standard deviation to the last significant digits.

state were extrapolated, and the remaining constants in the $A^2\Pi$ state were fixed close to the value for the last vibrational level varied.

The H-W effect in CP is small in the lower vibrational bands, but not negligible in the higher vibrational bands for which lines are reported. For example, the largest difference between the matrix elements for reported transitions within a vibrational band and the reference matrix element for that band is 1.7% for the (0,0) band, 2.0% for the (4,3) band (the largest difference for an observed band), but 23% for the (5,3) band (the largest difference for any band), and so it was decided that it should be accounted for in the calculated line list.

The remaining calculations were analogous to those for the CN $A^2\Pi$-$X^2\Sigma^+$ system, using the TDMF from de Brouckère and Feller (1998), and resulting in a line list of 75 possible vibrational bands with J up to between 30.5 and 55.5, depending on the band.

4.6.3 Results and Analysis

An example of the difference between the intensity distributions resulting from the use of the "N only" and "transformation" methods (Sections 2.5.6 and 2.5.4) is shown in Figure 4.11. It shows again that when the H-W effect is strong, the two methods give non-negligibly different results.

A portion of the spectrum of the (0,0) band near the ${}^{q}Q_{11}$ and ${}^{r}R_{11}$ heads of the $A^2\Pi$-$X^2\Sigma^+$, (0,0) band is presented in Figure 4.10, comparing the simulated and the observed spectrum. As can be seen, a good correspondence exists. A portion of the observed spectrum of the $A^2\Pi$-$X^2\Sigma^+$, (1,0) band (upper plot) near the ${}^{r}R_{22}$ and ${}^{s}R_{21}$ heads has been compared with the simulated spectrum (lower plot) in Figure 4.12, again showing a good agreement. Figure 4.13 provides a portion of the ${}^{s}R_{21}$ branch of the (0,0) band, and compares the relative intensity of a few rotational lines in the observed (upper) and simulated (lower) spectra.

So far no experimental values of lifetimes of electronic states of CP are available for comparison with our computed lifetimes.

4.7 Conclusion

MEs were calculated using the previously described method. Their J dependence was quantified and the effect of rotation on the matrix elements was included before their

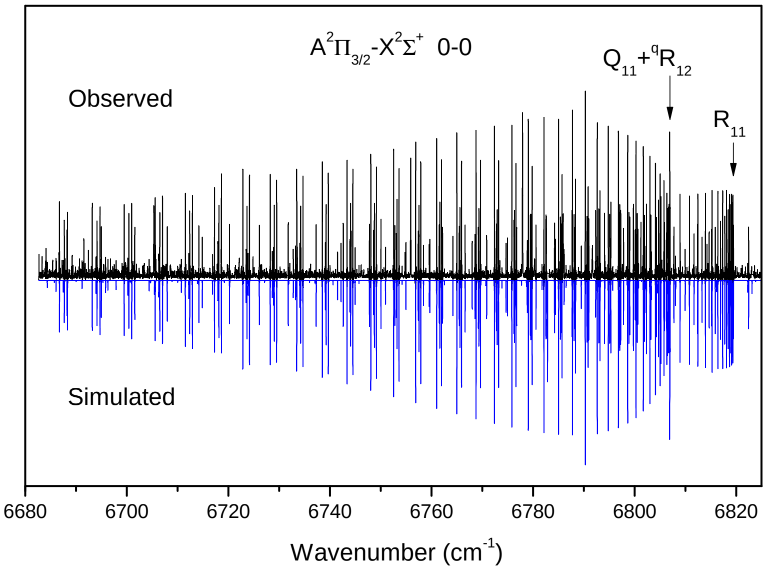

Figure 4.10 – A comparison of intensity distribution in the observed (upper) and simulated (lower) spectra of the CP $A^2\Pi$-$X^2\Sigma^+$, (0,0) band, showing good agreement. Reprinted from JQSRT, 138, Ram et al., Einstein A-values and oscillator strengths of the $A^2\Pi$-$X^2\Sigma^+$ system of CP, 107-115, Copyright (2014), with permission from Elsevier.

input into PGOPHER. A line list consisting of line positions, Einstein A coefficients and f-values for 290 bands of the $A^2\Pi$-$X^2\Sigma^+$ system with vibrational levels v′=0-22, v″=0-15, 250 bands of the $B^2\Sigma^+$-$X^2\Sigma^+$ transition with v′=0-15, v″=0-15, and 136 bands of the rovibrational transitions within the $X^2\Sigma^+$ state with v=0-15 has been generated. The Einstein A values have been used to compute radiative lifetimes in the $A^2\Pi$ and $B^2\Sigma^+$ states. The calculated f-values of the two transitions agree with the theoretical values of Knowles and Werner (1988), Bauschlicher et al. (1988) and Cartwright and Hay (1982), and the values adopted by Bakker and Lambert (1998). The $A^2\Pi$ state lifetimes have also been calculated with the modified TDMs (increased by 15%) which compare well with the recent experimental values for the lower vibrational levels of the $A^2\Pi$ state, but the use of the unmodified ab initio values has more validity. The $B^2\Sigma^+$ state lifetimes and f-values have good agreement with the previously reported experimental and theoretical values as well as the values adopted values by Bakker and Lambert (1998) in their chemical abundance analyses. The Einstein $A_{v'v}$ values for the $X^2\Sigma^+$ state rovibrational transitions are significantly smaller than previous values from Langhoff and Bauschlicher (1989), but the reason for this is explained in Section 4.4.3 and in Figure

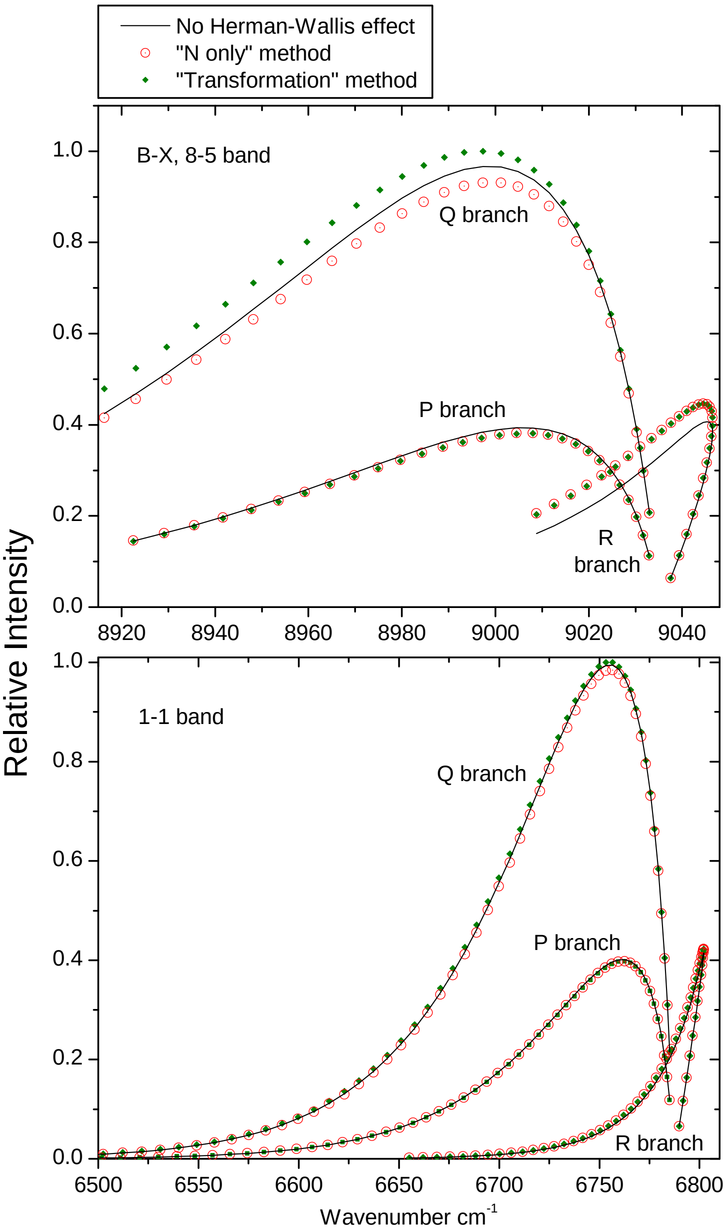

Figure 4.11 – Relative intensities of the CP $A^2\Pi$-$X^2\Sigma^+$, (1,1) and (8,5) bands. The black lines are calculated by using only one TDM matrix element for the whole band and including no H-W effect. The green diamonds include the H-W effect and the Hund's case (b) to (a) transformation of the matrix elements. The red circles are calculated by not performing Hund's case transformation, and using the " N only" method, described in Section 2.5.6. For both parts of the figure, the intensities have been calculated using a rotational temperature of 500 K. J up to 55.5 is shown for the (1,1) band and to 30.5 for the (8.5) band. The (1,1) band was used as a typical example of the difference between the methods for the observed vibrational levels. The (8.5) band is shown as an example of when the H-W effect is strong. Reprinted from JQSRT, 138, Ram et al., Einstein A-values and oscillator strengths of the $A^2\Pi$-$X^2\Sigma^+$ system of CP, 107-115, Copyright (2014), with permission from Elsevier.

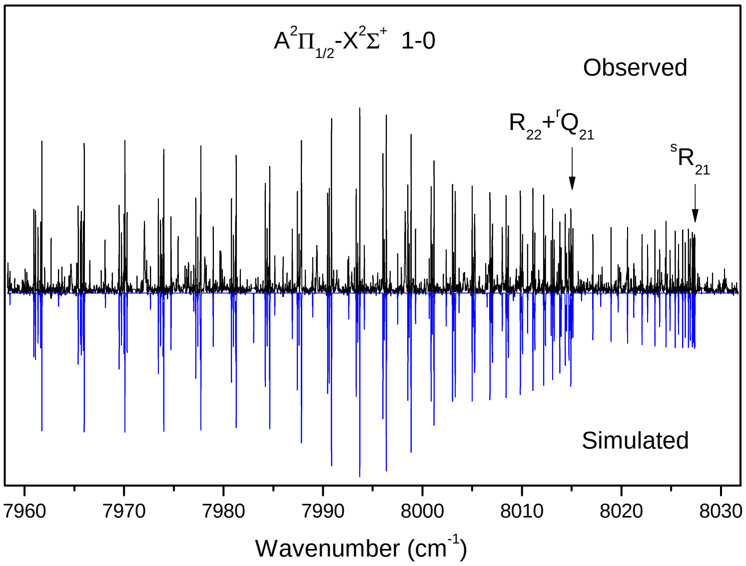

Figure 4.12 – A comparison of a portion of the observed (upper) and simulated (lower) spectra of the $A^2\Pi$-$X^2\Sigma^+$, (1,0) band of CP, showing a good correspondence between the two spectra. Reprinted from JQSRT, 138, Ram et al., Einstein A-values and oscillator strengths of the $A^2\Pi$-$X^2\Sigma^+$ system of CP, 107-115, Copyright (2014), with permission from Elsevier.

4.5, and the new DMF is believed to be more accurate. To validate the calculated relative line intensities, laboratory spectra were simulated and good agreement has been found between observed and calculated spectra.

Previously available CN line lists suffered from some substantial line position uncertainties, and these lists provide more extensive and accurate line positions and intensities. As an example of where such a list line could be used is in large scale surveys such as The Apache Point Observatory Galactic Evolution Experiment (APOGEE; Eisenstein et al. (2011)). This is a high resolution near-infrared spectroscopic study of chemical abundances of around 100,000 red giants. Nitrogen elemental abundances have been calculated using CN $A^2\Pi$-$X^2\Sigma^+$ transitions (Smith et al., 2013), from the APOGEE master line list (M. Shetrone et. al. (submitted)). The line list produced in this work would be very useful if incorporated into such a list, and has the potential to result in different nitrogen abundances being calculated for thousands of stars (Sneden et al., 2014).

CN lines have also been used in calculations of the nitrogen abundance in the Sun, although NH lines and nitrogen atomic lines are given more weight in such calculations

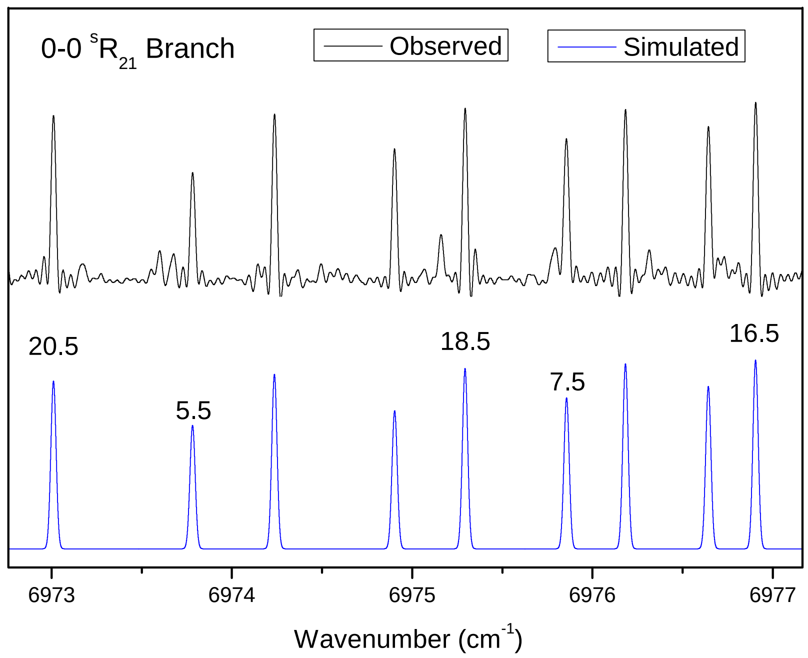

Figure 4.13 – Comparison of the observed (upper) and simulated (lower) spectra of the (0,0), $^sR_{21}$ branch, showing good agreement. Reprinted from JQSRT, 138, Ram et al., Einstein *A*-values and oscillator strengths of the $A^2\Pi$-$X^2\Sigma^+$ system of CP, 107-115, Copyright (2014), with permission from Elsevier.

(Asplund et al., 2009), as CN is only a trace species. Sneden et al. (2014) calculated the nitrogen abundance in the solar photosphere to be log ϵ(N)=8.05 $\big($where log ϵ(x) is the abundance of element x in dex, equal to $\log_{10}$ $(N_x/N_{\text{hydrogen}})$ + 12$\big)$, using only CN transitions, with the line list reported here. Although this is higher than the value of log ϵ(N)=7.83, the abundances obtained were highly consistent using a number of different lines, and some of the difference could be due to the use of a 1D model (Holweger and Mueller, 1974), compared to the more sophisticated 3D model used by Asplund et al. (2009). This suggests that the line list will be of some but limited use for the Sun, but could be very useful for large scale nitrogen abundance analyses when more importance is placed on CN lines, such as the APOGEE study mentioned above.

There does not appear to have been a CP $A^2\Pi$-$X^2\Sigma^+$ line list available previously that contains both rotationally resolved positions and intensities, and one is now available to astronomers investigating phosphorus chemistry.

At the conclusion of the CN and CP work, the calculation methods had been improved as described, to properly take into account the effect of rotation on the vibrational wavefunctions. This means that they could then be applied with more confidence to other molecules, but in particular to molecules that exhibit a strong H-W effect. This was particularly prudent, as the next molecule studied was the NH radical, the light hydrogen atom of which absolutely requires the inclusion the H-W effect for all bands.

Chapter 5

NH $X^3\Sigma^-$ Ground State Rovibrational and Rotational Transitions

5.1 Preface

The next system for which a line list was produced was the ground state vibration-rotation system of NH (another astronomically important molecule), which involves transitions within the $X^3\Sigma^-$ state. The calculation method was not developed further for this work as in the previous chapter, but it still required an adjustment to a $^3\Sigma^-$-$^3\Sigma^-$ system, the first calculation of rotational transitions, and some experimental work at Old Dominion University, Norfolk, VA, USA. The previous inclusion of the H-W effect in the calculation method was absolutely vital for the work, due to the light H atom causing rotation to have a large effect on the vibrational wavefunctions.

5.2 Introduction

NH is an important molecule in the study of astronomical environments, as it is present in cool stars (Lambert and Beer, 1972; Lambert et al., 1984; Smith and Lambert, 1986; Aoki and Tsuji, 1997), comets (Litvak and Kuiper, 1982), diffuse interstellar clouds (Meyer and Roth, 1991; Crawford and Williams, 1997; Goicoechea et al., 2004; Weselak et al., 2009) and the Sun (Roach, 1939; Farmer and Norton, 1989; Grevesse et al., 1990; Geller et al., 1991; Grevesse et al., 2007). It has also been magnetically trapped at temperatures

$<$ 1 K (Campbell et al., 2007; Hoekstra et al., 2007; Campbell et al., 2008; Hummon et al., 2008), and there is potential for trapping (Kajita, 2006; Janssen et al., 2011*a*; Janssen et al., 2011; Janssen et al., 2011*b*) and chemical reactions (Janssen et al., 2013) at ultracold temperatures ($<$ 1 mK) (Kajita, 2006; Wallis and Hutson, 2009; Wallis et al., 2011), applications for which include high precision spectroscopy (Kajita, 2006; Bethlem and Ubachs, 2009) and quantum computing (Demille, 2002). NH is also important in the nitrogen chemistry that occurs in combustion processes (Miller and Bowman, 1989; Smoot et al., 1998), and is a key species in the transformation of N_2 to NH_3 (and vice versa) in stellar and exoplanet atmospheres (Lodders and Fegley, 2002; Moses et al., 2011).

The rovibrational transitions within the $X^3\Sigma^-$ ground state are the focus of this chapter, and their importance is illustrated by the fact that as well being used to calculate NH abundance, they have been used to calculate the total nitrogen abundance in cool stars (Lambert et al., 1984; Lambert et al., 1986; Smith and Lambert, 1986; Aoki and Tsuji, 1997) and the Sun (Grevesse et al., 1990; Asplund et al., 2009). The CN molecule has also been used for this purpose (Asplund et al., 2009) but it is less useful as the spectroscopic knowledge has been less complete, although this situation has recently been improved (Brooke et al., 2014*b*).

The first observations of these transitions were of the 1-0 band by Bernath and Amano in 1982 (Bernath and Amano, 1982). In 1986, Boudjaadar et al. observed the Δv=1 sequence up to the 5-4 band (Boudjaadar et al., 1986), and transitions in these bands were detected for a greater number of N values by Ram et al. (1999), at the National Solar Observatory at Kitt Peak, Arizona. Ram and Bernath reported additional lines in these bands (Ram and Bernath, 2010), and also transitions in the previously unobserved 6-5 band. In 1989, Chackerian et al. (1989) studied the relative intensities of the lines recorded by Boudjaadar et al. (1986).

Pure rotational transitions were first seen by Radford and Litvak (1975), who observed only the N=1-0 transition in the v=0 level. Wayne and Radford then detected more rotational transitions within both v=0 and 1 (1976). van den Heuvel et al. (1982) reported more observations of the v=0, N=1-0 transition, but higher N transitions remained undetected. Solar spectra recorded in space by the ATMOS FTS (Geller et al., 1991) (FTS; part of Spacelab 3 onboard some Space Shuttle flights) provided infrared rotational lines between 600 and 900 cm^{-1}, covering N''=20-35 in v=0, and N''=21-29 in v=1. Similar solar spectra taken by ACE (Bernath et al., 2005; Hase et al., 2010), also from LEO, provided higher N rotational lines; up to N''=42 in v=0. More recent laboratory measurements of lower N rotational transitions have been made for v=0 by Klaus et al. (1997) (N=1-0), Lewen et al. (2004) (N=2-1) and Flores-Mijangos et al. (2004) (up to N=5-4). Robinson et al. (2007) observed transitions up to N=5-4 in v=1, and also for the first time in v=2 (up to N=5-4).

The most recent set of molecular constants for the $X^3\Sigma^-$ state were reported by Ram and Bernath (2010). Their calculations used rovibrational lines from Ram et al. (1999), Geller et al. (1991), Bernath and Amano (1982), spectra from the ACE mission (Hase et al., 2010) and their new 6-5 band observations reported in that paper. They used pure rotational lines from Robinson et al. (2007), Flores-Mijangos et al. (2004), Lewen et al. (2004), Klaus et al. (1997), Geller et al. (1991) and the ATMOS instrument (Geller et al., 1991). They performed a line position fit to provide updated molecular constants for vibrational levels up to v=6.

An experimental average ground state dipole moment, μ_0, of 1.389±0.07 D was obtained in 1974 by Scarl and Dalby. They compared it to theoretical dipole moments available at the time, which varied widely between 0.36 and 2.17 D. Dipole moments and DMFs have been calculated several times since then using various theoretical methods, and a summary of such studies showing their resulting values of μ_e and μ_0 is shown in Table 5.1. Using μ_e as a comparison, there is still some disagreement between these values, and all of them are somewhat higher than the experimental value of μ_e=1.405±0.077 (Scarl and Dalby, 1974; Chackerian et al., 1989; Muenter, 1975). The difference between the full DMFs is more complicated than this of course (see Section 4.4.3 for an example). Values for μ_e are compared in Table 5.1 as they are readily available in the literature and give an indication of the quality of the calculations. More recent theoretical studies of NH include those of Feller and Sordo (2000) and Temelso et al. (2004), in which high levels of theory were used to calculate potential energy curves and spectroscopic constants, but no DMFs were reported. Currently available line intensities in the JPL (Pickett et al., 1998) and CDMS (Müller et al., 2001, 2005) spectroscopic databases are based on the dipole moment from 1974 of Scarl and Dalby. These line intensities are still being used, for example by Goicoechea et al. (2004). Grevesse et al. (1990) and Asplund et al. (2009) calculated the nitrogen abundance in the Sun (Grevesse et al., 1990; Asplund et al., 2009), and they used the 1975 DMF of Meyer and Rosmus to calculate their own line intensities. Aoki and Tsuji (1997) also used this DMF in their

Table 5.1 – Summary of equilibrium dipole moments, μ_e, and v=0 averaged dipole moments, μ_0, for the $X^3\Sigma^-$ ground state of NH, since 1974. All but Paldus and Li (1996) and the experimental study calculated full dipole moment functions. Our calculated values are also included.

Year	Authors	μ_e (debye)	μ_0 (debye)
1974	Scarl and Dalby (1974) (expt.)	1.405±0.077[a]	1.389±0.075
1974	Das et al. (1974)	1.5353[b]	1.5155[b]
1975	Meyer and Rosmus (1975)	1.578	1.5546[b]
1976	Hay and Dunning (1976)	1.526	...
1987	Goldfield and Kirby (1987)	1.511	1.480
1992	Stallcop et al. (1992)	1.530	...
1992	Cantarella et al. (1992)	1.5054	1.4827
1996	Paldus and Li (1996)	1.536	...
2014	This work	1.5434	1.5246

[a] Calculated by Chackerian et al. (1989); Muenter (1975) using the reported data of Scarl and Dalby (1974)

[b] Calculated by Cantarella et al. (1992) using the reported data of Das et al. (1974) or Meyer and Rosmus (1975)

calculations of N abundance in oxygen-rich giants. A new DMF would be useful to resolve the above discrepancies and calculate a new set of line intensities.

In 2008, Campbell et al. magnetically trapped NH to obtain an accurate experimental vibrational lifetime for v=1 of $37.0 \pm 0.5_{\text{stat}}{}^{+2.0}_{-0.8\text{syst}}$ ms. They found disagreement with the previous values of Dodd et al. (1991), who used the DMF of Goldfield and Kirby (1987) to calculate $A_{10} = 51.7\ \text{s}^{-1}$ ($\tau_{v=1} = 19.3$ ms), and with Rosmus and Werner (1980) who gave $A_{10} = 34.9\ \text{s}^{-1}$ ($\tau_{v=1} = 28.7$ ms). To compare their experimental result to theory, they calculated a new DMF using the MRCI method with an aug-cc-pV6Z basis set. The resulting lifetime of 36.99 ms is an excellent match to their experimental lifetime. They calculated a value of μ_0 of 1.5246 D. The DMF itself was not published, and the purpose of this chapter is to use this DMF and the positions from Ram and Bernath (2010) to create a new line list for the NH $X^3\Sigma^-$ state rovibrational transitions, complete with positions and absolute intensities. The range of the DMF has been extended for this study to 0.6-20 a_0 (0.32-10.6 Å).

5.3 NH $X^3\Sigma^-$ Ground State

As a Σ state has no orbital angular momentum, it has no spin-orbit coupling. The energy levels are therefore arranged in the manner of a Hund's case (b) state. For each N level,

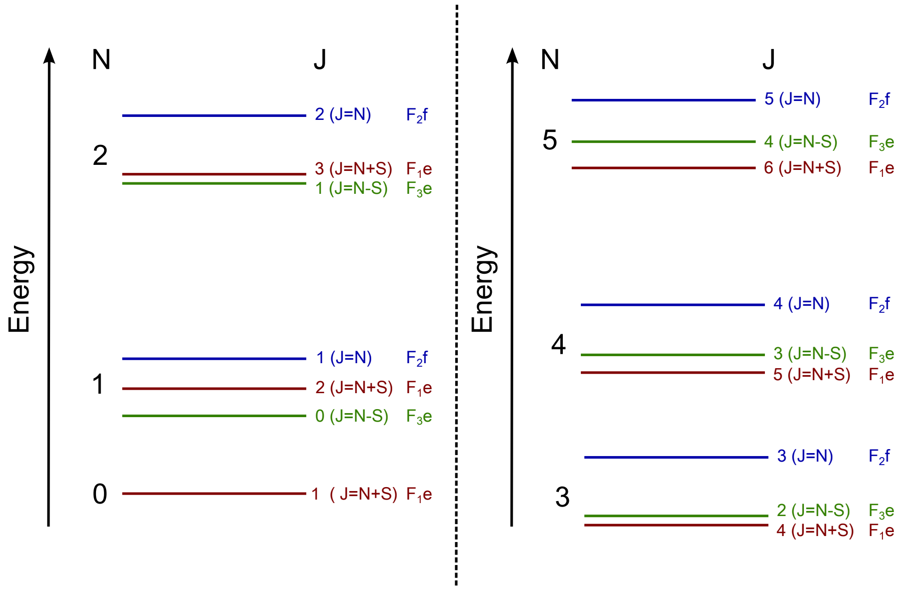

Figure 5.1 – Energy levels of the NH $X^3\Sigma^-$ state. The distribution of F levels within each N level is approximately correct, but the difference between the F levels is greatly exaggerated.

there are three J states, labelled F_1, F_2, and F_3 for the three fine structure levels arising from interaction of the spin angular momentum (S=1) with the nuclear rotational angular momentum. For F_1, N=J-S, for F_2, N=J, and for F_3, N=J+S. The order of the energy levels is shown in Figure 5.1.

For P and R branch transitions (in terms of J), $e \rightarrow e$ and $f \rightarrow f$ transitions are possible, and for the Q branch, $e \rightarrow f$ and $f \rightarrow e$ transitions are possible. This results in ΔN =-3, -1, 1, and 3. The $\Delta N = \pm 3$ transitions are very weak, and as shown above, N is the quantum number that has the main effect on the energy level. Therefore, the main features of the spectrum of one vibrational band are a P and R branch in terms of N. Each P or R branch N transition (except where $N = 0$ in either state) has six J transitions. The three strongest of these have $\Delta J = \Delta N$ and F'=F'', and make up the main triplet. There are then two weaker transitions with $\Delta J = 0$ and $J = N'$ or $J = N''$. Finally, there is one very weak transition where $\Delta J = -\Delta N$, which is between the F_{1e} and F_{3e} components. This is shown in Figure 5.2, using transitions from the $N' = 6$ level as an example.

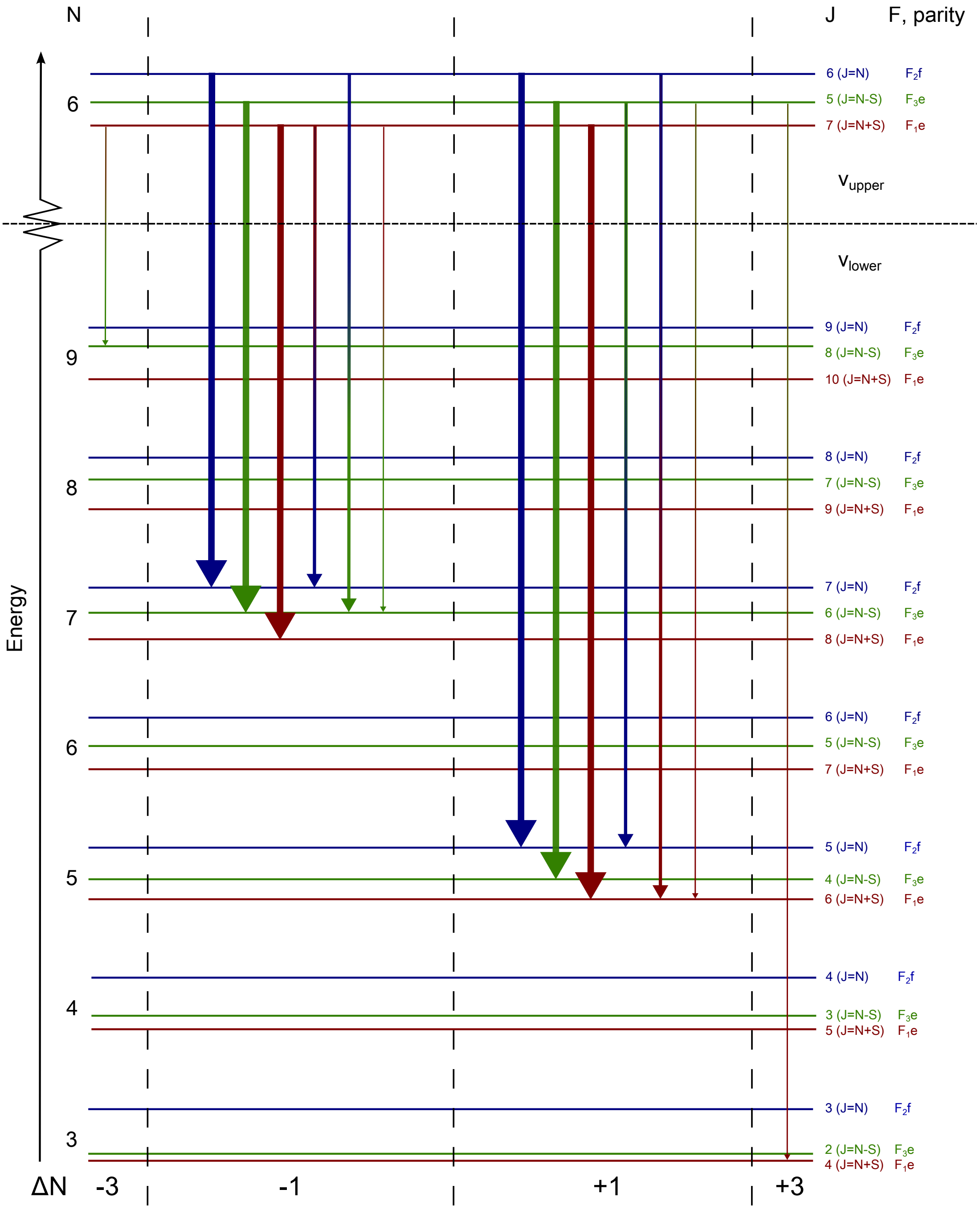

Figure 5.2 – Possible transitions in emission from an N=6 level in the NH X$^3\Sigma^-$ state. The distribution of F levels within each N level is approximately correct, but the difference between the F levels is greatly exaggerated.

Table 5.2 – Equilibrium molecular constants for the NH $X^3\Sigma^-$ state

Constant[a]	Value
ω_e	$3282.220(15)$[b]
$\omega_e x_e$	$78.513(15)$
$\omega_e y_e$	$0.1341(61)$
$\omega_e z_e$	$-0.0066(11)$
$\omega_e \eta_e$	$-0.003141(70)$
B_e	$16.667704(29)$
α_{e_1}	$0.649670(91)$
α_{e_2}	$0.001674(71)$
α_{e_3}	$-0.000067(25)$
α_{e_4}	$-0.0000633(24)$

[a] These constants are the usual power series expansions in v+1/2, with negative signs in front of $\omega_e x_e$ and α_{e_1}.

[b] Numbers in parentheses indicate one standard deviation to the last significant digits of the constants.

5.4 Calculation of line intensities

The general procedure for the calculation of line intensities described in Section 2 was used. The equilibrium constants (as described in Section 2.1.4) calculated from fitting to G_v and B_v values are shown in Table 5.2. The RKR potential energy curve is shown in Figure 5.3. LEVEL was run using $\Lambda = 0$, providing one ME for each possible N transition.

5.4.1 Calculation of the New Dipole Moment Function

The DMF calculation was performed by Gerrit Groenenboom (Radboud University, Nijmegen, The Netherlands) and Marc C. van Hemert (Universiteit Leiden, Leiden, The Netherlands), and was described by Campbell et al. (2008), and it will be briefly explained here.

It was calculated with the ab initio icMRCI method (Werner and Knowles, 1988; Knowles and Werner, 1988), using MOLPRO 2006.1 (Werner et al., 2006), and a large aug-cc-pV6Z one electron basis set (Dunning, 1989; Woon and Dunning, 1995; Wilson et al., 1996) was employed. A large active space of five σ, four π, and one δ orbitals was used to generate reference configurations. In Campbell et al., the DMF used had been calculated for internuclear distances between 1.0 and 3.0 a$_0$ (0.53 to 1.59 Å). In order to be able to accurately calculate MEs for vibrational levels up to v=6 and J=40, this range

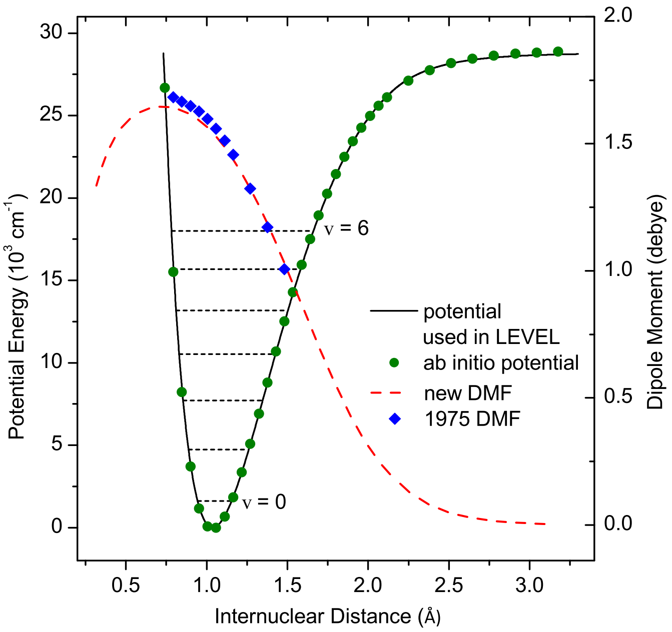

Figure 5.3 – Calculated potential energy curves and DMFs for the $X^3\Sigma^-$ ground state of NH. The black line is the potential used in LEVEL, and the green circles are the ab initio potential (calculated along with the DMF and reported by Campbell et al. (2008)). The red dashed line is the DMF used in this study (reported by Campbell et al. (2008)), and the blue diamonds are the DMF calculated by Meyer and Rosmus (1975). Reprinted with permission from Brooke et al. JCP, 141, 054310, (2014). Copyright 2014, American Institute of Physics.

was later extended to 0.6-20 a_0 (0.32-10.6 Å). The calculated DMF is shown in Table 5.1 (converted from atomic units using 1 D = 0.39343031369 ea_0 and 1 A = 1.88972612 a_0).

This ab initio DMF is believed to be the most accurate DMF available, based on arguments provided by Campbell et al. (2008). In the MRCI calculations, the DMF was used to compute the radiative lifetime of the v=1 vibrational state of NH, and the result was 36.99 ms, in perfect agreement with the experimental value of 37.0±0.5 ms determined in the same study. It was also shown that a DMF computed with another high-level ab initio method, the RCCSD(T) method, gave very similar results and that the dipole moment of the v=0 state computed with the MRCI DMF is in good agreement with the high level ab initio calculation of Paldus and Li (1996).

5.4.2 Hund's case (b) to (a) transformation

The case (b) to case (a) transformation equation is:

$$\begin{aligned}\langle\eta'\Lambda'|T^k_q(J'\Omega'J\Omega)|\eta\Lambda\rangle &= (-1)^{J'-\Omega'}\begin{pmatrix} J' & k & J \\ -\Omega' & q & \Omega\end{pmatrix}^{-1} \\ &\times\sum_{N,N'}(-1)^{N-N'+S+J+k+\Lambda}(2N'+1)(2N+1)\begin{pmatrix} J' & S & N' \\ \Omega' & -\Sigma & -\Lambda'\end{pmatrix}\begin{pmatrix} J & S & N \\ \Omega & -\Sigma & -\Lambda\end{pmatrix} \\ &\times\begin{Bmatrix} N' & J' & S \\ J & N & k\end{Bmatrix}\begin{pmatrix} N' & k & N \\ -\Lambda' & q & \Lambda\end{pmatrix}\langle\eta'\Lambda'|T^k_q(N'N)|\eta\Lambda\rangle,\end{aligned} \tag{5.1}$$

which in this case is:

$$\begin{aligned}\langle\eta'\Lambda'{=}0|T^1_0(J'\Omega'J\Omega)|\eta\Lambda{=}0\rangle &= (-1)^{J'-\Omega'}\begin{pmatrix} J' & 1 & J \\ -\Omega' & 0 & \Omega\end{pmatrix}^{-1} \\ &\times\sum_{N,N'}(-1)^{N-N'+J+2}(2N'+1)(2N+1)\begin{pmatrix} J' & 1 & N' \\ \Omega' & -\Sigma & 0\end{pmatrix}\begin{pmatrix} J & 1 & N \\ \Omega & -\Sigma & 0\end{pmatrix} \\ &\times\begin{Bmatrix} N' & J' & 1 \\ J & N & 1\end{Bmatrix}\begin{pmatrix} N' & 1 & N \\ 0 & 0 & 0\end{pmatrix}\langle\eta'\Lambda'{=}0|T^1_0(N'N)|\eta\Lambda{=}0\rangle.\end{aligned} \tag{5.2}$$

This equation was derived mainly for use with the CN (Brooke et al., 2014*b*) and

CP (Ram et al., 2014) $A^2\Pi$-$X^2\Sigma^+$ transitions, as the upper A state is case (a) for CP and a mixture of (a) and (b) for CN, and therefore transformation from the LEVEL case (b) MEs was obviously important. However, it still has an effect when the involved states are case (b) because of the use of the case (a) basis set by PGOPHER, and so as the transformation was possible, it was also used for the $B^2\Sigma^+$-$X^2\Sigma^+$ transition and the $X^2\Sigma^+$ state rovibrational transitions of CN (Brooke et al., 2014*b*), and it is used in the calculations for NH for the same reason.

For an $X^3\Sigma^-$ state, PGOPHER uses the Hund's case (a) basis states $|\eta\Lambda; S\Sigma; J\Omega{=}{+}1\rangle$, $|\eta\Lambda; S\Sigma; J\Omega{=}0\rangle$ and $|\eta\Lambda; S\Sigma; J\Omega{=}{-}1\rangle$. For the P and R branches (in terms of ΔJ), there are three non-zero MEs between these basis states:
$\langle\eta'\Lambda'; S'\Sigma';\ J'\,\Omega' = +1|T^1_0|\eta\Lambda; S\Sigma; J\Omega = +1\rangle$, $\langle\eta'\Lambda'; S'\Sigma';\ J'\,\Omega' = 0|T^1_0|\eta\Lambda; S\Sigma; J\Omega = 0\rangle$ and $\langle\eta'\Lambda'; S'\Sigma';\ J'\,\Omega' = -1|T^1_0|\eta\Lambda; S\Sigma; J\Omega = -1\rangle$ (except for where J'' or J' are 0). For the Q branch, the non-zero MEs are $\langle\eta'\Lambda'; S'\Sigma';\ J'\,\Omega' = +1|T^1_0|\eta\Lambda; S\Sigma; J\Omega = +1\rangle$ and $\langle\eta'\Lambda'; S'\Sigma';\ J'\,\Omega'{=}{-}1|T^1_0|\eta\Lambda; S\Sigma; J\Omega{=}{-}1\rangle$. $\langle\eta'\Lambda'; S'\Sigma';\ J'\,\Omega'{=}{+}1|T^1_0|\eta\Lambda; S\Sigma; J\Omega{=}{+}1\rangle$ and $\langle\eta'\Lambda'; S'\Sigma';\ J'\,\Omega' = -1|T^1_0|\eta\Lambda; S\Sigma; J\Omega = -1\rangle$ are equal by symmetry, as they are invariant to reversal of the signs of all the projections (Λ=0 and Σ=Ω). Therefore, values must be calculated for five MEs for each lower J level:
$\langle\eta'\Lambda'; S'\Sigma';\ J'\,\Omega' = +1|T^1_0|\eta\Lambda; S\Sigma; J\Omega = +1\rangle$ and $\langle\eta'\Lambda'; S'\Sigma';\ J'\,\Omega' = 0|T^1_0|\eta\Lambda; S\Sigma; J\Omega = 0\rangle$ for both the P and R branches, and $\langle\eta'\Lambda'; S'\Sigma';\ J'\,\Omega'{=}{+}1|T^1_0|\eta\Lambda; S\Sigma; J\Omega{=}{+}1\rangle$ for the Q branch. Values for these MEs for all required rotational transitions were calculated using Equation 5.4.2. The resulting case (a) MEs were set up in PGOPHER, which first transforms these pure Ω MEs into symmetrised case (a) MEs, and then performs the diagonalisation of the Hamiltonian in the symmetrised case (a) basis, resulting in a transformed transition matrix in terms of the true states. This is described in more detail in Section 2.5.7.

The summation part of the equation is over all N'-N'' transitions that are possible for a particular J and Ω transition. For the R branch transitions (except for where J'' or J' are 0), there are four N transitions that contribute to the overall intensity. These are, for example, for the R(6) transition, $N' - N''$ = 6-5, 6-7, 8-7 and 7-6. These are included in the summation part for the calculation of both the $\langle\eta'\Lambda'; S'\Sigma';\ J'\,\Omega'{=}{+}1|T^1_0|\eta\Lambda; S\Sigma; J\Omega{=}{+}1\rangle$ and $\langle\eta'\Lambda'; S'\Sigma';\ J'\,\Omega'{=}0|T^1_0|\eta\Lambda; S\Sigma; J\Omega{=}0\rangle$ MEs. Similarly, there are four N transitions for the P branch $\langle\eta'\Lambda'; S'\Sigma';\ J'\,\Omega'{=}{+}1|T^1_0|\eta\Lambda; S\Sigma; J\Omega{=}{+}1\rangle$ and
$\langle\eta'\Lambda'; S'\Sigma';\ J'\,\Omega'{=}0|T^1_0|\eta\Lambda; S\Sigma; J\Omega{=}0\rangle$ MEs, and four for the Q branch ME.

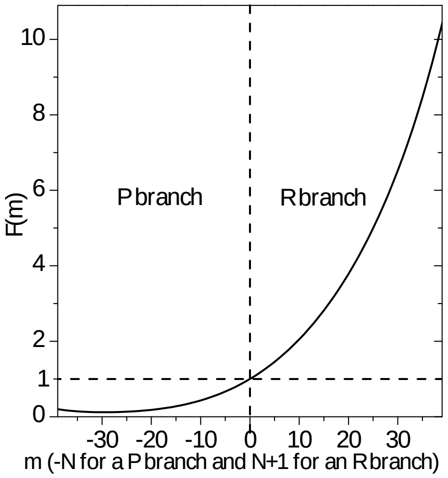

Figure 5.4 – H-W effect for the NH $X^3\Sigma^-$ state (1,0) band. $F(m)$ is equal to the ME divided by the ME for the Q(0) transition.

5.4.3 H-W Effect

As described in Section 2.5.5 and shown in Figure 2.17, the H-W effect is strong for NH due to the light hydrogen atom. Figure 5.4 shows how the MEs for the (1,0) band vary with N, which clearly means that the R branch will be much stronger than the P branch, as seen in the spectra.

5.5 Results and Discussion

5.5.1 New NH FTS Spectrum

To validate the results it is useful to compare the relative intensities of a calculated spectrum with an observed spectrum (recorded at Old Dominion University, Norfolk, VA, USA), as the measurement of absolute intensities is extremely difficult. The H-W effect has a major impact on the spectrum, with a decrease in intensity of the P branches relative to the R branches. To see if the inclusion of the H-W effect has been done correctly, the intensities need to be compared over a large enough wavenumber range to cover both branches. The spectrum observed by Ram and Bernath (2010) would probably suffice for this purpose, but its y-axis had not been calibrated for the instrument response, and so the intensity may drift over the wavenumber range observed.

A new spectrum was recorded at Old Dominion University, Norfolk, VA, USA, with the aim of providing relative intensities that are calibrated across the full wavenumber range. NH was created in a microwave discharge of a mixture of N_2 (0.8 Torr), H_2 (0.3

Torr) and He (0.9 Torr). The emission spectrum was recorded with a Bruker IFS 125 HR FTS, using a CaF_2 beam splitter and a liquid nitrogen cooled InSb detector. Data were recorded between 1800 and 5000 cm^{-1}, limited by the InSb detector and a Ge filter. As intensities but not line positions were important, a relatively low resolution of 0.04 cm^{-1} was used to improve the SNR, and 688 scans were coadded to give the uncalibrated spectrum. Immediately afterwards, the discharge cell was replaced by a 1256 K blackbody, and 144 scans were coadded under the same conditions. The instrument function was corrected for by dividing the NH spectrum by the blackbody spectrum and the baseline was then subtracted to give the final spectrum.

The relevant wavenumber range is shown along with the calculated spectrum in Figure 5.5, and a good match is seen. The calculated spectrum was convolved with a Gaussian function to best match the observed broadening, and rotational and vibrational temperatures of 1800 K and 5000 K, respectively, were found to give the closest match. In the microwave discharge, energy transfer between the excited gases and various vibrational and rotational levels of the NH molecules will occur, resulting in level populations that are not in thermodynamic equilibrium. This means that specifying separate rotational and vibrational temperatures provides only an approximate model for the spectrum. This also explains why the two temperatures are very different, and why, as can be seen in Figures 5.5 and 5.7, the intensity within the R branch decreases more quickly with increasing wavenumber in the calculated spectrum than in the observed spectrum. However, this is not an issue when comparing the H-W effect, as explained in the following section.

5.5.2 Spectral Validation

In checking that the H-W effect has been applied correctly, it is the difference in intensity between the R and P branch that is most important. To quantify this, the observed and calculated intensities in the 1-0 band were compared for as many N' levels as were available in both branches. For each observed N' level, the peak heights of the F_1-F_1, F_2-F_2 and F_3-F_3 lines (where available) were summed for the R and P branches separately, and the R branch total was divided by the P branch total, giving the R/P ratio. The same was done for the calculated spectrum, using exactly the same peaks (the intensities vary with temperature, but the R/P ratio does not). The results are shown in Figure 5.6. The inclusion of the H-W effect is clearly an improvement. This improvement

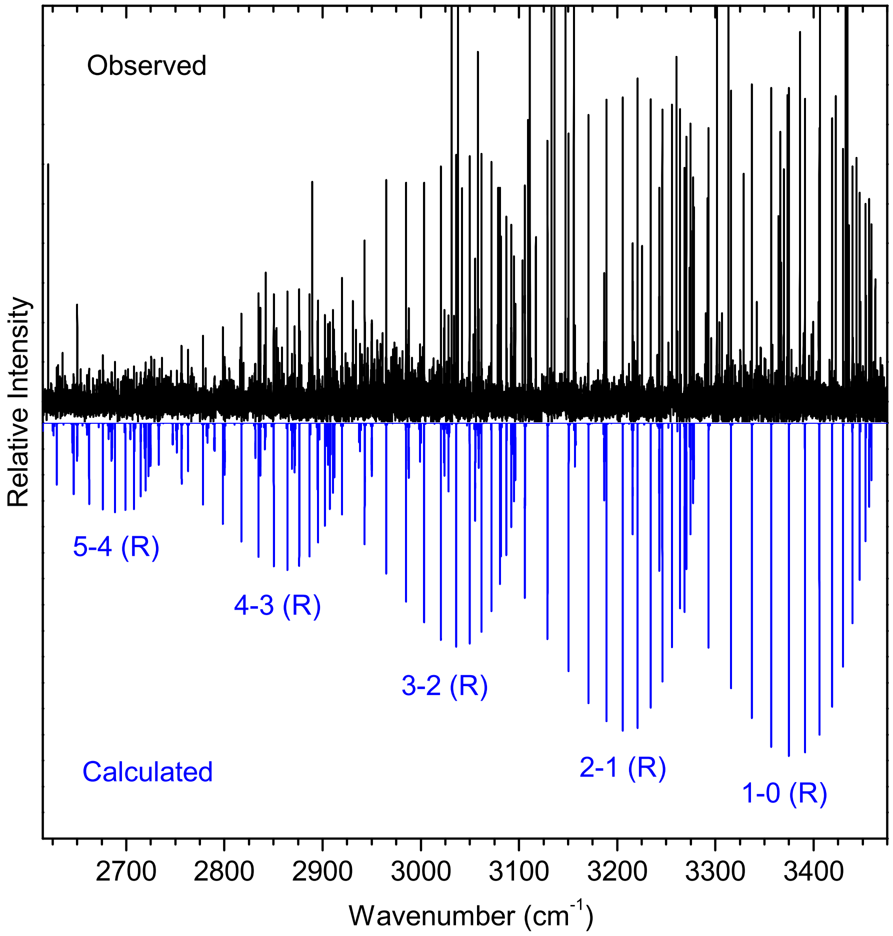

Figure 5.5 – Observed (at Old Dominion University, Norfolk, VA, USA) and calculated spectra of NH. The lines that continue past the top of the y-axis are intense atomic lines. The features that can clearly be seen are the R branches of the 1-0, 2-1, 3-2, 4-3 and 5-4 bands. The calculated spectrum was convolved with a Gaussian function to best match the observed broadening. Effective rotational and vibrational temperatures of 1800 K and 5000 K were used, respectively. Reprinted with permission from Brooke et al. JCP, 141, 054310, (2014). Copyright 2014, American Institute of Physics.

is also seen in Figure 5.7, where the spectrum calculated (using the conditions described in Section 5.5.1) using the H-W effect clearly better matches the difference between R and P branch intensity in the observed spectrum.

Observed intensities were also obtained from Chackerian et al. (1989), who analysed the spectra observed by Boudjaadar et al. (1986). They reported reduced intensities, in the form ln($6.23 \times 10^{23} \times S_{J''}^{\Delta J} I \tilde{\nu}^4$), where $S_{J''}^{\Delta J}$ is the Hönl-London factor, and *I* is the required observed intensity. They described how they calculated their Hönl-London factors, and so values for *I* could be calculated. The resulting R/P ratios are also shown in Figure 5.6.

5.5.3 Lifetimes and Band Strengths

The experimental lifetime of the NH v=1 level of Campbell et al. (2008) of $37.0 \pm 0.5_{\text{stat}}{}^{+2.0}_{-0.8\text{syst}}$ms matches very well with their calculated lifetime of 36.99 ms. Vibrational lifetimes have been calculated using our final Einstein *A* values, by taking the reciprocal of the sum of the Einstein *A* values for all possible transitions from the same N'=0, J'=1 level. This results in a lifetime of 36.77 ms, which compares well to recent values of Campbell et al.. Similarly, lifetimes of 17.09, 10.93, 8.10, 6.57 and 5.71 ms were calculated for v=2-6, respectively.

Einstein $A_{\text{v}'\text{v}}$ values have been calculated for all reported vibrational bands, and the observed Δv=1 sequence values are shown in Table 5.3, where disagreement with those of Dodd et al. (1991) and Rosmus and Werner (1980) is shown. These are calculated by summing over the Einstein *A* values for all possible transitions with N'=1, J'=1, for each band. The Einstein $A_{\text{v}'\text{v}}$ values have also been converted into vibrational band oscillator strengths ($f_{\text{v}'\text{v}}$-values) using Equation 2.131, where $\Lambda' = \Lambda'' = 0$.

Our value for μ_0 of 1.5246 D compares well to the values of the theoretical studies shown in Table 5.1 (μ_e is also shown to enable comparison with all studies). However, it lies just outside the error bounds of the experimental value obtained in 1974 by Scarl and Dalby. As discussed above, our v=1 lifetime shows excellent agreement with the experimental value measured recently by Campbell et al. (2008) using magnetic trapping. Scarl and Dalby determined μ_0 from the Stark shift in the $A^3\Pi$-$X^3\Sigma^-$ transition, assuming that μ_0(A) = 1.3 D. μ_0(A) was calculated here at the same level of theory as the ground state, and a value of 1.412 D was found. If we adapt Equation 10 of the Scarl and Dalby paper by replacing 2.80±0.13 in the numerator by $2.80 \times (1.412/1.3)^2$, μ_0(X) is found to be equal to 1.38...1.52 D, where the upper limit agrees with the ab initio value calculated

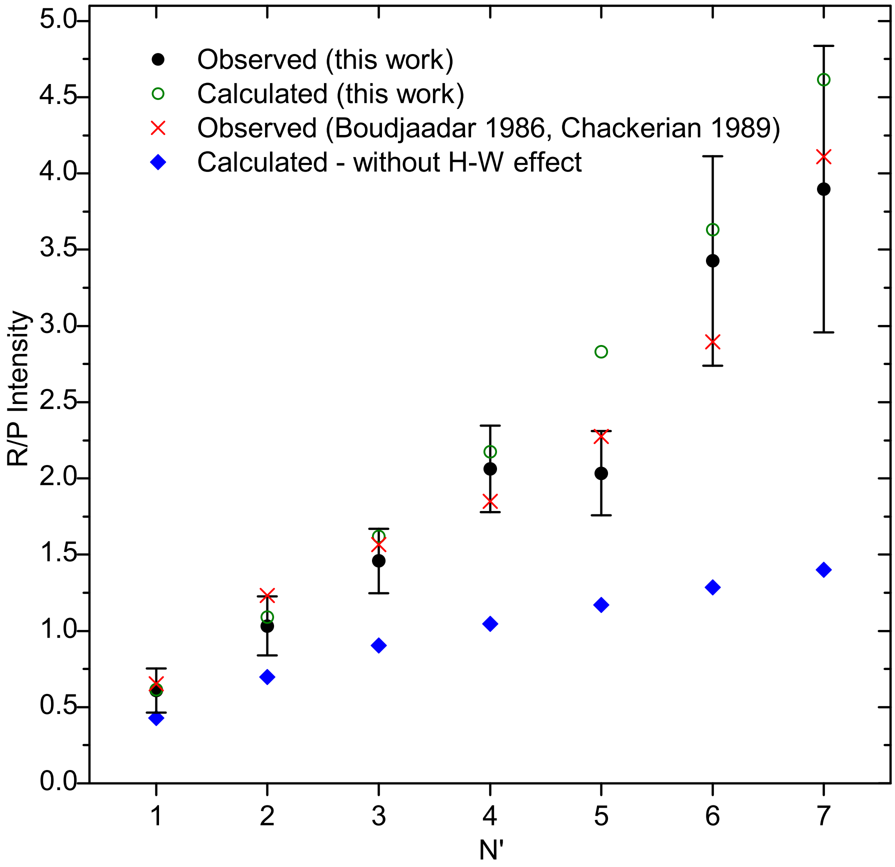

Figure 5.6 – Ratio of P and R branch relative intensities for the new experimental spectrum (recorded at Old Dominion University, Norfolk, VA, USA), the calculated spectrum, the spectrum observed by Boudjaadar et al. (1986) and analysed by Chackerian et al. (1989), and the calculated spectrum without the inclusion of the H-W effect. The error bars are large for the higher N' values due to the low signal to noise ratio observed in the P branch. A good match is seen between both sets of observed values and the calculated values including the H-W effect, except for N'=5 from the spectrum observed in this work. This could be due to a line overlapping the $^{\mathrm{P}}\mathrm{P}_3(6)$ line as this appears more intense than expected. Reprinted with permission from Brooke et al. JCP, 141, 054310, (2014). Copyright 2014, American Institute of Physics.

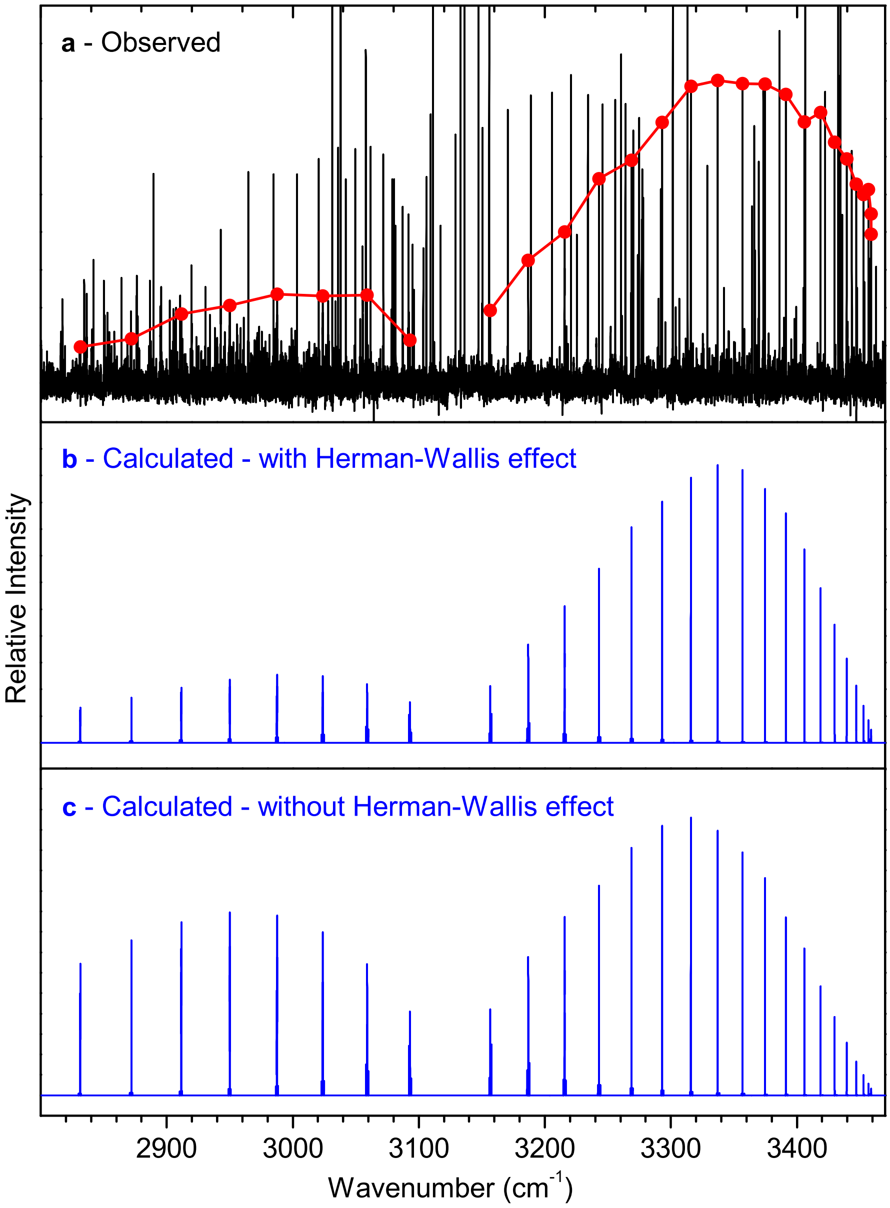

Figure 5.7 – Observed and calculated IR spectra of NH. a - FTS spectrum obtained at Old Dominion University, Norfolk, VA. The red line and dots indicate the intensity of the 1-0 band P branch (left) and R branch (right). The lines that continue past the top of the y axis are intense atomic lines. The R branches of the 2-1, 3-2, and 4-3 bands are the other features that are clearly visible here. b and c - Calculated spectra of the NH 1-0 band only, with and without the inclusion of the H-W effect. Its inclusion gives a better relative intensity difference between the P and R branches. The calculated spectrum was convolved with a Gaussian function to best match the observed broadening. A rotational temperature of 1300 K was used. Reprinted with permission from Brooke et al. JCP, 141, 054310, (2014). Copyright 2014, American Institute of Physics.

Table 5.3 – Einstein $A_{\mathrm{v}'\mathrm{v}}$ and $f_{\mathrm{v}'\mathrm{v}}$ values for vibrational transitions within the X$^3\Sigma^-$ state of NH, where Δv=1

	Einstein $A_{\mathrm{v}'\mathrm{v}}$ (s^{-1})				
	Ours	D[a]	R&W[b]	M&R[c]	$f_{\mathrm{v}'\mathrm{v}}$
1-0	27.19	51.7	34.9	31.69	3.941(-6)[d]
2-1	57.91	92.3		69.18	9.349(-6)
3-2	90.14	144.4		108.12	1.632(-5)
4-3	121.40			144.49	2.481(-5)
5-4	148.70			173.94	3.461(-5)
6-5	168.92			191.70	4.527(-5)

[a] Dodd et al. (1991)

[b] Rosmus and Werner (1980)

[c] Our calculations repeated using the 1975 DMF of Meyer and Rosmus (1975)

[d] Numbers in parentheses indicate the exponent.

in this work.

In 1989, Chackerian et al. measured the Herman-Wallis effect from an observed spectrum and used this along with the value of μ_0 from Scarl and Dalby in their calculations of the matrix element $\langle$v=1$|\mu|$v=0$\rangle$. If, in their Equation 3, all of the terms are replaced by our values (μ_0=1.52456, ω_e and B_e from Table 5.2, and C_0^1=0.07895), the result is 0.0559 D, which shows a much better match to our ab initio value of 0.05615 D.

5.5.4 Calculations With the 1975 Meyer and Rosmus Dipole Moment Function

As the Meyer and Rosmus DMF from 1975 has previously been used to calculate NH rovibrational line intensities, the full set of calculations described in this chapter were also performed with this DMF as a test. The resulting Einstein $A_{\mathrm{v}'\mathrm{v}}$ values can be seen in Table 5.3. This shows that even though the values of μ_e of the new DMF and the 1975 DMF only disagree by ~3.5%, the differences between the full DMFs and the amount of extrapolation necessary cause the resulting line intensities to disagree by a much greater percentage. The two DMFs are shown in Figure 5.3.

5.6 Conclusion

Discrepancies have previously been seen in NH line strengths (see Sections 5.2 and 5.5.3), and with the aim of helping to resolve them, a new DMF for the X$^3\Sigma^-$ state of NH has been reported that is believed to be the most accurate to date. It has been used along with the data of Ram and Bernath (2010) to calculate a new line list of rotational and rovibrational transitions, including line positions and intensities in the form of Einstein *A* values and *f*-values, taking the H-W effect into account.

The NH line list could also provide another method of improving or further validating the value for nitrogen abundance in the Sun. Before 2001 (Allende Prieto et al., 2001), the recommended nitrogen abundance in the solar photosphere was log ϵ(N)=8.05 (Anders and Grevesse, 1989), where log ϵ(x) is the abundance of element x in dex, equal to $\log_{10}$ ($N_x/N_{hydrogen}$) + 12, but this has recently been revised downward to 7.83 (Asplund et al., 2009). This value was calculated using N_I, NH, and CN lines, and could be reevaluated using the updated NH line strengths. A small change would be observed, due to the differences shown in Table 5.3. This line list will also be useful for the study of NH in other astronomical environments, cold and ultracold molecular systems, and in the nitrogen chemistry of combustion. To ensure that the NH line list is likely to be used by other groups in the future, it is likely that it will be included in the next edition of the HITRAN database.

This work was expected to be the last line list based chapter of this thesis. The work on OH that follows was initially considered to be a small extra project, that used the same methods as used in this chapter, but slightly adjusted for a different electronic state. However, an extensive investigation into intensity discrepancies had to be performed, which resulted in a change to the transformation equation. This means that ultimately, the intensities obtained in this chapter will need to be recalculated, which will be the subject of a future short publication. This could also be done for the CN intensities, but there the change is mostly negligible due to the much smaller H-W effect.

Chapter 6

The OH $X^2\Pi$ Rovibrational Transitions

6.1 Preface

The OH ground state rovibrational transitions are discussed in this chapter, which is the final line list based chapter in this thesis. It was initially expected to be a short project that was not to be included in the thesis, with no changes to the calculation method and no new molecular constant fit. However, some new observations were discovered, and more importantly, a change in the transformation equation was required to give a good match to observed intensity ratios. This meant that it became a larger project, and the results were relevant to the previous chapters. Also, OH is arguably the most important molecule discussed in this thesis, due to its presence in astronomical environments and role in the Earth's atmosphere. Because of the above, the work described in this chapter is ongoing, and a brief description of the study and an analysis of the initial results is presented here.

6.2 Introduction

The OH radical is very important in atmospheric chemistry due to its high reactivity with volatile organic compounds (Atkinson and Arey, 2003; Lelieveld et al., 2004), and it is the major oxidising species in the lower atmosphere (Prinn et al., 1995). OH is also produced in the upper atmosphere in excited vibrational levels, and near infra-red emission to lower levels is the main cause of the nighttime airglow of the upper atmosphere (Meinel, 1950; Oliva and Origlia, 1992). This airglow is often an unwanted feature in astronomical observations (Maihara et al., 1993), but has sometimes been used for wavelength calibration (Oliva and Origlia, 1992) and atmospheric temperature retrievals (Sivjee and Hamwey, 1987). OH is also present in stars (Wilson et al., 1972), interstellar clouds (Heiles, 1968), extra-terrestrial atmospheres (Piccioni et al., 2008; Atreya and Gu, 1994), and often in relatively large concentrations (Settersten et al., 2003) in flames (Maillard et al., 1976; Ewart and O'Leary, 1986; Abrams et al., 1994).

The transitions of interest in this work are in the Meinel system, which are the rovibrational transitions within the $X^2\Pi$ ground state. These have been used to calculate the oxygen abundance in the Sun (Grevesse et al., 1984) and other stars, for example by Meléndez and Barbuy (2002) and Smith et al. (2013).

There have been several ab initio DMFs calculated for the OH ground state (Stevens et al., 1974; Langhoff et al., 1986; Langhoff et al., 1989; van der Loo and Groenenboom, 2008). Accurate experimental dipole moments were obtained for the v=0, 1, and 2 levels by Peterson et al. (1984), and these were used by Nelson et al. (1989; 1990) in combination with their own experimental line intensities to calculate an experimental DMF at internuclear distances between 0.70 and 1.76 Å. Another experimental DMF was obtained by Turnbull and Lowe (1988), also using the Peterson et al. values and their own experimental intensities. The various DMFs have all disagreed to some extent (Nelson et al., 1990) (also see Figure 6.1), including around the equilibrium internuclear distance (r_e), which is where the DMF peaks.

A list of transition probabilities was calculated by Mies (1974), and more recently Goldman et al. (1998) produced a list of Einstein A values, which is now the most widely used, for example by Meléndez and Barbuy (2002). This list by Goldman et al. is currently in the HITRAN database (Rothman et al., 2013), and the intensities are based on the DMF of Nelson et al. (1990) between 0.70 and 1.76 Å, and that of Langhoff et al. (1989) at other distances. Another line list including Einstein $A_{J'F'JF}$ values was calculated recently (van der Loo and Groenenboom, 2008), however it did not cover all of the available vibrational levels, the accuracy of the line positions compared to experiment can be improved, and the DMF calculated used the relatively small aug-cc-pVQZ basis set. This DMF is included in the comparisons in Figure 6.1

The OH $X^2\Pi$ state has both large A_v (around 140 cm^{-1}) and B_v (around 18 cm^{-1} at low v) values. This means that it is reasonably well described by Hund's case (a)

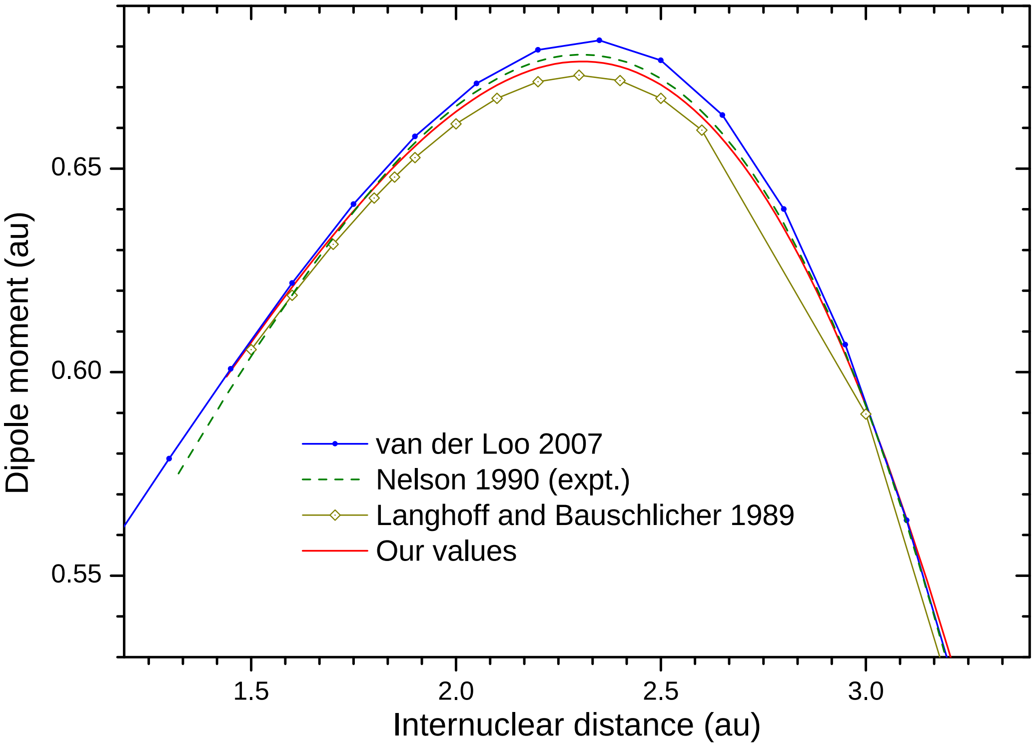

Figure 6.1 – Calculated and experimental dipole moment functions for the OH $X^2\Pi$ state.

at very low J, and the state quickly becomes closer to case (b) as J increases. The resulting spectrum of a vibrational band consists of strong ${}^{r}R_{11}$, ${}^{r}R_{22}$, ${}^{p}P_{11}$, ${}^{p}P_{22}$, ${}^{q}Q_{11}$, ${}^{q}Q_{22}$ branches. The P and R branch lines that cross spin components are extremely weak. The lines of the same branch (in terms of J only), but between different spin components clearly appear as doublets (except at very low J), with the F_{11} lines being stronger than the F_{22} lines. All of these lines are split into further doublets due to the two possible parity transitions.

6.3 Initial Calculations

A new fit of molecular constants was performed using the data of Bernath and Colin (2009), who in turn used data from several previous studies (Melen et al., 1995; Farmer and Norton, 1989; Colin et al., 2002; Abrams et al., 1994, 1996) for rovibrational bands with v up to a maximum of 13, and pure rotational transitions up to v=4. New pure rotational data from Martin-Drumel et al. (2011) was included in the fit, as it has a higher accuracy than the previously available lines. The same molecular constants as calculated

Table 6.1 – Calculated and experimental lifetimes of the OH $X^2\Pi$, v=1, J=1.5, F_1 level (all values in ms).

DMF	Reported by Authors	Calculated with our methods, potential, and line positions
van de Meerakker et al. (2005)	59 ± 2	...
van der Loo and Groenenboom (2008)	56.84	56.97
Nelson et al. (1990)	62.8	56.6
Langhoff et al. (1989)	73.3	66.7
HITRAN 2004 (Rothman et al., 2005)	56.6 ± 10-20%	56.6
This work	...	65.36

by Bernath and Colin were used, and the constants that were fixed in their fits were also fixed here.

A new DMF was calculated by Gang Li (Harvard-Smithsonian Center for Astrophysics) using MOLPRO 2012.1 (Werner et al., 2012), with the averaged coupled-pair functional (ACPF) method and the aug-cc-pV6Z basis set. This followed a complete active space self-consistent field (CASSCF) calculation using an active space of four σ, four π, and one δ orbital. All core correlation was included. A comparison of this new dipole moment and three previous DMFs is shown in Figure 6.1.

6.4 Initial Data Analysis

Validation of the new DMF was performed by comparing results to the experimental dipole moments of Peterson et al. (1984), and an experimental lifetime obtained recently by van de Meerakker et al. (2005). The dipole moments (Figure 6.2) show a better match to those of Peterson et al. than the other DMFs, except for that of Nelson et al., which is expected as it is partly based on these experimental measurements. Unfortunately, the calculated lifetime does not fall within the error bounds of the recent experimental measurement (Table 6.1).

The calculated Einstein $A_{J'F'JF}$ values were compared to those of HITRAN, and the comparison is shown in Figure 6.3, with HITRAN intensity units on the x-axis. The results are expected to be different, however the disparities seen in Figure 6.3 are clearly greater than would be expected. The intensities for the lines that have been observed do compare reasonably well, and so a further comparison (Figure 6.4) was performed by removing the less important lines that cross spin components. An improvement is seen, but the differences are still greater than expected. This and the discrepancy in the lifetime

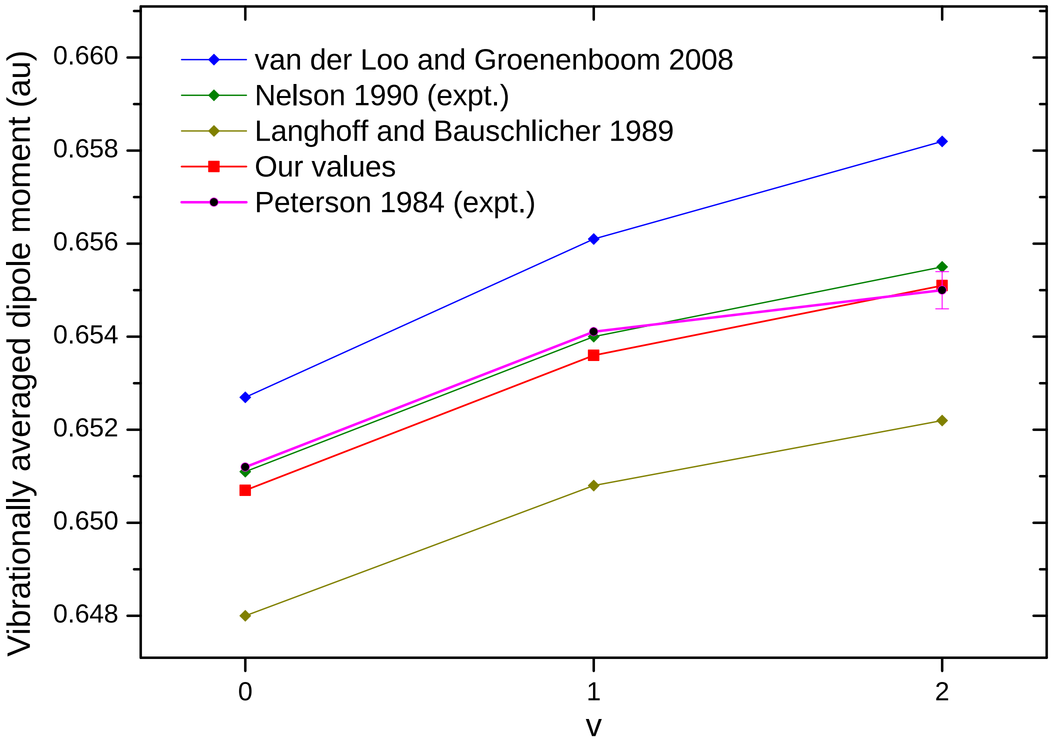

Figure 6.2 – Calculated and experimental μ_v values of OH ($X^2\Pi$). The error bars of the experimental values for v=0 and v=1 are not shown as they are slightly smaller than the size of the symbols.

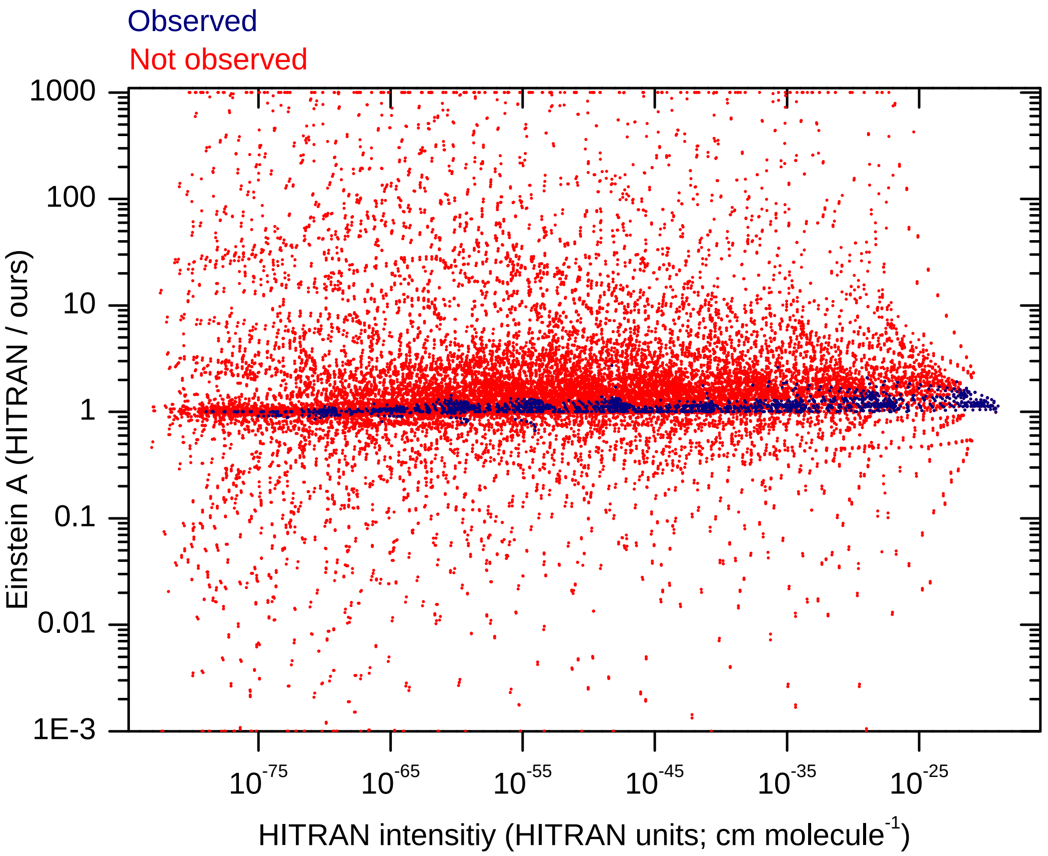

Figure 6.3 – Ratio of Einstein $A_{J'F'JF}$ values calculated in this work to those in HITRAN. Intensities for lines that have been observed are shown in blue, while non-observed lines are in red.

prompted a thorough investigation into the calculation of the intensities.

6.5 Intensity Investigation

A worthwhile test of the calculations is to perform them using the molecular constants, potential, and DMF used for HITRAN by Goldman et al. (1998), to attempt to replicate their intensities using the methods described in this thesis. A DMF that was effectively equivalent to that used by Goldman et al. (1998) was constructed (hereafter referred to as the HITRAN DMF), and their molecular constants and potential were obtained. The results of these calculations did not match the HITRAN intensities, but the differences were systematic, and depended on the branch that is considered. For example, the intensities are slightly too high for the $^{r}R_{11}$ branch, and too low by a similar amount for the $^{r}R_{22}$ branch. A similar but opposite effect was seen in for the ^{p}P branches, but the ^{q}Q branches matched almost perfectly. All transitions that crossed spin components showed

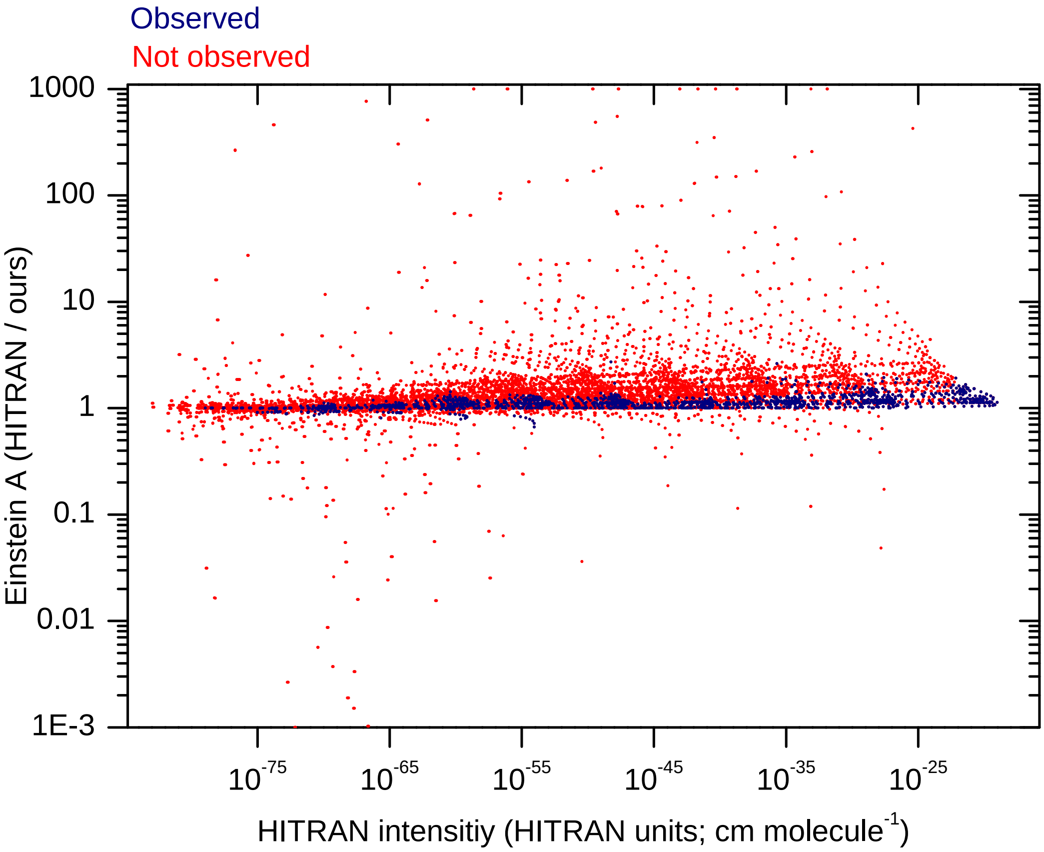

Figure 6.4 – Ratio of Einstein $A_{J'F'JF}$ values calculated in this work to those in HITRAN. Intensities for lines that have been observed are shown in blue, while non-observed lines are in red. Only transitions with F'=F'' are present.

similar systematic differences, but the discrepancies were larger. These effects were reproduced in all of the analysed vibrational bands. An equivalent test was performed by using the data from van der Loo and Groenenboom (2008) and attempting to replicate their intensities. Similar systematic differences were found, which can be described as a difference in the distribution of intensity between F transitions for the same J transition.

The calculated intensities were compared to an experimental FTS spectrum from Abrams et al. (1994). This spectrum was recorded at the Kitt Peak National Observatory, Arizona, by observing OH emission from an ozone flame, and the SNR was excellent. The y-axis was calibrated using a lamp spectrum that was recorded using the same equipment. The strongest and cleanest OH lines were found to be in the $\Delta \mathrm{v} = 2$ region, and the (2,0) band was chosen for analysis. As was done for NH (Section 5.5.2), the strong H-W effect present in OH was exploited for a relative intensity comparison. This is extremely useful as all effects from energy level population are cancelled in the results. This includes the effects from rotational, vibrational and spin temperatures, and the partition function. An equivalent figure to the NH figure (5.6) was produced (Figure 6.5a).

Figure 6.5a shows that the new results are closer to the observed values than those of HITRAN. However, an important feature to observe in these graphs is the "splitting" of the solid (F_{11} transitions) and dotted (F_{22} transitions) lines of the same colour. This splitting is affected by the distribution of intensity between the F_{11} and F_{22} transitions, which was causing the differences described above between these and the HITRAN calculations. In Figure 6.5a, the splitting of the red lines clearly does not match the observed lines. The splitting of the HITRAN lines matches the observed splitting well, but the lines are displaced upwards on the graph from the observed lines. This displacement of lines upwards on the graph can be caused by a change in the DMF, as can be seen in Figure 6.5b, in which the calculations of the red lines use the HITRAN DMF. The major effect of changing the DMF between Figures 6.5a and 6.5b is a displacement upwards of the red lines, and the splitting is still too large compared to the observed and HITRAN values.

A further attempt was made to replicate the HITRAN results by using their data with the N only method (Section 2.5.6). The results of this are shown in Figure 6.5d, and it is seen that the values are closer than with the use of the transformation equation. Using the N only method with the new DMF gives the values in Figure 6.5c, which is clearly a

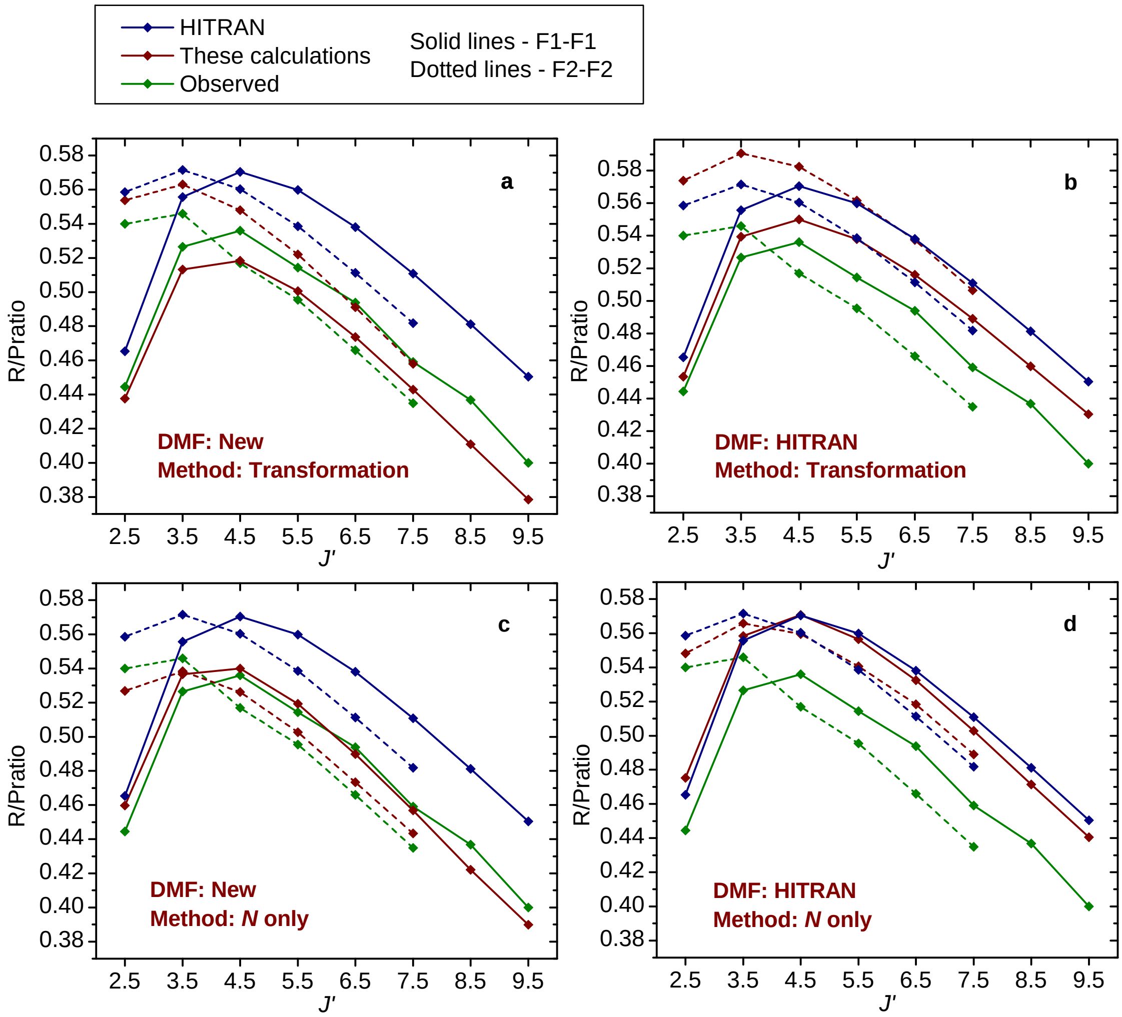

Figure 6.5 – H-W effect in the OH $X^2\Pi$, (2,0) band. The values plotted are equal to the R branch intensity divided by the P branch intensity for specified F transitions that share an upper level. The observed (green) and HITRAN (blue) lines are the same on each graph, and are present for the purpose of comparison with our calculations using four different methods (red lines). The red lines on the top row are calculated using the transformation method, and those on the bottom use the N only method. The red lines on the left use the newly calculated DMF, and those on the right use the HITRAN DMF.

better match to the observed values than with the transformation method.

6.6 Hund's Case (b) and Adjusted Transformation Methods

To attempt to resolve this issue, various tests were performed, including performing all of the calculations in a Hund's case (b) basis. This involved transforming the Hamiltonian matrix so that it was in a case (b) basis, and using Equation 2.5.4 to generate transition matrices from the LEVEL MEs, then transforming the transition matrix as before (Section 2.5.7). Using this new method and the HITRAN DMF, the HITRAN Einstein $A_{J'F'JF}$ values were replicated almost exactly. Therefore, it appears that the transformation equation is causing small inaccuracies in the intensities. The transformation equation was adjusted and the changes were described in Section 2.5.4, but they are repeated here for clarity.

The transformation equation is

$$\begin{aligned}\langle\eta'\Lambda'|T_q^k(J'\Omega'J\Omega)|\eta\Lambda\rangle &= (-1)^{J'-\Omega'}\begin{pmatrix} J' & k & J \\ -\Omega' & q & \Omega \end{pmatrix}^{-1} \\ &\times \sum_{N,N'}(-1)^{N-N'+S+J+k+\Lambda}(2N'+1)(2N+1)\begin{pmatrix} J' & S & N' \\ \Omega' & -\Sigma & -\Lambda' \end{pmatrix}\begin{pmatrix} J & S & N \\ \Omega & -\Sigma & -\Lambda \end{pmatrix} \\ &\times \begin{Bmatrix} N' & J' & S \\ J & N & k \end{Bmatrix}\begin{pmatrix} N' & k & N \\ -\Lambda' & q & \Lambda \end{pmatrix}\langle\eta'\Lambda'|T_q^k(N'N)|\eta\Lambda\rangle. \end{aligned} \tag{6.1}$$

In the derivation, the assumption was made that $\Delta\Sigma = 0$. This removed the sum over q that was present in Equation 2.5.4, and also made the Σ term in the second 3-j symbol equal to Σ'' as opposed to Σ'. If this assumption is not made, S and Σ can be retained in

Table 6.2 – Left - Symmetrised *e* transition matrix for the (2,0), R(1.5) example transition level with original transformation equation. Right - including $\Delta\Sigma \neq 0$ MEs.

	$\lvert{}^2\Pi_{(1.5)}(e/f)\rangle$	$\lvert{}^2\Pi_{(0.5)}(e/f)\rangle$
$\lvert{}^2\Pi_{(1.5)}(e/f)\rangle$	-0.01157	0
$\lvert{}^2\Pi_{(0.5)}(e/f)\rangle$	0	-0.01418

	$\lvert{}^2\Pi_{(1.5)}(e/f)\rangle$	$\lvert{}^2\Pi_{(0.5)}(e/f)\rangle$
$\lvert{}^2\Pi_{(1.5)}(e/f)\rangle$	-0.01157	-0.0002774
$\lvert{}^2\Pi_{(0.5)}(e/f)\rangle$	-0.0001114	-0.01418

the case (a) ME, and the transformation equation can be rewritten as

$$\begin{aligned}\langle\eta'\Lambda';S'\Sigma'|T_q^k(J'J)|\eta\Lambda;S\Sigma\rangle &= (-1)^{J'-\Omega'}\begin{pmatrix} J' & k & J \\ -\Omega' & \Omega'-\Omega & \Omega\end{pmatrix}^{-1} \\ &\times\sum_{N,N'}(-1)^{N'-N+\Omega'-\Omega+S+J+\Lambda'+k}(2N'+1)(2N+1)\begin{pmatrix} J' & S & N' \\ \Omega' & -\Sigma' & -\Lambda'\end{pmatrix}\begin{pmatrix} J & S & N \\ \Omega & -\Sigma & -\Lambda\end{pmatrix} \\ &\times\begin{Bmatrix} N' & J' & S \\ J & N & k\end{Bmatrix}\begin{pmatrix} N' & k & N \\ -\Lambda' & \Lambda'-\Lambda & \Lambda\end{pmatrix}\langle\eta'\Lambda'|T_q^k(N'N)|\eta\Lambda\rangle.\end{aligned} \tag{6.2}$$

If this modified transformation equation is used, very small off-diagonal MEs are present in the transition matrix. For example, for the (2,0), R(1.5) transition, the transition matrix changes from that on the left, to that on the right of Table 6.2 The Einstein $A_{J'F'JF}$ values calculated using this new method and the HITRAN data also match the HITRAN Einstein $A_{J'F'JF}$ values, and the splitting of intensity between spin-components shows a better match with the observed data. However, the calculated lifetime remains the same as when using the original transformation equation (65.36 ms).

6.7 Conclusion

The initial results of the OH study have shown that it is likely that more accurate intensities are obtained by removing the $\Delta\Sigma = 0$ assumption made in the derivation of the transformation equation. Of the three pieces of experimental data that the initially calculated OH intensities have been compared to, the H-W effect and dipole moments show a very good match, but the calculated lifetime (65.36 ms) of the v=1 level does not match within the experimental error bars (59±2 ms). This experimental lifetime was obtained by magnetic trapping of OH radicals, and by measuring the temporal decay of the population of the X$^2\Pi$, v=1, J=1.5, F_1 level (van de Meerakker et al., 2005), and this is expected to be a high quality measurement. As there have been various DMF calculations that have all shown discrepancies, the error is likely to be in the DMF. The next stage in this OH work is to fit a DMF to the three types of experimental data mentioned above. Due to time constraints, so far the H-W effect has only been extracted from the observed spectrum for the (2,0) band, but more bands are available and will be included in this fit. The resulting line list should be the most accurate available for the OH Meinel system, in terms of positions and intensities, and is likely to be included in the next iteration of the HITRAN database.

A line list will ultimately be produced, that includes transitions for v up to 13, and J up to between 9.5 and 59.5, depending on the band. It will be useful in the areas of atmospheric chemistry, combustion science, and astronomy. Oxygen is the third most abundant element in the universe, after hydrogen and helium, and knowledge of its abundance is important in understanding stellar and galactic evolution (Asplund et al., 2009). After the comprehensive summary of elemental abundance in the solar photosphere by Anders and Grevesse (1989), the recommended solar oxygen abundance was log ϵ(O)=8.93. This was significantly revised downwards in 2001 (Allende Prieto et al.) to log ϵ(O)=8.69±0.05. Several other studies have suggested similar values (Caffau et al., 2008; Scott et al., 2009), and a recent review by Asplund et al. (2009) also suggested log ϵ(O)=8.69±0.05.

OH rovibrational and rotational lines have been used to calculate solar oxygen abundances previously (Grevesse et al., 1984; Sauval et al., 1984; Meléndez, 2004; Asplund et al., 2004), and the recent value suggested by Asplund et al. (2009) is an averaged result obtained using OH rovibrational and rotational lines, and O atomic transitions. A paper describing the OH vibration-rotation line part has not yet been published, but the absolute intensities used are most likely to have been those from HITRAN. It would be helpful for these calculations to be repeated with the new line list discussed here, to improve the reliability of the solar oxygen abundance.

A preliminary line list has been produced using the method described in the first paragraph of this section, and calculations using the new intensities of the Δv=2 transitions have been performed, in which the oxygen abundance in the solar photosphere and five other stars was obtained (Table 6.3). An abundance of log ϵ(O) = 8.72 was obtained for the solar photosphere, which is in excellent agreement with the recommended value, and is closer than that previously calculated using the OH Δv=2

Table 6.3 – Stellar Model Parameters and Abundance Summary

Star	T_{eff} K	log ϵ(O) lit.	log ϵ(O) OH
Sun	5780	8.69 ± 0.05[c]	8.72
Arcturus	4286	8.76 ± 0.17[d]	8.68
HIP54048	5100	8.60[e]	8.59
M67[a]	4623	...	8.74
M71[b]	4314	...	8.44
HD122563	4600	6.73[f]	6.71

[a] star 2M08490674+1129529 in open cluster M67
[b] star 2M19533986+1843530 in globular cluster M71
[c] Asplund et al. (2009)
[d] Ramírez and Allende Prieto (2011)
[e] Afşar et al. (2012)
[f] Sneden et al. (2014)

transitions (Meléndez, 2004). Similarly good matches to literature data were obtained for Arcturus , HIP54048, and HD122563, and new oxygen abundances were calculated for two stars in the M67 and M71 clusters. These calculations were performed using a 1D solar model (Holweger and Mueller, 1974) and only OH Δv=2 transitions, and so they are not likely to be as accurate as the literature values, and the agreement shown is good evidence for the reliability of the new intensities.

The infrared OH transitions discussed here are used in the large-scale red giant APOGEE study (Eisenstein et al., 2011; first mentioned in Section 4.7). They are favoured here as opposed to atomic oxygen lines because the stars are cooler than the Sun, which means that OH concentrations will be relatively higher, and the intensity of infrared radiation emitted by the stars will be higher. This project is currently using the HITRAN intensities, and incorporation of the new intensities into the line list for projects such as this would provide more reliable oxygen abundances.

This concludes the diatomic molecular line intensity section of this thesis. The next chapter describes a different project, which is still connected to the general theme through the use of spectroscopic line intensities.

Chapter 7

IRDAS

7.1 Preface

The work in this chapter departs from the main theme of this thesis, but is still connected through the subject of spectroscopic line intensities. It describes IRDAS-EXP (InfRared long range Differential Absorption experiment for trace gas measurementS - EXPeriment), a ground based demonstration of a potential future satellite mission, funded by ESA (European Space Agency). The IR part of the satellite mission would be aimed at measuring greenhouse gas concentrations in the atmosphere, and this demonstration measured carbon dioxide concentrations along a 144 km path between two of the Canary Islands, La Palma and Tenerife.

7.2 Introduction

Climate change is primarily driven by anthropogenic greenhouse gas emissions, with the largest positive radiative forcing contribution due to increasing levels of long-lived carbon dioxide (CO_2) in the atmosphere (Solomon et al., 2007). Atmospheric CO_2 is therefore monitored by in situ observations at ground stations and in aircraft as well as by remote sensing methods.

In situ measurements include numerous precise instruments on the ground, for example at Mauna Loa Observatory, Hawaii (Keeling et al., 1976; Komhyr et al., 1989); on tall towers, for example in Europe for the CHIOTTO project (Continuous HIgh-precisiOn Tall Tower Observations of greenhouse gases; Vermeulen et al., 2011) as well as in the US (Bakwin et al., 1998); and in aircraft, for example in the CARIBIC project (Civil Aircraft for the Regular Investigation of the atmosphere Based on an Instrument Container; Schuck et al., 2009), for calibration of the TCCON (Total Carbon Column Observing Network; Wunch et al., 2010) and as part of the NACP network (North American Carbon Program; Crevoisier et al., 2006).

Remote sensing of column CO_2 is carried out from the ground using direct sunlight in the near-infrared in the TCCON (Wunch et al., 2010); recently from low Earth orbit (LEO) using reflected sunlight, for example by SCIAMACHY (SCanning Imaging Absorption spectroMeter for Atmospheric ChartographY; Schneising et al., 2011) and GOSAT (Greenhouse gases Observing SATellite; Yoshida et al., 2011); and using thermal infrared emission, for example by AIRS (Aumann et al., 2003) and IASI (Clerbaux et al., 2009). As a further fundamental advance, carbon cycle science would benefit from an accurate and long-term, stable, global set of altitude-resolved greenhouse gas measurements as recently proposed using an infrared laser occultation technique (Kirchengast and Schweitzer, 2011).

The short-wave infrared (SWIR) spectral region, in particular 2.0 µm to 2.5 µm, is attractive for active remote sensing measurements because of the availability of high quality lasers and detectors in this region, which contains rovibrational absorption lines of many greenhouse gases and their isotopologues (e.g. H_2O, HDO, $H_2{}^{18}O$, CO_2, $^{13}CO_2$, $C^{18}OO$, CH_4, N_2O, O_3, CO) (Kirchengast and Schweitzer, 2011). Natural background radiation is also low in the SWIR region because it lies between the thermal IR region at longer wavelengths, where radiation is emitted by the Earth, and the visible region at shorter wavelengths, where emitted sunlight peaks (Liou, 2002).

The application of the IR laser occultation technique to satellite remote sensing requires measurements to be taken in a limb geometry, with a laser source on one satellite and a detector on a second, resulting in atmospheric path lengths of several hundred kilometers. The laser radiation is absorbed by molecules in the atmosphere and is subject to a number of "broadband" effects, such as aerosol and Rayleigh scattering, atmospheric scintillation and cloud absorption, that have weaker wavelength dependence than sharp molecular absorption lines (Schweitzer et al., 2011*a*). The influence of these broadband effects can largely be cancelled by making a differential measurement with two laser beams: one tuned to the peak absorption of a suitable rovibrational line and the other to a nearby "reference" wavelength subject only to broadband effects (Kirchengast and Schweitzer, 2011). This concept is part of a satellite mission called ACCURATE

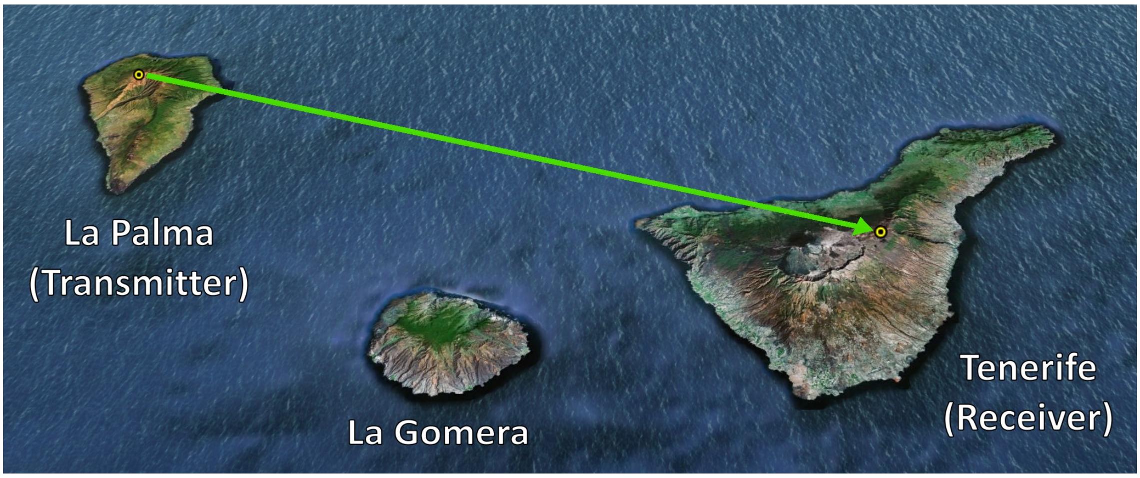

Figure 7.1 – Illustration of the laser link between the Canary Islands La Palma and Tenerife. Image 2012 Google © 2012 TerraMetrics © and 2012 GRAFCAN ©.

(Kirchengast et al., 2010) that was proposed as an Earth Explorer Mission to ESA and viewed by ESA evaluation panels to be of very high scientific value and meriting further studies.

7.3 Plan

7.3.1 Basic Setup, Site, and Equipment Design

The experiment would consist of two optical setups, a laser transmitter (Tx) and a receiver (Rx), on two mountain tops in the Canary Islands, 144 km apart (Figure 7.1). Due to the clear skies and dry climate around the Canaries, the astronomical "seeing" is very good at higher elevations, and so the islands offer an ideal site for atmospheric measurements with long path lengths. There are several astronomical observatories on the Canaries, including the Roque de los Muchachos Observatory (ORM) on La Palma and the Teide Observatory (OT) on Tenerife, both at altitudes of ~2.4 km. There is a clear line of sight between these two observatories, which has previously been used for quantum communication experiments (Ursin et al., 2007).

The Tx would be located close to the Nordic Optical Telescope (NOT) at the ORM, and a receiver connected to ESA's Optical Ground Station telescope (OGS) at the OT. At the NOT site, the Tx would be located in a parking area near the telescope building and the laser beam transmitted through a commercial 15 cm Newtonian telescope. The 1 m OGS telescope would collect the incoming radiation, and pass it to the Rx, installed near

Table 7.1 – SWIR lasers and regions.

Laser	Type	Region (cm^{-1})	Species
L1	Primary	4765-4780	CO_2, H_2O
L2	Reference	4765-4780	CO_2, H_2O
L3	Primary	4340-4350	CH_4
L4	Reference	4318-4325	CH_4

Table 7.2 – Originally selected absorption lines.

Absorption species	Wavenumber (cm^{-1})
$^{13}CO_2$	4772.657
$^{13}CO_2$	4766.641
$C^{18}OO$	4767.041
H_2O	4771.968
None (CO_2 region absorption minimum)	4770.150
CH_4	4348.166
None (CH_4 region absorption minimum)	4322.927

the focal point from the telescope. IRDAS-EXP planned to test the SWIR occultation method by investigating CO_2, CH_4 and H_2O. Appropriate microwindows within the SWIR region containing absorption lines of these species were chosen (Kirchengast et al., 2010), and tuneable distributed feedback diode (DFB) diode lasers covering these regions were purchased. Two SWIR regions would be tested, ~2.1 µm (mainly CO_2 absorption) and ~2.3 µm (mainly CH_4 absorption), hereafter referred to as the CO_2 and CH_4 regions, respectively. Predicted spectra for these regions, showing CO_2 or CH_4 absorption and also the absorption of all species, are shown in Figures 7.2, 7.3, and 7.4. These regions were chosen to include lines where almost all of the absorption is due to the target species, and regions of almost no absorption ("reference" points; explained later). The original target lines are shown in Table 7.2.

The initial planned setup can be seen in Figures 7.5 and 7.6. Four diode lasers with (~4 to ~10 mW) emitted power would scan within these regions (Table 7.1): two devoted for use as CO_2 region lasers (L1 and L2), and two for the CH_4 region (L3 and L4). The emitted laser wavelength could be tuned by adjusting the laser temperature and the applied current. Each laser was tuneable with high spectral resolution over a maximum spectral range of about 4 cm^{-1} (fine tuning) by adjusting the current, and about 10 cm^{-1} (coarse tuning) by adjusting the temperature.

At any one time only two lasers would be in use, either L1 and L2, or L3 and L4. L1 and L3 are hereafter referred to as the "primary" lasers, and L2 and L4 the

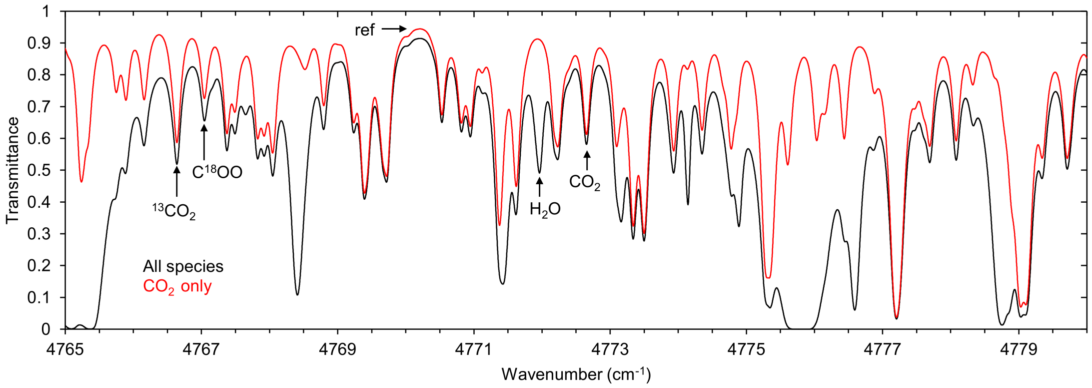

Figure 7.2 – Calculated spectrum of the CH_4 (2.1 µm) region. This shows the region covered by the two IR lasers for CH_4 and H_2O measurements (L1 and L2). CH_4 only - calculated for CH_4 only. All species - calculated including all relevant atmospheric species; almost all extra absorption is due to H_2O. The labels indicate the originally targeted absorption line positions and reference (minimum absorption) position (Table 7.2). Depending on actual frequency scan ranges (Table 7.1), other spectral sections are used. For conditions see Section 7.6.8.

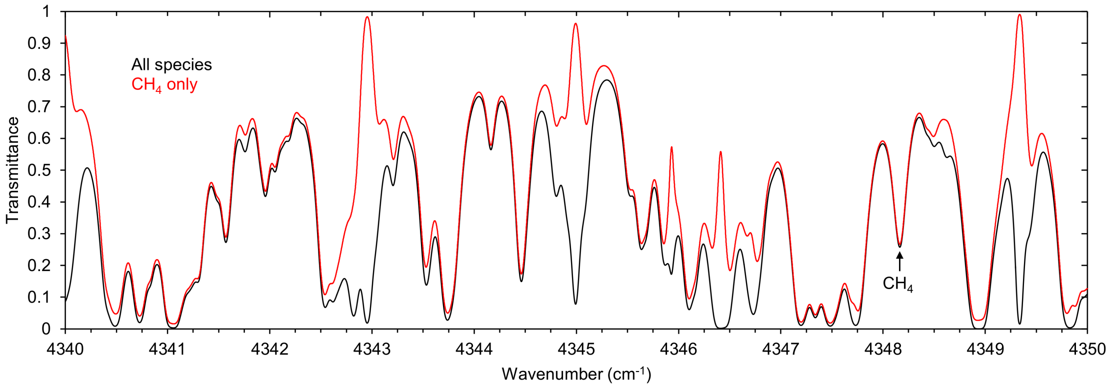

Figure 7.3 – Calculated spectrum of the CH_4 (2.3 µm) signal region. This region is covered by the IR laser for CH_4 measurements (L4). CH_4 only - calculated for CH_4 only. All species - calculated including all relevant atmospheric species; almost all extra absorption is due to H_2O. The label indicates the target absorption line position (Table 7.2). Depending on actual frequency scan ranges, other spectral sections can be used. For conditions see Section 7.6.8.

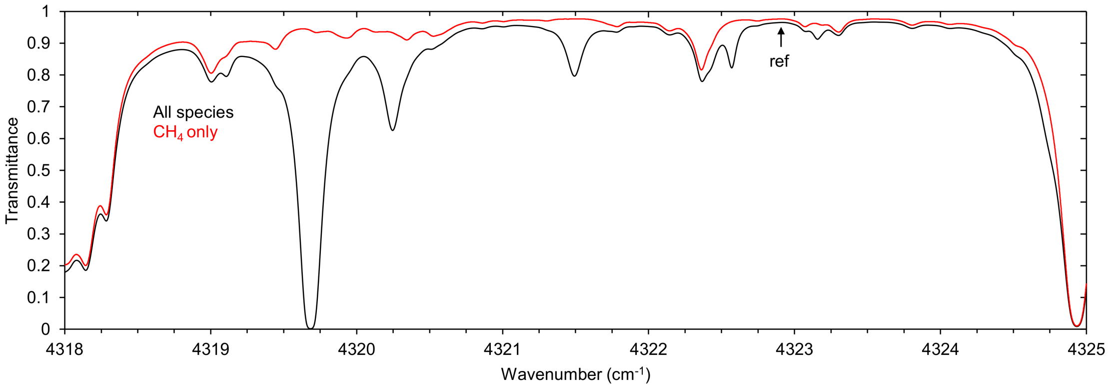

Figure 7.4 – Calculated spectrum of the CH_4 (2.3 µm) reference region. This region is covered by the IR laser for CH_4 reference measurements (L3). CH_4 only - calculated for CH_4 only. All species - calculated including all relevant atmospheric species; almost all extra absorption is due to H_2O. The label indicates the target reference (minimum absorption) position (Table 7.2). Depending on actual frequency scan ranges, CH_4 might also be retrieved in this region. For conditions see Section 7.6.8.

"reference" lasers. They would be polarised at 90° to each other, so that their beams could be combined by a polarising beam splitter, to then pass through a mechanical chopper running at 500 Hz (depending on mode). The beams would then be separated at the Rx based on wavelength using a custom designed étalon (hereafter referred to as the Rx étalon), so that their power could be recorded separately. A green Nd:YAG laser (200 mW) would be used for alignment purposes. A wavemeter would record the SWIR laser wavelength when necessary, and photodiode detectors would record the laser power at both sides. National Instruments (NI) data acquisition boards (analogue to digital / digital to analogue converters; ADCs) would be used at both the Tx and Rx. These units are able transform a digital input signal from LabVIEW into an analogue voltage/current, and vice-versa. The main purpose of the LabVIEW programs was to use the ADCs to apply voltages to the lasers at the Tx, and record the voltage signal from the detectors at both sides.

7.3.2 Initial Measurement Mode

IRDAS-EXP was expected to mimic the "differential absorption" measurement mode of the potential ACCURATE mission. This would consist of setting the lasers to constant wavelengths; one situated at the peak of a selected absorption line, and the other at a "reference" point (a point of minimum absorption), and recording transmission. If the

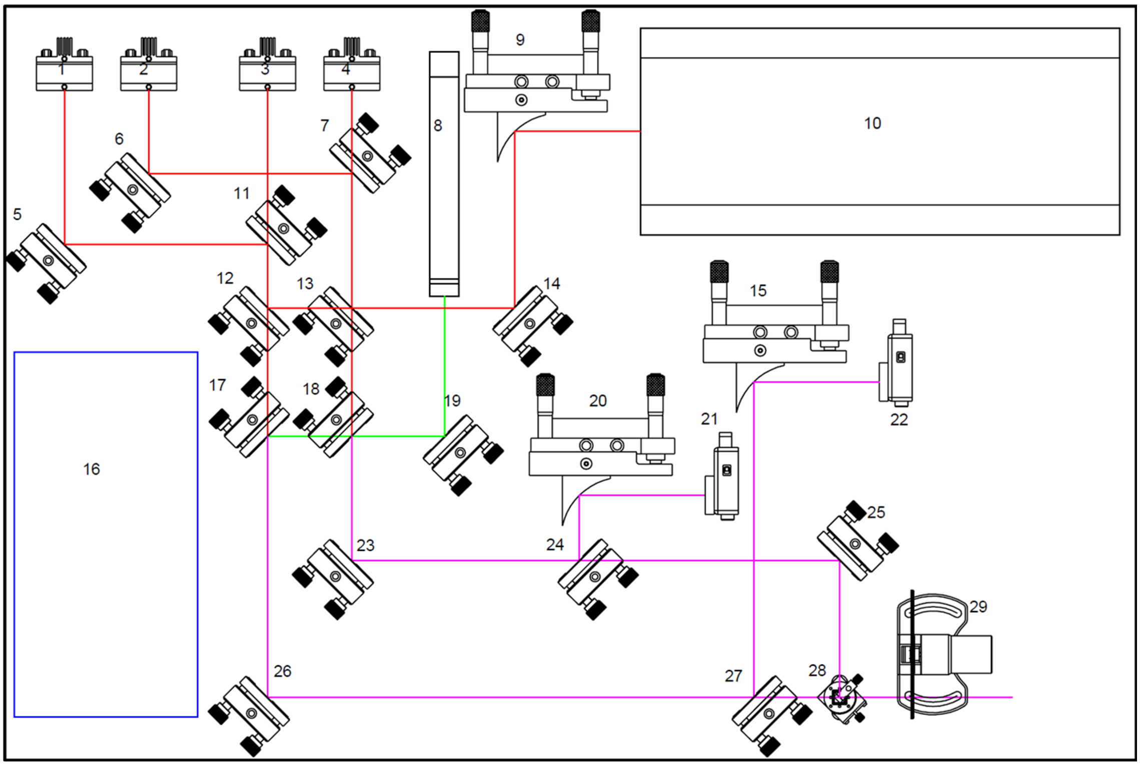

Figure 7.5 – Initial Tx breadboard schematic
1-4: SWIR diode lasers
10: 1-5 µm wavemeter
5, 6, 14, 19, 23, 25, 26: Protected silver-coated mirrors with reflectivity of ca. 96% at 2.1 µm
7, 11: Dichroic mirrors: Maximum reflectivity at ca. 2310 nm and maximum transmission at ca. 2096 nm
12, 13, 17, 18, 24, 27: Beam splitters
21, 22: InGaAs Photodiode detectors
28: Polarising beam splitter (used as combiner)
29: Chopper
15, 20: parabolic mirror

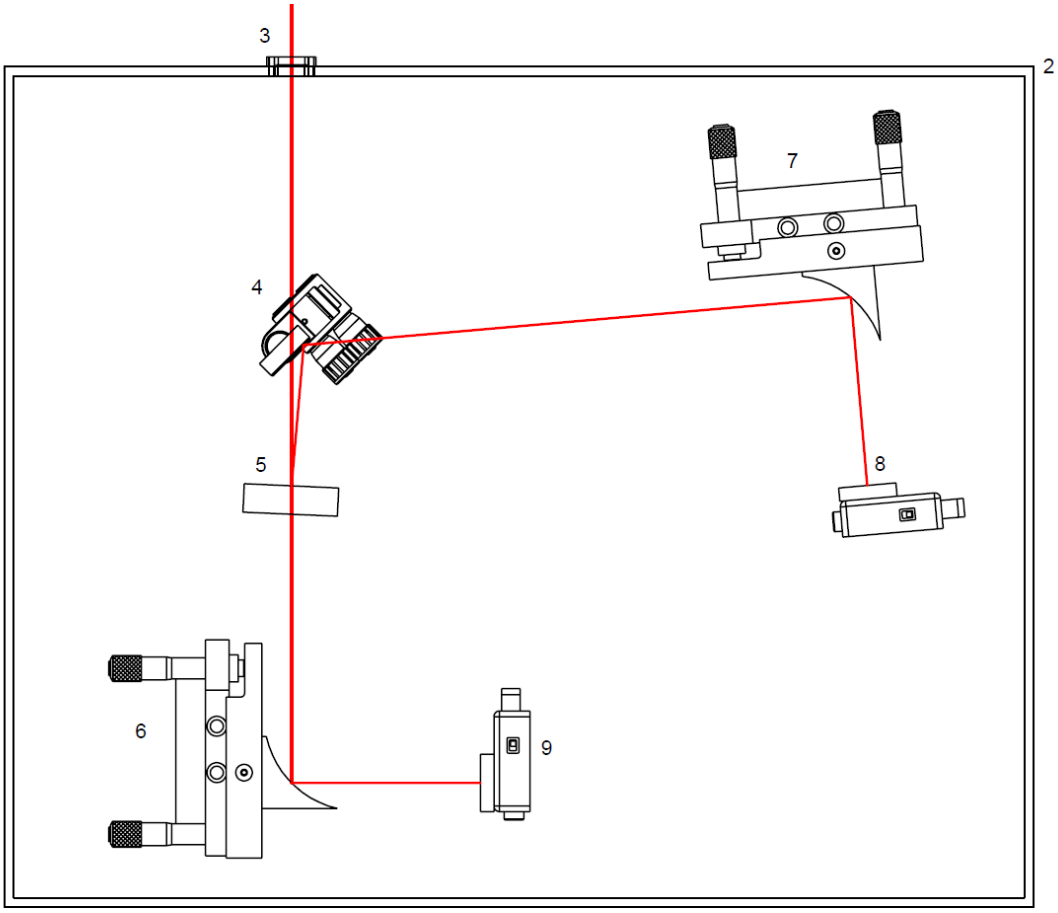

Figure 7.6 – Initial Rx breadboard schematic
3: Beam from telescope
4: Rx Étalon
5: Protected silver-coated mirror with reflectivity of ca. 96% at 2.1 µm
6, 7: Parabolic Mirrors
8, 9: InGaAs Photodiode detectors

intensity was too low to be observed directly, a mechanical chopper would be used in conjunction with a lock-in amplifier at the Rx. This was named the "static mode". See Figures 7.2, 7.3, and 7.4 for the spectral positions of the reference and peak positions.

7.4 Preparation and Testing

7.4.1 First Gas Cell Tests

To verify the performance of the system, a series of tests were performed, initially on a laboratory bench. The equipment was set up using the minimum required optics for simplicity, and a 1 m sample cell containing either CH_4 or CO_2 was positioned in the beam path.

"Slow scans" were performed by adjusting over several minutes the current applied to the laser diode and, therefore, the wavelength of the emitted light. These scans were successful for CH_4 (lasers 3 and 4), and resulted in the spectra with clearly resolved peaks. For the CO_2 scans, however, the intensities of the targeted lines were extremely low, as they had been selected to give reasonable levels of absorbance over 144 km, and the atmospheric volume mixing ratio (VMR) of CO_2 is $\sim$200 times greater than that of CH_4. As a result, the CO_2 lines could not be detected by the "slow scan" method.

7.4.2 Fast Scan Mode

It was decided at an IRDAS-EXP meeting that another measurement mode should be used during the campaign, which was named the "fast scan" mode. The purpose of this mode was to scan a specific wavelength range quickly and repeatedly (at several hundred hertz) using one laser, providing many individual (and sometimes noisy) spectra that can then be averaged to yield a final spectrum, with a much greater SNR than the "slow scan" method. This is achieved by applying a repeating ramp voltage to the primary laser via the ADC (Figure 7.7).

The detectors at the Tx also record signals, so that the laser power change with changing wavelength can be observed and later accounted for. The data acquisition can continue for up to a few seconds (longer fills the computer's RAM), yielding a final spectrum. This process will hereafter be referred to as a 4 s repeat.

Before each 4 s repeat, the primary laser would begin scanning and the reference laser would be turned on, and after a short time, the reference laser power would briefly

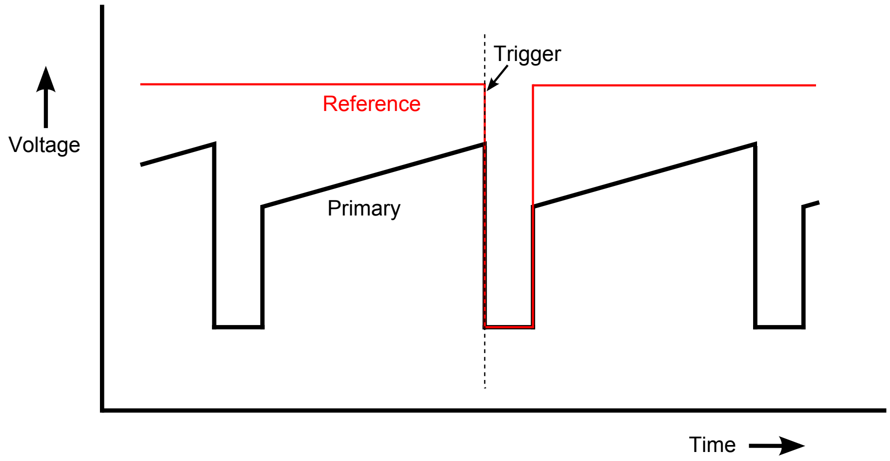

Figure 7.7 – Pre-campaign fast scan mode

drop to zero to trigger data acquisition at both sides, as shown in Figure 7.7. Before each section of 4 s repeats, the voltage applied to the reference laser would be automatically adjusted to find the correct wavenumber. A similar process would occur for the primary laser.

The final fast scans planned pre-campaign would scan both broad and narrow spectral regions, aiming at several or single lines, take 3000 or 1000 samples per ramp (spectrum) at 133 or 400 Hz (ramps per second), respectively. Data points would be sampled at 400 kHz, and repeats would last 4 s. Using an early version of this mode that used only the primary laser, the CO_2 gas cell experiment was repeated, and a spectrum was obtained, in which several CO_2 peaks were clearly visible.

7.4.2.1 Preliminary Wavelength Calibration for Fast Scan

A linear ramp voltage was applied to scan the laser, but the laser wavenumber is not a linear function of the applied voltage. The wavenumber axis had to be calibrated separately for each chosen scan range. To achieve this, each scan was performed while the beam passed through étalons. This results in transmission fringes, with their peaks separated by the étalon's free spectral range (FSR).

To ensure that each scan covered the desired wavenumber range, rough wavenumbers near the start and end of the scan were found using an étalon with an FSR much larger than the scan range, so that only one fringe is observed in one scan (the Rx étalon). A constant current near the end of the scan range was set, wavenumber recorded by the wavemeter, étalon angle set to maximum transmission, and scan performed. This showed one fringe where the scan sample number at maximum transmission corresponds to the recorded wavenumber. It was repeated for another constant current near the start of the scan range. The sample numbers at the two maximum transmissions were recorded (S1 and S2).

The relative wavenumber change was obtained accurately by scanning the laser wavelength with the beam passing through a second étalon, hereafter referred to as the Tx étalon, with an FSR of $\sim$0.0125 cm^{-1}. The fringes obtained were fitted to quantify the change in wavelength with sample number. To create a preliminary wavelength axis, the results from the first étalon scans were used to give one absolute wavenumber point (at S2), and to estimate a value for the small FSR (by dividing the wavenumber difference between S1 and S2 by the number of small fringes in that range). The digital sample number could then be transformed into wavenumber. A program was written to automatically perform scans, fit the transmission fringes, and create a calibrated wavenumber axis (using previous data from scans with the Rx étalon), so that this could be done pre-scan. This preliminary axis was improved later by fitting to a calculated spectrum.

7.4.3 Rx Étalon Performance

The Rx étalon was the last piece of equipment to be obtained. It has an FSR of $\sim$7 cm^{-1}, which would be large enough to easily separate two wavelengths. Its wavelength separation performance at the relevant wavelengths was tested and deemed acceptable (>95% maximum transmission and reflection of required wavelengths). This was later proved not to be the case, and actually it was only providing between 75 and 90% transmission, but still >95% reflection. The reason for this was believed to be that the beam hitting the étalon was not perfectly collimated, and therefore was hitting it at varying incident angles. To account for this as much as possible, before each scan, static or fast, the amount of reflection and transmission of each laser would be measured and recorded separately. For the fast scan, this meant making a profile of % transmission for the scanning primary laser as a function of sample number.

7.4.4 Corridor Testing

Tests were performed twice along the ca. 40 m corridor in the Department of Chemistry at the University of York (downstairs A-block) using the fully constructed Tx and Rx breadboards to demonstrate the quality of beam collimation from the transmitter and the sensitivity of the InGaAs detectors in the Rx. The only component missing from the system was, of course, the 1 m receiving telescope. Since it was expected on the campaign to receive a signal using a 1 m telescope to collect radiation from a 100 m wide beam, it was necessary in the test to be able to detect a signal using a 2.5 cm mirror and a 15 cm collimated beam. The results showed that good signal to noise ratio was readily obtainable and that the beam was well collimated over that distance. A cell containing CH_4 was also placed in the beam path, and the fast scan mode was tested using a separate computer at each end (but with no network link which would be required in the campaign). A spectrum was successfully obtained.

7.4.5 Static Modes

Two versions of the static were developed, one that used the lock-in amplifier and chopper (static mode A) and one that did not (static mode B). For both, the primary and reference lasers would be on simultaneously, and the Rx étalon would separate the reference beam by transmission, and the signal beam by reflection. The two Rx detectors would constantly record the signal of their respective lasers. As with the fast scan mode, the Tx detectors would record the laser power so that this could be accounted for in post-processing.

Pre-scan, for both static modes, the applied voltage would be adjusted automatically until the required wavenumber was produced, for both lasers. This would be repeated every few minutes in case there had been any wavenumber drift. Ideally, the wavenumber would have been monitored and adjusted during data acquisition, but this would have required a non-negligible amount of the beam to be diverted.

Static mode A would include 5 ms of zero voltage samples every 1 s for the purpose of recording detector offsets. For static mode B, the lock-in amplifier would correct for the offsets internally. The lock-in amplifier is able to take a chopped signal (i.e. half on and half off), as low as a few nV (from the detector), and produce a constant signal (Meade, 1982). It could only transform one signal at once, but it also outputs an oscillation signal which defines when the laser signal was on or off. This would also be recorded, along with the transformed primary laser signal and the untransformed reference laser signal. The reference signal could then be transformed in post-processing.

The reference beam, by definition, should suffer from a much lower level of loss due to molecular absorption, and therefore be of higher power at the Rx detector. For this reason, it was to be used as a trigger, so that data acquisition would start when the signal dropped below a certain level. This means that the start of the data at one site would correspond to the start at the other, and the laser power change recorded at the Tx could be taken into account. In the static mode however, data acquisition would continue for several minutes, and it is possible for there to be time drift between the clocks in the two ADC units. In order to synchronise and time-stamp the detector data from the Tx and Rx, GPS timing units with reported 30 ns accuracy were purchased. The GPS time signals would be recorded simultaneously with those from the detectors. The units have three outputs: data in ASCII format, analogue pulse per second signal (PPS), and an analogue 500 Hz square wave (FRQ). The PPS and FRQ signals would be recorded by the ADC along with the detector signals. The ASCII data would be output at 1 Hz, providing a timestamp. The PPS signal is a 1 Hz, 100 µm wide pulse, where the rising edge corresponds to the start of the next second (i.e. #.000 s). This enables a timestamp to be assigned to the data for the start of each second. The FRQ square wave enables timestamps to be assigned to the points in between.

7.4.6 Roof testing

Further tests were then carried out over a distance of ca. 500 m between the roofs of the Physics Department and Chemistry D-block at York. In all, three separate roof tests were performed. It was found that the green alignment laser could not be seen in daylight which made alignment extremely difficult. After dusk, the laser beam could easily be seen and alignment was then possible. It was decided to incorporate the spotting telescope, firmly attached to the transmitting telescope, to assist in alignment. In the first tests, at night, an IR signal from two lasers was eventually detected. In the second of these tests the chopper and lock-in amplifier were also tested, and signals detected from all four lasers, both with the chopper and lock-in amplifier and without them. In the final test, the fast scan and static modes were fully tested. Some "beam wander" over time was observed, but with occasional realignment, the signal was clearly stable enough for the modes to operate as intended. The atmospheric concentration of CO_2 and CH_4 is not high enough to allow their detection in the appropriate wavelength regions over only 500 m, and insertion into the system of a gas cell was not practical. Therefore, the signal was tested but no absorption lines were seen.

At various times during data acquisition, the Tx and Rx LabVIEW programs were required to communicate with each other. For example the Rx would say that it is will start data acquisition if triggered, and the Tx will then initiate the trigger. This communication was also tested successfully during the final roof test.

7.5 Campaign

For the campaign, eleven measurement nights were available (11/12 to 21/22 July 2011). Unfortunately, the first week was plagued by calima, a weather phenomenon blowing dust over the Canaries from sandstorms in the Sahara desert, through which the beams could not pass due to strong aerosol extinction.

7.5.1 Final Tx Setup

It was hoped that the Tx equipment could be housed inside our portacabin, but unfortunately this was not possible due to a lack of stability that caused the beam to move, and so it had to be positioned outside. This did mean that it was directly vulnerable to being shaken by the wind, and so beam movement was still a problem. To align the optics, a combination of a power meter, thermal paper, and a beam profiler were used. The power meter and the beam profiler were much more difficult to use in bright and/or windy conditions, and thermal paper was of course much less effective at cool or hot temperatures. Due to these difficulties, it was decided to simplify the Tx breadboard as much as possible for easier alignment. It was changed from a four to a two laser system, which would require realignment to use the other set of two lasers. The Tx étalon was also removed as it was extremely difficult to align correctly, partly because it was not specifically designed for this experiment. Tx étalon scans were performed post campaign in York.

The entrance lens of the telescope was adjusted to change the beam collimation produced by the telescope, thus enabling control of the beam size at the Rx. A scanning slit optical-IR beam profiler was used to spatially overlap the green and the two IR lasers. This beam overlap, complemented by collimation tests of the green laser over a path of about 500 m, was crucial to success.

Figure 7.8a shows the final Tx setup used.

7.5.2 Final Rx Setup

During the first week, the operators at the Rx had to devise a method to get the received beams from the inner focal point of the telescope to the Rx optics. On reaching the Rx étalon, it would need to be well collimated and small enough to pass through the 1 inch diameter étalon optics. Beam movement was also much greater than expected, which meant that the signal was extremely unstable. Eventually, after several attempts, it was decided that using the étalon would be too problematic, and it was removed. Figure 7.8b shows the final Rx setup used.

7.5.3 Changes to Modes of Operation

When the calima cleared, the green beam could be seen by the operators at the Rx, so it could be guided into position using the Tx angle adjustments. This beam was so bright that it was visible on the OGS building, and caused clearly visible shadows. The first IR signals (for CH_4) were successfully detected during night 7 using a $\sim$30 m beam diameter at the OGS. However, they were too unstable for a trigger to occur on the loss of a signal.

The operational modes then had to be adjusted to accommodate the changes made to the two breadboards, and an unstable signal. Only one laser could now be detected at a time, and so the static mode would not be able to correctly mimic the differential absorption method planned for the ACCURATE mission. Also, the time was not available to rewrite both modes and still take data. Therefore, it was decided that the static mode would not be used, and that all efforts would be concentrated on the fast scan mode.

The fast scan mode was adjusted to perform 4 s repeats, alternating between primary and reference lasers. During a scanning session, the ramp voltage was continuously applied to both lasers even when their signal was not being recorded, as this increases wavelength stability, and the motorised flip mirrors were used to automatically select which beam was used. Also, instead of using a trigger to synchronise the data on the two sides, the fast scan mode now also made use of the GPS signals for this purpose.

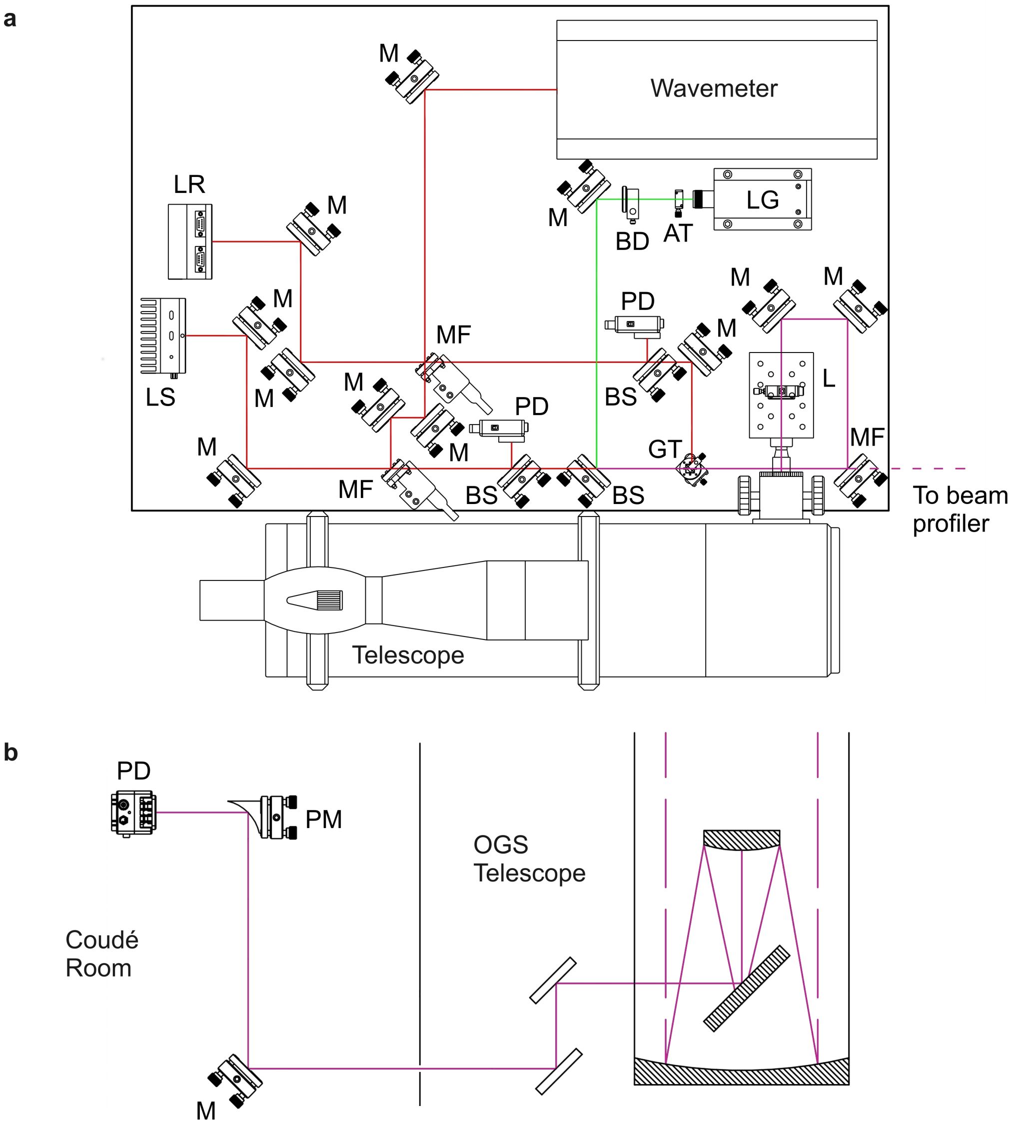

Figure 7.8 – Schematic diagram of the optical Tx and Rx breadboards. **a -** Tx. **b -** Rx.
AT - Neutral density filter to attenuate green laser (when necessary),
BD - Beam dump in motorized flipping mount,
BS - Dichroic beam splitter with transmission enhancing coating for ca. 2000 nm.
C - ARTEMIS beam collimator (focal length = 1350 mm, beam diameter = 34 mm),
GT - Glan-Thomson polarising prism, **L** - CaF2 lens (focal length = 10 mm),
LG - Frequency-doubled, Nd:YAG laser (200 mW, 532 nm).
LR - IR diode laser 2 (serial number 592/21-24/nanoplus) or 4 (592/21-19/nanoplus),
LS - IR diode laser 1 (264/3-9/nanoplus) or 3 (264/17-19/nanoplus),
M - Protected silver-coated mirrors with reflectivity of ca. 96% at 21 µm,
MF - Silver-coated IR mirrors (M) in motorised flipping mount,
PD - InGaAs photodiode detector, **PM** - Gold-plated parabolic mirror,
Wavemeter - 1.0-5.0 µm wavemeter (Bristol Instruments 621-a).

7.5.4 Good Data Acquisition

Over the last few days of the campaign, the wind increased, causing the transmitter to shake, so that beam movement became more of a problem. To compensate for this, the beam diameter was increased to $\sim$100 m at the OGS so that part of the beam would always hit the Rx telescope. This decreased the received intensity, and the beam movement brought great intensity variations. It was however, with occasional adjustments of the beams, consistent enough to take measurements. Nights 10 and 11 were mostly spent successfully acquiring data in the CO_2 region. Some CH_4 region data were obtained at the end of night 11. Table 7.3 lists the scans performed.

7.6 Data Analysis

The raw data obtained in the campaign were processed into the "level 1" format required by the Wegener Center. A detailed analysis of all the level 1 data was later carried out there, and a coauthor publication is currently under review. At the University of York, one spectrum was analysed from one 4 s repeat for CO_2, and another for CH_4, and these results are discussed in Section 7.6.2.

7.6.1 Level 0 to Level 1 Data Processing

The following procedure was applied to each 4 s repeat (recorded using one laser only) to obtain an averaged spectrum. There were two 4 s pieces of data, one from the Rx and one from the Tx. The detector offsets (measured every $\sim$1 min; see Section 7.6.7) were first subtracted. The data of the Tx were interpolated to use the same timestamps as the Rx data so that each Rx data point can then be divided by its corresponding Tx point to correct for the smooth laser power change over wavelength, thus normalising the data. The points at which the ramp (spectrum) ends were found by observing when sudden drops in signal intensity occurred in the Tx data. The timestamps of these points were used to separate the individual spectra, which were then normalised to the one of highest average signal intensity, based on their means. They were then averaged in a weighted averaging process, in which the weight was based on the original mean (before normalisation) of the individual spectra, giving one final raw spectrum for a 4 s period. The weighted averaging process was used to account for the variation in signal intensity between individual spectra in one 4 s period, which is caused primarily by the wind shaking the Tx and by atmospheric scintillations.

To complete the calibration of the wavenumber axis, the final spectra were compared to those calculated by the forward model (GATS Spectralcalc; see http://www.spectralcalc.com/). In all cases the spectra match extremely well, and there is minimal uncertainty in assigning peaks. For each scan type (see Table 7.3), a fit was then performed to minimise the residuals (observed minus calculated) between the observed and calculated peak positions (using only CO_2 or CH_4 peaks) with the FSR and wavenumber offset as the only changing parameters. The profile of non-linearity of wavenumber with respect to digital sample number recorded by the Tx étalon was therefore still used in the calibration.

7.6.2 Final Results

During the campaign, the VMRs of CO_2, CH_4 and H_2O were recorded at 1 s intervals using two cavity ring-down spectrometer (CRDS) units for validation purposes, complemented by routine meteorological station data both at the Rx and Tx. An average CO_2 VMR along the line of sight was retrieved, which is found to be in good agreement with the validation measurements as described below. Additionally, a CH_4 spectrum covering the spectral region 4345.96 cm^{-1} to 4348.43 cm^{-1} (Table 7.3, label 12, laser L3) is presented (Figure 7.10), however the VMR cannot readily be retrieved due to equipment problems in the final hours of the campaign (see Section 7.6.7).

7.6.3 Fitting

For the full fitting procedure see Section 7.6.5. The spectral region 4768.27 cm^{-1} to 4771.75 cm^{-1} was investigated (Table 7.3, label 7, laser L1), using the 4 s period of highest average signal intensity. A forward model based on the HITRAN 2008 line parameters (Rothman et al., 2009) and the line by line simulation procedure outlined by Rothman et al. (1998) was written and used to simulate and fit atmospheric transmittance spectra. A fit was performed, in which the simulation was repeated whilst altering several parameters including CO_2 concentration to minimise the residuals between the observed and calculated spectra; the resulting spectra are shown in Figure 7.9. The final CO_2 concentration from this fit was taken as the result, yielding 400.1 ppm ($\pm$14.7 ppm), which is consistent with the validation value of 386.7 ppm ($\pm$0.21 ppm; see Section 7.6.6).

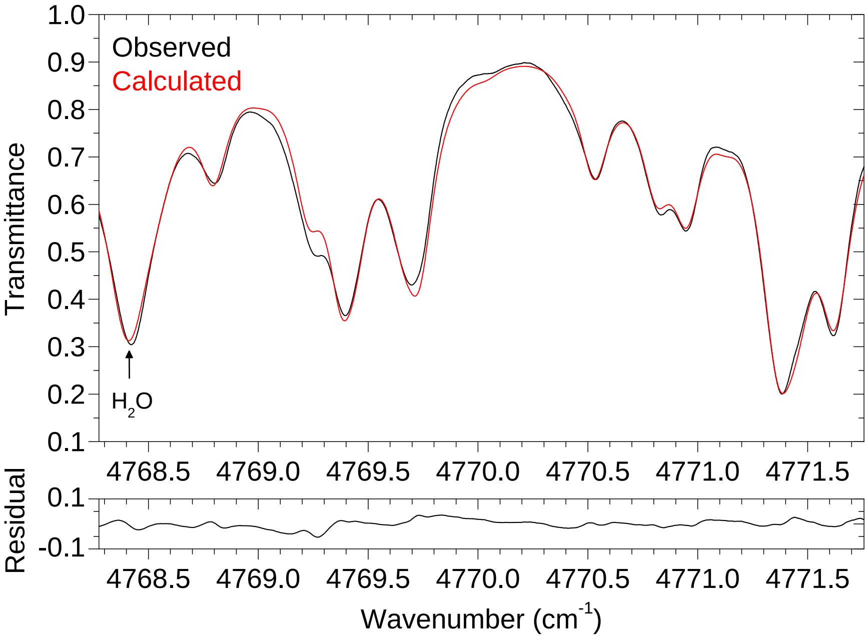

Figure 7.9 – Observed and calculated atmospheric transmittance spectra in the CO_2 region. All features arise from CO_2 absorption except for one, which is due to H_2O (labelled).

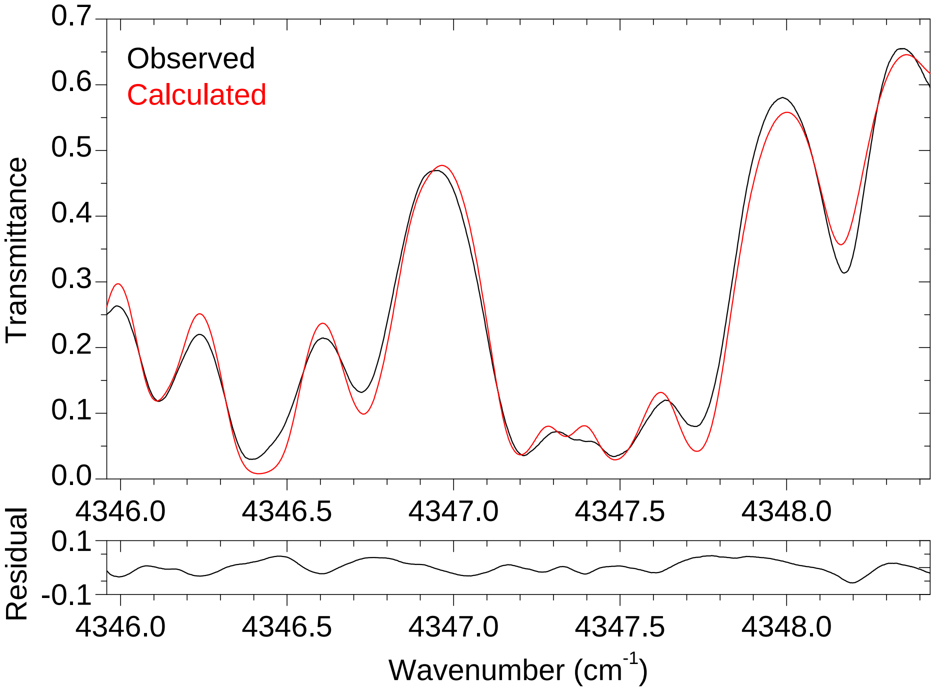

Figure 7.10 – Observed and calculated atmospheric transmittance spectra in the CH_4 region.

7.6.4 Error Calculations

Atmospheric pressure and temperature along the beam path for the time of the investigated scan were modelled using the atmospheric analyses from ECMWF (European Centre for Medium-range Weather Forecasts). For both of these variables, the calculated full beam path values were adjusted based on the difference between their computed values at the start and end points, and those recorded by the local weather stations. The adjusted ray path values were then averaged, giving 285.2 K and 795.8 mbar. The standard deviations resulting from this averaging were used as error bars. The fitting procedure was repeated using the minimum pressure and temperature values calculated from the error bars, and again with the maximum values. The difference between the CO_2 concentration results from these extra fits and that from the main fit were 11.3 ppm and 10.7 ppm. The larger of the two was taken as the error caused by temperature and pressure uncertainties. The path length of 143.65 km was calculated using the recorded GPS coordinates.

The fitting procedure provides a final error covariance matrix, from which the standard deviation in the CO_2 concentration estimate was extracted. For the main fit, this value was 9.0 ppm. This was combined with the temperature and pressure error of 11.3 ppm and the detector offset error of 2.7 ppm (see Section 7.6.7) using the root sum squares method, yielding the final error of 14.7 ppm.

7.6.5 Floated Fitting Parameters

Four parameters were adjusted by the fitting program. Two were the VMRs of CO_2 and H_2O. The observed spectrum obtained from the procedure outlined above is in units of volts, which is effectively an arbitrary number, and the real position of the baseline is unknown. To be able to compare the spectrum to a calculated transmittance spectrum, it was necessary to use a multiplicative scaling factor. This scaling factor was the third fitting parameter, which was applied to the whole calculated spectrum after all other calculations. For the final presented spectra, the calculated and observed spectra are both divided by this parameter, to scale them to transmittance spectra. The laser radiation will have been subject to aerosol scattering, but with no wavelength dependence across the scan regions. The effects of this scattering are taken into account by this multiplicative factor, and will therefore have no noticeable effect on the final spectra.

The final fitting parameter was used to increase the broadening of the calculated spectrum from the theoretical values, as the observed spectra are broader than the calculated ones (see Section 7.6.7). The spectra were fitted using Voigt lineshapes, a convolution of the Lorentzian and Gaussian lineshapes, resulting from a combination of mainly pressure-induced broadening and Doppler broadening, respectively. In the fit, the extent of pressure broadening was kept constant at the calculated level, and the multiplicative factor increased the influence of Gaussian broadening, effectively adding a Gaussian instrument function. The best broadening parameter from the fit was 1.31. The pressure, temperature and path length were kept constant in all the fits (see Section 7.6.7).

7.6.6 CO_2 and H_2O VMR Values

The validation CO_2 value reported is simply an average of the CRDS Rx and Tx values recorded at the time of the investigated scan. To estimate an error for this, the recorded CRDS CO_2 values for a ten minute period (five minutes either side of the actual scan time) from both the Tx and Rx were averaged, and the standard deviation was used as the error (±0.18 ppm). This was combined with the reported error of the CRDS units (±0.1 ppm) using the root sum squares method, giving the final validation error of ±0.21 ppm. The VMR of H_2O across the beam path is likely to vary much more than that of CO_2 and so an actual average value could not be confidently calculated, and therefore its VMR was floated in the fitting process.

7.6.7 Detector Gain and Offsets

It was necessary that the Rx detector used a high gain setting (∼70 dB) due to the extent of power loss over the full path. The losses are primarily due to beam divergence, Rayleigh and aerosol scattering, and molecular absorption. This high gain limited the bandwidth of the detector so that the detector could not respond fast enough to rapid changes in laser power for the scan speeds used (400 kHz sampling rate). This has affected the observed spectra in two ways. Firstly, all of the spectra recorded on the campaign have broader peaks than expected from simulations; an effect which was not observed in prior studies in the laboratory when lower gain settings were used. Secondly, detector offsets (hereafter referred to only as offsets) were not measured as often as intended. The original plan was to use 20 zero current samples at the start of each waveform so that an offset measurement could be taken regularly for each spectrum with zero laser power. This meant that any offset drift would be accounted for. The number of zero current samples used was kept small, as using more samples causes the laser wavelength not to respond as quickly to the applied current. This number of zero current samples was sufficient for recording an offset when using lower gain settings, but it was not satisfactory at higher gain settings. As a contingency, every ten 4 s repeats, a full 4 s repeat was recorded whilst both lasers were blocked, and the recorded values were averaged to give an offset value for that 4 s repeat time. These were used to provide the offsets used in the data processing. For each 4 s repeat, the two closest (in time) recorded offset values were used to estimate an offset for the 4 s repeat, assuming a linear offset change between the two recorded times.

After the campaign, laboratory tests were performed to confirm that the gain setting and not the laser linewidth was the cause of the broadened peaks and offset problem. A gas cell was filled with CH_4 and spectra were recorded using both a high and a low gain setting. The laser power was reduced using several layers of tissue. These tests showed the expected extra broadening and lack of offsets using the high gain setting.

To estimate the error due to the offsets, all of the offsets recorded during the scanning session that contains the investigated 4 s repeat were averaged. The standard deviation was added to and subtracted from the actual offset used, and final spectra were calculated for each case. The fitting procedure was repeated, and the larger of the two differences between the calculated VMRs and the main VMR result was taken as the offset-caused error. An error of 2.7 ppm was estimated in this manner for the sample spectrum of Figure 7.9.

To obtain a general idea of the possible effect of the offset variation on the 4 s repeats within a scanning session, the offset variation was quantified. The standard deviation of the recorded offsets was divided by the average received signal intensity. For the investigated CO_2 scanning session this gave a variation of $\sim$1.0%. For the best CH_4 session it is over 200%. The detailed reason for this high variation is unknown, but clearly there was a problem with the equipment when the CH_4 measurements were taken. For this reason, CH_4 spectra were not used in this study to retrieve concentrations, and the fit quality of the investigated CH_4 is significantly lower than that for CO_2. The underlying limitation is that CH_4 data could only be obtained in a short time at the end of the available measurement time; if more time had been available then better data could have been recorded.

Table 7.3 – SWIR lasers and regions

Label	Laser	Wavenumber range (cm^{-1}) Start	 End	Scan time
CO_2(1)	L1	4772.00	4772.84	Night 10
	L2	4768.03	4768.92	01:50-01:55
CO_2(2)	L1	4770.97	4774.53	Night 10
	L2	4766.36	4768.18	02:23-02:30, 02:31-02:39, 02:41-02:43
CO_2(3)	L1	4768.45	4769.34	Night 10
	L2	4765.32	4766.25	03:27-03:41
CO_2(4)	L1	4768.24	4771.18	Night 10
	L2	4763.94	4768.21	04:32-05:04
CO_2(5)	L1	4771.03	4771.86	Night 11
	L2	4768.55	4769.50	22:15-22:30, 22:37-22:44
CO_2(6)	L1	4770.35	4771.20	Night 11
	L2	4768.48	4769.42	22:59-23:00, 23:19-23:34
CO_2(7)	L1	4768.27	4771.75	Night 11
	L2	4764.11	4768.20	00:14-00:33, 00:34-00:43
CO_2(8)	L1	4770.91	4774.52	Night 11
	L2	4766.35	4768.19	00:54-01:13, 01:14-01:18
CO_2(9)	L1	4773.81	4777.55	Night 11
	L2	4766.35	4768.19	01:31-01:38, 01:56-02:09
CO_2(10)	L1	4771.17	4771.98	Night 11
	L2	4768.67	4769.60	02:55-03:09
CH_4(11)	L3	4346.48	4347.39	Night 11
	L4	4321.57	4323.72	05:44-05:51
CH_4(12)	L3	4345.96	4348.43	Night 11
	L4	4321.57	4323.72	06:21-06:38

7.6.8 Conditions for Calculated Spectra

The spectra shown in Figures 7.2 to 7.4 were calculated with the same forward model as was used in the fitting procedure, using the following conditions: altitude = 2.0 km and pressure = 795 hPa (to compensate for the varying altitude of the beam path due to the curvature of the Earth), temperature = 275.2 K, path length = 143.65 km, CO_2 VMR = 330 ppm, CH_4 VMR = 1700 ppb and H_2O VMR = 0.00463.

7.7 Conclusion and Future Work

It has been successfully demonstrated that atmospheric carbon dioxide concentrations can be determined from SWIR absorption measurements over very long path lengths, with relatively low power diode lasers ($\sim$4 to 10 mW). The accuracy of these demonstration measurements ($\pm$15 ppm for CO_2) is limited by errors in determining the temperature and pressure along the atmospheric path length, uncertainties in the least-squares fitting procedure (partly due to low SNR and errors in spectral line parameters - see below), and problems in the field associated with a detector offset error (see Section 7.6.7). The static link between the Islands also does not demonstrate the scanning of the atmosphere which occurs between LEO satellites, and the experiment was too short to monitor trace gas variability over time. A detailed description of how the monitoring with the LEO system works is given by (Kirchengast et al., 2010).

In general, the desired precision for remote sensing of CO_2 for carbon cycle science is about 1 ppm (Rayner and O'Brien, 2001); a detailed discussion of the observational requirements for the ACCURATE concept is available in (Larsen et al., 2009), adopted by the mission proposal of (Kirchengast et al., 2010). While the accuracy of this first demonstration experiment is not ideal, previous studies (Kirchengast and Schweitzer, 2011; Proschek et al., 2011) indicate that greenhouse gas profiles for an ACCURATE mission are obtainable with <1 to 4% r.m.s. error (outside clouds; above 5 km; the goal for CO_2 is $<1\%$). The sources of error contributing to the value of $\pm$15 ppm are expected to be significantly smaller for an ACCURATE mission than in this least-cost demonstration. The detector offset error is a fixable issue (see Section 7.6.7) and significantly more accurate frequency knowledge and higher SNRs will be available from advanced instrumentation. Furthermore, accurate temperature, pressure and humidity will be determined from simultaneous microwave occultation measurements

(Kirchengast and Schweitzer, 2011; Schweitzer et al., 2011*b*), and a more accurate retrieval algorithm (Proschek et al., 2011) will be used to extract greenhouse gas concentrations from the infrared occultation measurements.

Implicit in the high accuracy of the ACCURATE mission is as well the requirement for accurate spectroscopic line parameters. Unfortunately, the accuracy of the line parameters presently available in the HITRAN database limits the accuracy of the demonstration measurements. For example, the CO_2 line intensities in the SWIR spectral region have reported errors in the range $>$10% and $<$20%. It is necessary to improve the HITRAN line parameters for the targeted absorption lines substantially in order for the ACCURATE mission to meet its accuracy goals (Harrison et al., 2011). In summary, we conclude from this first experimental analysis that infrared laser occultation between LEO satellites (Kirchengast and Schweitzer, 2011) has a sound basis for monitoring CO_2 in the free atmosphere; other greenhouse gases such as methane, nitrous oxide and water vapour can be monitored in the same way. The next step is to use the lessons from this work to perform a more stringent demonstration.

Chapter 8

Summary, Conclusion, and Further Work

Spectroscopic line lists including both positions and absolute intensities have been produced for several molecules and transition types, including the C_2 and $^{12}C^{13}C$ Swan systems, the CN, ^{13}CN, and $C^{15}N$ $A^2\Pi$-$X^2\Sigma^+$ (red), $B^2\Sigma^+$-$X^2\Sigma^+$ (violet) and $X^2\Sigma^+$ state rovibrational systems, the CP $A^2\Pi$-$X^2\Sigma^+$ system, the NH $X^3\Sigma^-$ state rovibrational and rotational transitions, and the OH $X^2\Pi$ state rovibrational and rotational transitions.

8.1 General Calculation Method

The line lists have been produced using a procedure that is a combination of experimental and theoretical methods, which have been refined and improved throughout this work. The purpose of the method is to base the line positions mainly on experimental data, and the intensities mainly on theoretical calculations. This is because positions can easily be obtained to good accuracy and precision experimentally, but intensities rarely can (especially for unstable radicals as studied in this thesis), as described in Section 1.5.

The general procedure involves first combining all available experimental line positions for a particular spectroscopic system, and fitting molecular constants to them (using PGOPHER; Section 2.4). This enables line positions for transitions between all observed energy levels (and slightly more) to be estimated accurately. Equilibrium constants are then calculated by fitting to the molecular constants, and these are used to obtain potential energy curves using the program RKR1. These are combined in the program LEVEL with ab initio (transition) dipole moment functions to produce vibrational wavefunctions and then transition matrix elements, from which absolute line intensities can be calculated (using PGOPHER; Section 2.5).

8.1.1 Changes to Calculation Method

The method has evolved somewhat as the work progressed, mainly in the calculation and treatment of the MEs before their use in the calculation of the final absolute intensities (in the form of Einstein A values). The wavefunctions, $\Psi_{\mathrm{v}J}(r)$, calculated from the potentials in LEVEL are vibrational wavefunctions, and these are then combined with the transition dipole moment to calculate transition MEs of the form $\langle\Psi_{\mathrm{v}'J'}(r)|R_e(r)|\Psi_{\mathrm{v}J}(r)\rangle$. The MEs calculated for the C_2 work included only one transition ME for each vibrational band. As indicated by the J subscripts, the wavefunctions are affected by rotation, which is due to the presence of a centrifugal term that affects the potential (Equation 2.18). This results in the MEs being dependent on rotation, an effect which is much greater for lighter molecules, which is clear from Equation 2.18 as the reduced mass, μ, is present in the denominator. This is called the Herman-Wallis effect when applied to rovibrational transitions, but the term is used also for rovibronic transitions in this thesis, as the cause is the same.

The first calculations performed were those for the C_2 Swan system (Chapter 3), and the LEVEL output for this work included only one transition ME for each vibrational band. This ignores the H-W effect, but C_2 is a heavy enough molecule for it to be a very good approximation for most vibrational bands. The next project was expected to be the NH work (Chapter 5), which clearly involves a much lighter molecule, and the inclusion of the H-W effect was vital. A method for its inclusion was partially developed, but then the CN and CP (Chapter 4) work took precedence, which was actually the next work completed.

It has been found throughout this work that vibrational bands with lower absolute intensities are generally subject to a stronger H-W effect, which is because the overlap between the wavefunctions is small in these cases, and any change to the wavefunctions is more likely to have a greater effect on the resulting overlap. As transitions in all possible vibrational bands were planned to be included in the final line list, including extremely weak bands, and as the H-W effect had been partly studied for the future NH work already, it was decided that it would be included for CN.

LEVEL calculates MEs in terms of the quantum number N (Section 2.2.4.2), as it does not include electron spin, and these are considered to be in a Hund's case (b) basis. PGOPHER takes case (a) MEs in the molecular frame as input (and converts them to the laboratory frame), and this needs to be considered when transferring MEs from LEVEL to PGOPHER. Case (a) and (b) wavefunctions can be expressed as linear combinations of each other, but if the H-W effect is not included, then all wavefunctions for a single vibrational band are identical, whether case (a) or (b), and therefore case (a) and (b) MEs are also identical. This means that for the C_2 work, no transformation of MEs between LEVEL and PGOPHER was necessary. However for CN, as the H-W was to be included, a method of transformation between case (b) and (a) MEs was required. The "transformation " equation (Equation 2.5.4) was derived for this purpose by Colin Western.

The transformation equation was used for all of the CN and CP transitions, and also for the NH work. During the final OH project (Chapter 6), it was discovered that an approximation had been made in the derivation of the transformation equation, and with its removal, the relative intensity results give a much better match to observed values (Section 6.6). This resulted in a refined method that is very effective in the calculation of line intensities for diatomic molecules, and will be of use to astronomers, materials scientists, and combustion scientists in their analyses of the C_2 Swan system.

The problems mentioned above were solved by investigating the comparison in Figure 6.5, which shows the H-W effect for the various calculation methods, the HITRAN values, and a set of observed values. Performing this comparison could not have been as conclusive in the previous studies. This is because, for CN, the H-W effect is far too small in the observed bands to be able to resolve the differences between these methods, and for NH, the observed spectrum has a much lower SNR than the OH spectrum, resulting in large error bars. However, now that this adjusted transformation equation is available, Figure 5.6 can be reproduced to show the change in the NH H-W results, and this is shown in Figure 8.1. The new results appear to be slightly better when compared to the observed values.

8.2 Summary of Results

For the C_2 Swan system, a large amount of data was obtained, and an extensive refit of molecular constants was performed with the inclusion of some recently obtained

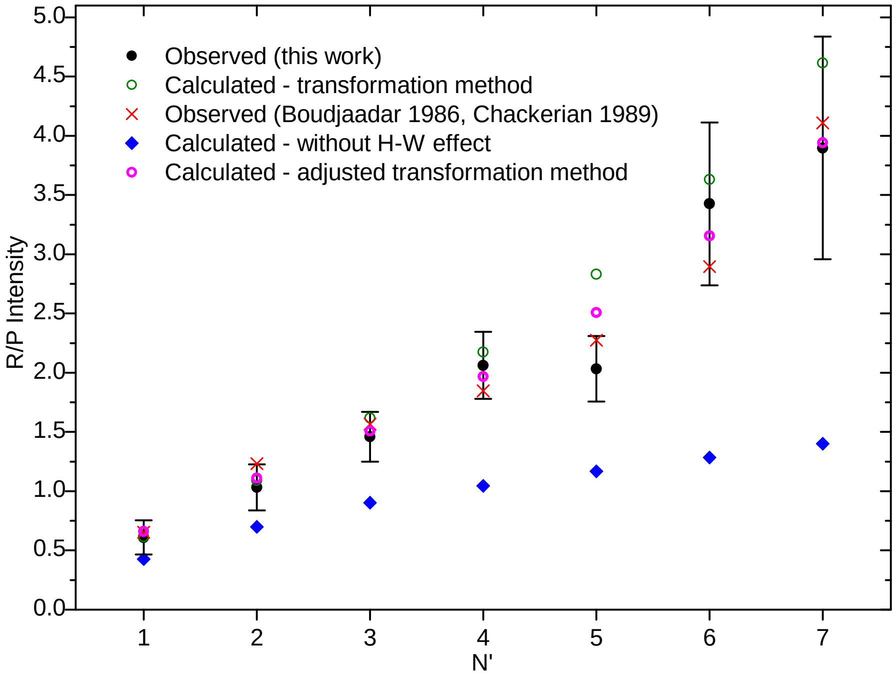

Figure 8.1 – H-W effect for the NH $X^3\Sigma^-$, (1,0) band, including the results with the adjusted transformation equation.

perturbation constants. Intensity calculations were performed as described above, and the final line list includes positions, f-values and Einstein A values for lines in all possible vibrational bands between v′=10 and v′=9, up to a maximum J of between 34 and 96, depending on the band. The line list previously in common use contained many incorrectly assigned lines, which means that many positions and intensities will be inaccurate, and any abundances resulting from its use may suffer from inaccuracies. This new line list provides the most comprehensive set of positions and intensities for the C_2 Swan system that is available.

An equivalent but much less extensive list was produced for the $^{12}C^{13}C$ Swan system, containing all possible rovibronic transitions between v=0-2 in both electronic states, up to J=60. It includes intensities and line position improvements, especially where v is greater than 0. A list with this many transitions and with this accuracy was not previously available.

The CN line list contains line positions, Einstein A-values and f-values for 295 possible vibrational bands (63 observed), and rotational lines with J up to between 25.5 and 120.5, depending on the band. Similar lists were produced for the ^{13}CN and $C^{15}N$ isotopologues. Previously available line lists have some substantial line position uncertainties (Jørgensen and Larsson, 1990; Hill et al., 2002; Kurucz, 2011), and are not as extensive. This work provides increased line position and intensity accuracy in an internally consistent data set. In particular, the rovibrational transitions previously available are based either on an experimental dipole moment from 1968 (Thomson and Dalby) or a dipole moment function from 1989 (Langhoff and Bauschlicher). The differences obtained from these new calculations are around 30% lower for the strongest (Δv=1) bands. This will result in significantly different abundances if calculated using the CN rovibrational transitions.

Another line list was calculated for the CP $A^2\Pi$-$X^2\Sigma^+$ system, for 75 possible vibrational bands with v$'$ and v$''$ up to 8, and J up to between 30.5 and 55.5, depending on the band. This appears to be the first available line list with both positions and intensities for the CP $A^2\Pi$-$X^2\Sigma^+$ system.

Previously available NH rovibrational intensities are based on an experimental dipole moment from 1974 (Scarl and Dalby, 1974), which based on all calculations since, appears to have suffered from some inaccuracy. A more accurate DMF has also been used in abundance calculations (Meyer and Rosmus, 1975), but these results, obtained from using a new DMF calculated at a higher level of theory, give intensities approximately 20% lower for the most important Δv=1 transitions. The line list contains transitions for all possible bands up to v=6, and for J up to between 25 and 44.

The final OH line list will contain all possible transitions in the Meinel (ground state rovibrational) system, with v$'$ and v$''$ up to 13, and J up to between 9.5 and 59.5. OH is arguably the most important molecule discussed in this thesis, due to its importance in both astronomy and atmospheric chemistry. Preliminary results suggest that the difference in line intensities compared to those previously available will be around 10% for the strongest Δv=1 transitions

8.3 Application to Astronomy

As discussed in Section 1, knowledge of molecular and elemental abundances in various astronomical environments is vital for the understanding of galactic, stellar and planetary evolution (Tsuji, 1986; Grevesse and Sauval, 1998; Bernath, 2009). They are generally obtained by observing absorption lines of atoms and molecules, where the light source is either that of the star being measured, or in the case of non-stellar observations, a star behind the absorbing system on the line of sight of the observation. The intensity of a particular spectral line can be used to calculate the concentration as described in Section 1.4. The quantities required are the lower state energy, the line position, an absolute line intensity, and the temperature. The line lists produced in this thesis contain the first three of these properties, and it is extremely useful for astronomers to have access to extensive and reliable lists such as these.

Astronomers will use these line lists to generate synthetic spectra for comparison with observations, and the more accurate the intensities are that they are provided with, the more accurate the spectral lines that they synthesise and the concentrations that they retrieve will be. Another factor that should be considered when evaluating the importance of these line lists and their accuracy, is that in reality multiple line lists will be used at once, due to the presence of the spectral features of many different atoms and molecules. This means that the new line lists will not only be useful for direct retrievals using the lines themselves, but also for more accurately taking into account the effects of these lines when they overlap with target lines of different species.

Transitions of all of the molecules studied in this thesis except for CP have been used to calculate elemental abundances as well as their own abundance (Eisenstein et al., 2011; Smith et al., 2013; Sneden et al., 2014; Asplund et al., 2009; Sauval et al., 1984; Meléndez, 2004; Asplund et al., 2004; Ram et al., 2014). For the calculation of oxygen and nitrogen abundances, CN, NH, and OH transitions are commonly used in conjunction with atomic transitions (Asplund et al., 2009). C_2 is sometimes used to calculate carbon abundances (Hema et al., 2012), but this is more often accomplished using CH and CN, and atomic C transitions (Asplund et al., 2009). C_2 transitions are commonly used to calculate the $^{12}C/^{13}C$ ratio in various cosmic environments (Cohen et al., 2006; Hema et al., 2012; Rousselot et al., 2012), which is another important parameter for understanding the evolution of astronomical systems (Busso et al., 1999). Transitions of ^{13}CN are also used for this purpose and are contained in one of the line lists produced in this thesis.

The C_2, CN, and OH lists have been used to calculate carbon, nitrogen, and oxygen abundances in the Sun, and good agreement with literature data has been observed (see Sections 3.7, 4.7, and 6.7 for more details). CN and C_2 are not normally used for such calculations because there is more oxygen than carbon in the solar photosphere, and as explained in Section 3.7, this means that carbon containing molecules (other than CO) will have low abundances. The fact that good agreement is seen with values calculated mainly using C and N atomic lines, and NH and CH lines, is good evidence for the reliability of these line lists. The oxygen abundance result was compared to values derived from atomic O lines, and this good agreement suggests that the new OH list can also be used with confidence.

Elemental abundances for other stars were calculated in the same studies, that were chosen as their conditions made them appropriate for studies of C_2, CN, and OH lines. Arcturus is a well studied, mildly metal-poor red giant (Ramírez and Allende Prieto, 2011). Its cool temperature and C/O ratio (in favour of oxygen) make it extremely well suited for studying OH lines, but neither of these properties are so extreme as to exclude a CN and C_2 analysis. Good agreement with literature values was seen for all three elements. Other stars analysed included two extremely metal-poor carbon stars, for which CN and C_2 lines were used, and a very metal-poor giant star, for which OH rovibrational lines were analysed. These were chosen firstly as carbon-containing molecules have relatively high abundances in carbon stars, and secondly as OH lines are stronger in this star than usual due to very little CO formation, a low temperature, and low C/O ratio. Again, good agreement with literature values was found for carbon, oxygen and nitrogen abundances, and for $^{12}C/^{13}C$ ratios, where calculated. For details of all of the results described here, see Sections 3.7, 4.7, and 6.7. Similar studies have not yet been performed with the NH line list, but this will be carried out in the near future.

All of the line lists that have been produced in this thesis are improvements over what was previously available. For the C_2 Swan list, many line positions had been assigned incorrectly (Tanabashi et al., 2007; Brooke et al., 2013), and although new positions were recently made available (Tanabashi et al., 2007), intensities had not yet been calculated based on the fully correctly assigned lines. The intensities that were available were also based on very old data (Querci et al., 1971), and this has often resulted in astronomers calculating their own intensities; for recent examples see Hema et al. (2012) and Rousselot et al. (2012). This new list, along with the new list for the $^{12}C^{13}C$ isotopologue, can now be used with confidence by astronomers to perform such studies as those described above.

For the CN lists, previously available line lists have some substantial line position uncertainties (Jørgensen and Larsson, 1990; Hill et al., 2002; Kurucz, 2011), and intensities were based on older (transition) dipole moment functions. The new lists are also self-consistent in terms of positions and intensities for all three electronic states and systems, and so astronomers can use this one list easily for most CN transitions.

For NH, the regularly used intensities in the JPL (Pickett et al., 1998) and CDMS

(Müller et al., 2001, 2005) catalogues are based on a dipole moment from 1974 (Scarl and Dalby), with which most more recent calculations disagree. When astronomers have not used this standard list, they have, like with C_2, opted to calculate their own intensities. For example, for the NH transitions used to calculate the nitrogen abundance in the Sun (Grevesse et al., 1990; Asplund et al., 2009), the authors used a DMF that is now quite old (Meyer and Rosmus, 1975). The new DMF, which was calculated at a higher level of theory is believed to be the most accurate currently available (Campbell et al., 2008), and it produces significantly different intensities (Section 5.5.4). Therefore, the new list would be very useful if adopted by astronomers in any reevaluation of the solar nitrogen abundance, and also in other stars and astronomical environments, particularly cool stars where there is more infrared radiation.

There was previously an OH line list available that was in standard use (Goldman et al., 1998), and so unlike for C_2 and NH, astronomers were not forced to produce their own intensities. It has, however, been shown that the new intensities are more accurate than in the previous list, based on comparisons to observed H-W ratios, an experimental lifetime (van de Meerakker et al., 2005), and experimental dipole moments (Peterson et al., 1984). This new list will be particularly useful to atmospheric chemists investigating OH abundances in the atmosphere or performing temperature retrievals using the OH airglow, and to astronomers who wish to calculate oxygen abundances. For stellar atmospheres, OH Meinel transitions will be most effective for cool stars with a low C/O ratio.

A specific example of the type of study for which the line lists would be extremely useful, other than the small-scale studies described above, is the APOGEE project (Eisenstein et al., 2011). This is a survey of over 100,000 red giants using transitions in the near-infrared, including lines of the CN $A^2\Pi$-$X^2\Sigma^+$ and $B^2\Sigma^+$-$X^2\Sigma^+$ systems, the OH Meinel system, and some lines from the C_2 Swan system. A master line list has been produced for this project in an easily accessible form, so that all of the individual studies will be consistent, and will not require any manual line intensity calculations. The new lists from this thesis are also presented in a self-consistent and easily accessible form, and if incorporated into such a master list, would provide the same benefits and more reliable results. There would also be less or no need for the mixing of multiple lists, as the line lists produced here span all of the transitions that are at all likely to be observed.

8.4 Further Work

There is further work that could build directly on what has been described in this thesis. The NH intensities will soon be updated to incorporate the changes to the transformation equation, and the OH work will continue as described. For the C_2 Swan system, the recalculation of the intensities with the inclusion of the H-W effect, the addition of more perturbation constants, and the use of the new transformation method would provide a more accurate list of positions and intensities. For the CN systems, the new transformation method will soon be used to update the line list, which will provide some improvements in the unobserved bands.

It has been observed that to obtain the best possible line positions it is often necessary to collect available experimental data from the literature, consider other effects such as local perturbations, and perform a refit of molecular constants. The ab initio calculation of the (T)DMF also requires specific considerations of the molecule and electronic state. It would be possible, however, to mostly automate the remainder of the calculations, if a large number of checks and comparisons were also automatically performed, and this is something that may be considered in the future. The whole method described in this thesis is shown as a flow chart in Figure 2.19, in which the parts that could be mostly automated are highlighted.

The recent OH work has helped to finalise the method of line intensity calculations, and this has been shown to be an efficient and effective way of combining experimental and theoretical data to create line lists for diatomic molecules containing line positions and intensities. Similar calculations could be performed for other molecules and systems using this method.

Line intensities have been a part of all of the work in this thesis, having been calculated in most of the projects, and they were also important in Chapter 7 for the retrieval of atmospheric concentrations of CO_2 and CH_4. Overall, line intensities are vital in a number of scientific fields, such as astronomy, combustion science, and atmospheric science; and the complex models that are created in these fields would not be possible without them.

Abbreviations

ACCURATE	Atmospheric Climate and Chemistry in the UTLS Region And climate Trends Explorer
ACE	Atmospheric Chemistry Experiment
ADC	Analogue/Digital Converter
CASSCF	Complete Active Space Self-Consistent Field
CDMS	Cologne Database for Molecular Spectroscopy
DMF	Dipole Moment Function
ESA	European Space Agency
FRQ	analogue 500 Hz square wave
FSR	Free Spectral Range
FTS	Fourier Transform Spectrometer
GPS	Global Positioning System
HITRAN	HIgh-resolution TRANsmission molecular absorption database
H-W	Herman-Wallis
IR	InfraRed
IRDAS-EXP	InfraRed Differential Absorption Spectroscopy - EXPeriment
JPL	Jet Propulsion Laboratory
LEO	Low Earth Orbit
ME	Matrix Element
MRCI	Multi-Reference Configuration Interaction
NOT	Nordic Optical Telescope

OGS	Optical Ground Station
ORM	Roque de los Muchachos Observatory
OT	Teide Observatory
PPS	Pulse Per Second
RCCSD(T)	spin Restricted Coupled Cluster Singles Doubles (Triples)
RKR	Rydberg-Klein-Rees
Rx	Receiver
SNR	SNR
SWIR	Short-Wave InfraRed
TDM	Transition Dipole Moment
TDMF	Transition Dipole Moment Function
Tx	Transmitter
UV	UltraViolet
VMR	Volume Mixing Ratio
WKB	Wentzel-Kramers-Brillouin
APOGEE	The Apache Point Observatory Galactic Evolution Experiment

Bibliography

Abrams, M. C., S. P. Davis, M. L. P. Rao, R. Engleman, Jr., and J. W. Brault. *Astrophys. J. Suppl. S.*, 93; 351, 1994. doi:10.1086/192058

Abrams, M. C., A. Goldman, M. R. Gunson, C. P. Rinsland, and R. Zander. *App. Optics*, 35; 2747, 1996. doi:10.1364/AO.35.002747

Adamczak, J. and D. L. Lambert. *Astrophys. J.*, 765; 155, 2013. doi:10.1088/0004-637X/765/2/155

Adams, F. C. and G. Laughlin. *Rev. Mod. Phys.*, 69; 337, 1997. doi:10.1103/RevModPhys.69.337

Afşar, M., C. Sneden, and B.-Q. For. *Astronom. J.*, 144; 20, 2012. doi:10.1088/0004-6256/144/1/20

Allen, M. G., R. D. Howe, and R. K. Hanson. *Opt. Lett.*, 11; 126, 1986. doi:10.1364/OL.11.000126

Allende Prieto, C., D. L. Lambert, and M. Asplund. *Astrophys. J. Lett.*, 556; L63, 2001. doi:10.1086/322874

Amiot, C. *Astrophys. J. Suppl. S.*, 52; 329, 1983. doi:10.1086/190870

Amiot, C., J. Chauville, and J.-P. Maillard. *J. Mol. Spectrosc.*, 75; 19, 1979

Amiot, C. and J. Verges. *Astrophys. J.*, 263; 993, 1982. doi:10.1086/160567

Anders, E. and N. Grevesse. *Geochim. Cosmochim. Acta*, 53; 197, 1989. doi:10.1016/0016-7037(89)90286-X

Aoki, W. and T. Tsuji. *Astron. Astrophys.*, 328; 175, 1997

Asplund, M., N. Grevesse, A. J. Sauval, C. Allende Prieto, and D. Kiselman. *Astron. Astrophys.*, 417; 751, 2004. doi:10.1051/0004-6361:20034328

Asplund, M., N. Grevesse, A. J. Sauval, and P. Scott. *Annu. Rev. Astron. Astrophys.*, 47; 481, 2009. doi:10.1146/annurev.astro.46.060407.145222

Atkinson, R. and J. Arey. *Chem. Rev.*, 103; 4605, 2003. doi:10.1021/cr0206420

Atreya, S. K. and Z. G. Gu. *J. Geophys. Res.*, 99; 13133, 1994. doi:10.1029/94JE01085

Aumann, H. H., M. T. Chahine, C. Gautier, M. D. Goldberg, E. Kalnay, L. M. McMillin, H. Revercomb, P. W. Rosenkranz, W. L. Smith, D. H. Staelin, L. L. Strow, and J. Susskind. *IEEE Trans. Geosci. Remote Sensing*, 41; 253, 2003. doi:10.1109/TGRS.2002.808356

Bakker, E. J. and D. L. Lambert. *Astrophys. J.*, 502; 417, 1998. doi:10.1086/305879

Bakwin, P. S., P. P. Tans, D. F. Hurst, and C. Zhao. *Tellus B*, 50; 401, 1998. doi:10.1034/j.1600-0889.1998.t01-4-00001.x

Baronavski, A. P. and J. R. McDonald. *J. Chem. Phys.*, 66; 3300, 1977. doi:10.1063/1.434306

Bauer, W., K. H. Becker, M. Bielefeld, and R. Meuser. *Chem. Phys. Lett.*, 123; 33, 1986. doi:10.1016/0009-2614(86)87008-7

Bauschlicher, Jr., C. W., S. R. Langhoff, and P. R. Taylor. *Astrophys. J.*, 332; 531, 1988. doi:10.1086/166675

Bayet, E., S. Viti, T. W. Hartquist, and D. A. Williams. *Astrophys. J.*, 417; 627, 2011. doi:10.1111/j.1365-2966.2011.19304.x

Bengtsson, P.-E., M. Aldn, S. Krll, and D. Nilsson. *Combust. Flame*, 82; 199 , 1990. doi:http://dx.doi.org/10.1016/0010-2180(90)90098-C

Bernath, P. F. *Spectra of atoms and molecules. 2nd ed.* (Oxford University Press, 2005)

Bernath, P. F. *Int. Rev. Phys. Chem.*, 28; 681, 2009. doi:10.1080/01442350903292442

Bernath, P. F. and T. Amano. *J. Mol. Spectrosc.*, 95; 359, 1982. doi:10.1016/0022-2852(82)90135-7

Bernath, P. F. and R. Colin. *J. Mol. Spectrosc.*, 257; 20, 2009. doi:10.1016/j.jms.2009.06.003

Bernath, P. F., C. T. McElroy, M. C. Abrams, C. D. Boone, M. Butler, C. Camy-Peyret, M. Carleer, C. Clerbaux, P.-F. Coheur, R. Colin, P. DeCola, M. DeMazière, J. R. Drummond, D. Dufour, W. F. J. Evans, H. Fast, D. Fussen, K. Gilbert, D. E. Jennings, E. J. Llewellyn, R. P. Lowe, E. Mahieu, J. C. McConnell, M. McHugh, S. D. McLeod, R. Michaud, C. Midwinter, R. Nassar, F. Nichitiu, C. Nowlan, C. P. Rinsland, Y. J. Rochon, N. Rowlands, K. Semeniuk, P. Simon, R. Skelton, J. J. Sloan, M.-A. Soucy, K. Strong, P. Tremblay, D. Turnbull, K. A. Walker, I. Walkty, D. A. Wardle, V. Wehrle, R. Zander, and J. Zou. *Geophys. Res. Lett.*, 32, 2005. doi:10.1029/2005GL022386

Bethlem, H. L. and W. Ubachs. *Faraday Discuss.*, 142; 25, 2009. doi:10.1039/b819099b

Bleekrode, R. and W. C. Nieuwpoort. *J. Chem. Phys.*, 43; 3680, 1965. doi:10.1063/1.1696536

Bornhauser, P., G. Knopp, T. Gerber, and P. P. Radi. *J. Mol. Spectrosc.*, 262; 69, 2010. doi:10.1016/j.jms.2010.05.008

Bornhauser, P., Y. Sych, G. Knopp, T. Gerber, and P. P. Radi. *J. Chem. Phys.*, 134; 044302, 2011. doi:10.1063/1.3526747

Boudjaadar, D., J. Brion, P. Chollet, G. Guelachvili, and M. Vervloet. *J. Mol. Spectrosc.*, 119; 352, 1986. doi:10.1016/0022-2852(86)90030-5

Brault, J. W., L. Testerman, N. Grevesse, A. J. Sauval, L. Delbouille, and G. Roland. *Astron. Astrophys.*, 108; 201, 1982

Brooke, J. S. A., P. F. Bernath, G. Kirchengast, C. B. Thomas, J.-G. Wang, K. A. Tereszchuk, G. González Abad, R. J. Hargreaves, C. A. Beale, J. J. Harrison, S. Schweitzer, V. Proschek, P. A. Martin, V. L. Kasyutich, C. Gerbig, O. Kolle, and A. Loescher. *Atmos. Meas. Tech.*, 5; 2309, 2012. doi:10.5194/amt-5-2309-2012

Brooke, J. S. A., P. F. Bernath, T. W. Schmidt, and G. B. Bacskay. *J. Quant. Spectrosc. Radiat. Transfer*, 124; 11, 2013. doi:10.1016/j.jqsrt.2013.02.025

Brooke, J. S. A., P. F. Bernath, C. M. Western, M. C. van Hemert, and G. C. Groenenboom. *J. Chem. Phys.*, 141; 054310, 2014*a*

Brooke, J. S. A., R. S. Ram, C. M. Western, D. W. Schwenke, G. Li, and P. F. Bernath. *Astrophys. J.Supp. Ser.*, 210; 23, 2014*b*. doi:10.1088/0067-0049/210/2/23

Brown, J. and A. Carrington. *Rotational Spectroscopy of Diatomic Molecules*. Cambridge Molecular Science (Cambridge University Press, 2003)

Brown, J. and A. Merer. *J. Mol. Spectrosc.*, 74; 488, 1979. doi:10.1016/0022-2852(79)90172-3

Brown, J. M. and B. J. Howard. *Mol. Phys.*, 31; 1517, 1976. doi:10.1080/00268977600101191

Burbidge, E. M., G. R. Burbidge, W. A. Fowler, and F. Hoyle. *Rev. Mod. Phys.*, 29; 547, 1957. doi:10.1103/RevModPhys.29.547

Busso, M., R. Gallino, and G. J. Wasserburg. *Annu. Rev. Astron. Astrophys.*, 37; 239, 1999. doi:10.1146/annurev.astro.37.1.239

Caffau, E., H.-G. Ludwig, M. Steffen, T. R. Ayres, P. Bonifacio, R. Cayrel, B. Freytag, and B. Plez. *Astron. Astrophys.*, 488; 1031, 2008. doi:10.1051/0004-6361:200809885

Callomon, J. H. and A. C. Gilby. *Can. J. Phys.*, 41; 995, 1963. doi:10.1139/p63-105

Campbell, W. C., G. C. Groenenboom, H.-I. Lu, E. Tsikata, and J. M. Doyle. *Phys. Rev. Lett.*, 100, 2008. doi:10.1103/PhysRevLett.100.083003

Campbell, W. C., E. Tsikata, H.-I. Lu, L. D. van Buuren, and J. M. Doyle. *Phys. Rev. Lett.*, 98; 213001, 2007. doi:10.1103/PhysRevLett.98.213001

Cantarella, E., F. Colot, and J. Liévin. *Phys. Scripta.*, 46; 489, 1992. doi:10.1088/0031-8949/46/6/003

Cartwright, D. C. and P. J. Hay. *Astrophys. J.*, 257; 383, 1982. doi:10.1086/159998

Casu, S. and C. Cecchi-Pestellini. *Astrophys. J.*, 749; 48, 2012. doi:10.1088/0004-637X/749/1/48

Chackerian, Jr., C., G. Guelachvili, A. López-Piñeiro, and R. H. Tipping. *J. Chem. Phys.*, 90; 641, 1989. doi:10.1063/1.456143

Chaffee, Jr., F. H. and B. L. Lutz. *Astrophys. J.*, 221; L91, 1978. doi:10.1086/182671

Child, S. *Semiclassical Mechanics with Molecular Applications* (Clarendon Press, Oxford, 1991)

Clerbaux, C., A. Boynard, L. Clarisse, M. George, J. Hadji-Lazaro, H. Herbin, D. Hurtmans, M. Pommier, A. Razavi, S. Turquety, C. Wespes, and P.-F. Coheur. *Atmos. Chem. Phys.*, 9; 6041, 2009

Climenhaga, J. L., B. L. Harris, J. T. Holts, and J. Smolinski. *Astrophys. J.*, 215; 836, 1977. doi:10.1086/155420

Cohen, J. G., A. McWilliam, S. Shectman, I. Thompson, N. Christlieb, J. Melendez, S. Ramirez, A. Swensson, and F.-J. Zickgraf. *Astronom. J.*, 132; 137, 2006. doi:10.1086/504597

Colin, R. and P. F. Bernath. *J. Mol. Spectrosc.*, 273; 30, 2012. doi:10.1016/j.jms.2012.01.007

Colin, R., P.-F. Coheur, M. Kiseleva, A. C. Vandaele, and P. F. Bernath. *J. Mol. Spectrosc.*, 214; 225, 2002. doi:10.1006/jmsp.2002.8591

Cooley, J. W. *Math. Comp.*, 15; 363, 1961. doi:10.1090/S0025-5718-1961-0129566-X

Crawford, I. A. and D. A. Williams. *Mon. Not. R. Astron. Soc.*, 291; L53, 1997

Crevoisier, C., M. Gloor, E. Gloaguen, L. W. Horowitz, J. L. Sarmiento, C. Sweeney, and P. P. Tans. *Tellus B*, 58; 366, 2006. doi:10.1111/j.1600-0889.2006.00214.x

Curtis, M. C. and P. J. Sarre. *J. Mol. Spectrosc.*, 114; 427, 1985. doi:10.1016/0022-2852(85)90235-8

Danylewych, L. L. and R. W. Nicholls. *Proc. R. Soc. Lond. A Math. Phys. Sci.*, 339; 197, 1974

Das, G., T. Janis, and A. C. Wahl. *J. Chem. Phys.*, 61; 1274, 1974. doi:10.1063/1.1682049

Das, G., A. C. Wahl, and W. J. Stevens. *J. Chem. Phys.*, 61; 433, 1974. doi:10.1063/1.1681663

Davis, S. P., M. C. Abrams, M. L. P. Rao, and J. W. Brault. *J. Opt. Soc. Am. B*, 8; 198, 1991. doi:10.1364/JOSAB.8.000198

Davis, S. P., M. C. Abrams, Sandalphon, J. W. Brault, and M. L. P. Rao. *J. Opt. Soc. Am. B*, 5; 1838, 1988. doi:10.1364/JOSAB.5.001838

de Brouckère, G. and D. Feller. *J. Phys. B*, 31; 5053, 1998. doi:10.1088/0953-4075/31/23/005

de Jong, W. A., R. J. Harrison, and D. A. Dixon. *J. Chem. Phys.*, 114; 48, 2001. doi:10.1063/1.1329891

Demille, D. *Phys. Rev. Lett.*, 88; 067901, 2002. doi:10.1103/PhysRevLett.88.067901

Deskevich, M. P., D. J. Nesbitt, and H.-J. Werner. *J. Chem. Phys.*, 120; 7281, 2004. doi:10.1063/1.1667468

Dhumwad, R. K., A. B. Patwardhan, V. T. Kulkarni, and M. I. Savadatti. *J. Mol. Spectrosc.*, 85; 177, 1981. doi:10.1016/0022-2852(81)90317-9

Dixon, T. A. and R. C. Woods. *J. Chem. Phys.*, 67; 3956, 1977

Dodd, J. A., S. J. Lipson, D. J. Flanagan, W. A. M. Blumberg, J. C. Person, and B. D. Green. *J. Chem. Phys.*, 94; 4301, 1991. doi:10.1063/1.460616

Douay, M., R. Nietmann, and P. F. Bernath. *J. Mol. Spectrosc.*, 131; 261, 1988. doi:10.1016/0022-2852(88)90237-8

Douglas, M. and N. M. Kroll. *Ann. Phys.*, 82; 89, 1974. doi:10.1016/0003-4916(74)90333-9

Dunham, J. L. *Phys. Rev.*, 41; 721, 1932. doi:10.1103/PhysRev.41.721

Dunning, Jr., T. H. *J. Chem. Phys.*, 90; 1007, 1989. doi:10.1063/1.456153

Duric, N., P. Erman, and M. Larsson. *Phys. Scripta*, 18; 39, 1978. doi:10.1088/0031-8949/18/1/012

Dyson, J. and D. Williams. *Physics of the Interstellar Medium* (Manchester University Press, 1980). URL `http://books.google.co.uk/books?id=BHi7AAAAIAAJ`

Eisenstein, D. J., D. H. Weinberg, E. Agol, H. Aihara, C. Allende Prieto, S. F. Anderson, J. A. Arns, É. Aubourg, S. Bailey, E. Balbinot, and et al. *Astronom. J.*, 142; 72, 2011. doi:10.1088/0004-6256/142/3/72

Emerson, D. *Interpreting Astronomical Spectra* (Wiley, 1996). URL `http://books.google.co.uk/books?id=avns1CRdaCYC`

Ewart, P. and S. V. O'Leary. *Opt. Lett.*, 11; 279, 1986. doi:10.1364/OL.11.000279

Farmer, C. B. and R. H. Norton. *A high-resolution atlas of the infrared spectrum of the sun and the earth atmosphere from space. A compilation of ATMOS spectra of the region from 650 to 4800 cm*$^{-1}$ *(2.3 to 16 μm). Vol. I. The Sun.* (National Aeronautics and Space Administration, Hampton, VA, USA. Langley Research Center, 1989)

Federman, S. R. and W. T. Huntress, Jr. *Astrophys. J.*, 338; 140, 1989. doi:10.1086/167187

Feller, D. and J. A. Sordo. *J. Chem. Phys.*, 112; 5604, 2000. doi:10.1063/1.481135

Ferrin, I. R. *Astrophys. Space Sci.*, 52; 11, 1977. doi:10.1007/BF00647154

Flores-Mijangos, J., J. M. Brown, F. Matsushima, H. Odashima, K. Takagi, L. R. Zink, and K. M. Evenson. *J. Mol. Spectrosc.*, 225; 189, 2004. doi:10.1016/j.jms.2004.02.026

Fowler, A. *Proc. Rpy. Soc. A*, 86; 118, 1912. doi:10.1098/rspa.1912.0006

Fray, N., Y. Bénilan, H. Cottin, M.-C. Gazeau, and J. Crovisier. *Planetary Space Sci.*, 53; 1243, 2005. doi:10.1016/j.pss.2005.06.005

Fujita, Y. *Jap. J. Astron. Geophys.*, 17; 17, 1939

Gaydon, A. G. *The spectroscopy of flames* (Wiley, 1957)

Geller, M., C. B. Farmer, R. H. Norton, A. J. Sauval, and N. Grevesse. *Astron. Astrophys.*, 249; 550, 1991

Gies, D. R. and D. L. Lambert. *Astrophys. J.*, 387; 673, 1992. doi:10.1086/171116

Goicoechea, J. R., N. J. Rodríguez-Fernández, and J. Cernicharo. *Astrophys. J.*, 600; 214, 2004. doi:10.1086/379704

Goldfield, E. M. and K. P. Kirby. *J. Chem. Phys.*, 87; 3986, 1987. doi:10.1063/1.452901

Goldman, A., W. G. Schoenfeld, D. Goorvitch, C. Chackerian, Jr., H. Dothe, F. Mélen, M. C. Abrams, and J. E. A. Selby. *J. Quant. Spectrosc. Radiat. Transf.*, 59; 453, 1998. doi:10.1016/S0022-4073(97)00112-X

Goulay, F., L. Nemes, P. E. Schrader, and H. A. Michelsen. *Mol. Phys.*, 108; 1013, 2010. doi:10.1080/00268971003627824

Goulay, F., P. E. Schrader, L. Nemes, M. A. Dansson, and H. A. Michelsen. *P. Combust. Inst.*, 32; 963 , 2009. doi:http://dx.doi.org/10.1016/j.proci.2008.05.030. URL `http://www.sciencedirect.com/science/article/pii/S1540748908001697`

Gredel, R., E. F. van Dishoeck, and J. H. Black. *Astron. Astrophys.*, 251; 625, 1991

Green, S. *Annu. Rev. Phys. Chem.*, 32; 103, 1981. doi:10.1146/annurev.pc.32.100181.000535

Greenstein, J. L. *Astrophys. J.*, 128; 106, 1958. doi:10.1086/146521

Grevesse, N., M. Asplund, and A. J. Sauval. *Space Sci. Rev.*, 130; 105, 2007. doi:10.1007/s11214-007-9173-7

Grevesse, N., D. L. Lambert, A. J. Sauval, E. F. van Dishoeck, C. B. Farmer, and R. H. Norton. *Astron. Astrophys.*, 232; 225, 1990

Grevesse, N. and A. J. Sauval. *Astron. Astrophys.*, 27; 29, 1973

Grevesse, N. and A. J. Sauval. *Space Sci. Rev.*, 85; 161, 1998. doi:10.1023/A:1005161325181

Grevesse, N., A. J. Sauval, and E. F. van Dishoeck. *Astron. Astrophys.*, 141; 10, 1984

Guelin, M., J. Cernicharo, G. Paubert, and B. E. Turner. *Astron. Astrophys.*, 230; L9, 1990

Hagan, L. G. *The absolute intensity of c_2 swan bands*. Thesis, California. Univ., Berkeley. Lawrence Radiation Lab., 1963

Halpern, J. B., Y. Huang, and T. Titarchuk. *Astrophys. Space Sci.*, 236; 11, 1996. doi:10.1007/BF00644317

Hase, F., L. Wallace, S. D. McLeod, J. J. Harrison, and P. F. Bernath. *J. Quant. Spectrosc. Radiat. Transfer*, 111; 521, 2010. doi:10.1016/j.jqsrt.2009.10.020

Hay, P. J. and T. H. Dunning, Jr. *J. Chem. Phys.*, 64; 5077, 1976. doi:10.1063/1.432180

Hedrosa, R. P., C. Abia, M. Busso, S. Cristallo, I. Domínguez, S. Palmerini, B. Plez, and O. Straniero. *Astrophys. J. Lett.*, 768; L11, 2013. doi:10.1088/2041-8205/768/1/L11

Heiles, C. E. *Astrophys. J.*, 151; 919, 1968. doi:10.1086/149493

Hema, B. P., G. Pandey, and D. L. Lambert. *Astrophys. J.*, 747; 102, 2012. doi:10.1088/0004-637X/747/2/102

Hempel, F., J. Röpcke, A. Pipa, and P. B. Davies. *Mol. Phys.*, 101; 589, 2003. doi:10.1080/0026897021000014929

Herbst, E. *J. Phys. Chem.A*, 109; 4017, 2005. doi:10.1021/jp050461c

Herman, R. and R. F. Wallis. *J. Chem. Phys.*, 23; 637, 1955. doi:10.1063/1.1742069

Herzberg, G., A. Lagerqvist, and C. Malmberg. *Can. J. Phys.*, 47; 2735, 1969. doi:10.1139/p69-335

Herzberg, G. and J. W. T. Spinks. *Molecular spectra and molecular structure. Volume I: Spectra of diatomic molecules* (Van Nostrand Reinhold, 1950)

Hess, B. A. *Phys. Rev. A*, 32; 756, 1985. doi:10.1103/PhysRevA.32.756

Hess, B. A. *Phys. Rev. A*, 33; 3742, 1986. doi:10.1103/PhysRevA.33.3742

Hill, V., B. Plez, R. Cayrel, T. C. Beers, B. Nordström, J. Andersen, M. Spite, F. Spite, B. Barbuy, P. Bonifacio, E. Depagne, P. François, and F. Primas. *Astron. Astrophys.*, 387; 560, 2002. doi:10.1051/0004-6361:20020434

Hirota, E., J. M. Brown, J. T. Hougen, T. Shida, and N. Hirota. *Pure Appl. Chem.*, 66; 571, 1994. doi:10.1351/pac199466030571

Hobbs, L. M. and B. Campbell. *Astrophys. J.*, 254; 108, 1982. doi:10.1086/159711

Hobbs, L. M., J. A. Thorburn, T. Oka, J. Barentine, T. P. Snow, and D. G. York. *Astrophys. J.*, 615; 947, 2004. doi:10.1086/424733

Hoekstra, S., M. Metsälä, P. C. Zieger, L. Scharfenberg, J. J. Gilijamse, G. Meijer, and S. Y. T. van de Meerakker. *Phys. Rev. A*, 76; 063408, 2007. doi:10.1103/PhysRevA.76.063408

Hollas, J. *Modern Spectroscopy* (Wiley, 2004)

Holweger, H. and E. A. Mueller. *Sol. Phys.*, 39; 19, 1974. doi:10.1007/BF00154968

Horká, V., S. Civiš, V. Špirko, and K. Kawaguchi. *Collect. Czech. Chem. Commun.*, 69; 73, 2004. doi:10.1135/cccc20040073

Hougen, J. T. *The calculation of rotational energy levels and rotational line intensities in diatomic molecules*. NBS Monograph 115, US Government Printing Office, Washington, D.C., 1970

Huang, Y., R. Lu, and J. B. Halpern. *Appl. Opt.*, 32; 981, 1993. doi:10.1364/AO.32.000981

Huber, K. P. and G. Herzberg. *Molecular spectra and molecular structure. Volume IV: Constants of diatomic molecules*. Molecular Spectra and Molecular Structure (Van Nostrand Reinhold, 1979)

Hübner, M., M. Castillo, P. B. Davies, and J. Röpcke. *Spectrochim. Acta A*, 61; 57, 2005. doi:10.1016/j.saa.2004.03.012

Hummon, M. T., W. C. Campbell, H.-I. Lu, E. Tsikata, Y. Wang, and J. M. Doyle. *Phys. Rev. A*, 78; 050702, 2008. doi:10.1103/PhysRevA.78.050702

Islami, K. and C. Amiot. *J. Mol. Spectrosc.*, 118; 132, 1986. doi:10.1016/0022-2852(86)90230-4

Ito, H., K. Kuchitsu, S. Yamamoto, and S. Saito. *Chem. Phys. Lett.*, 186; 539, 1991. doi:10.1016/0009-2614(91)90464-K

Ito, H., Y. Ozaki, K. Suzuki, T. Kondow, and K. Kuchitsu. *J. Mol. Spectrosc.*, 127; 143, 1988. doi:10.1016/0022-2852(88)90015-X

Ito, H., Y. Ozaki, K. Suzuki, T. Kondow, and K. Kuchitsu. *J. Chem. Phys.*, 96; 4195, 1992. doi:10.1063/1.462838

Jackson, W. M. *J. Chem. Phys.*, 61; 4177, 1974. doi:10.1063/1.1681715

Jackson, W. M. *J. Photochem.*, 5; 107, 1976. doi:10.1016/0047-2670(76)85014-9

Jakowski, J., S. Irle, and K. Morokuma. *Phys. Chem. Chem. Phys.*, 14; 6273, 2012. doi:10.1039/c1cp22035g

Janssen, L. M. C., P. S. Żuchowski, A. van der Avoird, G. C. Groenenboom, and J. M. Hutson. *Phys. Rev. A*, 83; 022713, 2011*a*. doi:10.1103/PhysRevA.83.022713

Janssen, L. M. C., A. van der Avoird, and G. C. Groenenboom. *Eur. Phys. J. D*, 65; 177, 2011*b*. doi:10.1140/epjd/e2011-20093-4

Janssen, L. M. C., A. van der Avoird, and G. C. Groenenboom. *Phys. Rev. Lett.*, 110; 063201, 2013. doi:10.1103/PhysRevLett.110.063201

Janssen, L. M. C., P. S. Żuchowski, A. van der Avoird, J. M. Hutson, and G. C. Groenenboom. *J. Chem. Phys.*, 134; 124309, 2011. doi:10.1063/1.3570596

Jeunehomme, M. *J. Chem. Phys.*, 42; 4086, 1965. doi:10.1063/1.1695898

Jørgensen, U. G. and M. Larsson. *Astron. Astrophys.*, 238; 424, 1990

Johnson, J. R., U. Fink, and H. P. Larson. *Astrophys. J.*, 270; 769, 1983. doi:10.1086/161168

Johnson, M. A., M. L. Alexander, I. Hertel, and W. C. Lineberger. *Chem. Phys. Lett.*, 105; 374, 1984. doi:10.1016/0009-2614(84)80044-5

Kaiser, R. I. *Chem. Rev.*, 102; 1309, 2002

Kaiser, R. I., N. Balucani, D. O. Charkin, and A. M. Mebel. *Chem. Phys. Lett.*, 382; 112, 2003. doi:10.1016/j.cplett.2003.10.023

Kajita, M. *Phys. Rev. A*, 74; 032710, 2006. doi:10.1103/PhysRevA.74.032710

Kajita, M. *Phys. Rev. A*, 74; 035403, 2006. doi:10.1103/PhysRevA.74.035403

Kaler, J. *Stars and Their Spectra: An Introduction to the Spectral Sequence* (Cambridge University Press, 1997)

Kappeler, F., H. Beer, and K. Wisshak. *Rep. Prog. Phys.*, 52; 945, 1989. doi:10.1088/0034-4885/52/8/002

Katayama, D. H., T. A. Miller, and V. E. Bondybey. *J. Chem. Phys.*, 71; 1662, 1979. doi:10.1063/1.438504

Kaźmierczak, M., M. R. Schmidt, A. Bondar, and J. Krełowski. *Mon. Not. R. Astron. Soc.*, 402; 2548, 2010. doi:10.1111/j.1365-2966.2009.16065.x

Keeling, C. D., R. B. Bacastow, A. E. Bain-Bridge, C. A. Ekdahl, Jr., P. R. Guenther, L. S. Waterman, and J. F. S. Chin. *Tellus*, 28; 538, 1976

Kendall, R. A., T. H. Dunning, Jr., and R. J. Harrison. *J. Chem. Phys.*, 96; 6796, 1992. doi:10.1063/1.462569

King, R. B. *Astrophys. J.*, 108; 429, 1948. doi:10.1086/145078

Kirchengast, G., P. F. Bernath, S. Buehler, G. Durry, L. Facheris, C. Gerbig, L. Haimberger, J. Harris, A. Hauchecorne, E. Kurölä, G. B. Larsen, R. Sausen, R. A. Anthes, M. E. Gorbunov, E. R. Kursinski, S. S. Leroy, K. Trenberth, B. Ran- del, J. Gille, and T. Tsuda. *ACCURATE - climate benchmark profiling of greenhouse gases and thermodynamic variables and wind from space (ESA Earth Explorer Opportunity Mission EE-8 proposal).* Technical report, Sci. Rep. No. 36, Wegener Center Verlag, Graz, Austria, 2010. URL `http://wegcwww.uni-graz.at/publ/wegcreports/2010/WCV-SciRep-No36-GKirchengastetal-Jul2010.pdf`

Kirchengast, G. and S. Schweitzer. *Geophys. Res. Lett.*, 38; L13701, 2011. doi:10.1029/2011GL047617

Klaus, T., S. Takano, and G. Winnewisser. *Astron. Astrophys.*, 322; L1, 1997

Klein, H., E. Klisch, G. Winnewisser, A. Knigshofen, and J. Hahn. *Z. Naturforsch. A*, 54; 187, 1999

Klein, O. *Z. Phys.*, 76; 226, 1932. doi:10.1007/BF01341814

Klisch, E., T. Klaus, S. P. Belov, G. Winnewisser, and E. Herbst. *Astron. Astrophys.*, 304; L5, 1995

Klochkova, V. G., R. Szczerba, and V. E. Panchuk. *Astron. Lett.*, 26; 88, 2000. doi:10.1134/1.20372

Knowles, P. and H. Wener. *Theor. Chim. Acta*, 84; 95, 1992. doi:10.1007/BF01117405

Knowles, P. J. and H.-J. Werner. *Chem. Phys. Lett.*, 115; 259, 1985. doi:10.1016/0009-2614(85)80025-7

Knowles, P. J. and H.-J. Werner. *Chem. Phys. Lett.*, 145; 514, 1988. doi:10.1016/0009-2614(88)87412-8

Knowles, P. J., H.-J. Werner, P. J. Hay, and D. C. Cartwright. *J. Chem. Phys.*, 89; 7334, 1988. doi:10.1063/1.455264

Kokkin, D. L., G. B. Bacskay, and T. W. Schmidt. *J. Chem. Phys.*, 126; 084302, 2007. doi:10.1063/1.2436879

Komhyr, W. D., T. B. Harris, L. S. Waterman, J. F. S. Chin, and K. W. Thoning. *J. Geophys. Res.*, 94; 8533, 1989. doi:10.1029/JD094iD06p08533

Kotlar, A. J., R. W. Field, J. I. Steinfeld, and J. A. Coxon. *J. Mol. Spectrosc.*, 80; 86, 1980. doi:10.1016/0022-2852(80)90272-6

Kurucz, R. L. *Can. J. Phys.*, 89; 417, 2011. doi:10.1139/p10-104

Lambert, D. L. and R. Beer. *Astrophys. J.*, 177; 541, 1972. doi:10.1086/151730

Lambert, D. L., J. A. Brown, K. H. Hinkle, and H. R. Johnson. *Astrophys. J.*, 284; 223, 1984. doi:10.1086/162401

Lambert, D. L. and A. C. Danks. *Astrophys. J.*, 268; 428, 1983. doi:10.1086/160969

Lambert, D. L., B. Gustafsson, K. Eriksson, and K. H. Hinkle. *Astrophys. J.Supp. Ser.*, 62; 373, 1986. doi:10.1086/191145

Lambert, D. L. and L. M. Ries. *Astrophys. J.*, 217; 508, 1977. doi:10.1086/155599

Langhoff, S. R., C. W. Bauschlicher, and P. R. Taylor. *J. Chem. Phys.*, 91; 5953, 1989. doi:10.1063/1.457413

Langhoff, S. R. and C. W. Bauschlicher, Jr. *Astrophys. J.*, 340; 620, 1989. doi:10.1086/167423

Langhoff, S. R., H.-J. Werner, and P. Rosmus. *J. Mol. Spectrosc.*, 118; 507, 1986. doi:10.1016/0022-2852(86)90186-4

Larsen, G. B., G. Kirchengast, and P. F. Bernath. *Science objectives and observational requirements of the ACCURATE mission concept*. Technical report, DMI/ESA IRDAS/ObsReq/Oct2009, Danish Meteorol. Inst., Copenhagen, Denmark, 2009. URL `http://due.esrin.esa.int/stse/files/project/131-176-149-94201138102155.pdf`

Larsson, M. *Astron. Astrophys.*, 128; 291, 1983

Larsson, M., P. E. M. Siegbahn, and H. Agren. *Astrophys. J.*, 272; 369, 1983. doi:10.1086/161302

Lavendy, H., G. Gandara, and J. M. Robbe. *J. Mol. Spectrosc.*, 106; 395, 1984. doi:10.1016/0022-2852(84)90170-X

Le Roy, R. J. *RKR1 2.0: A computer program implementing the first-order RKR method for determining diatomic molecule potential energy functions*. University of waterloo chemical physics research report, University of Waterloo, 2004. URL `<scienide2.uwaterloo.ca/∼rleroy/rkr/>`

Le Roy, R. J. *LEVEL 8.0: A computer program for solving the radial Schrödinger equation for bound and quasibound levels*. University of waterloo chemical physics research report, University of Waterloo, 2007. URL `<scienide2.uwaterloo.ca/∼rleroy/level/>`

Le Roy, R. J. and E. R. Vrscay. *Can. J. Phys.*, 53; 1560, 1975

Leach, S. *Can. J. Chem.*, 82; 730, 2004. doi:10.1139/v04-036

Leach, S. *Mon. Not. R. Anstron. Soc.*, 421; 1325, 2012. doi:10.1111/j.1365-2966.2011.20390.x

Lelieveld, J., F. J. Dentener, W. Peters, and M. C. Krol. *Atmos. Chem. Phys.*, 4; 2337, 2004

Lewen, F., S. Brünken, G. Winnewisser, M. Šimečková, and Š. Urban. *J. Mol. Spectrosc.*, 226; 113, 2004. doi:10.1016/j.jms.2004.03.012

Liou, K. N. *An introduction to atmospheric radiation, 2nd Edn.* (Elsevier, San Diego, California, 2002)

Litvak, M. M. and E. N. R. Kuiper. *Astrophys. J.*, 253; 622, 1982. doi:10.1086/159664

Lloyd, G. M. and P. Ewart. *J. Chem. Phys.*, 110; 385, 1999. doi:10.1063/1.478070

Lodders, K. and B. Fegley, Jr. *Icarus*, 155; 393, 2002. doi:10.1006/icar.2001.6740

Lu, R., Y. Huang, and J. B. Halpern. *Astrophys. J.*, 395; 710, 1992. doi:10.1086/171691

Luk, C. K. and R. Bersohn. *J. Chem. Phys.*, 58; 2153, 1973. doi:10.1063/1.1679482

Maihara, T., F. Iwamuro, T. Yamashita, D. N. B. Hall, L. L. Cowie, A. T. Tokunaga, and A. Pickles. *Astro. Soc. Pac.*, 105; 940, 1993. doi:10.1086/133259

Maillard, J. P., J. Chauville, and A. W. Mantz. *J. Mol. Spectrosc.*, 63; 120, 1976. doi:10.1016/0022-2852(67)90139-7

Martin-Drumel, M. A., O. Pirali, D. Balcon, P. Brchignac, P. Roy, and M. Vervloet. *Rev. Sci. Instr.*, 82; 113106, 2011. doi:http://dx.doi.org/10.1063/1.3660809

Mayer, P. and C. R. O'Dell. *Astrophys. J.*, 153; 951, 1968. doi:10.1086/149721

McQuarrie, D. *Quantum Chemistry* (University Science Books, 2008)

Meade, M. L. *J. Phys. E Sci. Inst.*, 15; 395, 1982. doi:10.1088/0022-3735/15/4/001

Meinel, I. A. B. *Astrophys. J.*, 111; 555, 1950. doi:10.1086/145296

Melen, F., A. J. Sauval, N. Grevesse, C. B. Farmer, C. Servais, L. Delbouille, and G. Roland. *J. Mol. Spectrosc.*, 174; 490, 1995. doi:10.1006/jmsp.1995.0018

Meléndez, J. *Astrophys. J.*, 615; 1042, 2004. doi:10.1086/424591

Meléndez, J. and B. Barbuy. *Astrophys. J.*, 575; 474, 2002. doi:10.1086/341142

Mentall, J. E. and R. W. Nicholls. *Proc. Phys. Soc.*, 86; 873, 1965. doi:10.1088/0370-1328/86/4/326

Meyer, D. M. and M. Jura. *Astrophys. J.*, 297; 119, 1985. doi:10.1086/163509

Meyer, D. M. and K. C. Roth. *Astrophys. J.Lett.*, 376; L49, 1991. doi:10.1086/186100

Meyer, W. and P. Rosmus. *J. Chem. Phys.*, 63; 2356, 1975. doi:10.1063/1.431665

Mies, F. H. *J. Mol. Spectrosc.*, 53; 150, 1974. doi:10.1016/0022-2852(74)90125-8

Milam, S. N., D. T. Halfen, E. D. Tenenbaum, A. J. Apponi, N. J. Woolf, and L. M. Ziurys. *Astrophys. J.*, 684; 618, 2008. doi:10.1086/589135

Miller, J. A. and C. T. Bowman. *Prog. Energy Combust. Sci.*, 15; 287, 1989. doi:10.1016/0360-1285(89)90017-8

Mitrushchenkov, A. and H.-J. Werner. *Mol. Phys.*, 105; 1239, 2007. doi:10.1080/00268970701326978

Moses, J. I., C. Visscher, J. J. Fortney, A. P. Showman, N. K. Lewis, C. A. Griffith, S. J. Klippenstein, M. Shabram, A. J. Friedson, M. S. Marley, and R. S. Freedman. *Astrophys. J.*, 737; 15, 2011. doi:10.1088/0004-637X/737/1/15

Muenter, J. S. *J. Mol. Spectrosc.*, 55; 490, 1975. doi:10.1016/0022-2852(75)90287-8

Müller, H. S. P., F. Schlöder, J. Stutzki, and G. Winnewisser. *J. Mol. Struct.*, 742; 215, 2005. doi:10.1016/j.molstruc.2005.01.027

Müller, H. S. P., S. Thorwirth, D. A. Roth, and G. Winnewisser. *Astron. Astrophys.*, 370; L49, 2001. doi:10.1051/0004-6361:20010367

Mumma, M. J. and S. B. Charnley. *Annu. Rev. Astron. Astrophys.*, 49; 471, 2011. doi:10.1146/annurev-astro-081309-130811

Nakajima, M., J. A. Joester, N. I. Page, N. J. Reilly, G. B. Bacskay, T. W. Schmidt, and S. H. Kable. *J. Chem. Phys.*, 131; 044301, 2009. doi:10.1063/1.3175013

Naulin, C., M. Costes, and G. Dorthe. *Chem. Phys. Lett.*, 143; 496, 1988. doi:10.1016/0009-2614(88)87402-5

Nelson, D. D., A. Schiffman, D. J. Nesbitt, J. J. Orlando, and J. B. Burkholder. *J. Chem. Phys.*, 93; 7003, 1990. doi:10.1063/1.459476

Nelson, Jr., D. D., A. Schiffman, D. J. Nesbitt, and D. J. Yaron. *J. Chem. Phys.*, 90; 5443, 1989. doi:10.1063/1.456450

Nemes, L. and S. Irle. *Spectroscopy, dynamics and molecular theory of carbon plasmas and vapors: Advances in the understanding of the most complex high-temperature elemental system* (World Scientific, 2011)

Neogrády, P., M. Medvěd, I. Černušák, and M. Urban. *Mol. Phys.*, 100; 541, 2002. doi:10.1080/00268970110095660

Nishi, N., H. Shinohara, and I. Hanazaki. *J. Chem. Phys.*, 77; 246, 1982. doi:10.1063/1.443648

Nyholm, K., M. Kaivola, and C. G. Aminoff. *Opt. Comm.*, 107; 406, 1994. doi:10.1016/0030-4018(94)90356-5

Nyholm, K., M. Kaivola, and C. G. Aminoff. *Appl. Phys. B*, 60; 5, 1995. doi:10.1007/BF01082066

Oliva, E. and L. Origlia. *Astron. Astrophys.*, 254; 466, 1992

Ozaki, Y., H. Ito, K. Suzuki, T. Kondow, and K. Kuchitsu. *Chem. Phys.*, 80; 85, 1983*a*. doi:10.1016/0301-0104(83)85170-2

Ozaki, Y., T. Nagata, K. Suzuki, T. Kondow, and K. Kuchitsu. *Chem. Phys.*, 80; 73, 1983*b*. doi:10.1016/0301-0104(83)85169-6

Paldus, J. and X. Z. Li. *Can. J. Chem.*, 74; 918, 1996. doi:10.1139/v96-101

Peterson, K. I., G. T. Fraser, and W. Klemperer. *Can. J. Phys.*, 62; 1502, 1984. doi:10.1139/p84-196

Phillips, J. G. *Astrophys. J.*, 125; 153, 1957. doi:10.1086/146290

Phillips, J. G. *J. Mol. Spectrosc.*, 28; 233, 1968. doi:10.1016/0022-2852(68)90008-8

Phillips, J. G. and S. P. Davis. *The Swan system of the* C_2 *molecule. The spectrum of the HgH molecule* (U. California Press, 1968)

Piccioni, G., P. Drossart, L. Zasova, A. Migliorini, J.-C. Gérard, F. P. Mills, A. Shakun, A. García Muñoz, N. Ignatiev, D. Grassi, V. Cottini, F. W. Taylor, S. Erard, and Virtis-Venus Express Technical Team. *Astron. Astrophys.*, 483; L29, 2008. doi:10.1051/0004-6361:200809761

Pickett, H. M., R. L. Poynter, E. A. Cohen, M. L. Delitsky, J. C. Pearson, and H. S. P. Müller. *J. Quant. Spectrosc. Radiat. Transfer*, 60; 883, 1998. doi:10.1016/S0022-4073(98)00091-0

Plez, B. *unpublished line list of the CN red system*, 2011

Prasad, C. V. V. and P. F. Bernath. *Astrophys. J.*, 426; 812, 1994. doi:10.1086/174118

Prinn, R. G., R. F. Weiss, B. R. Miller, J. Huang, F. N. Alyea, D. M. Cunnold, P. J. Fraser, D. E. Hartley, and P. G. Simmonds. *Science*, 269; 187, 1995. doi:10.1126/science.269.5221.187

Proschek, V., G. Kirchengast, and S. Schweitzer. *Atmos. Meas. Tech.*, 4; 2035, 2011. doi:10.5194/amt-4-2035-2011

Querci, F., M. Querci, and V. G. Kunde. *Astron. Astrophys.*, 15; 256, 1971

Radford, H. E. and M. M. Litvak. *Chem. Phys. Lett.*, 34; 561, 1975. doi:10.1016/0009-2614(75)85562-X

Ram, R. S. and P. F. Bernath. *J. Mol. Spectrosc.*, 122; 282, 1987. doi:10.1016/0022-2852(87)90005-1

Ram, R. S. and P. F. Bernath. *J. Mol. Spectrosc.*, 260; 115, 2010. doi:10.1016/j.jms.2010.01.006

Ram, R. S. and P. F. Bernath. *Astrophys. J. Suppl. S.*, 194; 34, 2011. doi:10.1088/0067-0049/194/2/34

Ram, R. S. and P. F. Bernath. *J. Mol. Spectrosc.*, 274; 22, 2012. doi:10.1016/j.jms.2012.03.008

Ram, R. S., P. F. Bernath, and K. H. Hinkle. *J. Chem. Phys.*, 110; 5557, 1999. doi:10.1063/1.478453

Ram, R. S., J. S. A. Brooke, P. F. Bernath, C. Sneden, and S. Lucatello. *Astrophys. J. Suppl. S.*, 211; 5, 2014. doi:10.1088/0067-0049/211/1/5

Ram, R. S., J. S. A. Brooke, C. M. Western, and P. F. Bernath. *J. Quant. Spectrosc. Radiat. Transfer*, 138; 107, 2014. doi:10.1016/j.jqsrt.2014.01.030

Ram, R. S., S. P. Davis, L. Wallace, R. Engleman, D. R. T. Appadoo, and P. F. Bernath. *J. Mol. Spectrosc.*, 237; 225, 2006. doi:10.1016/j.jms.2006.03.016

Ram, R. S., S. Tam, and P. F. Bernath. *J. Mol. Spectrosc.*, 152; 89, 1992. doi:10.1016/0022-2852(92)90119-9

Ram, R. S., L. Wallace, and P. F. Bernath. *J. Mol. Spectrosc.*, 263; 82, 2010*a*. doi:10.1016/j.jms.2010.07.002

Ram, R. S., L. Wallace, K. Hinkle, and P. F. Bernath. *Astrophys. J. Suppl. S.*, 188; 500, 2010*b*. doi:10.1088/0067-0049/188/2/500

Ramírez, I. and C. Allende Prieto. *Astrophys. J.*, 743; 135, 2011. doi:10.1088/0004-637X/743/2/135

Rayner, P. J. and D. M. O'Brien. *Geophys. Res. Lett.*, 28; 175, 2001. doi:10.1029/2000GL011912

Rees, A. L. G. *Proc. Phys. Soc.*, 59; 998, 1947. doi:10.1088/0959-5309/59/6/310

Ridgway, S. T. and J. W. Brault. *Annu. Rev. Astron. Astrophys.*, 22; 291, 1984. doi:10.1146/annurev.aa.22.090184.001451

Riechers, D. A., F. Walter, P. Cox, C. L. Carilli, A. Weiss, F. Bertoldi, and R. Neri. *Astrophys. J.*, 666; 778, 2007. doi:10.1086/520335

Riffel, R., M. G. Pastoriza, A. Rodríguez-Ardila, and C. Maraston. *Astrophys. J. Lett.*, 659; L103, 2007. doi:10.1086/517999

Roach, F. E. *Astrophys. J.*, 89; 99, 1939. doi:10.1086/144022

Robinson, A., J. M. Brown, J. Flores-Mijangos, L. Zink, and M. Jackson. *Mol. Phys.*, 105; 639, 2007. doi:10.1080/00268970601162085

Rosmus, P. and H.-J. Werner. *J. Mol. Struct.*, 60; 405, 1980. doi:10.1016/0022-2860(80)80099-8

Rothman, L. S., I. E. Gordon, Y. Babikov, A. Barbe, D. Chris Benner, P. F. Bernath, M. Birk, L. Bizzocchi, V. Boudon, L. R. Brown, A. Campargue, K. Chance, E. A. Cohen, L. H. Coudert, V. M. Devi, B. J. Drouin, A. Fayt, J.-M. Flaud, R. R. Gamache, J. J. Harrison, J.-M. Hartmann, C. Hill, J. T. Hodges, D. Jacquemart, A. Jolly, J. Lamouroux, R. J.

Le Roy, G. Li, D. A. Long, O. M. Lyulin, C. J. Mackie, S. T. Massie, S. Mikhailenko, H. S. P. Müller, O. V. Naumenko, A. V. Nikitin, J. Orphal, V. Perevalov, A. Perrin, E. R. Polovtseva, C. Richard, M. A. H. Smith, E. Starikova, K. Sung, S. Tashkun, J. Tennyson, G. C. Toon, V. G. Tyuterev, and G. Wagner. *J. Quant. Spectrosc. Radiat. Transf.*, 130; 4, 2013. doi:10.1016/j.jqsrt.2013.07.002

Rothman, L. S., I. E. Gordon, A. Barbe, D. C. Benner, P. F. Bernath, M. Birk, V. Boudon, L. R. Brown, A. Campargue, J.-P. Champion, K. Chance, L. H. Coudert, V. Dana, V. M. Devi, S. Fally, J.-M. Flaud, R. R. Gamache, A. Goldman, D. Jacquemart, I. Kleiner, N. Lacome, W. J. Lafferty, J.-Y. Mandin, S. T. Massie, S. N. Mikhailenko, C. E. Miller, N. Moazzen-Ahmadi, O. V. Naumenko, A. V. Nikitin, J. Orphal, V. I. Perevalov, A. Perrin, A. Predoi-Cross, C. P. Rinsland, M. Rotger, M. Šimečková, M. A. H. Smith, K. Sung, S. A. Tashkun, J. Tennyson, R. A. Toth, A. C. Vandaele, and J. Vander Auwera. *J. Quant. Spectrosc. Radiat. Transf.*, 110; 533, 2009. doi:10.1016/j.jqsrt.2009.02.013

Rothman, L. S., D. Jacquemart, A. Barbe, D. C. Benner, M. Birk, L. R. Brown, M. R. Carleer, C. Chackerian, Jr., K. Chance, L. H. Coudert, V. Dana, V. M. Devi, J. M. Flaud, R. R. Gamache, A. Goldman, J. M. Hartmann, K. W. Jucks, A. G. Maki, J. Y. Mandin, S. T. Massie, J. Orphal, A. Perrin, C. P. Rinsland, M. A. H. Smith, J. Tennyson, R. N. Tolchenov, R. A. Toth, J. V. Auwera, P. Varanasi, and G. Wagner. *J. Quant. Spectrosc. Radiat. Transfer*, 96; 139, 2005. doi:10.1016/j.jqsrt.2004.10.008

Rothman, L. S., C. P. Rinsland, A. Goldman, S. T. Massie, D. P. Edwards, J.-M. Flaud, A. Perrin, C. Camy-Peyret, V. Dana, J.-Y. Mandin, J. Schroeder, A. McCann, R. R. Gamache, R. B. Wattson, K. Yoshino, K. Chance, K. Jucks, L. R. Brown, V. Nemtchinov, and P. Varanasi. *J. Quant. Spectrosc. Radiat. Transf.*, 60; 665, 1998. doi:10.1016/S0022-4073(98)00078-8

Rousselot, P., E. Jehin, J. Manfroid, and D. Hutsemékers. *Astron. Astrophys.*, 545; A24, 2012. doi:10.1051/0004-6361/201219265

Russell, H. N. *Astrophys. J.*, 79; 317, 1934. doi:10.1086/143539

Rydberg, R. *Z. Phys.*, 73; 376, 1932. doi:10.1007/BF01341146

Rydberg, R. *Z. Phys.*, 80; 514, 1933. doi:10.1007/BF02057312

Saito, S., S. Yamamoto, K. Kawaguchi, M. Ohishi, H. Suzuki, S.-I. Ishikawa, and N. Kaifu. *Astrophys. J.*, 341; 1114, 1989. doi:10.1086/167570

Sauval, A. J., N. Grevesse, R. Zander, J. W. Brault, and G. M. Stokes. *Astrophys. J.*, 282; 330, 1984. doi:10.1086/162206

Savage, C., A. J. Apponi, L. M. Ziurys, and S. Wyckoff. *Astrophys. J.*, 578; 211, 2002. doi:10.1086/342468

Saveliev, A. V., W. Merchan-Merchan, and L. A. Kennedy. *Combust. Flame*, 135; 27 , 2003. doi:http://dx.doi.org/10.1016/S0010-2180(03)00142-1. URL `http://www.sciencedirect.com/science/article/pii/S0010218003001421`

Scarl, E. A. and F. W. Dalby. *Can. J. Phys.*, 52; 1429, 1974

Schatz, G. and M. Ratner. *Quantum Mechanics in Chemistry* (Dover Publications, 2002)

Schmidt, T. W. and G. B. Bacskay. *J. Chem. Phys.*, 127; 234310, 2007. doi:10.1063/1.2806988

Schneising, O., M. Buchwitz, M. Reuter, J. Heymann, H. Bovensmann, and J. P. Burrows. *Atmos. Chem. Phys.*, 11; 2863, 2011. doi:10.5194/acp-11-2863-2011

Schuck, T. J., C. A. M. Brenninkmeijer, F. Slemr, I. Xueref-Remy, and A. Zahn. *Atmos. Meas. Tech.*, 2; 449, 2009

Schweitzer, S., G. Kirchengast, and V. Proschek. *Atmos. Meas. Tech.*, 4; 2273, 2011*a*. doi:10.5194/amt-4-2273-2011

Schweitzer, S., G. Kirchengast, M. Schwaerz, J. Fritzer, and M. E. Gorbunov. *J. Geophys. Res.*, 116; D10301, 2011*b*. doi:10.1029/2010JD014850

Schwenke, D. *Mol. Phys.*, 108; 2751, 2010. doi:10.1080/00268976.2010.523712

Scott, P., M. Asplund, N. Grevesse, and A. J. Sauval. *Astrophys. J. Lett.*, 691; L119, 2009. doi:10.1088/0004-637X/691/2/L119

Settersten, T. B., R. L. Farrow, and J. A. Gray. *Chem. Phys. Lett.*, 369; 584, 2003. doi:10.1016/S0009-2614(03)00022-8

Shi, D., H. Liu, X. Zhang, J. Sun, Z. Zhu, and Y. Liu. *J. Mol. Struct.: THEOCHEM*, 956; 10, 2010. doi:10.1016/j.theochem.2010.06.015

Sivjee, G. G. and R. M. Hamwey. *J. Geophys. Res.*, 92; 4663, 1987. doi:10.1029/JA092iA05p04663

Skatrud, D. D., F. C. De Lucia, G. A. Blake, and K. V. L. N. Sastry. *J. Mol. Spectrosc.*, 99; 35, 1983. doi:10.1016/0022-2852(83)90290-4

Smith, V. V., K. Cunha, M. D. Shetrone, S. Meszaros, C. Allende Prieto, D. Bizyaev, A. Garcìa Pèrez, S. R. Majewski, R. Schiavon, J. Holtzman, and J. A. Johnson. *Astrophys. J.*, 765; 16, 2013. doi:10.1088/0004-637X/765/1/16

Smith, V. V. and D. L. Lambert. *Astrophys. J.*, 311; 843, 1986. doi:10.1086/164823

Smoot, L. D., S. C. Hill, and H. Xu. *Prog. Energy Combust. Sci.*, 24; 385, 1998

Sneden, C. and D. L. Lambert. *Astrophys. J.*, 259; 381, 1982. doi:10.1086/160175

Sneden, C., S. Lucatello, R. S. Ram, J. S. A. Brooke, and P. F. Bernath. *Astrophys. J. Suppl. S.*, 213, 2014

Solomon, S., D. Qin, M. Manning, Z. Chen, M. Marquis, K. B. Averyt, M. Tignor, and H. L. Miller. In S. Solomon, D. Qin, M. Manning, Z. Chen, M. Marquis, K. B. Averyt, M. Tignor, and H. L. E. Miller, editors, *Climate change 2007: The physical science basis, Contribution of Working Group I to the Fourth Assessment Report of the Intergovernmental Panel on Climate Change - IPCC* (Cambridge University Press, 2007)

Sorkhabi, O., V. M. Blunt, H. Lin, M. F. A'Hearn, H. A. Weaver, C. Arpigny, and W. M. Jackson. *Planet Space Sci.*, 45; 721, 1997. doi:10.1016/S0032-0633(97)00077-9

Souza, S. P. and B. L. Lutz. *Astrophys. J.*, 216; L49, 1977. doi:10.1086/182507

Stallcop, J. R., C. W. Bauschlicher, Jr., H. Partridge, S. R. Langhoff, and E. Levin. *J. Chem. Phys.*, 97; 5578, 1992. doi:10.1063/1.463765

Stevens, W. J., G. Das, A. C. Wahl, M. Krauss, and D. Neumann. *J. Chem. Phys.*, 61; 3686, 1974. doi:10.1063/1.1682554

Suntzeff, N. B. *Astrophys. J. Suppl. S.*, 47; 1, 1981. doi:10.1086/190750

Suzuki, T., S. Saito, and E. Hirota. *J. Mol. Spectrosc.*, 113; 399, 1985. doi:10.1016/0022-2852(85)90278-4

Swain, M. R., G. Vasisht, G. Tinetti, J. Bouwman, P. Chen, Y. Yung, D. Deming, and P. Deroo. *Astrophys. J. Lett.*, 690; L114, 2009. doi:10.1088/0004-637X/690/2/L114

Swings, P. and A. McKellar. *Astrophys. J.*, 108; 458, 1948. doi:10.1086/145081

Taherian, M. R. and T. G. Slanger. *J. Chem. Phys.*, 81; 3814, 1984. doi:10.1063/1.448163

Tanabashi, A. and T. Amano. *J. Mol. Spectrosc.*, 215; 285, 2002. doi:10.1006/jmsp.2002.8645

Tanabashi, A., T. Hirao, T. Amano, and P. F. Bernath. *Astrophys. J. Suppl. S.*, 169; 472, 2007

Temelso, B., E. F. Valeev, and C. D. Sherrill. *J. Phys. Chem. A*, 108; 3068, 2004. doi:10.1021/jp036933+

Thomson, R. and F. W. Dalby. *Can. J. Phys.*, 46; 2815, 1968. doi:10.1139/p68-652

Treffers, R. R. *Astrophys. J.*, 196; 883, 1975. doi:10.1086/153480

Tsuji, T. *Annu. Rev. Astron. Astrophys.*, 24; 89, 1986. doi:10.1146/annurev.aa.24.090186.000513

Turnbull, D. N. and R. P. Lowe. *J. Chem. Phys.*, 89; 2763, 1988. doi:10.1063/1.455028

Turner, B. E. and R. H. Gammon. *Astrophys. J.*, 198; 71, 1975. doi:10.1086/153577

Tyte, D. C., S. H. Innanen, and R. W. Nicholls. *Identification atlas of molecular spectra, vol.5. the* c_2 $d^3\pi_g$-$a^3\pi_u$ *swan system*. Technical report, York University, Toronto, 1967

Uitenbroek, H. and A. Tritschler. *Astron. Astrophys.*, 462; 1157, 2007. doi:10.1051/0004-6361:20066286

Urban, M., J. Watts, and R. Bartlett. *Int. J. Quantum Chem.*, 52; 211, 1994. doi:10.1002/qua.560520121

Ursin, R., F. Tiefenbacher, T. Schmitt-Manderbach, H. Weier, T. Scheidl, M. Lindenthal, B. Blauensteiner, T. Jennewein, J. Perdigues, P. Trojek, B. Ömer, M. Fürst, M. Meyenburg, J. Rarity, Z. Sodnik, C. Barbieri, H. Weinfurter, and A. Zeilinger. *Nat. Phys.*, 3; 481, 2007. doi:10.1038/nphys629

van de Meerakker, S., N. Vanhaecke, M. van der Loo, G. Groenenboom, and G. Meijer. *Phys. Rev. Lett.*, 95; 013003, 2005. doi:10.1103/PhysRevLett.95.013003 van den Heuvel, F. C., W. L. Meerts, and A. Dymanus. *Chem. Phys. Lett.*, 92; 215, 1982. doi:10.1016/0009-2614(82)80262-5

van der Loo, M. P. J. and G. C. Groenenboom. *J. Chem. Phys.*, 128; 159902, 2008. doi:10.1063/1.2899016

Vardya, M. S. *Annu. Rev. Astron. Astrophys.*, 8; 87, 1970. doi:10.1146/annurev.aa.08.090170.000511

Vermeulen, A. T., A. Hensen, M. E. Popa, W. C. M. van den Bulk, and P. A. C. Jongejan. *Atmos. Meas. Tech.*, 4; 617, 2011. doi:10.5194/amt-4-617-2011

Wallace, L., K. Hinkle, and W. Livingston. *An atlas of the spectrum of the solar photosphere from 13,500-28,000 cm^{-1} (3570 to 7405 Å)*. Technical report, N.S.O. Technical Report # 98-001, National Solar Observatory, Tucson, 1998*a*. URL `ftp://ftp.noao.edu/fts/viratl/`

Wallace, L., K. Hinkle, and W. Livingston. *An atlas of the spectrum of the solar photosphere from 8900-13600 cm^{-1} (7350 to 11230 Å)*. Technical report, N.S.O. Technical Report # 93-001, National Solar Observatory, Tucson, 1998*b*. URL `ftp://ftp.noao.edu/fts/niratl/`

Wallerstein, G. and G. R. Knapp. *Annu. Rev. Astron. Astrophys.*, 36; 369, 1998. doi:10.1146/annurev.astro.36.1.369

Wallis, A. O. G. and J. M. Hutson. *Phys. Rev. Lett.*, 103; 183201, 2009. doi:10.1103/PhysRevLett.103.183201

Wallis, A. O. G., E. J. J. Longdon, P. S. Żuchowski, and J. M. Hutson. *Eur. Phys. J. D*, 65; 151, 2011. doi:10.1140/epjd/e2011-20025-4

Wang, M., C. Henkel, Y.-N. Chin, J. B. Whiteoak, M. Hunt Cunningham, R. Mauersberger, and D. Muders. *Astron. Astrophys.*, 422; 883, 2004. doi:10.1051/0004-6361:20035722

Wayne, F. D. and H. E. Radford. *Mol. Phys.*, 32; 1407, 1976. doi:10.1080/00268977600102771

Werner, H.-J. and P. J. Knowles. *J. Chem. Phys.*, 82; 5053, 1985. doi:10.1063/1.448627

Werner, H.-J. and P. J. Knowles. *J. Chem. Phys.*, 89; 5803, 1988. doi:10.1063/1.455556

Werner, H.-J., P. J. Knowles, G. Knizia, F. R. Manby, M. Schütz, P. Celani, T. Korona, R. Lindh, A. Mitrushenkov, G. Rauhut, K. R. Shamasundar, T. B. Adler, R. D. Amos, A. Bernhardsson, A. Berning, D. L. Cooper, M. J. O. Deegan, A. J. Dobbyn, F. Eckert, E. Goll, C. Hampel, A. Hesselmann, G. Hetzer, T. Hrenar, G. Jansen, C. Köppl, Y. Liu, A. W. Lloyd, R. A. Mata, A. J. May, S. J. McNicholas, W. Meyer, M. E. Mura, A. Nicklass, D. P. O'Neill, P. Palmieri, D. Peng, K. Pflüger, R. Pitzer, M. Reiher, T. Shiozaki, H. Stoll, A. J. Stone, R. Tarroni, T. Thorsteinsson, and M. Wang. *MOLPRO, version 2012.1, a package of ab initio programs*. 2012. http://www.molpro.net/

Werner, H.-J., P. J. Knowles, R. Lindh, F. R. Manby, M. Schütz, P. Celani, T. Korona, G. Rauhut, R. D. Amos, A. Bernhardsson, A. Berning, D. L. Cooper, M. J. O. Deegan, A. J. Dobbyn, F. Eckert, C. Hampel, Lloyd, S. J. McNicholas, W. Meyer, M. E. Mura, A. Nicklass, P. Palmieri, R. Pitzer, U. Schumann, H. Stoll, A. J. Stone, R. Tarroni, and T. Thorsteinsson. *Molpro, version 2006.1, a package of ab initio programs*. 2006. URL `http://www.molpro.net/`

Weselak, T., G. A. Galazutdinov, Y. Beletsky, and J. Krełowski. *Mon. Not. R. Astron. Soc.*, 400; 392, 2009. doi:10.1111/j.1365-2966.2009.15466.x

Western, C. M. *PGOPHER, a program for simulating rotational structure (v. 7.1.293)*. 2014. doi:10.5523/bris.huflggvpcuc1zvliqed497r2. URL `<http://pgopher.chm.bris.ac.uk>`

Whiting, E. E. and R. W. Nicholls. *Astrophys. J. Suppl. S.*, 27; 1, 1974. doi:10.1086/190286

Whiting, E. E., A. Schadee, J. B. Tatum, J. T. Hougen, and R. W. Nicholls. *J. Mol. Spectrosc.*, 80; 249, 1980. doi:10.1016/0022-2852(80)90137-X

Wiedemann, G. R., D. Deming, D. E. Jennings, K. H. Hinkle, and J. J. Keady. *Astrophys. J.*, 382; 321, 1991. doi:10.1086/170719

Wilson, A. K., T. van Mourik, and T. H. Dunning, Jr. *J. Mol. Struct.: THEOCHEM*, 388; 339, 1996. doi:10.1016/S0166-1280(96)80048-0

Wilson, W. J., P. R. Schwartz, G. Neugebauer, P. M. Harvey, and E. E. Becklin. *Astrophys. J.*, 177; 523, 1972. doi:10.1086/151729

Wood, P. In M. Jaschek and P. Keenan, editors, *Cool Stars with Excesses of Heavy*

Elements, volume 114 of *Astrophysics and Space Science Library*, pages 357–371 (Springer Netherlands, 1985)

Woon, D. E. and T. H. Dunning, Jr. *J. Chem. Phys.*, 103; 4572, 1995. doi:10.1063/1.470645

Wootten, A., S. M. Lichten, R. Sahai, and P. G. Wannier. *Astrophys. J.*, 257; 151, 1982. doi:10.1086/159973

Wunch, D., G. C. Toon, P. O. Wennberg, S. C. Wofsy, B. B. Stephens, M. L. Fischer, O. Uchino, J. B. Abshire, P. Bernath, S. C. Biraud, J.-F. L. Blavier, C. Boone, K. P. Bowman, E. V. Browell, T. Campos, B. J. Connor, B. C. Daube, N. M. Deutscher, M. Diao, J. W. Elkins, C. Gerbig, E. Gottlieb, D. W. T. Griffith, D. F. Hurst, R. Jiménez, G. Keppel-Aleks, E. A. Kort, R. Macatangay, T. Machida, H. Matsueda, F. Moore, I. Morino, S. Park, J. Robinson, C. M. Roehl, Y. Sawa, V. Sherlock, C. Sweeney, T. Tanaka, and M. A. Zondlo. *Atmos. Meas. Tech.*, 3; 1351, 2010. doi:10.5194/amt-3-1351-2010

Yeung, S.-H., M.-C. Chan, N. Wang, and A.-C. Cheung. *Chem. Phys. Lett.*, 557; 31, 2013. doi:10.1016/j.cplett.2012.11.092

Yoshida, Y., Y. Ota, N. Eguchi, N. Kikuchi, K. Nobuta, H. Tran, I. Morino, and T. Yokota. *Atmos. Meas. Tech.*, 4; 717, 2011. doi:10.5194/amt-4-717-2011

Zare, R. *Angular momentum: understanding spatial aspects in chemistry and physics* (Wiley, 1988)

Ziurys, L. M. *Proc. Natl. Acad. Sci.*, 103; 12274, 2006. doi:10.1073/pnas.0602277103